An Optical-fiber Interface to a Trapped-ion Quantum Computer

by

Tony Hyun Kim

S.B., Physics and Electrical Engineering, M.I.T., 2009

Submitted to the Department of Electrical Engineering and Computer Science
in Partial Fulfillment of the Requirements for the Degree of

Master of Engineering in Electrical Engineering and Computer Science

at the Massachusetts Institute of Technology

September 2011

Author . . . .
Department of Electrical Engineering and Computer Science
August 22, 2011

Certified by . . . .
Prof. Isaac L. Chuang
Professor of Electrical Engineering and Computer Science
Professor of Physics
Thesis Supervisor

Accepted by . . . .
Prof. Dennis M. Freeman
Chairman, Masters of Engineering Thesis Committee

An Optical-fiber Interface to a Trapped-ion Quantum Computer

by

Tony Hyun Kim

Submitted to the Department of Electrical Engineering and Computer Science
August 22, 2011
In Partial Fulfillment of the Requirements for the Degree of
Master of Engineering in Electrical Engineering and Computer Science

Abstract

The trapped-ion quantum computer is an atom-based implementation of a quantum computer that has successfully demonstrated numerous quantum algorithms and the potential for scalability. Fundamental to its operation is the short-range Coulombic interaction among its atomic ion registers, which has led to the development of *local*, single-chip devices.

In this work, we demonstrate the integration of an optical fiber with a planar ion trap, and show the physical interaction between fiber light and the trapped-ion qubit. As the single-mode fiber is well-suited to the transport of single photons, the fiber interface (when augmented by an optical cavity) represents a means to link distantly located quantum computers through a common optical network. Hence, this work represents a step towards the paradigm of *distributed* quantum computing: self-contained, technically-simple processors may be optically linked together to perform large-scale quantum computation.

This thesis is divided into two parts. In the first, we provide a thorough review of ion trap design and a detailed numerical analysis of trapped-ion motion. This theoretical discussion culminates with the development of an electronic technique that permits the arbitrary, *in situ* positioning of a trapped atom in the ion trap. The positioning ability is an enabling technology for optics integration as it allows for complete freedom in the alignment of the trapped atom with respect to the integrated element.

In the second part, the construction of the experimental setup and the integrated "fiber-trap" is described. In our experiment, a single $^{88}\mathrm{Sr}^+$ is trapped 670 μm above the end of an optical fiber in a cryogenic (8 K) surface-electrode ion trap. The fiber serves as an integrated source of laser light, which drives the quadrupole qubit transition of $^{88}\mathrm{Sr}^+$. Using *in situ* translation of the ion, the Gaussian beam profile of the fiber output is imaged, and the fiber-ion displacement, in units of the mode waist at the ion, is optimized to within 0.13 ± 0.10 of the mode center despite an initial offset of 3.30 ± 0.10 arising from fabrication. We also quantify the perturbative effects of the fiber dielectric on ion trap operation. Light-induced charging by 125 μW of 674 nm fiber light is measured as an induced electric field of ~ 10 V/m at the ion, with charging and discharging time constants of 1.6 ± 0.3 s and 4.7 ± 0.6 s. These measurements are of general importance to trapped-ion quantum computing, where the scalability of the platform depends crucially on the feasibility of on-chip optics integration.

Thesis Supervisor: Prof. Isaac L. Chuang
Title: Professor of Electrical Engineering and Computer Science
Professor of Physics

Acknowledgments

This thesis describes my research effort of the last two years in the Quanta group, advised by Prof. Isaac Chuang. At the same time, it is also a document that concludes a wonderful six years of learning at MIT. As such, there are many people to thank.

In 1997, my parents left a life of financial security and familiarity in Korea so that I may pursue the best opportunities in the world. And, from the beginning, they have supported my efforts with an open mind regardless of my meandering direction. Their sacrifice and support underlie everything that I have been able to achieve. As for this thesis, the ultimate form of Chapter 1 has been significantly molded by conversations with my father regarding the meaning of my work. And, to my sister: I hope I have been an adequate role model of an earnest, hard-working individual for you as you begin your independent life.

At EWHS, Mr. Quinn, Mr. Howell and Frau Hilson were my teachers in philosophy, math and German, who encouraged me to pursue knowledge not only for academic interest, but also as a personal passion. And, in 2004, I met Prof. Mookie Baik at Indiana University, who was reckless enough to introduce a high school junior to the subject of quantum chemistry, and to the tremendous idea that, with sufficient theoretical knowledge, the empirical world of chemistry can be simulated and understood. This experience encouraged me to seek “how things work” from the atomic level; a desire that brought me to the current experiments with isolated single atoms in the context of quantum information science.

At MIT, Prof. Bob Field had the remarkable ability to recognize my affinity for experiment before even I had realized it. He introduced me, then a sophomore, to the experimental group of Profs. Wolfgang Ketterle and Dave Pritchard, where I began the process of mapping theoretical concepts onto aspects of reality. I recall my first impression of experimental physics as sensory overload; thankfully Jae Choi and Caleb Christensen parsed the overall system and ideas into units that I could digest. Gyuboong Jo, Yeryoung Lee and Tom Pasquini also tutored me during this time. We were subsequently joined by Tout Wang. Even after leaving the Ketterle group, all BEC3 members remain good friends. In the classroom, Tom Hayes awakened my fascination for engineering in the course “Art of Electronics”; Prof. Cardinal Warde and Bill Herrington helped generalize my passion for electronics to include optics. And, more recently, I had the fortune of sitting in insightful photonics and quantum mechanics courses by Prof. Franz Kärtner.

I would also like to thank my teachers who enabled my adventures in Germany: Frau Hilson from EWHS, and Profs. Crocker and Weise, Dr. Sigrid Berka and Erin Schenck at MIT. Largely due to the excellent guidance of my company advisor Dr. Thorsten Feiweier, I had a fun and productive time working with MRI at Siemens, an inspirational technology that demonstrates to me the far-reaching potential of fundamental physics.

Back at MIT, Ike was exactly the mentor that I needed at this point of my education. Most importantly, I was given the freedom and responsibility to take an abstract idea from concept to realization. The experience of this individual and ultimately successful effort, especially given the numerous difficulties encountered along the way, leaves a deep impression as I progress to the next phase of my career. Moreover, Ike's challenge, of not only being *inspired* but to be *inspiring*, sets a new standard for myself along the various dimensions in which I interpret those words.

I was also fortunate to benefit from numerous contributions from other Quanta group members in completing this work. Chris Pearson and Taehyun Kim originally investigated the theory of the symmetric point Paul trap, and obtained experimental verification of the design using macroions. Rob Clark began the construction of the closed-cycle cryostat experiment. Dave Leibrandt began the experimental investigation of optics integration in our group, and Liz George made an early attempt at fiber-optic integration. My work is firmly rooted in those initial efforts. Yufei Ge and I initially collaborated in trying out a few of the fabrication strategies for fiber integration. My understanding of how to build helical resonators comes from reverse-engineering a donated sample from Paul Antohi. Peter Herskind is a light-wizard and the original architect of the laser distribution system utilized in lab, including a three-laser combining setup that greatly simplified the light delivery at the experiment. Peter also served as a critical editor on the papers published from this work, for which I am especially grateful. Shannon Wang is extremely meticulous in her work, and was instrumental in the proofreading and finalizing of this thesis document. She also has the most know-how regarding the experimental infrastructure of the Quanta lab, and is always eager to help. On that note, I would like to credit Jarek Labaziewicz for originating many of the ultra-reliable data acquisition and experiment control systems still in daily use. Shankari Rajagopal and I worked on implementing room-temperature and cryogenic instrumentation for use with the cryostat, which was very fun. I also benefited from and enjoyed discussions with all other Quanta and the nearby Berggren group members: Molu

Shi, Jeff Russom, Adam McCaughan, David Meyer, Nathan Lachenmyer, Sam Ocko, Simon Lu, Anders Mortensen, Amira Eltony who implemented the macro-point Paul trap featured in Fig. 2-8, Arolyn "future doctor" Conwill, Michael Gutierrez, Hans Andersen who shares my affinity for loud music in lab, Hasan Korre, Faraz Najafi.

I would also like to thank many friends who enriched my experience at MIT: Mike Vasquez, Bryan Hernandez, Enky Zurgaanjin, Chris Resto, Ylaine Gerardin, Paresh Malalur, Nevada and Ashley Sanchez, Ilan Almog, Connor McEntee, Charles Herder, Lin Lee Cheong, Grace Cheung. I am so fortunate to have met you all!

Contents

List of Figures

List of Tables

Chapter 1

Introduction

By 1990, man achieved the ability to position individual atoms with atomic precision [ES90]. Beginning with a random distribution of xenon atoms dosed on a nickel surface as shown in Fig. 1-1(a), the researchers Eigler and Schweizer demonstrated their unprecedented control over the fundamental building blocks of matter:

> To move an atom we follow the sequence of steps. . . We place the tip [of a scanning tunneling microscope] directly above the atom to be moved. . . We then increase the tip-atom interaction by lowering the tip towards the atom. . . We then move the tip under closed-loop conditions across the surface at a speed of 4 Å per second to the desired destination, dragging the xenon atom with it. The tip is then withdrawn. . . This effectively terminates the attraction between the xenon and the tip, leaving the xenon bound to the surface at the desired location.

One-by-one they produce the iconic image of Fig. 1-1(f), where the positions of 35 xenon atoms have been deliberately and individually manipulated according to human will. This image foreshadows the possibility for technology assembled at the level of individual atoms.

The technical capability that underlies the vision of "atomic electronics" today is far more intricate than the basic spatial control of individual atoms. Rather, the level of physical understanding and experimental control reaches deep into the internal degrees of freedom of an atomic system. For example, the xenon atoms that make up Fig. 1-1 are themselves composed of constituent particles – electrons bound to a nuclear core – with their own set of associated physical coordinates. This is a level of the physical world that is

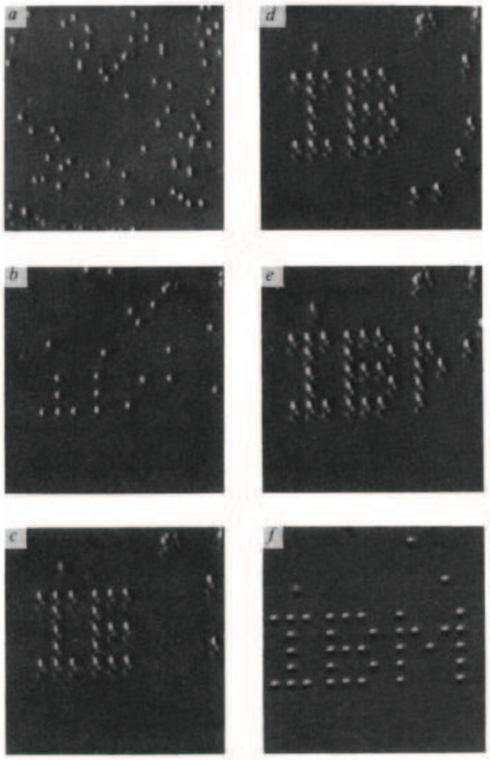

Figure 1-1: A sequence of scanning tunneling microscope images demonstrating the positioning of individual xenon atoms with atomic precision, reproduced from Ref. [ES90]. Individual atoms are “pinched” by the tip of the microscope, and are precisely positioned on a nickel surface. Each letter is 5 nm from top to bottom.

unambiguously governed by the counterintuitive and fascinating laws of quantum mechanics. Nonetheless, given the tools available to modern science, the properties of even subatomic particles can be routinely observed and probed. For instance, we[1] will demonstrate in this thesis our ability to deliberately set, manipulate, and detect the mechanical properties of a single bound electron and the orientation of its spin. The simultaneous control of both the internal state and the external position of a single atom is a major achievement of 20th century science that enables our current discussion of atomic-level electronics.

What are the ultimate implications of bottom-up device assembly from the atomic scale? Firstly, what useful systems can be designed at all that makes use of the particular mechanisms exposed by individual atoms (and molecules, and photons)? Secondly, given the concurrent industrial effort to extend the concepts of conventional electronics to the few 10 nm scale and below, what is the comparative merit of the bottom-up approach relative to

---

[1] While the current work reflects my individual contributions (unless otherwise noted), I will utilize the first-person plural “we” throughout this thesis as a stylistic device.

the top-down scheme of traditional lithography? And finally, is there a common engineering framework that integrates all of the technical components necessary for atomic electronics, so that its unique potential may be realized in practice?

1.1 Quantum information processing

What is the connection between atomic manipulation and technology in general? At the most fundamental level, all computing is implemented by physical processes: e.g. the thermal emission of electrons in a vacuum tube, the transverse field effect in a modern transistor, the representation of binary information in the charge state of a microscopic capacitor. Each illustrate the ways in which information has been encoded by the physical world. By utilizing now the states of a bound electron for the representation of information, a single atom fulfills the functional role of a computational register. Conventionally, the encoding is chosen such that a single atom represents a single *quantum bit* of information which is referred to as a *qubit*. This way, each of the 35 atoms of Fig. 1-1 could serve as a single-qubit register from which a general-purpose computer may be assembled. As a corollary, note that atomic-level electronics envisions device construction at a physical scale and density that is yet unparalleled by the typical roadmaps of conventional, transistor-based electronics.

When data is encoded in the internal state of an atomic register, any information processing must occur according to the laws of quantum mechanics. Remarkably, the basic computing logic that emerges from the principles of quantum mechanics is fundamentally distinct from classical Boolean logic which mathematically represents all computing devices hitherto explored. For one example of the difference, all basic operations of *quantum information processing* (QIP) possess the mathematical property of reversibility. (Note: we omit the discussion of quantum measurement for simplicity.) The requirement of reversibility is in stark contrast to the basic nature of Boolean logic which consists of many irreversible functions, such as the two-input not-AND (NAND) gate. Nevertheless, it has been shown that one can efficiently implement a quantum version of the the classical NAND gate by introducing extra "scratch space" for the computation [Tof80, Ben73]. Since the NAND gate is functionally complete for Boolean logic, it follows that the computational capability of a quantum mechanical computer is *at least* as powerful as classical digital electronics.

In fact, the computational power of QIP is a strict superset of classical computing. The quantum mechanical phenomena of *superposition*, *entanglement*, and *wavefunction collapse* are inextricably woven into the logic of a quantum computer with no counterparts in classical devices. We are thus left with a compelling premise. A general-purpose computer assembled at the level of individual atoms will reproduce, in principle, all of the capabilities of a modern computer at a physical scale and density that exceed the foreseeable limits of semiconductor technology. But, more profoundly, the atomic computer also introduces fundamentally new concepts and computing capability at the most primitive level of its operation.

What applications exist, then, that take advantage of the unique and exclusive capabilities of a quantum computer? As it turns out, the logic of quantum information processing is exceptionally well-suited towards the realm of information security and cryptography. We cite two prominent examples:

- In 1994, an efficient (polynomial-time) quantum computing algorithm was discovered for factorizing a large integer into its primes [Sho94], now known as *Shor's algorithm*. The supposed intractability of the prime-factorization problem is responsible for the security of the ubiquitous RSA public-key cryptosystem [RSA78]. Hence, the realization of a practical quantum computer compromises a significant portion of the modern information security infrastructure.

- On the other hand, the quantum mechanical phenomenon of wavefunction collapse yields a communication protocol that self-detects the presence of eavesdroppers [BB84]. Such quantum communication channels may be utilized for the secure distribution of cryptographic keys [a practice known as *quantum key distribution* (QKD)] that, in turn, permit absolutely secure communication between two parties guaranteed by the laws of physics [GRTZ02].

Not long after their theoretical discovery, each of these quantum algorithms were validated experimentally. Shor's algorithm, for instance, was demonstrated in a proof-of-principle system [VSB$^+$01], and quantum key distribution packages are even available commercially [LWW$^+$10] for applications requiring utmost secrecy.

We shall relegate the more extensive discussion of quantum information science to general reviews such as Ref. [NC00]. Fascinating historical accounts are also given in the introductions of Refs. [Sho96, GRTZ02] which are highly recommended. For now, we cite two more examples that highlight the surprising applicability of quantum mechanical logic i.e. superposition and entanglement.

Consider the problem of unstructured search: we seek to identify a unique item in a database of N-elements that satisfies some search criterion. With no prior organization of the database (i.e. prior sorting), it is readily apparent that one has to examine on average $N/2$ elements against the criterion to obtain the desired item. However, when this problem of "searching for a needle in a haystack" is formulated for a quantum computer, it is found that only $O(\sqrt{N})$ comparisons against the criterion are necessary for the solution [Gro97]! The technological implications of fast quantum search are discussed in Ref. [Bra97]. At its core, this counter-intuitive result owes to the mechanism of superposition: the initial "search query" is prepared so that it represents all database elements simultaneously through quantum superposition.

Finally, the quantum mechanical property of entanglement imparts non-local correlations between pairs (or more) of particles. In the current context, if two atomic registers are prepared in an entangled state, the manipulation and measurement of one of the atoms has an instantaneous consequence on the entangled partner even when the pair is physically separated by an arbitrarily large distance. One may then wonder whether such "action at a distance" can be employed for useful purposes. In accordance with the laws of causality, however, it is known that entanglement does not permit instantaneous information transfer. Nevertheless, it was discovered in 1993 that entanglement is a basic resource for achieving non-instantaneous *teleportation* of quantum information: a qubit can be transferred from one node of a distantly-separated entangled pair to another without being physically transmitted through the intervening space [BBC$^+$93]. One natural application of teleportation lies again in the field of information security. Given a shared pool of entangled pairs, two communicating parties may transfer the qubit stream of the QKD protocol directly to one another through teleportation. As a result, not only does the protocol self-detect the presence of eavesdroppers, it never even exists in the intervening space where the messages are likely to be intercepted!

These are a few of the remarkable applications that await the realization of a practical quantum computer – envisioned in this thesis in the form of atomic electronics. Let us now examine some of the fundamental considerations in the experimental pursuit of an atom-based quantum processor.

1.2 Trapped-ion quantum computer

So far, we have motivated the possibility of an atom-based quantum computer based on our technical capability to regard a single atom as a single-qubit computational register. However, a general-purpose processor clearly involves many components in addition to information storage. Throughout this thesis, we will examine many of these additional requirements in detail, e.g. the tools that allow for detection of single atoms and the manipulation and readout of their internal states, etc. Here, we introduce the fundamental concepts of *quantum interconnect* and *decoherence*, and explain how the platform of *trapped-ion quantum computing* offers a roadmap for the experimental realization of an atom-based quantum processor.

1.2.1 Quantum interconnect

In both classical and quantum computing, any nontrivial information processing operation involves more than one (qu)bit. Indeed, the basic physical mechanism that underlies all existing digital logic is the use of the transistor as a switch, where one *gate* voltage influences the value taken by another *drain* voltage. Similarly, when multiple qubits are encoded in distinct atoms, we must also devise an inter-atomic physical interaction that mediates the information content of each atom. If this interaction is consistent with the unitary dynamics of quantum physics, we shall refer to that physical mechanism as a *quantum interconnect*.

In the engineering of an atom-based processor, what quantum interconnect is available to link together the information contained in distinct atomic registers? The list of possible mechanisms is narrowed by recognizing that the dominant interactions at the atomic scale are electromagnetic in nature. (This fact is readily apparent by recalling that an atom is composed of negatively-charged electrons bound electrostatically to a positively-charged nucleus.) However, while powerful electromagnetic forces are present inside of an atom, the forces between separate atoms are much weaker since the atom is charge-neutral as a whole. Thus, to engineer an appreciable physical interaction among the constituent parts of the proposed processor, we will base our design around *atomic ions*, in which one of the bound electrons has been removed (i.e. *ionized*) to give the atom an overall positive charge.

When every atom possesses a net positive charge, there exists $1/r^2$-Coulomb interaction among all pairs that can be used to communicate the information content of one atom to another. The paradigm of using the Coulomb force between atomic ions as a quantum interconnect was proposed in Ref. [CZ95], and further advanced by work such as Ref. [SM99]. The basic concept is as follows: using precise laser pulses, we impart a mechanical vibration (a "kick") on an atom that is conditioned on its internal qubit state. The modulated vibration is transmitted to neighboring atoms through the Coulomb force. This way, a distant atom can receive mechanically the qubit content of the original, "kicked" atom. Soon after its theoretical proposal, the Coulombic quantum interconnect has become a foundation for atom-based quantum information processing [BW08].

The use of ion registers and the Coulombic interaction as a quantum interconnect has two practical consequences that are relevant to this thesis work. Firstly, since our atomic registers are positively charged, the atoms will always repel one another and an external "trapping" force is required to stabilize the overall system. The apparatus that provides the confining potential is called an *ion trap*, which will be discussed shortly. Secondly, given the $1/r^2$-falloff in the strength of the Coulombic force, all interacting atomic registers must lie in close spatial proximity. At the time of writing, typical ion-ion distances in the Coulombic interconnect are on the order of a few micrometers, with a record separation of 50 μm [HLB$^+$11, BOC$^+$11].

1.2.2 Decoherence

What is the fundamental challenge, then, in the experimental construction of a large-scale quantum computer? Today, it is understood that the core difficulty lies in the extreme fragility of quantum information [LJL$^+$10]. The ion registers, for instance, interact not only with one another but with all other charged entities in its vicinity. These extraneous and uncontrolled interactions can perturb the encoded qubit from its intended computational role, a phenomenon known as *decoherence*. As an additional example, an atom in empty space is perturbed by random fluctuations of the vacuum electromagnetic field, which leads to decay of a qubit towards the system's ground state.

In the literature, decoherence is extensively studied both experimentally (e.g. what is the phenomenology and mechanism of decoherence [TKK$^+$00, DOS$^+$06]; how can its rates be reduced [LGA$^+$08]) as well as theoretically (e.g. can quantum algorithms be performed in the presence of finite decoherence [CLSZ95]; are there error-correcting protocols that permit universal quantum computing despite decoherence [CS96]; are certain encoding schemes

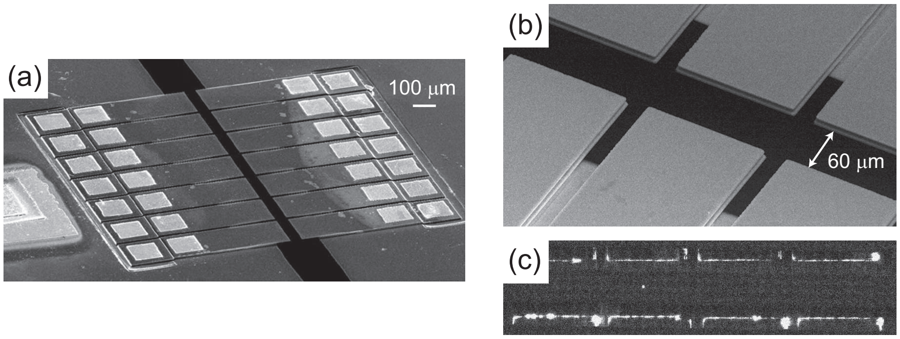

Figure 1-2: A modern ion trap implemented in a semiconductor chip, reproduced from Ref. [SHO$^+$06]. The rectangular pads seen in panels (a,b) generate electromagnetic fields that can confine a charged particle in the gap between the electrodes. Panel (c) shows a single Cd$^+$ atomic ion trapped halfway in the 60 μm gap between the electrodes.

less susceptible to particular forms of decoherence [LW03]) For this thesis, a much more primitive view suffices: uncontrolled interactions of a qubit register with its environment leads to decoherence – i.e. loss of quantum information – which is a clear impediment to quantum computation. Thus, to realize a practical quantum computer, the ion registers must be isolated from its environment as much as physically possible.

1.2.3 Microfabricated ion traps

The ion trap is a Nobel prize-winning invention that has led to advances in fundamental science as well as wide applications in industry as a mass spectrometer [Pau93, Gho95]. More recently, the ion trap has also become the essential hardware for atom-based quantum computation [SKHG$^+$03].

A modern incarnation of the ion trap, intended for quantum computing, is shown in Fig. 1-2 [SHO$^+$06]. As shown in panels (a) and (b), the ion trap consists of many electrodes that generate specifically-shaped electromagnetic fields which are used to “trap” charged particles in otherwise empty space. In panel (c), a single Cd$^+$ atomic ion is trapped halfway in the 60 μm gap between the electrodes. (The discussion of the exact trapping mechanism and ion trap design is a major part of this thesis, and is postponed until Chapter 2.) Note that the ion trap satisfies the basic requirements noted in our prior discussion of the Coulombic quantum interconnect and decoherence. Firstly, the device provides the confining forces that are necessary to stabilize a collection of self-repelling ions. Secondly, the ions are trapped in empty space (as opposed to lying on a material surface as in Fig. 1-1),

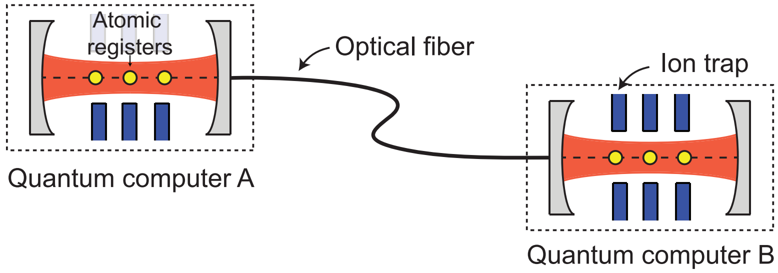

Figure 1-3: The optical fiber as an arbitrary-distance quantum interconnect between physically separated trapped-ion quantum computers.

where the quantum computer is isolated from material contaminants on the surface that can contribute to excess decoherence [DOS$^+$06].

A crucial aspect of modern ion trap technology, as implied in Fig. 1-2, is that its construction is compatible with the planar microfabrication techniques originating from the microelectronics industry. This means, in principle, that the overall size of the trapped-ion quantum computer may be readily scaled to accommodate arbitrarily many ion registers [KMW02]. To date, a fully-instrumented "programmable" two-qubit processor has been demonstrated [HHJ$^+$10], and up to 14 ions have been simultaneously involved in a single quantum operation [MSB$^+$11].

1.3 An arbitrary-distance quantum mechanical interconnect

In parallel to the efforts in developing *localized* quantum computers based on the Coulombic interconnect, the current work is motivated by the vision of a *distributed* quantum computer based on an arbitrary-distance *optical quantum interconnect*.

For the basic intuition, recall that the infrastructure of the modern Internet consists of a worldwide optical fiber network that routes information between distantly-located computing nodes. As shown in Fig. 1-3, we wish to extend the same concept to QIP, so that distantly-located trapped-ion quantum computers (we show just two) may communicate to one another through an optical fiber network. The combination of localized processors with a long-distance distributed network would not only have immediate applications in aforementioned quantum cryptography and teleportation, but it also provides an organizational principle for the construction of large-scale systems: i.e. self-contained, technically-simple processors may be linked together to perform large-scale quantum computation, provided that they possess a “networking port” in the form of an optical fiber.

Hence, the basic objective of this work is to develop the necessary hardware for an optical interconnect, by integrating an optical fiber with a trapped-ion quantum computer and demonstrating the physical interaction of the fiber light with the trapped ion.

To be more precise, the optical fiber is just one part of a complete optoelectronic system that implements the optical quantum interconnect. The fundamental physics that underlies such a network is the transfer of quantum information stored in the ion register into the quantum mechanical state of a single photon. The unitary conversion between atomic and photonic qubits may be performed with the aid of state-of-the-art optical cavities that enhance the atom-photon coupling rate relative to the decoherence channels associated with such a system [HWS+11]. The fiber provides the means to extract the photonic qubit from the cavity, and allows it to be routed with high fidelity to distantly-located quantum computers. Through such an infrastructure, the entanglement generated among local ion registers in a single trapped-ion quantum computer can be distributed to other nodes of the network to enable large-scale applications [CZKM97].

Let us make one technical comment regarding optical fibers at the outset. Today, optical fibers are available in many different types with various waveguiding properties which owe to their differing physical construction. In this thesis, we shall make a particular distinction between *single-mode* and *multi-mode* fibers. The reason is the following: when a single photon is being transported along a multi-mode fiber, its quantum information couples easily to the many optical modes supported by the structure, so that it is generally impossible to reconstruct the original state following propagation. Conceptually, a photonic qubit in a multimode fiber suffers high rates of decoherence. In contrast, a single-mode fiber is ideally suited for the coherent transport of a single photon over kilometer length-scales [GRTZ02, TBZ+98]. Such kilometer-length optical links may be cascaded and extended over arbitrary distances by the use of quantum repeaters [BDCZ98, DLCZ01]. On the other hand, the integration of a single-mode fiber demands significantly greater technical precision in experimental fabrication, as its feature sizes are generally an order-of-magnitude smaller than those of multi-mode fibers.

In the remainder of this thesis, we provide a technical documentation of the fiber-integration project. Before we begin, let us briefly reflect on the historical trajectory that precedes the quantum optical network envisioned in Fig. 1-3.

It is well-known that the development of quantum physics in the 20th century was fraught with controversies and paradoxes regarding the implications of the theory. Historically, one of the most contentious aspects of quantum mechanics has been the non-local correlation implied by quantum entanglement. Indeed, in 1935, Einstein and coworkers famously raised the question "Can Quantum-Mechanical Description of Physical Reality Be Considered Complete?" in which they argued, assuming *a priori* the physical impossibility of non-local correlations, that quantum physics failed to predict knowable properties of certain (entangled) physical systems. Their logical conclusion was that an alternate theory must exist that captures the variables that are "hidden" to quantum mechanics [EPR35].

The ensuing debate, now known as the *EPR paradox* after the original authors, touches upon many foundational themes in the philosophy of physics: e.g. the locality of a physical interaction, the causality between events, the nature of wavefunction collapse, and the possibility of a non-quantum *hidden-variable* theory. The conceptual breakthrough came in 1964 when J. S. Bell showed that there are measurable consequences that distinguish between the non-local quantum theory of entanglement and all other (local) hidden-variable theories [Bel64]. In the ensuing decades, numerous tests involving "naturally occurring" entangled systems were performed [KMWZ95, WJS$^+$98] that confirmed the non-locality of quantum entanglement as a part of physical reality. To resolve the apparent conflict between non-local "action at a distance" and relativian causality, the analysis of entanglement was refined to show that one could not perform instantaneous transfer of information through the non-local correlations. Thus, the non-local nature of quantum entanglement became a part of the accepted physics paradigm. However, it remained more-or-less a curious fact of nature: a mechanism to test the validity of quantum physics but little more.

The most recent development of this story is the discovery of the teleportation protocol in 1993, which demonstrated that remote entanglement is not only a fact of nature but a means to achieve information processing. This discovery profoundly altered the common-sense expectations regarding what useful systems can be engineered in the physical world. Since then, the pursuit of quantum information science has yielded man-made systems such as the trapped-ion quantum computer in which entangled states can be generated "on demand." The distributed quantum network of Fig. 1-3, which motivates the current work, represents the needed infrastructure to consume such "engineered entanglement" to enable the purposeful use of quantum mechanical reality.

1.4 Scope and outline of the thesis

The objective of this thesis is to design and implement a trapped-ion quantum computer with an integrated optical fiber interface to the trapped atom. To this end, the current work makes two main contributions:

1. **We demonstrate for the first time a planar ion trap with a built-in, single-mode optical fiber.** In our system, the internal qubit state of a trapped ion can be accessed through the integrated port that appears, at the "input" end, as a conventional optical fiber. When augmented by an optical cavity, the integrated fiber may serve as part of a long-distance quantum interconnect between physically separated trapped-ion quantum computers.

2. **We implement a novel electronic technique for ion traps that achieves arbitrary positioning of the trapped atom.** The positioning technique is an enabling technology for general integrated-trap development (such as our fiber-trap system), as it allows complete freedom in the alignment of the atom with respect to the integrated element.

In the first part of this thesis, we focus on the theoretical aspects of ion trap design. We will begin with an basic explanation of the confinement mechanism in an ion trap, then introduce a series of increasingly sophisticated numerical models that capture the dynamics of a trapped atomic ion. After developing these foundations, we present an advanced electronic technique for ion traps that enables arbitrary spatial manipulation of a single atom in the device. A detailed synopsis of the first part of the thesis is given below:

- In Ch. 2 – Ion trap fundamentals, we explain the basic principle of operation underlying radiofrequency (RF) ion traps. We acquaint the reader with standard terminology and concepts used in the field of ion traps. Furthermore, we introduce the basic *point Paul trap* design, which is central to our fiber-integration project.

- In Ch. 3 – Atomic motion in the fiber mode, we develop a precise numerical model for the motion of an atomic ion under laser cooling. A quantitative understanding of ion motion is necessary due to the finite spatial extent of the fiber mode.

- In Ch. 4 – RF ion positioning, a novel electronic technique is introduced that achieves arbitrary spatial manipulation of an atom in the ion trap. Arbitrary translation of the ion is an enabling technique for fiber-ion integration, as it allows us to overcome any alignment errors arising from trap fabrication.

In the second part of the thesis, we discuss the experimental aspects of trapped-ion quantum computing. We begin with a description of our apparatus which is unique in its remarkably short turnaround-time (12 h) compared to typical atomic experiments. We then document the implementation of the fiber-integrated trap.

- In Ch. 5 – Experimental setup, we give a technical account of the experimental apparatus that enables atomic ion trapping. We have conceptualized the requirements for successful ion trapping along four main components: vacuum, ion source, electronics, and laser light. We provide an extensive discussion of each of these topics. This chapter is written as a practical guide for future experimental work.
- In Ch. 6 – Surface-electrode ion trap with an integrated light source, we report on the design, fabrication, and experimental validation of a surface-electrode ion trap with an integrated single-mode fiber as an interface to the internal state of a trapped atom.

Finally, in Ch. 7 – Outlook, we suggest future research directions based on the accomplishments of this work.

1.5 Acknowledgments and publications

While the majority of the work described in this thesis are my own contributions, I was also fortunate to benefit from other Quanta group members in completing this work. Chris Pearson and Taehyun Kim originally investigated the theory of the symmetric point Paul trap, and obtained experimental verification of the design using macroions [Pea06]. Rob Clark began the construction of the closed-cycle cryostat experiment [Cla09]. Dave Leibrandt began the investigation of optics integration in our group [Lei09], and Liz George made an early attempt at fiber-optic integration [Geo08]. My work is firmly rooted in those initial efforts. My understanding of helical resonators comes from reverse-engineering a donated sample from Paul Antohi, and Peter Herskind architected the laser distribution system utilized in lab, including a three-laser combining setup that greatly simplified the light delivery at the experiment. Peter also served as a critical editor on the papers published from this work, for which I am especially thankful. Shankari Rajagopal assisted me in the development of electronic instrumentation for the cryogenic experiment.

Parts of this thesis have been published in the following journal articles:

- **Tony Hyun Kim**, Peter F. Herskind, Taehyun Kim, Jungsang Kim, and Isaac L. Chuang. Surface-electrode point Paul trap. *Physical Review A*, 82:043412, 2010.
- **Tony Hyun Kim**, Peter F. Herskind, and Isaac L. Chuang. Surface-electrode ion trap with integrated light source. *Applied Physics Letters*, 98:214103, 2011.

Chapter 2

Ion trap fundamentals

The basic principle of operation underlying radiofrequency (RF) ion traps is the use of oscillating electric fields to confine and isolate charged particles in free space. The origin of the technique lies in the fields of molecular beam physics, mass spectrometry and particle accelerator physics, where electromagnetic fields are used to lense and focus charged particle trajectories [Pau93]. Today, the ion trap is an essential hardware for quantum metrology [MBH$^+$04] and quantum information science [BW08], as isolated particles in free space (in vacuum) represent ideal qubit registers in a low-decoherence environment.

In this chapter, we develop a physical intuition for the mechanism of RF ion trapping:

- Ions can have bounded trajectories about the node of an oscillating electric field, provided that the electric field has a "quadrupole" shape (Section 2.1).
- Ion motion in an RF quadrupole field is given by the Mathieu equation (Section 2.2).
- A suitable arrangement of electrodes on a 2D plane, i.e. a "surface-electrode" design, can give rise to a quadrupole electric field (Section 2.3).

We also perform a detailed mathematical analysis of a specific surface-electrode design, known as the point Paul trap, that is central to this thesis (Section 2.4). Early work on the basic, *symmetric* point Paul trap was initiated in the Quanta group by Chris Pearson [Pea06] who verified the design using macroions. I subsequently implemented and published the design for atomic ion trapping [KHK$^+$10], and developed the *asymmetric* variants of the design (Section 2.5) which were crucial for the eventual fiber integration.

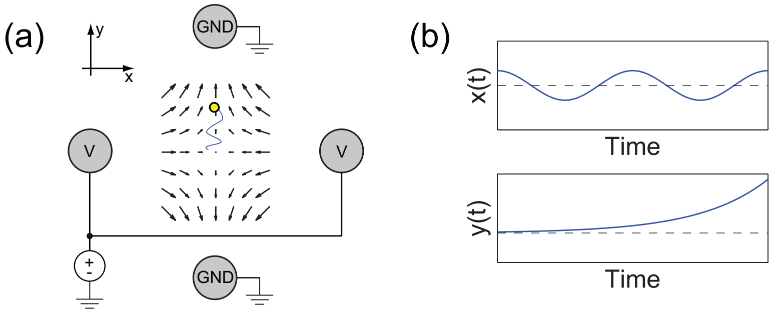

Figure 2-1: Unbounded motion of an ion in a static quadrupole electric field. (a) An arrangement of four metal rods (running normal to the page) biased to a DC voltage V giving rise to a quadrupole electric field (Eq. 2.1) at the center of the assembly. The origin of the coordinate system is at the nodal point of the quadrupole field. Yellow circle represents an ion and the blue trace its trajectory in the static field. (b) The ion experiences bounded harmonic motion along x, but exponential runaway from the node along y.

2.1 Charged particle in an oscillating quadrupole field

Consider a point particle with charge Q and mass M in a static, two-dimensional *quadrupole* field given by

$$\vec{E}_{\text{quadrupole}}(\vec{x}) = -Vf \cdot (x\hat{e}_x - y\hat{e}_y) \tag{2.1}$$

where f is a scalar constant of unit [length]$^{-2}$ that represents the "slope" of the quadrupole field per unit voltage, and $\{\hat{e}_i\}$ are basis vectors[2]. Such a field geometry may originate from an arrangement of four metal rods, two of which are biased at a DC voltage V as shown in Fig. 2-1(a). The equation of motion is trivially decoupled into the x- and y-components as

$$\begin{aligned} M\ddot{x} &= -QVf \cdot x && (2.2) \\ M\ddot{y} &= +QVf \cdot y, && (2.3) \end{aligned}$$

yielding bounded (i.e. "trapped") simple harmonic motion in x, but exponentially unbounded motion in y as shown in Fig. 2-1(b). The observation that charged particles cannot be stably trapped in free space by static electric fields is a well-known mathematical result known as *Earnshaw's theorem*. We are thus motivated to examine nonstatic field configurations in order to achieve stable charge confinement.

Clearly, the quadrupole field of Eq. 2.1 is insufficient for ion confinement because only

---

[2] In this thesis, vectors are denoted by an arrow as in $\vec{x}$, or by a caret $\hat{x}$ in the case of unit vectors. Dot products will be denoted by an explicit transpose as in $\vec{x}^T \cdot \vec{y}$. Matrices are indicated by a boldface as in $\mathbf{A}$.

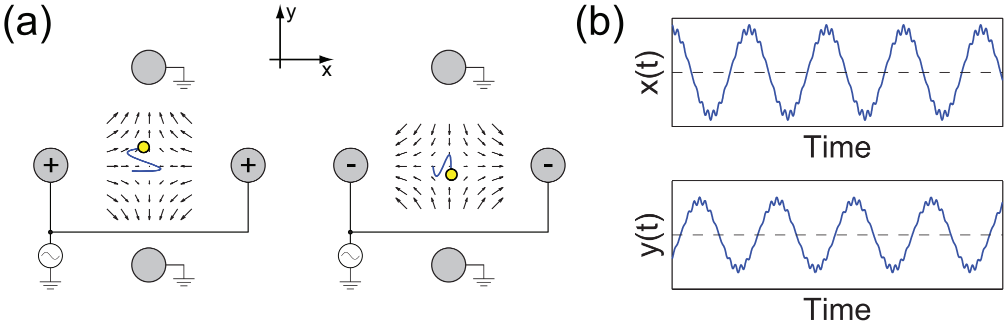

Figure 2-2: Bounded ("trapped") motion of an ion in an oscillating quadrupole field. (a) Applying a sinusoidal source to the previously DC-biased rods will result in oscillation of the sign of the quadrupole field. Both + and − phases of the field are illustrated. (b) Possible solution trajectories for the ion in the oscillating field are shown. Note that the equations of motion along x and y are equivalent up to a time-translation.

one of the two directions x or y may be stable for any given sign of f, leaving the other statically unstable. Intuitively, we can then attempt to "time-multiplex" the stability between the x- and y-directions, by rapidly oscillating the sign of the quadrupole coefficient f, in order to attain possibly a "time-averaged" stability along both x and y. A simple implementation of this idea is to apply a sinusoidal RF source, again at amplitude V and at frequency $\Omega = 2\pi \times f_{\mathrm{RF}}$ to the two previously DC-biased rods. This physical configuration is illustrated in Fig. 2-2(a), and essentially constitutes the original quadrupole RF ion trap invented by Wolfgang Paul in 1953 [PS53]. Writing explicitly the time-variation, we find that the equations of motion in Eqs. 2.2-2.3 are modified to

$$M\ddot{x} = -QVf\cos(\Omega t)\cdot x \tag{2.4}$$

$$M\ddot{y} = +QVf\cos(\Omega t)\cdot y. \tag{2.5}$$

Conceptually, the RF frequency Ω can be interpreted as a rate at which stability is multiplexed between the x- and y-directions. Note that the sign difference between Eqs. 2.4 and 2.5 can now be absorbed into the phase of the sinusoid, and hence the functional form of solutions along the two directions are expected to be mathematically identical, unlike the case of the DC quadrupole.

The time-varying differential equations in Eqs. 2.4-2.5 no longer possess trivial solutions. Indeed, depending on the coefficients Q, V, f and Ω, there can exist both bounded and unbounded trajectories. However, these equations are instances of the well-known Mathieu differential equation, which are known to yield bounded solutions [e.g. Fig. 2-2(b)] in a small region of parameter space, as we will show in the following section. This is the essential mechanism underlying RF traps: ions are dynamically confined about the node of an oscillating quadrupole electric field by stability multiplexing. Hence, any electrode configuration that gives rise to such a field can potentially be utilized as a RF ion trap.

2.2 The Mathieu equation

The canonical Mathieu equation is given by

$$\frac{d^2x}{d\tau^2} + (a_x + 2q_x \cos 2\tau) \cdot x = 0, \tag{2.6}$$

with nondimensional Mathieu parameters a and q. The x equation of motion (Eq. 2.4) is shown to be equivalent to the canonical form by defining a nondimensional time $\tau = \Omega t/2$, and by setting $a_x = 0$ and $q_x = \frac{2QVf}{M\Omega^2}$. Note: for all trap designs presented in this thesis, the Mathieu a-parameter is zero. Also, $q_y = -q_x$ in the analogous equation for y.

The Mathieu equation has been extensively studied and its mathematical properties tabulated [AS64], as it describes a large variety of physical phenomena such as the mechanical vibration of elliptical membranes. In this thesis, however, we will emphasize a numerical understanding of the Mathieu equation (Section 2.2.1), as we will quickly build on Eq. 2.6 to account for additional experimental complications associated with the task of optics-integration in a surface-electrode, atomic ion trap (Section 2.2.2).

2.2.1 Numerical trajectories

The only independent parameter in the Mathieu equation is $q_x = \frac{2QVf}{M\Omega^2}$. Given a target ion, the charge-to-mass ratio Q/M is determined. However, one can choose RF parameters $\{\Omega, V\}$ arbitrarily, as well as the field coefficient f by trap design. Thus the Mathieu q-parameter is tunable over a wide range, and, in applications of ion trapping, typically ranges from $|q| = 0.05$–0.3. It can be mathematically shown, that the Mathieu equation yields bounded solutions for $|q| < 0.9$ [WMI$^+$98].

Fig. 2-3 shows solutions to the Mathieu equation for a series of Mathieu q-parameters, with an initial condition of $(x, \dot{x}) = (1, 0)$. To aid the discussion, the power spectral density

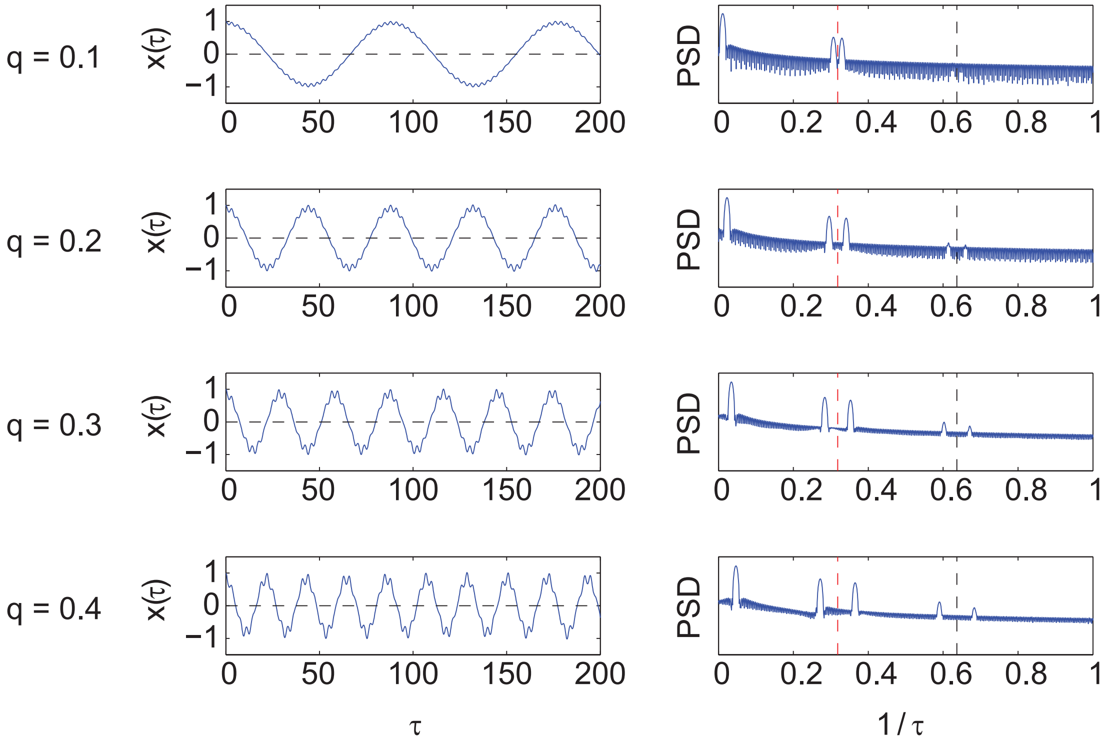

Figure 2-3: Solutions to the Mathieu equation in both (nondimensional) time and frequency domains for a variety of Mathieu q-parameters relevant to ion trap experiment. In the time domain, the trajectory can be conceptually divided into a slow *secular* motion, and a superimposed, fast *micromotion* which occurs at sidebands of the RF frequency $1/\pi \approx 0.32$ (dashed red line).

(PSD) of each trajectory is also presented in a log-y plot. Note that the analysis is performed in nondimensional time τ. We observe the following:

- For q-parameters up to 0.3, the ion trajectory is clearly dominated by a relatively large-amplitude, "low-frequency" sinusoidal motion, known as the *secular motion* of the ion. The *secular frequency* increases with the q-parameter.

- The trajectory also contains small-amplitude, high-frequency motion, which is known as *micromotion*. Micromotion occurs at secular frequency sidebands of the harmonics of the RF drive. (In nondimensional time τ, the RF drive is represented by $\cos(2\tau)$ and hence the RF frequency is $f_{\mathrm{RF}} = \frac{2}{2\pi} = \frac{1}{\pi} \approx 0.32$.)

- The amplitude of the micromotion, relative to the amplitude of the secular motion, apparently increases with q.

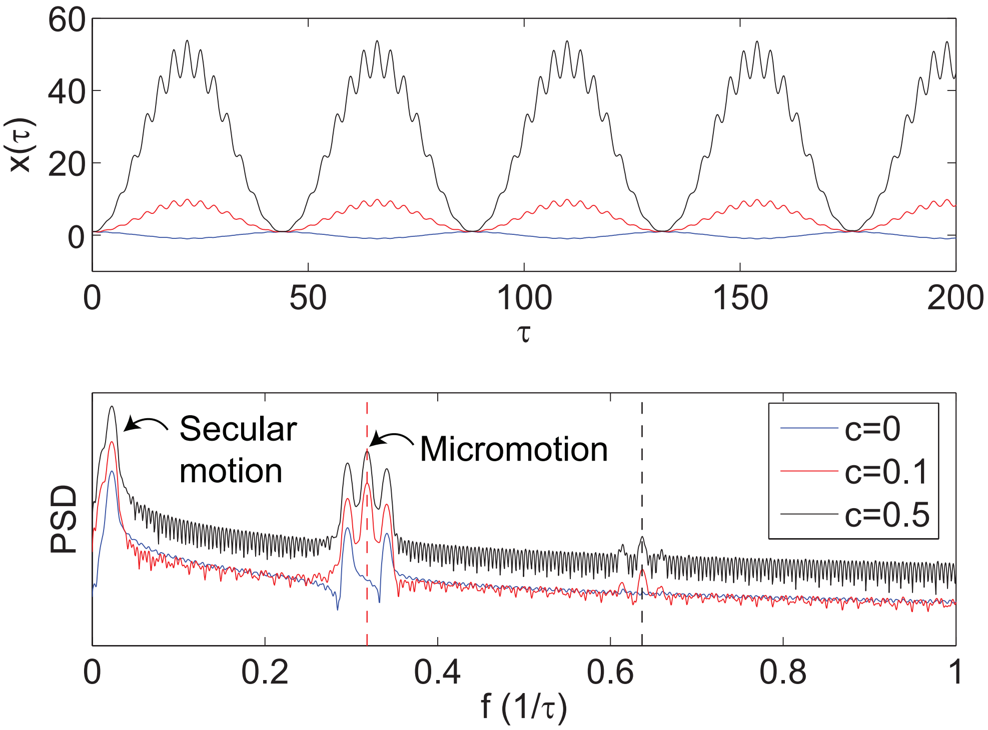

Figure 2-4: The effect of the stray field term c in the Mathieu equation (Eq. 2.7) for $q = 0.2$. Stray field can increase the amplitude of the trajectory by over an order of magnitude at experimentally observed stray field strengths of few 10 V/m ($c \approx 0.1$), contributing to both secular and micromotion components. PSDs have been highpass-filtered in order to remove DC offset and highlight the oscillatory components.

The clear dominance of secular motion in the numerical solutions motivates the definition of a conservative harmonic potential, especially in the regime $q \ll 1$. We will return to this mathematical idea in Section 2.4 after we introduce the specific trap design that will be used throughout the thesis.

2.2.2 DC compensation

In an actual ion trap experiment, the charge environment in the vicinity of the ion cannot be perfectly controlled. For example, the ion source, in addition to providing the desired ion for trapping, will in general contaminate the experimental environment with charge [BLW⁺07]. If the charge environment evolves at a slow timescale, the effect can be modeled by the inclusion of a DC stray field $\vec{E}_{\text{stray}}$ in the ion's equation of motion as

$$M\ddot{\vec{r}} = Q\left(\vec{E}_{\text{quadrupole}}(\vec{r}) \cdot \cos\Omega t + \vec{E}_{\text{stray}}\right). \tag{2.7}$$

The stray field can be captured in the canonical Mathieu equation (Eq. 2.6) by the inclusion of a constant driving term $c = \frac{4Q}{M\Omega^2} \cdot E_{\text{stray}}$ with units of $[x]$, as in

$$\frac{d^2x}{d\tau^2} + (a_x + 2q_x \cos 2\tau) \cdot x = c. \tag{2.8}$$

As shown in Fig. 2-4 for $q = 0.2$, a nonzero c can have immense influence on the character of the solution. In particular, stray field increases the amplitude of the trajectory by over an order of magnitude at experimentally observed stray field strengths of few 10 V/m ($c \approx 0.1$), contributing to both secular and micromotion components. Note that stray field-induced, "excess" micromotion occurs at the RF frequency rather than at its sidebands as was the case for "intrinsic" micromotion that was shown in Fig. 2-3. In the context of trapped-ion quantum computation, any excess ion motion is extremely detrimental as it results in broadening of atomic transitions [BMB+98] and, in integrated-traps, contributes to uncertainty in the interaction strength between the ion and integrated element due to time variation in their spatial overlap. In other cases, stray fields can even prevent stable trapping. Surface-electrode trap designs are especially susceptible to stray field-induced instability due to their significant non-quadrupolar component in the field profile (see Section 3.4). When the stray field at the ion is nulled by deliberately superposing DC potentials through additional trap electrodes, the ion is said to be "compensated."

2.3 Surface-electrode point Paul trap

The traditional ion trap is a three-dimensional structure requiring precise machining in its construction and careful assembly, such as the four-rod linear Paul trap shown in Fig. 2-5(a). Recently, however, the four-rod trap has been transformed into a two-dimensional structure, above which ions can be trapped [CBB+05]. This new class of *surface-electrode* or *planar* ion traps offer a tremendous advantage over their predecessors in that electrodes can be defined lithographically with extremely high precision, and that construction can leverage the techniques of microfabrication, with the possibility of directly integrating technologies such as CMOS electronic devices [KPM+05] and on-chip photonics [KK09]. These aspects are particularly attractive to trapped-ion quantum information processing where limitations currently, by a large degree, pertain to the scalability of devices for trapping as well as other elements of infrastructure such as optics, laser light delivery and control electronics.

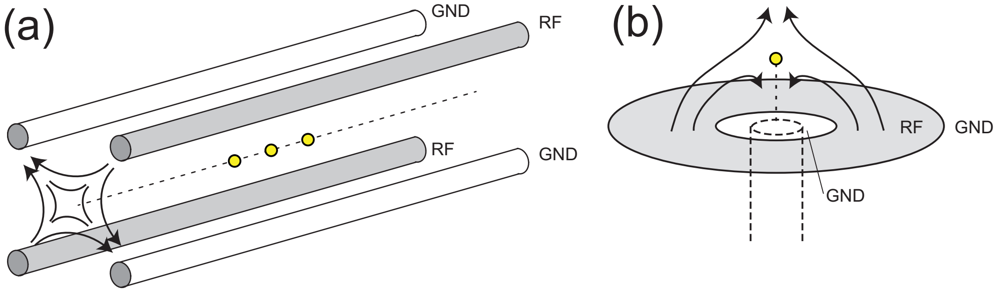

Figure 2-5: Comparison of the traditional four-rod linear Paul trap (a) to the surface-electrode point Paul trap (b). Arrows indicate electric field. The latter design achieves quadrupole ion confinement through RF on a single, ring-shaped electrode. Dashed lines suggest how cylindrical elements, such as optical fibers, may be introduced to the point Paul geometry.

2.3.1 The generic point Paul trap

Fundamental to this thesis work is a type of surface-electrode trap with a circular symmetry in its electrode geometry [KHK$^+$10, Pea06]. The generic design of this trap, which we shall refer to as the *point Paul trap*, is shown in Fig. 2-5(b) and may consist of any number of concentric electrodes of arbitrary widths to which different voltages can be applied. The axial symmetry of the trap is intended to facilitate the integration of optical elements, such as fibers, that also possess similar symmetry. The optical fiber, for instance, can be introduced through the electrodes directly beneath the ions with minimal perturbation of the trapping fields. Another unique feature of the point Paul trap design is that confinement is achieved in three dimensions using only an RF field [SGA$^+$05] as opposed to linear trap designs that also require a static DC quadrupole along the axis defined by the nodal line of the RF quadrupole field [Hou08]. This simplicity enables, as we show in Chapter 4, a robust electronic method for precise *in situ* ion positioning and therefore a procedure for correcting any ion-fiber alignment error that arises from trap fabrication. For now, our immediate tasks are to:

1. Demonstrate that the electric field profile corresponding to the point Paul geometry contains a quadrupole node, and
2. Relate the details of the quadrupole field (location, shape, strength, etc.) to the electrode geometry and the RF drive.

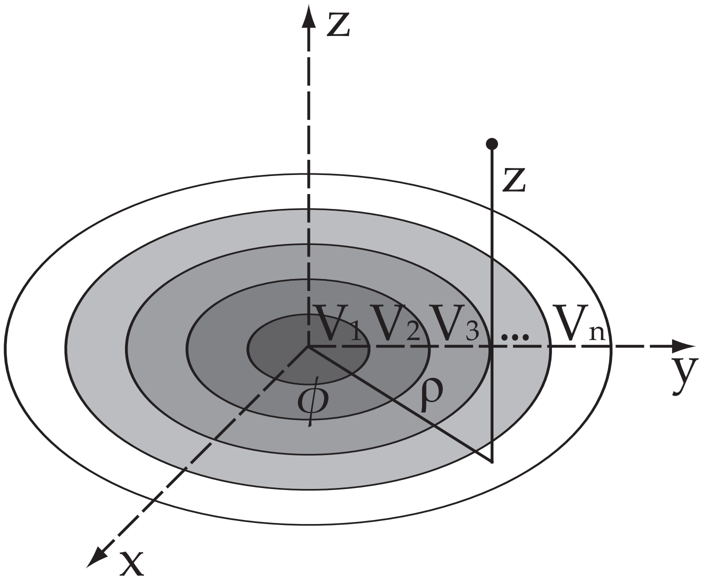

Figure 2-6: The generic layout of the point Paul trap, which consists of concentric annular electrodes (denoted by shading) with arbitrary widths.

2.3.2 Electric potential from annular planar electrodes

The generic point Paul trap consists of an arbitrary number of circular electrodes, as shown in Fig. 2-6. Our first step is to determine the electric potential Φ in the upper half-space $z \geq 0$ for any instantaneous configuration of the voltages $\{V_i\}$.

We begin with the general solution to the Laplace equation in charge-free space, expressed in cylindrical coordinates for $z \geq 0$ [Jac99]:

$$\Phi(z, \rho, \phi) = \sum_{m=0}^{\infty} \int_0^{\infty} e^{-kz}\ J_m(k\rho)\ \left[\mathcal{A}_m(k) \cos(m\phi) + \mathcal{B}_m(k) \sin(m\phi)\right] dk, \tag{2.9}$$

where $J_m(k\rho)$ are the Bessel functions and $\mathcal{A}_m(k)$ and $\mathcal{B}_m(k)$ are coefficients to be determined based on the boundary conditions of the problem. Based on the azimuthal symmetry of the point Paul trap (Fig. 2-6), there cannot be any dependence on ϕ, and hence Eq. 2.9 simplifies to:

$$\Phi(z, \rho) = \int_0^{\infty} e^{-kz}\ J_0(k\rho)\ \mathcal{A}_0(k)\ dk. \tag{2.10}$$

The expansion coefficient $\mathcal{A}_0$ can be related to the physical dimensions of each annular ring and its voltage as $\mathcal{A}_0(k) = \sum_i^n A_i(k)$, where

$$A_i(k) = kV_i \int_{\alpha_i}^{\beta_i} \rho J_0(k\rho) d\rho \tag{2.11}$$

accounts for the effect of a single annular electrode i with inner radius α_i, outer radius β_i and a voltage V_i which is constant across the electrode. The integral of Eq. (2.11) can be evaluated using the identity for the Bessel functions $\int_0^u vJ_0(v)dv = uJ_1(u)$ to yield

$$A_i(k) = V_i \left[\beta_i J_1(k\beta_i) - \alpha_i J_1(k\alpha_i)\right]. \tag{2.12}$$

This completes the general treatment of the problem. The electric potential above a surface at $z = 0$ with n concentric circular electrodes, each with independent voltages V_i and inner and outer radii of α_i and β_i respectively, is given by Eq. (2.10) with $\mathcal{A}_0(k) = \sum_i^n A_i(k)$, where the A_i coefficients are given by Eq. (2.12):

$$\Phi(z,\rho) = \sum_i V_i \int_0^\infty e^{-kz}\ J_0(k\rho)\ \left[\beta_i J_1(k\beta_i) - \alpha_i J_1(k\alpha_i)\right]\ dk. \tag{2.13}$$

This expression may be numerically integrated to yield the instantaneous electric potential (and hence also the electric field) in all space corresponding to any arbitrary voltage configuration $\{V_i\}$ on the electrodes.

2.3.3 The three-electrode point Paul trap

We now introduce the simplest implementation of the generic point Paul geometry that can be used to realize a quadrupole trapping field. Consider the simple geometry of only three electrodes defined by the following boundary conditions:

$$\Phi(z=0,\rho) = \begin{cases} 0 & \text{for } 0 < \rho < a, \\ V\cos(\Omega t) & \text{for } a \le \rho \le b, \\ 0 & \text{for } b < \rho < \infty, \end{cases} \tag{2.14}$$

where V is the amplitude of the applied voltage and Ω is the frequency. This configuration will be henceforth referred to as *the* point Paul trap.

According to the results of the previous section, we find the electric potential to be

$$\Phi(z,\rho,t) = V\cos(\Omega t)\kappa(z,\rho), \tag{2.15}$$

where

$$\kappa(z,\rho) = \int_0^\infty e^{-kz}\ J_0(k\rho)\ [bJ_1(kb) - aJ_1(ka)]\ dk. \tag{2.16}$$

In general, Eq. (2.16) has to be solved numerically. However, for the case of $\rho = 0$ the problem simplifies significantly and an analytic solution can be obtained. Note from the symmetry of the problem that the radial field E_ρ is zero exclusively on the central axis of the trap. We thus infer that if a nontrivial field zero ($\vec{E} = 0$) exists in the $z > 0$ half-space, it will be located on the axis defined by $\rho = 0$ and hence this scenario is worthy of attention.

The on-axis potential is integrated to yield:

$$\kappa(z,0) = \frac{1}{\sqrt{1+(\frac{a}{z})^2}} - \frac{1}{\sqrt{1+(\frac{b}{z})^2}}. \tag{2.17}$$

Taking the derivative of Eq. 2.17, it can be shown that the three-electrode point Paul trap provides an electric field null at a height

$$z_0 = \sqrt{\frac{b^{4/3}a^{4/3}}{b^{2/3}+a^{2/3}}} \tag{2.18}$$

above the center of the trap. One experimental implementation of this design, fabricated on a printed circuit board (PCB), is shown in Fig. 2-7(a), and the corresponding on-axis electric potential and field profile are shown in panels (b) and (c) respectively. For any physically-realizable parameterization (a,b) of the point Paul trap, an electric field node can be found at height z_0 above the trap center according to Eq. 2.18.

2.3.4 Three-dimensional field of the point Paul trap

In the vicinity of the node z_0, it is possible to derive further analytic insight into the field geometry by applying basic equations of electromagnetism. In the immediate neighborhood of the quadrupole node, we may approximate the electric field by a linear form

$$\vec{E}(\vec{r}) = \mathbf{A}\cdot\vec{r} \tag{2.19}$$

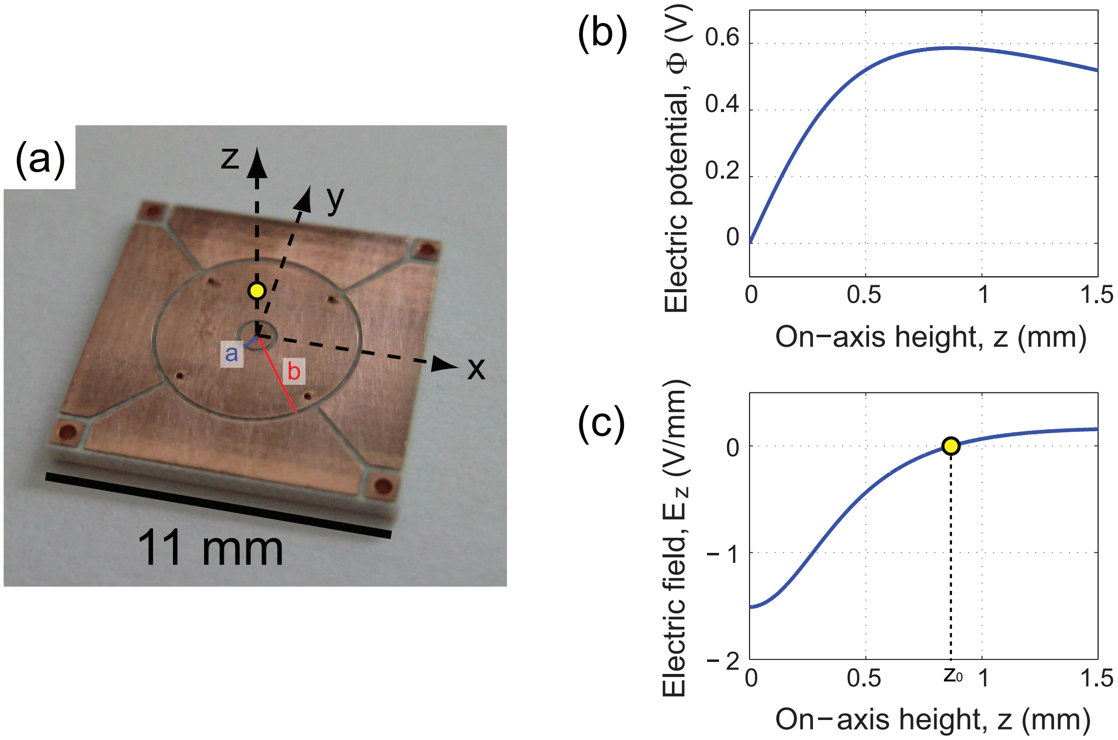

Figure 2-7: Experimental implementation of the three-electrode point Paul trap. (a) A PCB implementation of the design with inner and outer ring radii of $a = 0.55$ mm and $b = 3.24$ mm. The outermost ground has been segmented into four independent electrodes in order to achieve DC compensation of the ion. (b) The electric potential (Eq. 2.17) along the axis of the trap ($\rho = 0$) when the ring is biased to $V_{\mathrm{rf}} = 1$ V. (c) The on-axis electric field corresponding to the same potential. The yellow circle indicates the location of the electric field null at height $z_0 \approx 0.9$ mm above the surface, where ions may be trapped.

where $\mathbf{A}$ is a constant matrix and $\vec{r}$ denotes the displacement vector from the node. Discounting radiation, the electric field must satisfy Faraday's law $\nabla \times \vec{E} = 0$ that, when applied to Eq. 2.19, yields $A_{ij} = A_{ji}$. We conclude that the tensor $\mathbf{A}$ is symmetric and can be diagonalized into three spatially orthogonal directions $\{\hat{e}_1, \hat{e}_2, \hat{e}_3\}$ as in:

$$\vec{E}(\vec{r}) = V \cdot (f_1 r_1 \hat{e}_1 + f_2 r_2 \hat{e}_2 + f_3 r_3 \hat{e}_3) \tag{2.20}$$

$$= V \cdot (f_\rho x \hat{e}_x + f_\rho y \hat{e}_y + f \cdot (z - z_0)\, \hat{e}_z)\,. \tag{2.21}$$

The diagonalized directions of the quadrupole field (Eq. 2.20) are known as the *trap axes* or *principal axes* of the ion trap. In the case of the point Paul trap, the field is trivially diagonalized as in Eq. 2.21.

Additionally, because the node occurs at a charge-free point, it must also satisfy Gauss's

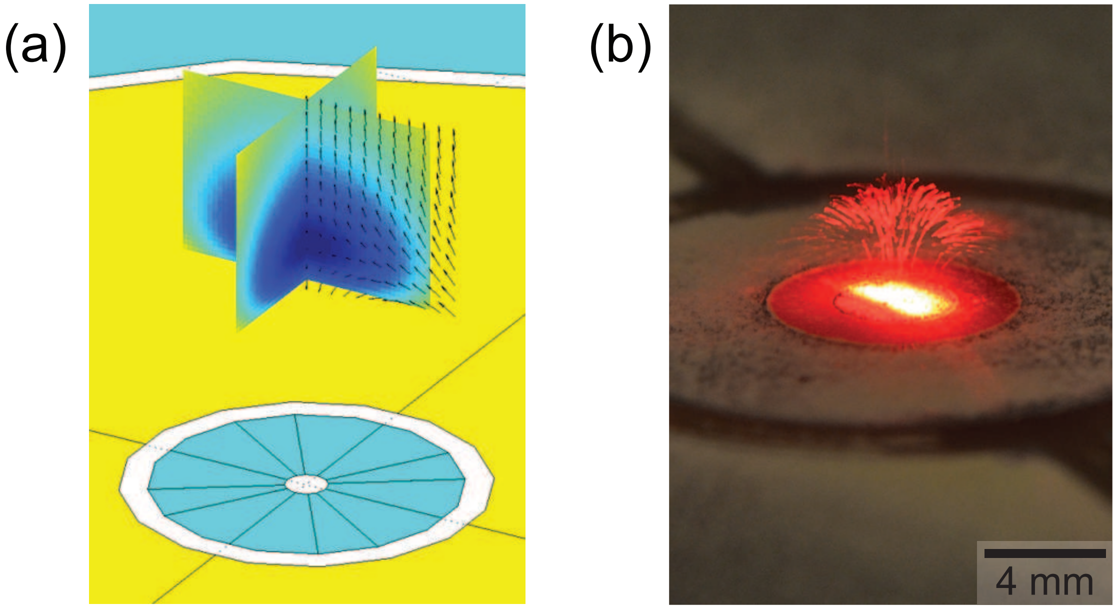

Figure 2-8: Experimental verification of the computed field profile. (a) A numerically computed field profile about the node of the point Paul trap is shown. Both the electric field (arrows) and pseudopotential (shading) are depicted. (b) A cloud of lycopodium particles are loaded into a macroscopic point Paul trap (at $\Omega = 60$ Hz and at $V \approx 1.5$ kV). Mutual repulsion displaces the charged particles from the field null, and each ion is driven along the direction of the local oscillating field, effectively imaging the field profile. The diameter of the central electrode is 4 mm.

equation $\nabla \cdot \vec{E} = 0$. In the diagonal basis of Eq. 2.21, we then find $f_\rho = -\frac{1}{2}f$ which reveals the basic "shape" of the quadrupole field in the point Paul trap. Namely, the field strengths along the radial directions are exactly $\frac{1}{2}$ that of the z-directional fields.

For large displacements from the nodal point, the field is computed numerically. However, there is an experimental technique to beautifully visualize the full three-dimensional field of the point Paul trap, which may then be compared to the numerically simulated fields as shown in Fig. 2-8. The visualization experiment is performed by constructing a "dust trap," which is a properly-scaled "RF" trap that confines macroscopic ions such as corn starch or lycopodium powder. When a large number of such macroions are loaded into the trap, their mutual repulsion displaces the particles from the field null, and ions are driven along the direction of the local oscillating field (i.e. micromotion) and appear enlongated along that direction, effectively imaging the field profile. The dust trap experiment shown in Fig. 2-8(b) was performed by Amira Eltony.

2.4 Approximate models

While the exact motion of a trapped ion is described by the Mathieu equation, it is useful to develop approximate models that still retain basic features of ion motion, so that important performance metrics of the ion trap may be easily related to the parameters of the electrode design. Here, we apply two common approximation models to the point Paul trap:

- In the vicinity of the field node, the trapping field may be approximated by a conservative harmonic potential. This *secular* or *harmonic approximation* is crucial for describing both the classical and quantum motion of a low-energy ("cold") trapped ion (Section 2.4.1). On the other hand, as this model neglects micromotion, it is unsuitable for describing the effect of stray fields.

- The *pseudopotential* model generalizes the harmonic approximation to beyond the linear regime, while continuing to neglect micromotion (Section 2.4.2). We use the pseudopotential model to identify key trapping parameters such as trap volume and depth. The trap design is then optimized with respect to these parameters.

2.4.1 Harmonic approximation

We expand the electric potential $\Phi(z,t)$ around the field node z_0 and use the resulting expansion to find the equation of motion for a particle of mass M and charge Q along the z-axis:

$$\begin{aligned} \ddot{z}(t) &= -\frac{Q}{M}\frac{\partial \Phi(z,t)}{\partial z} \\ &\simeq -\frac{QV}{M}\cos(\Omega t) \times \left[f(a,b)(z-z_0) + O(z-z_0)^2\right]. \end{aligned} \tag{2.22}$$

Provided $|z - z_0| \ll z_0$, which is a reasonable assumption for a trapped ion, terms of second and higher order can be neglected, and the equation of motion takes the form of the previously introduced Mathieu equation. With proper rescaling of variables, Eq. 2.22 can be cast into the canonical Mathieu form:

$$\ddot{\tilde{z}}(\tau) + 2q_z \cos(2\tau)\tilde{z}(\tau) = 0, \tag{2.23}$$

where we have substituted $\tilde{z} = z - z_0$ and $\tau = \Omega t/2$; and the Mathieu q_z-parameter has been defined as

$$q_z = \frac{2QV}{M\Omega^2} f(a,b). \tag{2.24}$$

Here, everything related to the trap geometry is collected into a single function $f(a,b)$ of unit $[\text{length}]^{-2}$ given, after significant algebra, by

$$f(a,b) = \sqrt{\frac{9(b^{\frac{2}{3}} - a^{\frac{2}{3}})^2(b^{\frac{2}{3}} + a^{\frac{2}{3}})^6}{b^{\frac{4}{3}} a^{\frac{4}{3}} (b^{\frac{4}{3}} + b^{\frac{2}{3}} a^{\frac{2}{3}} + a^{\frac{4}{3}})^5}}. \tag{2.25}$$

Note that in this treatment a denotes the inner radius of the RF electrode and not the Mathieu a-parameter, commonly used in the literature on Paul traps. The Mathieu a-parameter, which corresponds to the inclusion of a DC potential in the equation of motion (Eq. 2.22), is not necessary for the point Paul trap design as full three-dimensional confinement is achieved in this geometry by the RF field alone.

When the trap is operated such that $|q_z| \ll 1$, the equation of motion can be readily solved to yield [WMI$^+$98]

$$\tilde{z}(t) = \sigma_0 \left[1 - \frac{q_z}{2} \cos(\Omega t)\right] \cos(\omega_z t). \tag{2.26}$$

This is the usual result, familiar from our prior numerical exploration of the Mathieu equation in Section 2.2.1, where the motion is comprised of two distinct components: a slow *secular motion* with an amplitude σ_0 at the *secular* or *trap frequency*

$$\omega_z = \frac{q}{2\sqrt{2}} \Omega = \frac{QV}{\sqrt{2} M\Omega} f(a,b) \tag{2.27}$$

and a superimposed, fast *micromotion*, with a (lower) peak-to-peak amplitude of $q_z \sigma_0$, that occurs at the sidebands of the RF drive frequency Ω. Neglecting the micromotion – a reasonable approximation for $|q| \ll 1$ – we can associate an approximate harmonic potential that describes the ion motion near the quadrupole zero by the following

$$\Psi(z) = \frac{1}{2} M\omega_z^2 (z - z_0)^2 = \frac{Q^2 V^2}{4M\Omega^2} f^2(a,b)(z - z_0)^2, \tag{2.28}$$

which we generalize to include radial displacements according to our prior analysis of the

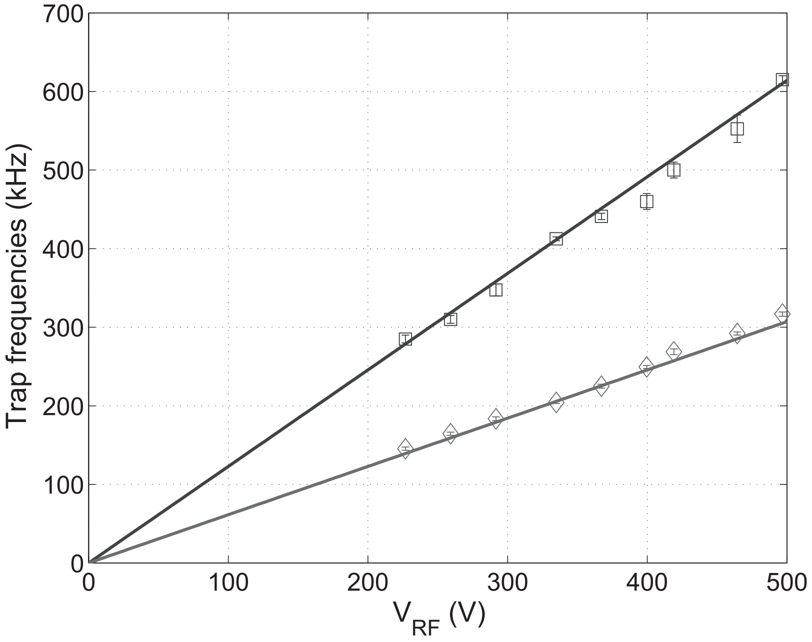

Figure 2-9: Measurements of axial (square markers) and radial (diamond markers) secular frequencies of the point Paul trap shown in Fig. 2-7(a). Data is taken at $z_0 = 940\ \mu$m with an RF frequency of $\Omega = 2\pi \cdot 8.07$ MHz. Also shown are theoretically expected secular frequencies (not fits) according to Eq. 2.27. Fits through the measured data yields a ratio of the radial to axial secular frequencies of $\omega_\rho/\omega_z = 0.51 \pm 0.01$, in agreement with the theoretically predicted $\omega_\rho/\omega_z = 1/2$.

quadrupole field shape, which implies $\omega_\rho = \frac{1}{2}\omega_z$:

$$\begin{aligned} \Psi(z,\rho) &= \frac{1}{2}M\omega_z^2(z-z_0)^2 + \frac{1}{2}M\omega_\rho^2\rho^2 && (2.29) \\ &= \frac{Q^2V^2}{4M\Omega^2}f^2(a,b)\left[(z-z_0)^2 + \frac{1}{4}\rho^2\right]. && (2.30) \end{aligned}$$

The harmonic model can be experimentally corroborated by measuring the secular frequencies of the trapped ion by, for example, tickle spectroscopy. In Fig. 2-9, excellent agreement is shown between the experimentally measured secular frequencies and the theoretical model for a $^{88}\mathrm{Sr}^+$ ion in the point Paul trap.

Finally, we note that the harmonic potential is in general related to the trap axes of the quadrupole field (Eq. 2.20) by

$$\Psi(\vec{r}) = \sum_{i=1}^{3} \frac{1}{2}M\omega_i^2 r_i^2 \tag{2.31}$$

where $\vec{r} = (r_1, r_2, r_3)$ denotes the displacement from the field node in the diagonalized basis and $\omega_i = \frac{QV}{\sqrt{2}M\Omega}f_i$.

2.4.2 Pseudopotential model

While the harmonic potential of Eq. 2.29 provides an intuitive connection to the physical, time-averaged motion of the trapped ion in the vicinity of the RF node, it does not reveal any information about the dynamics where the inequality $|z - z_0| \ll z_0$ is not satisfied. For instance, in a real device there is necessarily a finite trapping volume and trap depth. These quantities originate from the shape of the confinement field significantly beyond the harmonic region. In the limit $q \ll 1$, the effective potential energy beyond the harmonic regime – commonly referred to as the *pseudopotential* or the *ponderomotive potential* – may be expressed directly through the gradient of the electric potential, here written in terms of κ, as [Deh67, Gho95]

$$\Psi(z, \rho) = \frac{Q^2 V^2}{4M\Omega^2} \left|\nabla\kappa(z, \rho)\right|^2 . \tag{2.32}$$

The solid line in Fig. 2-10(a) shows the on-axis pseudopotential for the point Paul trap. Superimposed is the harmonic approximation (dashed line). Inserting the expression for κ (Eq. 2.17) into the expression for the pseudopotential yields two physically meaningful extrema. The first is the minimum of the pseudopotential:

$$z_0 = \sqrt{\frac{b^{4/3} a^{4/3}}{b^{2/3} + a^{2/3}}} \tag{2.33}$$

which clearly coincides with the location of the quadrupole node (Eq. 2.18) where $|\nabla\kappa| = 0$. The second is

$$z_{\max} = \sqrt{\frac{b^{6/5} - a^{6/5}}{a^{-4/5} - b^{-4/5}}}, \tag{2.34}$$

which denotes the turning-point of the pseudopotential. The difference $z_{\max} - z_0$ can thus be taken as a a linear measure of the effective trap volume. Furthermore, a corresponding trap depth can be defined as $D = \Psi(z_{\max}) - \Psi(z_0)$. Using Eq. (2.33) and Eq. (2.34), one finds that the trap depth is positive for all values of $b > a > 0$, and is given by:

$$D = \frac{Q^2 V_{\mathrm{rf}}^2}{4M\Omega_{\mathrm{rf}}^2} \left[a^2(a^2 + z_{\max}^2)^{-\frac{3}{2}} - b^2(b^2 + z_{\max}^2)^{-\frac{3}{2}}\right]^2 . \tag{2.35}$$

We prove that there are no alternative "holes" in the pseudopotential by examining its contour plot in the (ρ, z) plane, shown in Fig. 2-10(b). The inset shows the three-dimensional trapping volume, defined by the isosurface $\{\vec{r} \mid \Psi(\vec{r}) = D\}$, in relation to the trap electrodes.

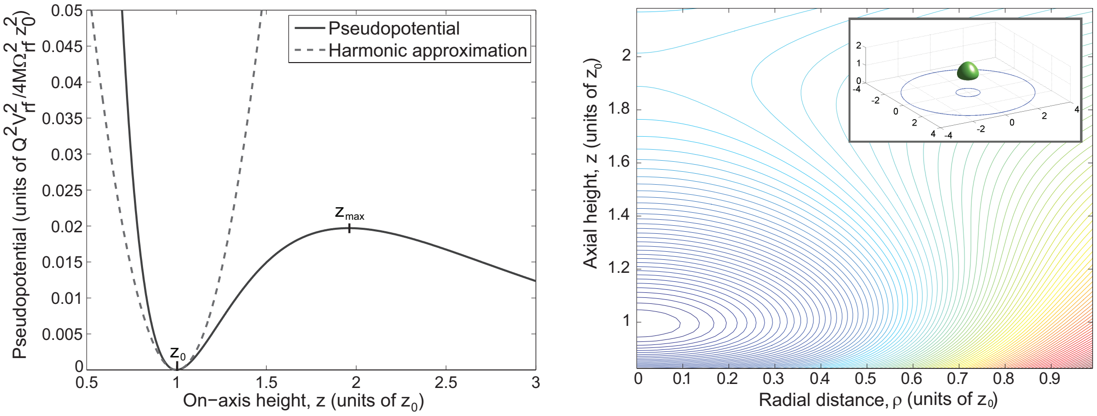

Figure 2-10: Approximate potentials for motion in the point Paul trap. Trap geometry (a, b) is chosen as in Table 2.1. (Left) The harmonic potential approximation (Eq. 2.29) and the pseudopotential (Eq. 2.32) along the z-axis of the trap. The pseudopotential identifies the trap turn-around point z_{max} in addition to the trapping height z_0. (Right) A 3D contour plot of the pseudopotential. The inset shows the 3D trapping isosurface in relation to the outlines of the RF ring electrode (units in z_0).

$a\,(z_0)$	$b\,(z_0)$	$z_{\text{max}}\,(z_0)$	$q\,(q_{\text{4rod}})$	$D\,(D_{\text{4rod}})$
0.651679	3.57668	1.957965	0.471565	0.019703

Table 2.1: Results of numerical optimization of the trap depth for a fixed trap height z_0. The optimal ratio of inner to outer circular electrode (i.e. $a : b$) is 1 : 5.5. The geometric parameters a, b and z_{max} scale with the desired ion height z_0. The Mathieu q-parameter and trap depth D are expressed using Eq. 2.36.

The trap depth is a reasonable quantity to be optimized in the design of the point Paul trap. However, unconstrained optimization of Eq. 2.35 over (a, b) will influence not only the trap depth but also the trap height z_0 above the surface through Eq. 2.33. Often in experiments, the trap height is a parameter of importance, and so a more reasonable strategy is to optimize the trap depth for a fixed value of z_0. This can in principle be done analytically; however, the results are more useful in their numerical form. Table 2.1 summarizes the results of this optimization. For the purpose of comparison with the four-rod linear Paul trap we have defined

$$q_{\text{4rod}} \equiv \frac{2QV_{\text{rf}}}{M\Omega_{\text{rf}}^2 z_0^2} \quad \text{and} \quad D_{\text{4rod}} \equiv \frac{Q^2V_{\text{rf}}^2}{4M\Omega_{\text{rf}}^2 z_0^2}, \tag{2.36}$$

which corresponds to the q-parameter and the trap depth, respectively, for the three-dimensional four-rod Paul trap with an ion-electrode distance of z_0.

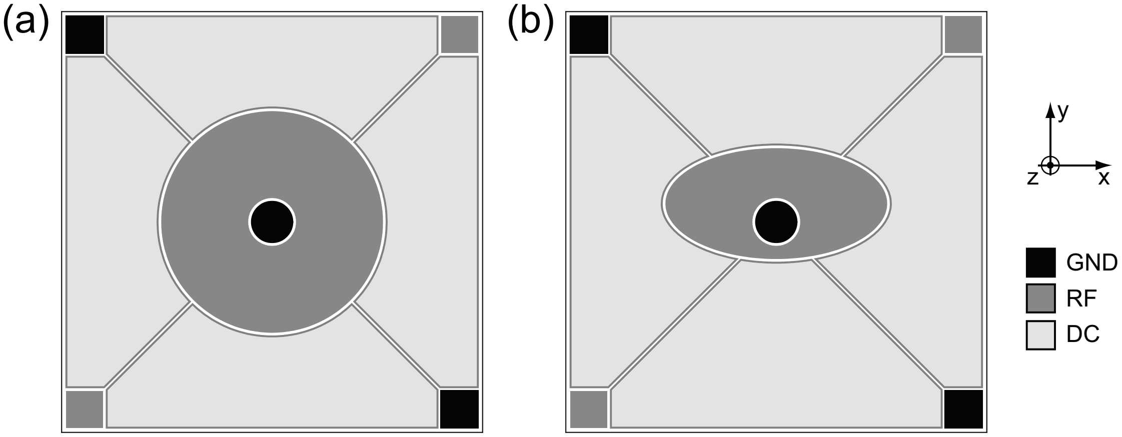

Figure 2-11: Variations on the ideal point Paul trap used in this thesis work. The board dimensions are 1.1 cm × 1.1 cm, electrode gaps are 100 μm, and square corners at pads allow electrical connection to the center and ring electrodes through vias. Outermost ground is segmented into four independent electrodes for DC compensation. (a) Design for the *symmetric* point Paul trap with $a = 0.65$ mm and $b = 3.24$ mm, yielding $z_0 = 940$ μm. (b) The *asymmetric* variant of the point Paul trap where the ring electrode is deformed into an ellipse (minor-to-major ratio of 1/2) and is shifted along y (by 0.5 mm). Asymmetries rotate the principal axes of the trap about the x-axis, and remove the trap frequency degeneracy between the x- and y-directions. Ion height is lowered to $z_0 = 670$ μm.

From the optimization results of Table 2.1, it is seen that the q-parameter of the point Paul trap is roughly a factor $\frac{1}{2}$ of the four-rod linear Paul trap while the trap depth is about a factor $\frac{1}{50}$. By comparison, the surface-electrode linear Paul trap that has recently attracted much attention in the context of quantum computing [SCR+06] has a q-parameter and a trap depth that are approximately a factor $\frac{1}{2\sqrt{3}}$ and $\frac{1}{72}$ respectively of the four-rod Paul trap. The decrease in trap depth is a one of the primary disadvantages associated with surface-electrode trap implementations [BCL+07].

2.5 Variations on the point Paul trap

The optimal three-electrode point Paul trap is given by Eq. 2.14 and Table 2.1. However, there are necessary deviations from the ideal geometry required for practical implementation. Firstly, the outermost electrode does not extend out to infinity, but is bounded by a 1.1 cm × 1.1 cm square due to the finite dimensions of the chip carrier. And second, the outermost ground electrode is segmented into four separate electrodes that gives sufficient degrees of freedom for the compensation of arbitrary stray fields at the ion location along all dimensions. These changes are depicted in Fig. 2-11(a), and the resultant design is referred to in the subsequent chapters as the *symmetric point Paul trap.*

As we will find in the following chapter, the spatial orientation of the trap axes $\{\hat{e}_1, \hat{e}_2, \hat{e}_3\}$ are of crucial importance in optics integration, where the ion motion must be sufficiently localized with respect to a microscopic mode field of the integrated element. In this respect, the design in Fig. 2-11(a) is deficient in that (1) the trap frequencies along x and y-directions are degenerate, and (2) the vertical trap axis along z has no projection on the xy-plane. Therefore, we show in Fig. 2-11(b) an asymmetric, elliptical variant of the point Paul trap, for which a numerical simulation reveals the trap axes to be

$$\hat{e}_1 = \hat{e}_x \tag{2.37}$$

$$\hat{e}_2 \approx +\cos(30^\circ)\ \hat{e}_y + \sin(30^\circ)\ \hat{e}_z \tag{2.38}$$

$$\hat{e}_3 \approx -\sin(30^\circ)\ \hat{e}_y + \cos(30^\circ)\ \hat{e}_z \tag{2.39}$$

i.e. a tilt of 30° in the yz-plane from the symmetric case, and a nondegenerate set of secular frequencies at a ratio $\omega_1 : \omega_2 : \omega_3 = 0.6 : 0.4 : 1$ (or, equivalently, a ratio of Mathieu q-parameters: $q_1 : q_2 : q_3 = 0.6 : 0.4 : 1$). The ion height is lowered to $z_0 = 670\ \mu$m. We shall henceforth refer to this design as the *asymmetric point Paul trap.* We will contrast ion motion in the *symmetric* and *asymmetric* designs in Chapter 3.

2.6 Summary

We have explained the principle of operation behind RF ion confinement, and set the framework for performing numerical analyses of ion trajectories based on the Mathieu differential equation. A detailed mathematical analysis of the surface-electrode point Paul trap was presented, including the harmonic approximation for describing trapped ion dynamics in the vicinity of the trapping point. The point Paul trap design is foundational to the ion-fiber integration efforts of this thesis work.

Chapter 3

Atomic motion in the fiber mode

In the previous chapter, we developed a general understanding of RF ion trapping by an oscillating quadrupole field. We now examine the fiber-trap system in detail, and derive the quantitative trajectory of a trapped atomic ion under typical experimental conditions, including laser cooling and stray field effects. Such effort in ion modeling is necessary for the fiber-ion integration project due to the finite, micron-level extent of the fiber mode.

The analysis of trapped atomic motion is developed as follows:

- First, we provide a general overview of the fiber-integrated point Paul trap, emphasizing the finite spatial dimensions of the fiber mode (Section 3.1).
- We then review basic laser-ion physics, which gives rise to Doppler cooling and the photon correlation technique for stray field compensation (Section 3.2).
- Finally, we arrive at the damped Mathieu equation, which models the motion of a trapped atomic ion under laser cooling. We use numerical simulations to reveal the effect of cooling and stray field on ion trajectory (Section 3.3).

This work represents the framework that we employed during the development of the fiber-trap system. The discussion is generally relevant for trap integration projects where three-dimensional ion localization with respect to a microscopic mode field is sought. Our numerical approach complements analytical treatments of the traditional linear Paul trap found in the literature (e.g. Ref. [BMB+98]). We also explore how the Mathieu model relates to more general, higher-order descriptions of ion motion (Section 3.4).

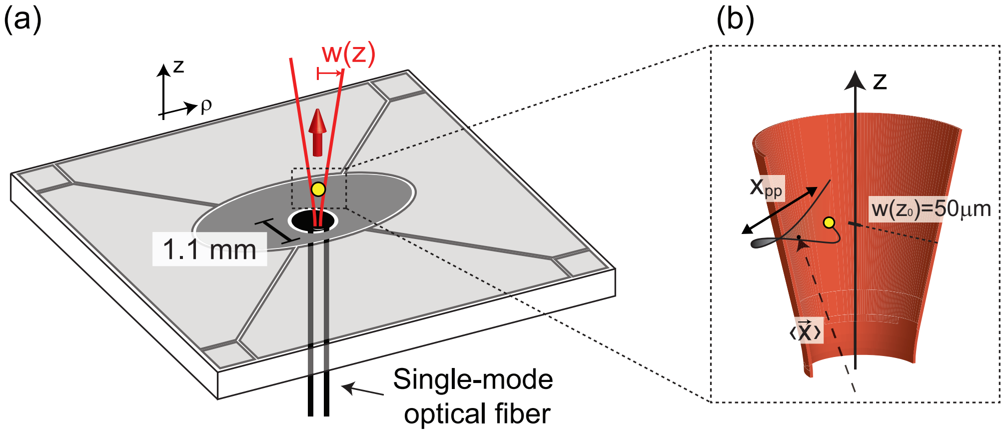

Figure 3-1: Illustration of ion trajectory in the fiber-integrated point Paul trap. (a) Basic schematic of the integrated system, which is based on the asymmetric point Paul trap. The fiber is embedded in the center electrode, and its output is a Gaussian beam propagating along $\hat{e}_z$. (b) Detailed ion trajectory $\vec{x}(t)$ relative to the fiber mode, which reveals how finite ion motion can affect fiber-ion coupling. Key parameters describing the orbit are: peak-to-peak amplitude x_{pp} and the mean offset $\langle\vec{x}\rangle$. Both are evaluated with respect to the fiber waist at ion height of $w(z_0 = 670\ \mu\mathrm{m}) = 50\ \mu\mathrm{m}$.

3.1 Fiber integration and ion motion

The goal of this thesis is to interface an atomic ion in a surface-electrode ion trap to an integrated single-mode optical fiber. Fig. 3-1(a) shows the basic geometry, in which the fiber is embedded within the center electrode of the asymmetric point Paul trap. Our design intent is to bring a trapped ion to rest directly above the axis of the fiber, which is then illuminated from below. However, a trapped ion in general will undergo finite-amplitude motion whose extent may be significant with respect to the fiber mode as illustrated in Fig. 3-1(b). Because laser-ion interaction is parametrized through the local optical intensity $I(\vec{x})$, fiber-integration demands that the ion orbit $\vec{x}(t)$ be localized relative to the optical mode. Namely, excess ion motion can impart undesired and potentially unpredictable intensity (and frequency) modulation onto the fiber-ion interaction. Thus, we state the requirements on $\vec{x}$ as follows:

1. The spatial extent of the ion trajectory, measured by the peak-to-peak amplitude x_{pp}, must be smaller than the mode waist at the ion height of $w(z_0 = 670\ \mu\mathrm{m}) = 50\ \mu\mathrm{m}$.

2. The mean position of the ion $\langle\vec{x}(t)\rangle$ must lie close to the fiber axis. Again, the relevant (radial) offset is measured in units of $w(z_0)$.

In other words, the correct operation of the fiber-trap system depends crucially on whether ion trajectories satisfy the spatial constraint:

$$x_{\mathrm{pp}}, \langle x \rangle_{\rho} \ll w(z_0) \sim 10\ \mu\mathrm{m}. \tag{3.1}$$

In this chapter, we shall address the former requirement $x_{\mathrm{pp}} \ll w(z_0)$. In order to describe ion motion at the sub-micron scale, we must first elaborate on the basic Mathieu equation theory of Chapter 2. As we have learned through multiple iterations of experiments and theoretical modeling, sub-micron localization is not implied by the Mathieu equation alone, but is crucially dependent on additional experimental factors, in particular:

- The details of the laser cooling implementation, e.g. the orientation of the cooling beam with respect to the trap axes,
- The presence of stray electric field at the ion which, in practice, should be assumed to be uncompensated until verified otherwise.

We will develop both topics in physical and quantitative detail, and incorporate them into our model of the fiber-trap system. By analyzing simulated trajectories of the expanded model, we derive an accurate understanding of the behavior of $\{x_{\mathrm{pp}}, \langle \vec{x} \rangle\}$, so that sub-micron localization and fiber-integration may be reliably implemented in experiment.

3.1.1 The Gaussian fiber mode

As previously noted, the detailed modeling of ion motion is necessitated by the finite spatial extent of the fiber mode. For completeness, we state its overall physical dimensions. The integrated single-mode fiber has a core diameter of $\sim 3\ \mu$m and a measured mode field diameter of $2w_0 \sim 5.5\ \mu$m at $\lambda = 674$ nm at the cleave plane. The free-space output is well-approximated as a fundamental Gaussian beam, which is described by the formulas:

$$\begin{aligned} I(z,\rho) &= I_0 \left(\frac{w_0}{w(z)}\right)^2 \cdot \exp\left(\frac{-2\rho^2}{w^2(z)}\right) && (3.2) \\ w(z) &= w_0 \cdot \sqrt{1 + \left(\frac{z}{z_R}\right)^2}, && (3.3) \end{aligned}$$

where $z = 0$ indicates the fiber facet plane and $z_R = \frac{\pi w_0^2}{\lambda} = \frac{\pi \cdot (5/2)^2}{0.674} = 35\ \mu$m is the Rayleigh range. These numbers yield a $1/e^2$-intensity mode waist at the ion height of $w(z_0) = 50\ \mu$m.

3.2 Laser-ion interaction

For the remainder of this thesis, we are concerned with the dynamics of trapped *atomic* ions. In contrast to the abstract point particle treated in Ch. 2, an atomic ion provides additional degrees of freedom in the form of its internal electronic structure, which must be captured into our conceptual and numerical models.

Of course, the physics of internal and external state manipulation by laser light and other forms of radiation is fundamental to trapped-ion quantum information, and is extensively covered in the literature including Refs. [WMI$^+$98, LBMW03]. Here, only an elementary discussion of laser-ion interaction is given: we focus exclusively on dipole transitions and Doppler cooling (Section 3.2.1). Our limited scope is warranted since Doppler cooling alone is sufficient for sub-micron ion confinement – and hence fiber-integration – when carefully implemented.

For our purposes, the relevant microscopic picture of light-ion interaction is that of incoherent scattering. When the atomic ion is illuminated by resonant light fields, an incident photon may be absorbed by the trapped ion, which is subsequently reemitted through spontaneous emission. The recoil impulse from each scattering event subtly but finitely alters the ion trajectory – a process that can be configured to reduce the ion velocity on average in Doppler laser cooling (Section 3.2.2). Additionally, the scattered photon stream carries information about the ion orbit $\vec{x}(t)$, which may then be used to detect and correct any excess ion motion (Section 3.2.3).

3.2.1 Dipole interaction

The singly-ionized $^{88}\text{Sr}^+$ atom, which is the target species in this work, has a single valence electron whose quantum state may be manipulated as the basis of trapped-ion quantum computing. Fig. 3-2(a) shows the relevant level structure [Gal67]. The time evolution of the atomic internal state is described by the optical Bloch equations [MvdS99]. Here, we consider exclusively the *dipole* transitions ($\Delta j = \pm 1$, where j is the total angular momentum of the electron) since they exhibit the strongest interaction with incident light and thus exert the most influence on the ion's external motion. Along a dipole transition, the photon scattering rate γ from a single ion (at rest) can be derived from the steady-state solution of the optical Bloch equations, and is given as a function of laser-ion frequency detuning δ

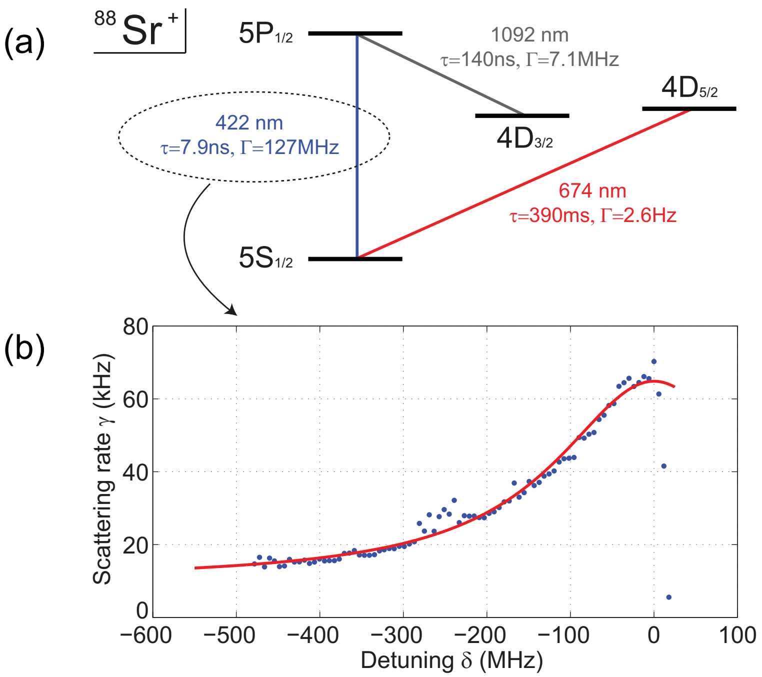

Figure 3-2: The internal electronic structure of $^{88}\mathrm{Sr}^{+}$. (a) The level structure relevant for this thesis work. The 422 and 1092 nm transitions are dipole transitions ($\Delta j = \pm 1$) whereas the 674 nm transition (driven by the integrated fiber) is a much weaker non-dipole transition. (b) Spectroscopy of the 422 nm transition of a single trapped $^{88}\mathrm{Sr}^{+}$ at rest, as the red-detuned laser is scanned towards the atomic resonance. Solid red line shows a fit to the Lorentzian profile of Eq. 3.4. The ion is continuously repumped from the dark $4\mathrm{D}_{3/2}$ state by concurrent illumination by a 1092 nm laser. The lineshape is clearly broadened beyond the natural linewidth (FWHM) of $\Gamma = 127$ MHz.

and illumination intensity I as

$$\gamma\left(\delta, s = \frac{I}{I_s}\right) = \left(\frac{s}{1+s}\right) \cdot \left(\frac{\Gamma/2}{1 + (2\delta/\Gamma')^2}\right), \tag{3.4}$$

where s is the *saturation parameter* defined through the *saturation intensity* $I_s = \frac{\pi h c}{3\lambda^3} \cdot \Gamma$ for a given transition, and $\Gamma' = \Gamma\sqrt{1+s}$ is the power-broadened linewidth. In the current context, Eq. 3.4 makes use of the two-level and ergodic assumptions.

From Eq. 3.4 it is evident that the single-ion scattering rate saturates to $\Gamma/2$ under resonant ($\delta = 0$) and bright ($s \gg 1$) illumination. Therefore, Γ is a direct measure of the interaction strength, and we may focus on the 422 nm transition of $^{88}\mathrm{Sr}^{+}$ (over the 1092 nm transition) due to its comparatively large decay rate of $\Gamma = 127$ MHz. Fig. 3-2(b) shows the 422 nm scatter from a single trapped ion as the laser frequency is scanned over the resonance. The peak detected scattering rate of 65 kHz rather than $\Gamma/2 \sim 60$ MHz is due to experimental constraints in imaging efficiency. (Note: throughout the scan, the ion is repumped from the dark $4D_{3/2}$ state by simultaneous 1092 nm illumination. We relegate the explanation of Doppler cooling in a three-level system to Ref. [Lab08].)

In Eq. 3.4, the ion is assumed to be at rest, so the interpretation of the laser-ion detuning is simply the absolute frequency difference $\delta = \omega_l - \omega_a$ where ω_l and ω_a are the laser and (at-rest) atomic transition frequencies. On the other hand, for an ion with velocity v, the effective detuning δ' is computed in the ion's rest frame as

$$\delta' = \omega_l \cdot \left(1 - \frac{v}{c}\right) - \omega_a = \delta - kv, \tag{3.5}$$

where $k = \frac{2\pi}{\lambda_l}$ is the lab-frame laser wavenumber, and the effective laser frequency has been Doppler-shifted assuming that the ion is copropagating in the direction of the laser (i.e. moving away from the source). Even at a fixed absolute detuning $\delta = \omega_l - \omega_a$, Eq. 3.5 shows that the scattering rate may still be modulated due to ion motion. It is customary to separate the contributions from the fixed laser-ion detuning δ and the ion velocity v. Accordingly, the photon scattering rate by an ion in motion is obtained by replacing the absolute detuning in Eq. 3.4 as $\delta \to \delta - kv$, yielding

$$\gamma\left(v, \delta, s = \frac{I}{I_s}\right) = \left(\frac{s}{1+s}\right) \cdot \left(\frac{\Gamma/2}{1 + [2(\delta - kv)/\Gamma']^2}\right), \tag{3.6}$$

which represents a coupling between the internal (scattering, γ) and external (ion velocity, v) degrees of freedom of an atomic ion. This important physical coupling gives rise to Doppler cooling, and also a mechanism for deterministic stray field compensation.

3.2.2 Doppler cooling

We now show that the ion can be Doppler cooled according to Eq. 3.6, i.e. that a velocity-dependent damping force can be engineered in the ion's equation of motion.

The origin of the damping force lies in each scattering event, which consists of an absorption and emission of a photon taking place under asymmetric conditions. Namely:

- The incident photon originates from a directional laser beam and thereby possesses a well-defined momentum $\hbar\vec{k}$ where $\vec{k}$ is the laser wavevector. Upon absorption, the photon transfers its momentum onto the atom.

- Subsequently, the excited atom emits a photon with momentum $\hbar\vec{k}'$ by spontaneous decay. This emission does not have a preferred direction in space, and hence the wavevector $\vec{k}'$ is randomized over a 4π solid angle.

On average, we then conclude that each scattering event will impart an impulse

$$\Delta\vec{p} = \langle \hbar\vec{k} - \hbar\vec{k}' \rangle = \hbar\vec{k} \tag{3.7}$$

on the atom. Along the $\vec{k}$-axis, the force on the atom due to scattering of the laser beam is computed by multiplying the average impulse by the scattering rate of Eq. 3.6

$$F = \hbar k \gamma\,(v, \delta, s) = F_0 - \beta v, \tag{3.8}$$

which we have expanded to first order in v, yielding a velocity-independent force F_0 and a velocity-dependent force with an effective coefficient β. The velocity-independent force F_0 may be lumped with the “stray field” term c in the equation of motion, which is treated independently. For the current discussion, we focus on the velocity-dependent term whose coefficient β is given, after significant algebra, by [MvdS99]

$$\beta = -\hbar k^2 \cdot \frac{4s(\delta/\Gamma)}{\left(1 + s + (2\delta/\Gamma)^2\right)^2}. \tag{3.9}$$

Note that the sign is determined by the fixed laser-ion detuning δ. When $\delta < 0$, the laser is said to be *red-detuned* with respect to the atomic transition, corresponding to $\beta > 0$. In this case, the velocity-dependent force in Eq. 3.8 opposes the instantaneous ion velocity, leading to dissipation of external motion. [However, the physical force from the laser is always in the direction of $\vec{k}$ (as captured mathematically by $F_0 - \beta v > 0$). The “damping force” simply accounts for the preferential scattering of the red-detuned laser when the ion is counterpropagating against the beam.]

In general, the damping coefficient β is a complicated function of the illumination intensity s and the laser-ion detuning δ. However, it can be shown that there exists an optimal set of parameters for Doppler-cooling, namely $(s, \delta) = (2, -\Gamma/2)$, that maximizes the damping coefficient at

$$\beta_{\max} = \hbar k^2/4. \tag{3.10}$$

Consistent with its underlying physical basis – momentum transfer by scattering of photons along a saturable atomic transition – we find that the damping coefficient also saturates at β_{max}, which evaluates to 5.8×10^{-21} Newton/(m/s) for the 422 nm transition of the $^{88}\text{Sr}^{+}$ ion. While microscopic, we show later that this cooling force can result in exponential damping of atomic trajectories with a typical time constant in the sub-millisecond regime. On the other hand, we note here that since Doppler cooling is based on stochastic photon scattering, it must yield a nonzero variance in ion momentum (and hence position) in the limit $t \to \infty$. However, in our numerical simulations, we shall neglect this *Doppler cooling limit* which becomes relevant at the length scale of few tens of nanometers. Formally, the scattering of individual photons is a random event, and thus the overall ion dynamics is actually described by a stochastic differential equation where the ion position is represented by a random process $X(t)$. Our deterministic ODE, in contrast, only describes the evolution of the ensemble mean $x(t) = \langle X(t) \rangle$.

Finally, we generalize our discussion to cooling in multiple dimensions. Consider a trapped ion in three dimensions, whose coordinates are given along the trap axes $\{\hat{e}_1, \hat{e}_2, \hat{e}_3\}$. As shown in Chapter 2, the ion's equation of motion decouples along each $\hat{e}_i$, and we are thus motivated to define a set of one-dimensional damping parameters β_i. Based on Eq. 3.10, we obtain $\beta_i = \hbar k_i^2/4$ where k_i is the projection of the laser wavevector onto the trap axis $\hat{e}_i$. Notably, it follows that $\sum_i \beta_i = \hbar k^2/4 = \beta_{\text{max}}$, implying that in multiple dimensions the maximum achievable damping β_{max} is divided "zero-sum" among the individual trap axes. This is indeed the expected result given that the underlying physical mechanism for Doppler cooling is saturable photon scattering.

3.2.3 Stray field compensation by photon correlation

Previously, we remarked that the charge distribution in the ion's environment is not *a priori* predictable, which gives rise to a stray DC electric field $\vec{E}_{\text{stray}}$ at the ion location. The effect of the field is to incur excess ion motion, which leads to modulation of the scattering rate through Eq. 3.6. This modulation is observable in the scattered photon stream through an important technique known as *photon correlation* [BMB+98]. We use this technique to deterministically eliminate stray field-induced ion motion.

As will be shown in Section 3.3, steady-state motion of a laser-cooled ion can only occur in the case of nonzero stray field, which results in excess ion motion in the micromotion component. The characteristic frequency of stray field-induced micromotion necessarily coincides with that of the RF drive $\Omega = 2\pi \times f_{\mathrm{RF}}$. Hence, the basic idea of photon correlation is to extract the modulation of the scattering rate using a digital lock-in amplifier operating at the RF frequency. Our implementation (owing to Jarek Labaziewicz) proceeds as follows:

1. The scattered photon stream from the trapped ion is detected by a photomultiplier tube in counting mode, whose output is digitized at a sampling rate of $f_s = 300$ MHz. This process yields a digital photon stream $s[i]$ which represents the number of scattered photons collected in the i-th bin of width T_s beginning at time $t = T_s \cdot i$, where $T_s = 1/f_s = 3.3$ ns is the sampling period. Because the sampling rate greatly exceeds the peak 422 nm scattering rate, photons will be sparsely distributed over the digital stream, which makes direct observation of modulation difficult.

2. The photon stream is correlated against the RF. The digital stream $s[i]$ is segmented into frames of the driving RF, which are added phase-coherently to produce the RF-correlated scatter as in

   $$c[k] = \sum_{n=0}^{N} s[k + \frac{T_{\mathrm{RF}}}{T_s} \cdot n], \tag{3.11}$$

   where $T_{\mathrm{RF}} = 1/f_{\mathrm{RF}}$ is the period of the RF drive, N is the number of RF cycles used for the correlation (we typically use an "integration time" of $T_{\mathrm{RF}} \cdot N = 100$ ms), and $k = 0, 1, \cdots, T_{\mathrm{RF}}/T_s - 1$ indicates the subphase $\phi = 2\pi \cdot k/(T_{\mathrm{RF}}/T_s)$ of the RF cycle. Note that Eq. 3.11 may also be written as

   $$c[k] = \sum_i p_k[i] \cdot s[i] \qquad \text{where} \qquad p_k[i] = \sum_j \delta[\frac{T_{\mathrm{RF}}}{T_s} \cdot j + k - i]. \tag{3.12}$$

   Here, $\delta[i]$ is the unit impulse and $p_k[i]$ is a digital impulse train with periodicity T_{RF}/T_s (which represents the RF frame) that has been shifted by k units. This alternate form of Eq. 3.11 makes apparent the mathematical operation of cross-correlation that is implemented by phase-coherent summation.

By collecting photon statistics over N-cycles, Eq. 3.11 readily reveals whether scattering by the ion shows a dependence on the subphase of the RF cycle as expected for an ion exhibiting stray field-induced micromotion. Examples of experimental RF-correlated scatter $c(t) \equiv c[k = \lfloor t/T_s \rfloor]$ are shown in Fig. 3-3. The successive rows show decreased modulation depth as the ion is increasingly brought to rest. A purely DC scattering rate indicates the

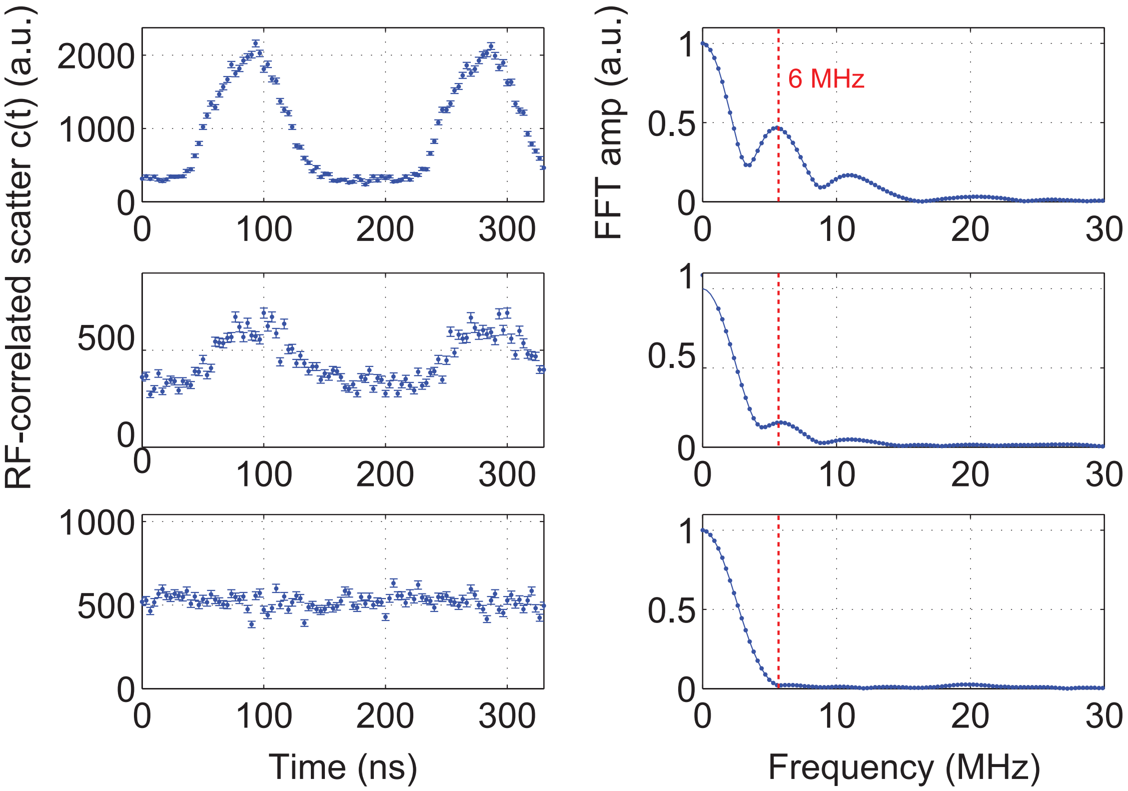

Figure 3-3: Measured modulation in the 422 nm scattering rate induced by the ion velocity. The modulation contrast $c(t) \equiv c[k = \lfloor t/T_s \rfloor]$ is produced by summing many properly-synchronized RF frames of the scattered photon stream (Eq. 3.11). Here, two RF periods ($T_{\mathrm{RF}} = 1/(6\,\mathrm{MHz}) = 167$ ns) have been stitched together to yield better frequency resolution in the FFTs. Each spectrum is normalized by the DC amplitude, and shows the dominant modulation frequency to coincide with the RF frequency of the ion trap. The ion can be deterministically compensated against E_{stray} by minimizing the modulation amplitude as in the final row.

desired condition of a compensated ion at rest. This way, we may use the photon correlation metric as an error signal for ion compensation.

Keep in mind that the technique will not produce modulation contrast if the ion velocity is orthogonal to the incident beam, as modulation relies on the first-order Doppler shift. Therefore, to correctly utilize the photon correlation technique for ion compensation, care must be taken in experiment to ensure that the ion cannot sustain closed motion in the plane orthogonal to the cooling laser. Or, equivalently, the beam must be arranged to have nonzero projections along all trap axes.

3.3 The damped Mathieu equation

So far, we have reviewed the electronic structure of $^{88}\mathrm{Sr}^{+}$ and demonstrated that the ion's internal structure can affect its external dynamics, giving rise to Doppler cooling: a velocity-dependent damping term in the ion's equation of motion. We now formulate the numerical model that encompasses laser cooling.

The damping force is included in the ion equation of motion along the i-th trap axis as

$$M\ddot{x}_i = -\beta_i \dot{x}_i + Q\left(V f_i \cdot x_i \cos \Omega t + E_{\mathrm{stray},i}\right), \tag{3.13}$$

where the origin of the coordinate system is the RF quadrupole node. Introducing $\tau = \Omega t/2$ as before, we obtain the normalized, *damped* Mathieu equation

$$\frac{d^2 x_i}{d\tau^2} + b_i \frac{dx_i}{d\tau} + 2q_i \cos 2\tau \cdot x_i = c_i, \tag{3.14}$$

where

- $q_i = \frac{2QV}{M\Omega^2} \cdot f_i$ is the previously defined Mathieu q-parameter,
- $b_i = \frac{2}{M\Omega} \cdot \beta_i$ is the nondimensional damping parameter from Doppler cooling, and
- $c_i = \frac{4Q}{M\Omega^2} \cdot E_{\mathrm{stray},i}$ is the normalized stray field parameter, in units of $[z]$.

For concreteness, we shall take $\Omega = 2\pi \times 6$ MHz in the subsequent discussion, which is a representative RF frequency for the experiments described in this thesis. Under such conditions, the nondimensional damping parameter corresponding to optimal Doppler cooling (Eq. 3.10) is $b = \frac{2}{M\Omega} \cdot \left(5.8 \times 10^{-21} \mathrm{N \cdot s/m}\right) = 0.0021$.

Our analysis of the damped Mathieu equation (Eq. 3.14) proceeds as follows. First, we present the exact experimental geometry for laser cooling in the asymmetric point Paul trap, and identify the damping coefficients along each trap axis (Section 3.3.1). We then choose the axis with the weakest damping, and simulate the ion trajectory in the case of no stray field (Section 3.3.2) and in the presence of stray fields (Section 3.3.3). Ultimately, we will see that the effects of Doppler damping and stray field are neatly decoupled into the secular and micromotion components of the ion trajectory. Given this framework, we quantitatively summarize the relationship between laser cooling and steady-state secular motion amplitude, and likewise for stray field and micromotion amplitude (Section 3.3.4).

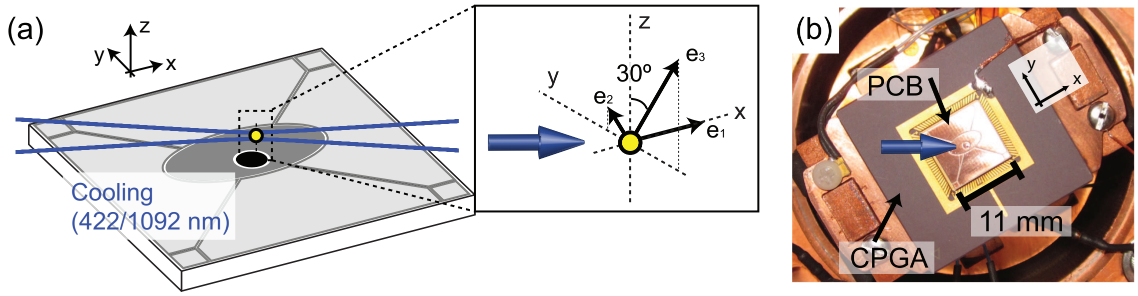

Figure 3-4: Doppler cooling in the fiber-trap system. (a) A schematic depiction of how the 422 nm Doppler cooling beam (and the 1092 nm repumper) is delivered to the ion in the asymmetric point Paul trap. As is typical for surface-electrode ion traps, the laser is confined to be parallel to the plane of the trap, and the cooling beam propagates along $\hat{e}_x - \hat{e}_y$. Inset shows the orientation of the trap axes $\{\hat{e}_i\}$ with respect to the trap xyz-frame. (b) Photograph of the experimental configuration, showing the cooling beam path with respect to the orientation of the trap.

3.3.1 The experimental cooling geometry

Surface-electrode ion traps, by their nature, restrict the optical access to the ion to the half-space above the chip. In order to avoid clipping of the incident beam by the trap electrodes, laser light is typically delivered parallel to the plane of the trap, i.e. in the xy-plane as shown in Fig. 3-4. As shown in both schematic and photograph forms, the 422 nm Doppler cooling beam is delivered to the fiber-trap system along $\hat{e}_x - \hat{e}_y$, with essentially zero projection along $\hat{e}_z$.

Due to such restrictions on the placement of the cooling beam, the trap layout is specifically engineered so that the trap axes $\{\hat{e}_1, \hat{e}_2, \hat{e}_3\}$ are rotated with respect to the xyz coordinate frame of the surface-electrode trap. Such design allows the single radial beam to have finite projections onto all axes of the trap. As noted in Section 2.5 and shown in the inset of Fig. 3-4(a), the asymmetric point Paul trap achieves a trap axis tilt of $\sim 30°$ in the yz-plane and a nondegenerate set of secular frequencies at a ratio $\omega_1 : \omega_2 : \omega_3 = 0.6 : 0.4 : 1$. Corresponding to this geometry, the damping parameter β is divided among the three axes according to the ratio

$$\beta_1 : \beta_2 : \beta_3 = 0.50 : 0.41 : 0.09, \tag{3.15}$$

showing that the weakest damping is along $\hat{e}_3$ due to its relatively weak projection $\hat{k}^T \cdot \hat{e}_3$. For this axis, the one-dimensional damping coefficient evaluates to $b_{3,\max} = 0.09 \times 0.0021 = 1.9 \times 10^{-4}$ assuming optimal Doppler cooling.

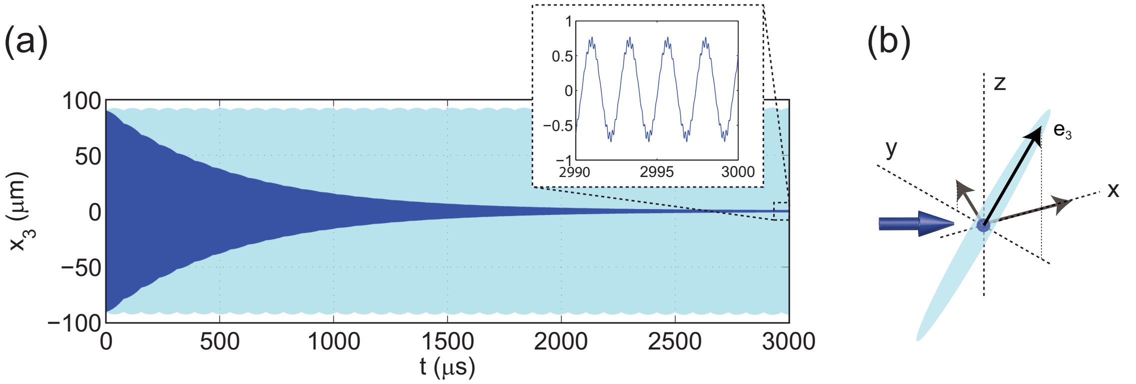

Figure 3-5: Damping of $^{88}\mathrm{Sr}^{+}$ trajectory (dark blue curve) along the $\hat{e}_3$ trap axis of the asymmetric point Paul trap by optimal Doppler cooling. (a) The ion is initialized at the quadrupole node ($x_3 = 0$) but is given an initial velocity of 200 m/s, which is a reasonable estimate given a thermal atomic source. The trajectory amplitude tends towards zero with a damping time constant of approximately $T_{\mathrm{sec}} = \frac{4}{b_3\Omega} = 560\ \mu\mathrm{s}$. By $t = 3000\ \mu\mathrm{s}$, the trajectory is brought to sub-micron amplitude. The light blue "background" represents the evolution of the same particle with no Doppler cooling. (b) The effect of laser cooling depicted qualitatively in the trap reference frame.

3.3.2 Damping of a compensated ion

Let us examine ion motion along the $\hat{e}_3$ axis, along which Doppler damping is the weakest. We restate the equation of motion:

$$\frac{d^2x_3}{d\tau^2} + b_3\frac{dx_3}{d\tau} + 2q_3\cos 2\tau \cdot x_3 = c_3, \tag{3.16}$$

in which x_3 denotes the displacement of the ion from the RF node along $\hat{e}_3$, and optimal Doppler cooling is assumed (i.e. $b_3 = 1.9 \times 10^{-4}$). We take a typical value for the Mathieu q-parameter: $q_3 = 0.2$. For convenience, we will omit the subscripts on the coefficients.

Fig. 3-5(a) shows the effect of the damping term in the Mathieu equation assuming a compensated ion, i.e. $c = 0$. The dark blue curve shows the ion trajectory under damping, where the ion has been initialized at the quadrupole node ($x_3 = 0$) but with an initial velocity of 200 m/s, which is a reasonable estimate given a thermal atomic source [BLW+07]. (We will take these initial conditions for all trajectories shown in this chapter.) As expected, the ion amplitude is damped towards zero. The apparent time constant is roughly 600 μs. Note that, under the harmonic approximation, one can derive an exponential damping factor of $\exp(-b_3/2 \cdot \tau)$ due to Doppler cooling. The corresponding time constant is $T = \frac{4}{b_3\Omega} = 560\ \mu\mathrm{s}$, which is in good agreement with the numerical result.

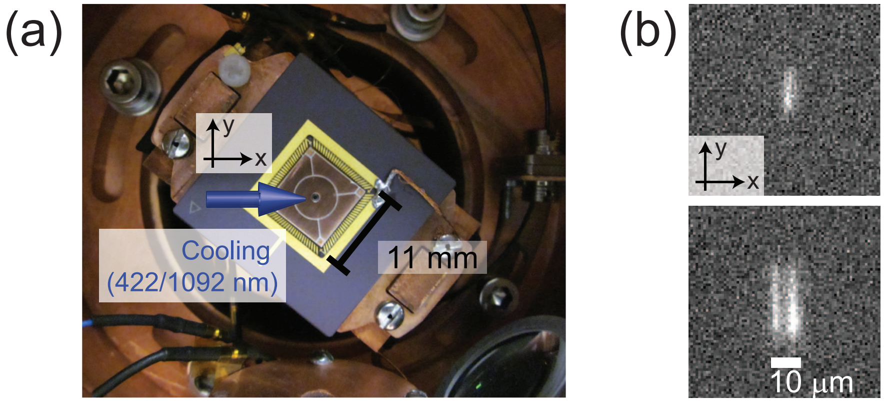

Figure 3-6: Ineffective Doppler cooling in the symmetric point Paul trap. (a) The cooling geometry in the symmetric point Paul trap. Given the cylindrical symmetry of the trap, we diagonalize the radial axes along the direction of the cooling laser. (b) Typical "elongated" ion orbits observed in the symmetric trap. As the exposure time of the CCD is much longer than the timescale of trapped ion motion, the ion appears smeared over its trajectory. In the axis of Doppler cooling, the ion amplitude is $x_{\mathrm{pp}} \sim 1$ μm. (Note that our imaging system cannot resolve sub-micron orbits.) In the orthogonal, uncooled axis, the amplitude is $y_{\mathrm{pp}} \sim 30$ μm, which is comparable to the mode waist of the integrated fiber.

In contrast, the light blue "background" of Fig. 3-5 shows the evolution of the same particle with no Doppler cooling. In this case, the peak-to-peak amplitude $x_{\mathrm{pp}} \approx 200$ μm is time-invariant and determined entirely by the initial conditions. The amplitude of the undamped trajectory significantly exceeds the mode waist of the integrated fiber, and is clearly unsuitable for the integration project. The difference between the two trajectories is illustrated schematically in the lab xyz-frame in Fig. 3-5(b).

A striking experimental validation of Fig. 3-5 has been obtained in our work with the *symmetric* point Paul trap. In this system, as shown in Fig. 3-6(a), a single cooling laser is delivered radially as is done for the asymmetric trap. However, given the cylindrical symmetry of the design, we are free to diagonalize the radial axes along the direction of laser propagation. It then follows that ion motion along $\hat{e}_x$ is Doppler cooled, but that motion along $\hat{e}_y$ and $\hat{e}_z$ are undamped. In Fig. 3-6(b), we show typical images of one- and two-ion crystals observed in the symmetric trap, where the ion appears smeared over its orbit $\vec{x}(t)$ due to the long exposure time of the camera. The calibration is provided by the inter-ion spacing of 10 μm, which indicates $x_{\mathrm{pp}} \sim 1$ μm and $y_{\mathrm{pp}} \sim 30$ μm. We find that the "elongation" of the ion remains orthogonal to the laser beam as the latter is rotated in the xy-plane, proving that the amplitude asymmetry originates from the cooling geometry.

3.3.3 Damping in the presence of stray field

While a compensated ion can be brought to rest by laser cooling, the actual experimental system is more likely to suffer from finite stray fields. Hence, we must consider the effect of stray field on the damped Mathieu equation.

We begin by estimating the typical magnitude c of stray field that is consistent with our experience with the fiber-trap system. Recall that the act of stray field compensation in experiment consists of searching for a set of DC voltages on supplementary electrodes that minimize excess ion motion according to the photon correlation signal. By applying a DC bias, the electric field generated by each electrode is superposed on the intrinsic field profile associated with the random charge environment. The overall goal is to null the electric field at the ion through superposition. Hence, it follows that the experimentally relevant range of intrinsic stray field magnitudes can be inferred by considering the voltages typically required to compensate an ion.

In the fiber-trap system, the compensation search usually spans several volts on the compensation electrodes, e.g. ±5 V. The DC potential can be translated into field magnitudes at the ion location through numerical computation of the field profile. Based on such conversion, we find a range of $|c| \leq 5\ \mu\text{m}$ (per Eq. 2.8) to be experimentally reasonable.

Fig. 3-7 shows the resultant ion trajectories as the ion is increasingly miscompensated. The chosen values for the stray field c lies well within the experimentally relevant range. Immediately, we observe that the ion is pushed off of the quadrupole node, and that, unlike the case of Doppler cooling of a compensated ion, a nonzero peak-to-peak amplitude emerges in the steady-state. By examining in detail a segment of steady-state evolution (namely, $t \in [2995, 3000]\ \ \mu\text{s}$), we note the following features:

- Even in the expanded model, the conceptual division of the trajectory into secular and micromotion components remains valid.
- Steady-state ion motion lies entirely in the micromotion component, which persists even in the presence of Doppler damping.
- In contrast, secular motion is exponentially damped, exactly as in the $c = 0$ case.

We tabulate the mean offset from the RF node $\langle x_3 \rangle$, and peak-to-peak amplitude $x_{\text{pp},3}$ as a function of stray field c in Table 3.1.

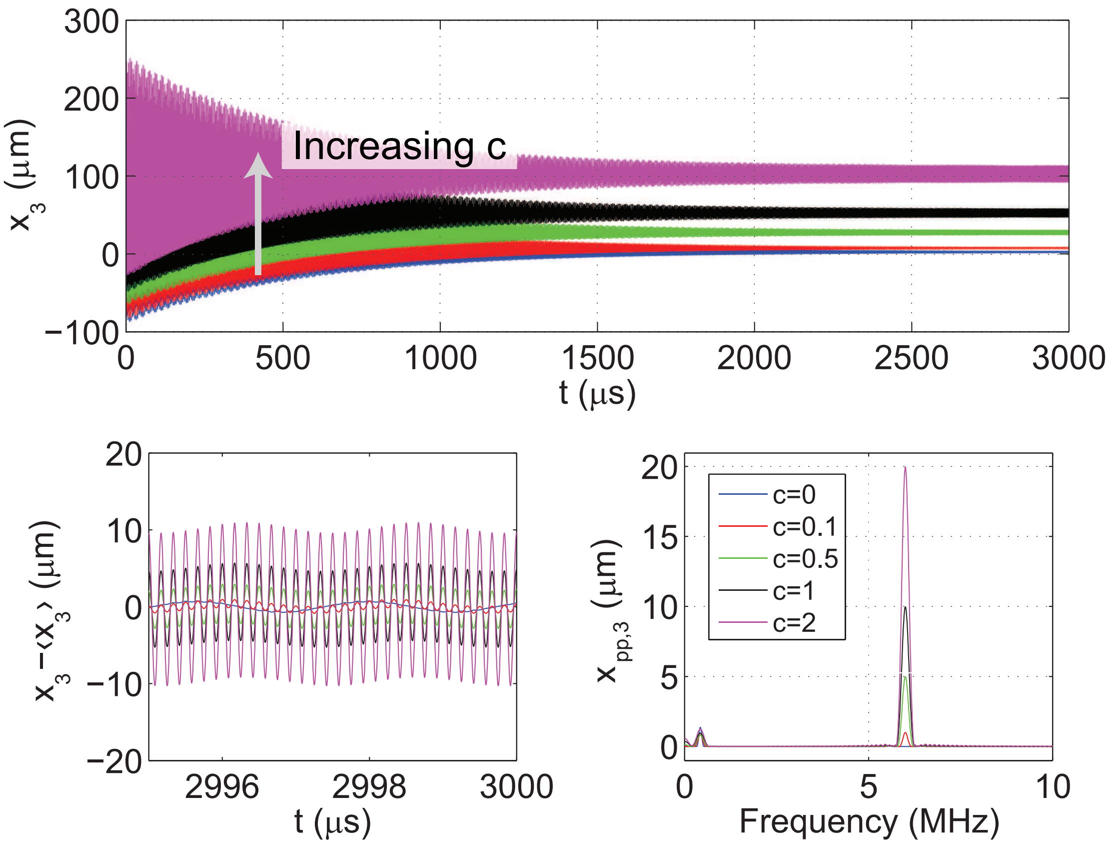

Figure 3-7: Effect of increasing stray field c (given in μm) on the simulated trajectories. There are two effects: (1) the ion is displaced from the quadrupole node, and (2) the ion experiences steady-state oscillation at the RF frequency of $\Omega = 2\pi \times 6$ MHz. In the lower-left panel, the mean offset has been subtracted, in order to emphasize the increase in peak-to-peak amplitude as the ion is subject to increasing c. The FFT of the trajectories illustrate that the solution can still be conceptualized as the superposition of secular motion and micromotion.

Stray field c (μm)	Mean deviation $\langle x_3 \rangle$ (μm)	Micromotion amp. $x_{\mathrm{pp},3}$ (μm)
0	0	0
0.1	5	1
0.5	25	5
1.0	50	10
2.0	100	20

Table 3.1: Mean deviation from the quadrupole node and the amplitude of the micromotion shown in the trajectories Fig. 3-7. Values have been rounded to the nearest micron. Note that both quantities are linearly proportional to the stray field term. Using the harmonic approximation, the mean displacement is $\langle x_3 \rangle = \frac{2c}{q^2}$. The peak-to-peak micromotion amplitude can be shown to be $x_{\mathrm{pp},3} = \frac{2c}{q}$.

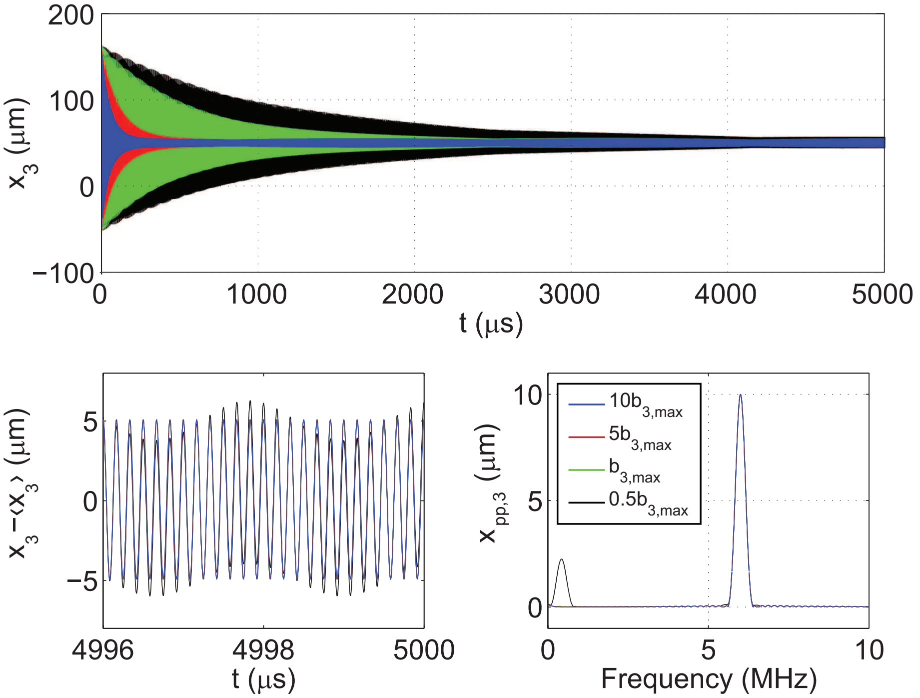

Figure 3-8: The resilience of stray field-induced micromotion against Doppler cooling. The simulated micromotion amplitude is invariant to an order of magnitude change in the damping parameter. Note, however, that the rate of secular damping is controlled by b.

One might now wonder whether stray field-induced micromotion may be better contained by increasing the damping coefficient. Fig. 3-8 shows the variation in ion trajectory at a fixed stray field of $c = 1$ μm as the damping coefficient is varied. Note that $10 \cdot b_{3,\mathrm{max}}$ is roughly equivalent to the physical cooling limit on the 422 nm transition (i.e. Eq. 3.10). It is found – perhaps surprisingly – that Doppler cooling has no effect on the micromotion amplitude, in contrast to the secular motion. The physical explanation is as follows: the basic effect of a stray field is to push the ion off of the RF quadrupole node, which enables ion interaction with the oscillating field. The magnitude of this electromagnetic force greatly exceeds any damping force realizable through laser cooling. Hence, micromotion induced by the stray field is essentially unaffected by laser cooling.

In conclusion, we find that steady-state ion motion amplitude can grow to several tens of micrometers, regardless of Doppler cooling, if the ion is not properly compensated. The exact relation can be shown to be $x_{3,\mathrm{pp}} = \frac{2c}{q}$ (left as an exercise to the reader!), which implies that the amplitude per unit stray field is expected to be even greater along the

$\hat{e_1}$ and $\hat{e_2}$ directions of the asymmetric point Paul trap for which the corresponding q-parameters are smaller. Since micron-level amplitudes are a considerable fraction of the mode waist of the integrated fiber, explicit compensation of the ion along all three trap axes is a strictly necessary condition for the fiber-integration project. Fortunately, stray field-induced motion lies exclusively in the high-frequency micromotion component, which allows it to be readily detected through the photon correlation technique as long as the cooling laser has a finite projection on all trap axes.

3.3.4 Summary of the damped Mathieu equation

We have learned that, even after Doppler cooling and stray fields have been added to the numerical model, ion motion in a RF trap can still be considered a superposition of secular motion and micromotion. In this framework, the effects of damping and stray field are neatly decoupled, which we now summarize for the i-th axis:

1. Doppler cooling exponentially dissipates secular motion with a time constant that is independent of stray field:
$$T_{\mathrm{sec},i} = \frac{4}{b_i \Omega}. \tag{3.17}$$
Without damping, secular amplitudes are indeed affected by stray fields; and can easily exceed 100 μm in steady-state, which is entirely unsuitable for fiber integration.

2. In contrast to secular motion, stray field-induced micromotion is virtually unaffected by laser cooling. Its peak-to-peak amplitude is determined solely by the stray field:
$$x_{\mathrm{pp},i} = \frac{2c_i}{q_i}, \tag{3.18}$$
which may grow as large as several tens of microns in the fiber-trap system given typical stray field magnitudes.

3. Stray field also causes a static offset of the ion from the RF node, given by
$$\langle x_i \rangle = \frac{2c_i}{q_i^2}. \tag{3.19}$$

Consequently, to obtain sub-micron orbits per the damped Mathieu equation, we require along each trap axis: (1) Doppler damping of secular motion, and (2) elimination of stray field-induced micromotion by ion compensation.

As an aside, note that using Eqs. 3.18 and 3.19 we may directly express the micromotion amplitude as a function of the offset from the quadrupole node:

$$x_{\mathrm{pp},i} = q_i \langle x_i \rangle. \tag{3.20}$$

This relation emphasizes the importance of the field node in RF ion trapping. Namely, in Chapter 2, we have found that ions undergo bounded motion in the vicinity of an oscillating quadrupole node. We now additionally understand that the ion can only be brought to rest when it is positioned exactly at the RF node.

3.3.5 Implications for the fiber-trap

Our study of the damped Mathieu equation is motivated by our need to achieve sub-micron localization of the ion in all three dimensions. The sufficient conditions of (1) Doppler cooling and (2) stray field compensation are achieved by a finite projection of the cooling laser on all trap axes. This requirement drives the asymmetric redesign of the point Paul trap, which we take as the basic layout for the fiber-integrated system.

3.4 Beyond the Mathieu equation

Thus far, we have presented the damped Mathieu equation as the governing equation of motion for a trapped atomic ion under laser cooling. While this model is valid in the immediate vicinity of the quadrupole node, it is important to realize that the Mathieu equation is fundamentally based on a linear-field approximation of the RF trapping field about the node. If the ion samples the electric field further away from the node – as in the case of large stray fields, for example – we should expect our earlier conclusions based on the damped Mathieu equation to become increasingly inaccurate.

Given our numerical approach to modeling the motion of trapped ions, we have the ability to incorporate arbitrary complications to the governing dynamics. The majority of these elaborations are only relevant when the ion trajectory takes a significant excursion away from the quadrupole node, and are thus not of particular interest in the context of sub-micron ion confinement. Nevertheless, we provide a cursory discussion of the "higher-order" numerical models: we highlight the limitations of the linear-field approximation

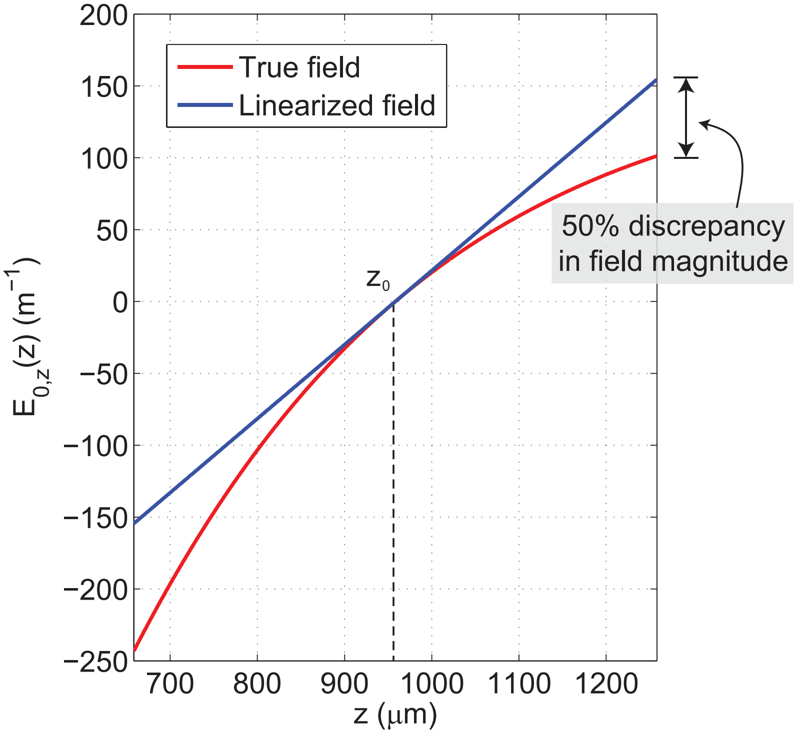

Figure 3-9: Comparison of the true and linearized electric field profiles along the z-axis of the symmetric point Paul trap. The trap is defined by $a = 0.65$ mm and $b = 3.24$ mm, which corresponds to our experimental sample. In the vicinity of a few 100 μm about the RF node, the linearized field deviates by about 50% from the actual field magnitude. Furthermore, note that the linear approximation overestimates the field magnitude for $z > z_0$, but underestimates for $z < z_0$. The implication is that a large-amplitude orbit $z(t)$ will be anisotropic about z_0 and biased towards $z > z_0$.

embodied in the Mathieu equation (Section 3.4.1) as well as the implications of introducing noise sources in the equation of motion (Section 3.4.2). The discussion thus seeks to suggest possible directions for future efforts in advanced trap modeling and design.

3.4.1 Higher-order field curvature

As a concrete example, let us return to the z-axis motion in the symmetric point Paul trap which was previously discussed in Section 2.4. Although we have identified the oscillating quadrupole field as the fundamental mechanism that enables ion confinement, we now choose instead to evaluate ion motion in the exact field profile $E_{0,\mathrm{z}}(z)$:

$$M\ddot{z} = -\beta\dot{z} + Q\left(V \cdot E_{0,\mathrm{z}}(z) \cdot \cos(\Omega t) + E_{\mathrm{stray,z}}\right) \tag{3.21}$$

where we have retained the terms corresponding to Doppler cooling and stray field.

In the case of the symmetric point Paul trap, with an annular RF ring defined by inner and outer radii of a and b, the voltage-normalized field $E_{0,\mathrm{z}}$ follows from Eq. 2.17 as

$$E_{0,\mathrm{z}}(z) = \frac{1}{b} \cdot \frac{(b/z)^3}{\{1 + (b/z)^2\}^{3/2}} - \frac{1}{a} \cdot \frac{(a/z)^3}{\{1 + (a/z)^2\}^{3/2}}, \tag{3.22}$$

where $z = 0$ corresponds to the plane of the trap rather than the quadrupole node. We use $\tilde{z} = z - z_0$ to denote the deviation from the node. The exact profile is illustrated in Fig. 3-9 for $a = 0.65$ mm and $b = 3.24$ mm. Also shown is the linear approximation for Eq. 3.22, which represents the Mathieu equation. In the vicinity of a few 100 μm about the RF node, the linearized field already deviates by about 50% from the actual field magnitude. Therefore, we can expect deviations from the Mathieu model within the ~ 100 μm neighborhood of the node. Furthermore, note that, due to the asymmetry of the true field about z_0, the ion orbit will also tend to be anisotropic about the RF node.

Deviations from the damped Mathieu equation

Previously, we have asserted that the damped Mathieu equation models the dynamics of a laser-cooled ion in the immediate vicinity of the quadrupole node. To quantify the notion of an "immediate vicinity," we can compare ion evolution in the linearized and true field profiles. The numerical experiment is as follows: (1) the ion is subject to increasing stray field, which pushes the ion further away from the node where it samples the increasingly nonlinear field profile; (2) the error between the "linear" and "true" trajectories is assessed as a function of the ion-node offset.

We present in Fig. 3-10 the discrepancy in the mean ion positions $\Delta\langle\tilde{z}\rangle$ as a function of the true ion-node offset $\langle\tilde{z}\rangle_t$. (Note that the error in steady-state amplitudes $\Delta\tilde{z}_{\mathrm{pp}}$ could also serve as a metric for the deviation.) At an ion-node offset of $\langle\tilde{z}\rangle_t = 28$ μm, we find a percentage error of $\frac{\Delta\langle z\rangle}{\langle z\rangle_t} = 11\%$ in the steady-state values. The error introduced by the linear field approximation increases to 40% when the ion is pushed further to $\langle z\rangle_t = 67$ μm. We conclude that the accuracy of the damped Mathieu equation, in the case of the point Paul trap, is limited to within ± 10 μm of the quadrupole node. Clearly, the range of validity of the Mathieu model depends on the nonlinear character of the exact electric field profile, which will vary from one trap design to another.

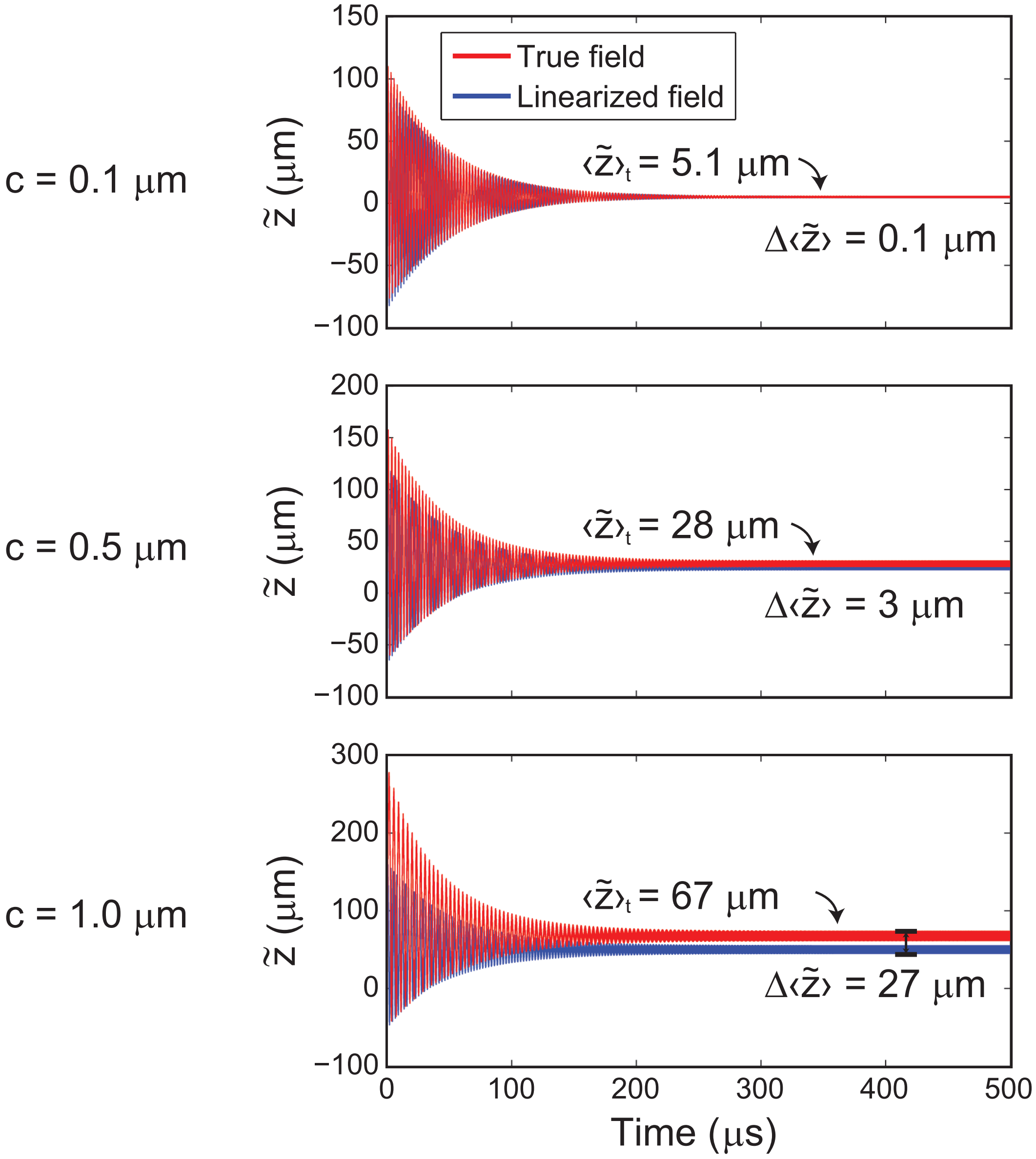

Figure 3-10: Comparison of ion evolution under the linearized and true fields along the z-axis of the symmetric point Paul trap with $a = 0.65$ mm and $b = 3.24$ mm; $\tilde{z}$ denotes the deviation from the RF node. The discrepancy between the trajectories is shown as a function of increasing stray field, which pushes the true position of the ion $\langle \tilde{z} \rangle_t$ away from the node. In these simulations, the RF frequency is $\Omega = 2\pi \times 6$ MHz, and optimal Doppler cooling ($b = 0.0021$) along $\tilde{z}$. The Mathieu q-parameter (in the linear model) is $q = 0.2$. The anisotropy of the true trajectory is evident in the $c = 1$ μm case.

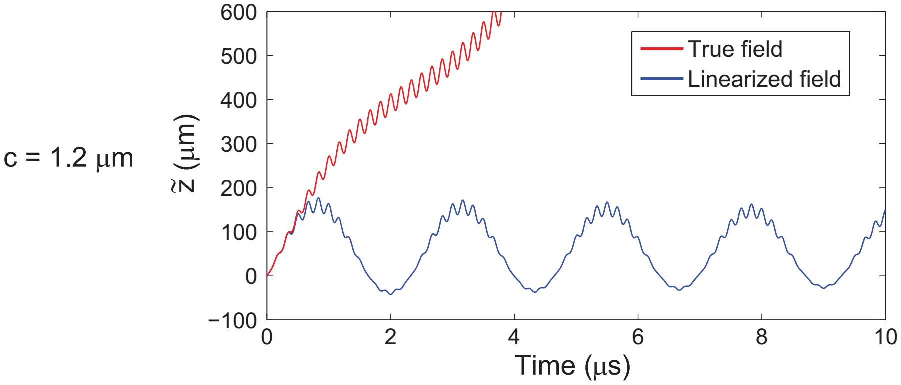

Figure 3-11: Demonstration of stray field-induced ion instability in the nonlinear field model. The system parameters are the same as in Fig. 3-10, while the stray field term has been slightly increased. Notably, the Mathieu q-parameter is well within the stability region: $0 < q = 0.2 < 0.9$. We find that the true trajectory of the ion is unbounded along $\tilde{z}$ while the Mathieu model suggests (incorrectly) a confined orbit characterized by $\{\tilde{z}_{\text{pp}} = 12\ \mu\text{m},\ \langle z \rangle = 60\ \mu\text{m}\}$.

Stray field-induced ion instability

We have shown that modeling of the higher-order nonlinearities in the trapping field introduces corrections to the damped Mathieu equation when the ion motion exceeds the $\pm 10\ \mu$m neighborhood of the RF node. More remarkably, the inclusion of the nonlinear field enables qualitatively different types of trajectories to emerge: namely, there is now the possibility that an ion will escape the quadrupole regime of the trapping field and become unbounded even when the (equivalent) Mathieu q-parameter lies within the stability region $0 < q < 0.9$. Thus, higher-order field modeling compels us to reexamine the notion of ion stability.

In Fig. 3-11, we increase the stray field beyond the range demonstrated in Fig. 3-10 while keeping all other parameters constant (notably, $q = 0.2$). It is observed that the true trajectory of the ion is unbounded, while the Mathieu model predicts a stable ion with a steady-state orbit characterized by $\{\tilde{z}_{\text{pp}} = 12\ \mu\text{m},\ \langle z \rangle = 60\ \mu\text{m}\}$. Here, we have made use of the formulas from our previous analysis of the damped Mathieu equation (Eqs. 3.17-3.19) which are *mathematically* valid regardless of the numerical values taken by the system parameters. Accordingly, it is impossible to destabilize an ion in a pure quadrupole field as long as the Mathieu q-parameter lies in the stability region: regardless of the magnitude of the stray field term, the trajectory will have the general shape as explored in Fig. 3-7 albeit at an unphysical scale.

In experiment, no ion trap has an infinite tolerance against stray fields even if the Mathieu q-parameter is kept well within the stability region. In fact, it is remarkably simple to destabilize a trapped ion in the point Paul trap in practice by applying an inappropriate DC field corresponding to a few volts. What is important to realize, then, is that the loss of the ion is caused by the interaction of the stray field term and the non-quadrupole regions of the trapping field, since it is mathematically impossible to destabilize an ion in a pure quadrupole field. To quantitatively reproduce the phenomenon of stray field-induced ion instability, the numerical model *must* describe the nonlinear curvature of the trapping field.

Once the dynamical model has been augmented to include the nonlinear features of the trapping field, the stability of the ion is no longer guaranteed solely by the Mathieu q-parameter. Instead, it is dependent on other system parameters such as the stray field term c. Abstractly, the stability condition in the nonlinear model is represented as a volume in a higher-dimensional phase space that includes the q-parameter and stray field c as two of its possibly many coordinates, rather than the one-dimensional condition $0 < q < 0.9$ corresponding to the Mathieu equation. (The Mathieu a-parameter is assumed to be 0 throughout this discussion.) Unfortunately, the nonlinear case is further complicated by the fact that the stability of a particle will now depend on the initial conditions, in addition to the parameters specifying the dynamical model. Hence, the higher-dimensional stability volume must be defined with respect to a set of initial conditions that physically represents the experimental loading mechanism.

Despite the numerous complications associated with the computation of the stability volume, it is this mathematical quantity – rather than the oversimplified Mathieu stability condition – that is directly relevant to the actual practice of ion trapping.

Higher-order trap design

What theoretical property of an ion trap design guarantees a robust experimental system? We propose that the design that possesses the greatest tolerance against stray field-induced instability – i.e. the largest nonlinear stability volume – will be the most reliable in practice. Our reasoning is as follows: the only quantity in the dynamical model that is totally unknown to and uncontrolled by the experimentalist is the initial stray field that originates from the intrinsic charge environment. This random parameter, when sufficiently large, can prevent trapping altogether in the true nonlinear profile. Thus, we desire a trap design that provides the largest nonlinear stability volume so that the trapping attempt is not likely to be thwarted by random and uncontrolled experimental factors.

Unfortunately, for the reasons cited previously, the direct computation of the stability volume is challenging. However, since stray field-induced instability originates from the nonlinear features of the trapping field, an alternate strategy for robust trap design is to explicitly eliminate or minimize the non-quadrupolar curvature of the trapping field through electrode layout.

3.4.2 Temporal perturbations: ion heating

In our summary of the damped Mathieu equation, we claimed that the secular motion of an ion is exponentially damped by laser cooling with a time constant of $T_{\mathrm{sec},i} = \frac{4}{b_i \Omega}$. Apparently then, even a vanishingly small projection of the cooling laser on the i-th axis can yield submicron confinement of a compensated ion. This claim is obviously unphysical and does not correspond to experimental practice, which routinely makes use of more substantial laser projections. What we have failed to address in our conceptual model are the sources of ion heating that generate excess ion motion.

In general, "heating" of the ion – randomly-driven ion motion in excess of the steady-state orbit – occurs when temporal perturbations are injected into the numerical model. For example, voltage noise on the trap electrodes will result in a random, time-varying electric field (along the i-th direction) at the ion position $e_i(t)$ which is incorporated into the equation of motion analogously to the stray field. Other sources of error, such as the mechanical vibration of the experimental setup, the AC dynamics of the charge environment, or even the Doppler cooling limit, can also be captured as an equivalent electric field noise. Intuitively, the overall effect of the noise term is to drive random ion motion.

Low-frequency perturbations

If the spectral content of the noise term is concentrated at frequencies below the RF frequency of the trap, we may utilize the secular approximation to derive the equilibrium ion amplitude under noise-induced heating. In the secular model, the governing equation of motion is approximated to be a damped harmonic oscillator with a transfer function $H_i(\omega) = \frac{X_i(\omega)}{E_i(\omega)}$ that relates the ion trajectory $x_i(t)$ to the driving field $e_i(t)$. Given the saturation limit on Doppler damping, the transfer function H is always underdamped. It follows that the gain at the secular frequency resonance is directly controlled by the magnitude of the damping parameter b_i, which can be shown to be: $|H_i(\omega_0)| \sim \frac{1}{b_i}$.

According to the transfer function model, given a noise source with a power spectral density (PSD) of $S_{ee}(\omega)$, the ion trajectory is also a random process with a PSD given by $S_{xx}(\omega) = |H_i(\omega)|^2 \cdot S_{ee}(\omega)$. In other words, the spectral features of the noise term are transmitted onto the ion motion through a shaping filter $|H_i(\omega)|^2$. It is seen that the magnitude of the damping parameter b_i will determine, in conjunction with S_{ee}, the nonzero equilibrium amplitude of the ion. For instance, we find at the secular frequency: $S_{xx}(\omega_0) \sim \frac{1}{b_i^2} \cdot S_{ee}(\omega_0)$. Note that, in the case of no Doppler damping $b_i = 0$, the transfer function $H(\omega)$ possesses a pole at the secular frequency. Consequently, the ion trajectory will not even be bounded in the presence of finite secular-frequency noise if no laser cooling is provided! The current discussion highlights how our basic understanding of ion motion can be qualitatively altered by the inclusion of noise sources in the equation of motion. Ultimately, we find in the experimental system a typical uncooled ion lifetime of ~ 10 s.

Arbitrary perturbations

While the low-frequency perturbations can be treated analytically through the techniques of linear signal processing, when the noise content occurs at frequencies exceeding that of the secular motion, the previous treatment is not appropriate. Fortunately, given our numerical framework for the analysis of trapped ion motion, we may incorporate arbitrary temporal perturbations directly into the dynamical system. In this *Monte-Carlo* approach, an ion is evolved in time under numerous instantiations of the random noise terms. Statistics are collected over multiple realizations of the trajectory, which is then analogous to the power spectrum $S_{xx}(\omega)$.

In the following chapter, we will demonstrate how our numerical framework may be expanded to study the effects of temporal instabilities in RF amplitude and phase.

3.4.3 The approximation hierarchy

In the previous two chapters, we have described ion motion at various levels of sophistication. In Fig. 3-12, we organize the various schemes as a succession of approximations.

At the most general level, *full dynamics* can represent the arbitrary interactions of the ion and its environment through an equivalent noise term $e_i(t)$. Additionally, any parameter

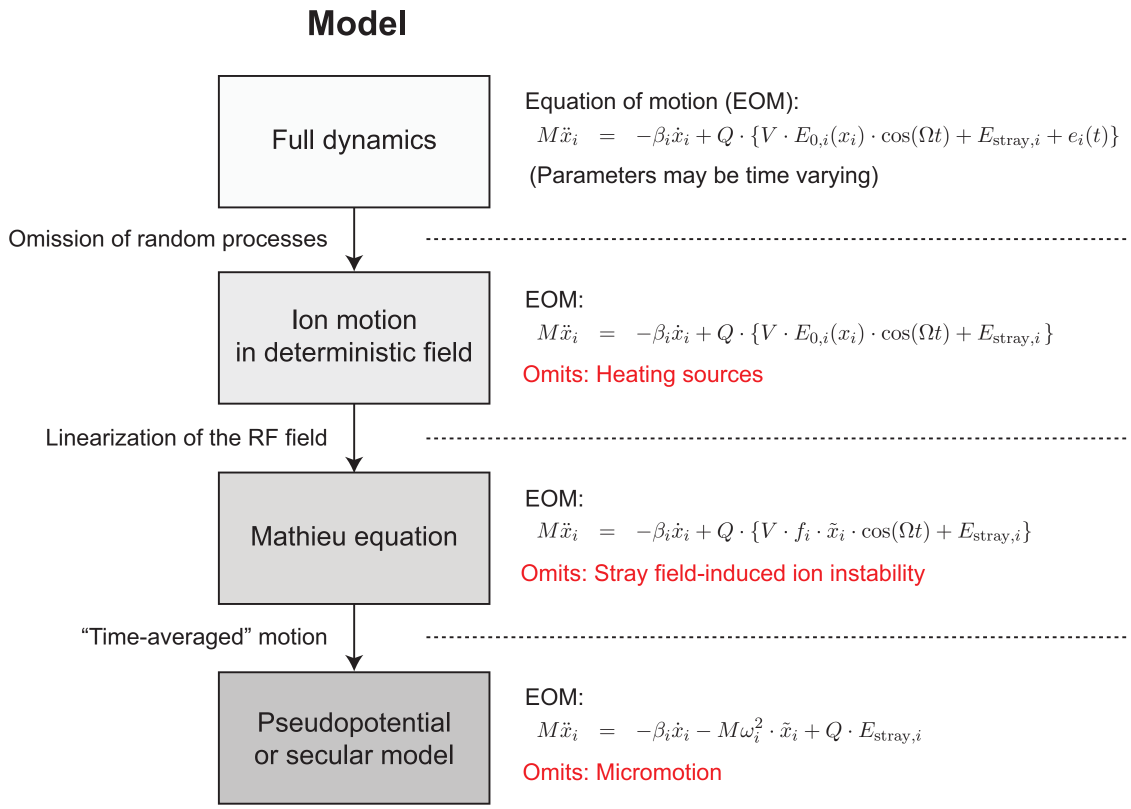

Figure 3-12: The approximation hierarchy for ion motion in an RF trap. The most general description – "full dynamics" – is indicated at the top, while the most restrictive model is at the bottom. For each level, we have indicated the governing equation of motion, and the aspects of ion trapping that are *omitted* by assuming a particular approximation.

in the dynamical system can be time-varying, which can be used to represent imperfections in the experimental system. The drawback of this description, of course, lies in the steep computational cost associated with a Monte-Carlo computational experiment.

By omitting random processes and temporal perturbations, we obtain *ion motion in a deterministic field*. Having adopted a deterministic equation of motion, we lose the ability to represent sources of ion heating.

By linearizing the field about the RF node, we arrive at the *Mathieu equation* which is a common starting point in the study of ion trap dynamics. In this chapter, we have relied on this level of description to study sub-micron ion confinement in the fiber-trap system. In comparison to the nonlinear model, the Mathieu approximation neglects the possibility of stray field-induced ion instability, and replaces the stability condition with a simpler criterion in the Mathieu aq-space that does not accurately represent the experimental system.

Finally, the *secular model* approximates ion dynamics as a harmonic oscillator. This approach is the most restrictive and is only valid for ions that are both compensated (as it omits micromotion) and cold (so that the linear-field approximation is valid).

3.5 Summary and outlook

We have specialized our understanding of RF ion traps to the confinement of atomic particles. The electronic structure of $^{88}\mathrm{Sr}^{+}$ was presented, and we demonstrated that the internal and external degrees of freedom of a trapped ion are coupled, giving rise to Doppler cooling of secular motion and the photon correlation technique for stray field compensation. We then formulated a numerical model for a trapped ion under laser cooling, which allowed us to analyze the effects of Doppler damping and stray field on the steady-state ion trajectory. Notably, the RF node was shown to be the unique position in space where sub-micron ion localization can be achieved.

In general, the development of integrated ion traps will require localization of the ion in three-dimensions with respect to the mode dimensions of the integrated element. In this chapter, we have emphasized: (1) the importance of Doppler cooling for dissipation of secular motion, and (2) the compensation of stray fields which can sustain induced micromotion even despite laser cooling. In practice, these conditions are satisfied by a sufficient projection of the cooling beam onto all trap axes.

Finally, we have described several higher-order schemes which extend the validity of the numerical model beyond the quadrupole region of an ion trap. In particular, by examining ion motion in the true nonlinear field, it was shown that stray fields can induce ion instabilities. In contrast, it is theoretically impossible to destabilize a trapped ion in a pure quadrupole field as long as the Mathieu q-parameter satisfies the stability condition ($0 < q < 0.9$). Our discussion of a high-dimensional stability volume offers an alternate optimization strategy in the general design of RF ion traps.

Chapter 4

RF ion positioning

In our analysis of laser-cooled atomic motion in RF ion traps, the quadrupole node was revealed to be a unique point in space where a trapped ion could be brought to absolute rest, up to the cooling limit. In this chapter, we introduce a novel technique for the *in situ* translation of the node by the use of multiple RF sources in a single trap, which permits ion translation without micromotion. This positioning ability is shown – through our work on fiber-integration – to be an enabling technology for the development of integrated traps.

Our exposition of the *multiple RF translation method* proceeds as follows:

- First, the need for *in situ* micromotion-free positioning is demonstrated in the context of fiber-integration (Section 4.1).
- We then analyze RF-based ion height variation along the z-axis of the symmetric point Paul trap, which provides an analytic model for RF translation (Section 4.2.1).
- Next, radial translation is presented for the asymmetric point Paul trap (Section 4.2.2).
- Lastly, we conduct a numerical study for the susceptibility of ion amplitude to selected errors in the multiple RF implementation (Section 4.3).

The idea and implementation of height variation and radial translation in the point Paul trap are my own work, and have been published in Refs. [KHK+10] and [KHC11]. Our efforts in positioning by multiple RFs may be considered an early implementation for the more general notion of "Reconfigurable trap arrays" [Chi11], which leverages the versatility of electrode design to enable new functionalities [VCA+10, HDM+09].

4.1 Ion positioning in integrated traps

In the previous chapter, we discussed the experimental requirements for the spatial localization of a trapped $^{88}\mathrm{Sr}^+$ with respect to the integrated fiber mode, where it was found that

1. The secular motion must be Doppler-damped along all trap axes, and
2. Steady-state micromotion amplitude must be eliminated by stray field compensation through the photon correlation (or some other) technique.

Regarding the latter point, we derived an important relation regarding the peak-to-peak micromotion amplitude x_{pp} and the offset of the ion $\langle x \rangle$ from the quadrupole node

$$x_{\mathrm{pp}} = q \cdot \langle x \rangle, \tag{4.1}$$

which shows that sub-micron ion confinement may be achieved only in the immediate vicinity of the quadrupole node where $\langle x \rangle \approx 0$. In other words, while the mean ion-node offset $\langle x \rangle$ may be adjusted by the deliberate addition of DC fields, the resultant ion location will not coincide with the zero of the RF field and therefore its motion will be driven by the rapidly changing RF fields, leading to increased micromotion. This “hot” ion motion whose amplitude is given by Eq. 4.1 makes the trapped ion unfavorable for QIP applications.

Therefore, we take the coincidence of the trapped ion and the quadrupole node as an absolute necessity. In the context of trap integration, it then follows that the trapping quadrupole fields must be carefully implemented so that they are precisely aligned with the integrated element. For instance, in our description of the fiber-trap system, we assumed that the ultimate ion location is coaxial with the axis of the fiber, which is indeed required for optimal coupling between the ion and the fiber at any given ion height. Such alignment, however, cannot be taken for granted but must be explicitly engineered by precise construction of the trap electrodes with respect to the integrated fiber.

In optics integration, precise construction is a matter of “life or death” as the typical optical mode is Gaussian which has an exponential fall-off in intensity in the transverse plane. In the fiber-trap system, the $1/e^2$-intensity mode waist is $w \approx 50\ \mu\mathrm{m}$ (Section 3.1). It is important to keep in mind that, at a deviation of one mode waist, the local field intensity drops to 13.5% of the peak value. Hence, to observe even basic interaction between

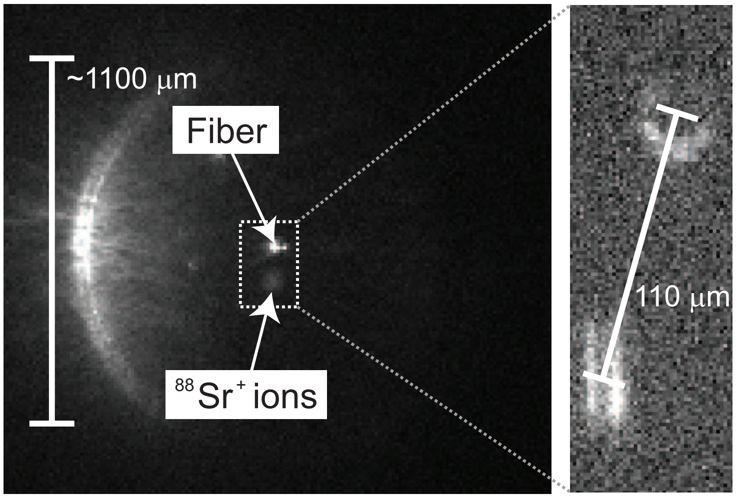

Figure 4-1: A typical offset between the trapping location (quadrupole node) and the center of the fiber mode. The 1100 μm feature is the centermost electrode of the point Paul trap, in which the fiber is embedded. The 10 μm spacing between the ions calibrates the high magnification image, and the offset between the centroid of the two-ion crystal and the center of the (unfocused) fiber image is measured to be 110 μm which significantly exceeds the fiber mode waist. The image was taken in the symmetric point Paul trap, which explains the elongated structure of the ion (due to poor damping of secular motion).

the ion and the fiber, the alignment between the quadrupole node and the fiber-axis must be good to a fraction of the optical waist, i.e. at the micron-level!

In general, the precise construction of an integrated trap system is technically challenging as it encompasses numerous degrees of freedom. For instance, the definition of the trap electrodes will vary within some given fabrication tolerance (±50 μm in our printed circuit board implementation) which gives rise to unpredicted shifts in the exact location of the quadrupole node. Material parameters, such as dielectric constants associated with trap materials, can also affect the exact field configuration, but were not modeled in our electromagnetic trap simulations. In the fiber-trap system, additional details include the exact tilt of the fiber with respect to the trap normal and the cleave angle of the fiber facet (typically a few degrees). One also has to deal with factory tolerances of the components used, such as the concentricity of the core and cladding in the optical fiber itself (a few microns). Taking all such factors into account, we have, unsurprisingly, found typical ion-fiber offsets on the order of 100 μm as shown in the CCD images of Fig. 4-1. The alignment problem is especially difficult to address preemptively, since the exact offset is not known until a successful ion signal is obtained, a process that may require significant preparatory work to bring the system to vacuum conditions neccesary for atomic ion trapping. In the past, the alignment challenge was typically addressed by physically moving the trap relative to external objects *in situ* [KLH$^+$04, LLVC09, DRB$^+$10], which is clearly inapplicable when the element of interest is integrated directly onto the trap structure.

While it may, in principle, be possible to construct a perfectly-aligned integrated system by improved technical construction, we present here an alternative, general solution based on the use of multiple RF sources in a single trap, which allows the quadrupole node to be translated *in situ* with respect to the integrated mode. In contrast to DC translation, the RF-based technique does not necessarily generate additional ion micromotion, making it compatible with QIP applications. The recent investigations (concurrent with this thesis) into the use of multiple RFs for ion position control has led to: (1) strong-coupling between a many-ion crystal and a cavity mode [HDA$^+$09], (2) novel transport of ions in 3D beyond conventional pseudopotential-"tube" shuttling [KLBK$^+$10], (3) spatial tuning of the ion fluorescence collection efficiency by an integrated multimode fiber [VCA$^+$10], among others. In this work, we engineer the coupling of a trapped $^{88}\mathrm{Sr}^+$ ion to an integrated Gaussian optical mode via RF-based position control. Future developments in optics integration will employ sub-10 μm waists, such as microcavities [HWS$^+$11] for the realization of quantum light-matter interfaces [CZKM97, KK09] or lensed fibers for faster gate times and optical trapping of ions [SEHS10], which underscores the importance of RF-based ion translation.

4.2 RF-based ion translation

In Chapter 2, we emphasized the oscillating quadrupole field as the basic physical mechanism enabling RF ion trapping. By using the superposition principle for electric fields, it is possible to translate the quadrupole node through multiple, synchronized RF sources applied to different trap electrodes. Field superposition is the simple notion that underlies RF-based ion translation.

We begin with a discussion of multiple RF drives in the symmetric point Paul trap that effects quadrupole node translation along the central z-axis (Section 4.2.1). Although our ultimate goal for ion translation is to mode-match the fiber-ion interaction in the radial plane (Section 4.2.2), there are two reasons for choosing the on-axis height variation for the initial discussion:

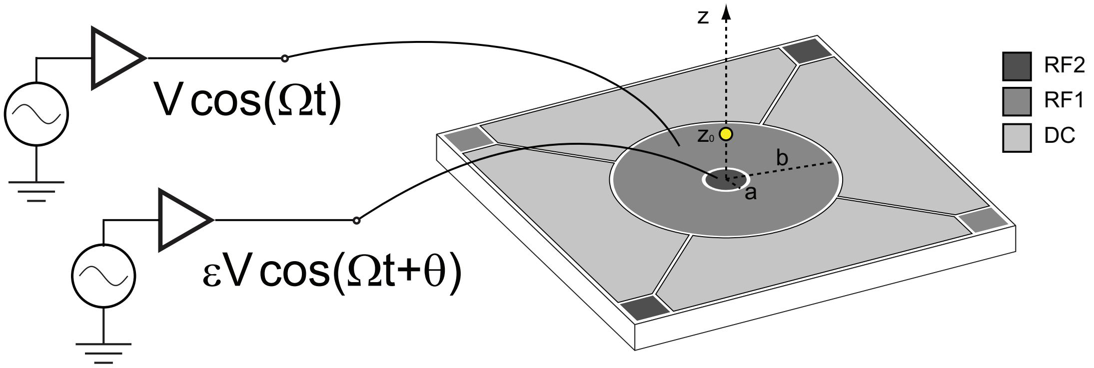

Figure 4-2: The use of two RF sources in the symmetric point Paul trap, that results in translation of the quadrupole node z_0 along the central z-axis. The original RF1 voltage is still applied on the ring electrode. The new source RF2 is brought to the previously-grounded center electrode. In practice, the contacts are made at the corner square pins which are connected to the circular electrodes through vias. Parameters ϵ and θ describe the relative amplitude and phase of RF2 with respect to RF1.

1. The symmetric point Paul trap offers closed-form solutions for the electric potential and fields along the z-axis. Thus, we can obtain an analytic understanding of RF-based translation.

2. Additionally, the height of the trapped ion in a surface-electrode ion trap is an experimental parameter of interest. The ability to vary the height *in situ* enables important experiments for trapped-ion QIP, especially in the study of anomalous heating.

4.2.1 Height variation in the symmetric trap

As noted, the basic principle of the method is to apply different amplitudes of RF potential on separate electrodes, causing a shift of the RF field node relative to those electrodes [HDA+09]. An implementation of this technique that results in ion height variation in the symmetric point Paul trap is particularly simple, where it is achieved by adding an RF field to the central, previously-grounded electrode, as shown schematically in Fig. 4-2. The corresponding boundary conditions for the electric potential are

$$\Phi(\rho, 0) = \begin{cases} \epsilon V \cos(\Omega t + \theta) & \text{for } 0 < \rho < a, \\ V \cos(\Omega t) & \text{for } a \leq \rho \leq b, \\ 0 & \text{for } b < \rho < \infty, \end{cases} \tag{4.2}$$

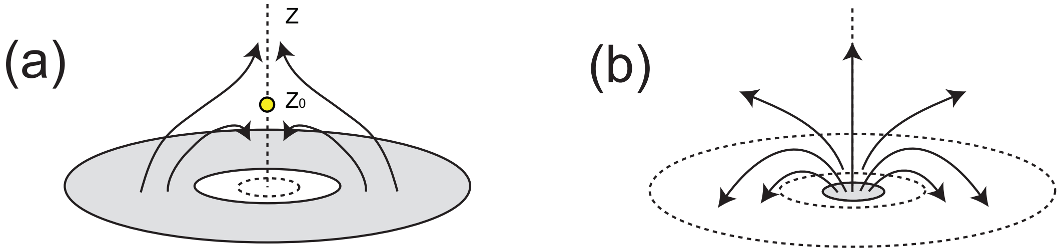

Figure 4-3: Qualitative depictions of the electric fields associated with each of the two RF electrodes. (a) The ring electrode, by itself, generates a quadrupole node at a height z_0 on the central axis. (b) The field due to the center electrode can be superimposed onto that of (a) in order to effect translation of the quadrupole node along the z-axis.

where ϵ and θ account for the amplitude and phase difference between the inner and outer RF electrodes, which are assumed to be under experimental control.

Before proceeding to find a solution to the potential in this configuration, it is useful to analyze the scenario in qualitative terms to gain some intuition about the influence of the second RF potential.

Along the z-axis, the RF field from the outer ring electrode reverses its sign around the quadrupole zero point z_0 [Fig. 4-3(a)], while the field from the inner RF electrode is always in the same direction on the z axis, pointing away from the trap surface [Fig. 4-3(b)]. If the two electrodes are driven in-phase, their fields will be of opposite sign for $z < z_0$ and the same sign for $z > z_0$. In that case, the effect of the second RF field is to decrease the magnitude of the field below the original trap location and increase it above, thus bringing the RF node closer to the electrodes. Conversely, if the two RF electrodes are driven out-of-phase the trapping point will move away from the electrode surface.

To develop a quantitative model, we solve for the electric potential in the entire half space $z > 0$ for the boundary conditions of Eq. 4.2. However, we specialize in the cases of in-phase ($\theta = 0$) and out-of-phase ($\theta = \pi$) drives. The scenario where the two electrodes are related by some other relative phase should be avoided, as it will result in excess micromotion, analogously to the case of the four-rod linear Paul trap [BMB$^+$98]. Absorbing the phase into the sign of ϵ, the spatial part of the resulting potential reads

$$\kappa(z,\rho) \;=\; \int_0^\infty e^{-kz}\, J_0(k\rho)\, \left[bJ_1(kb) - (1-\epsilon)aJ_1(ka)\right]\, dk,$$

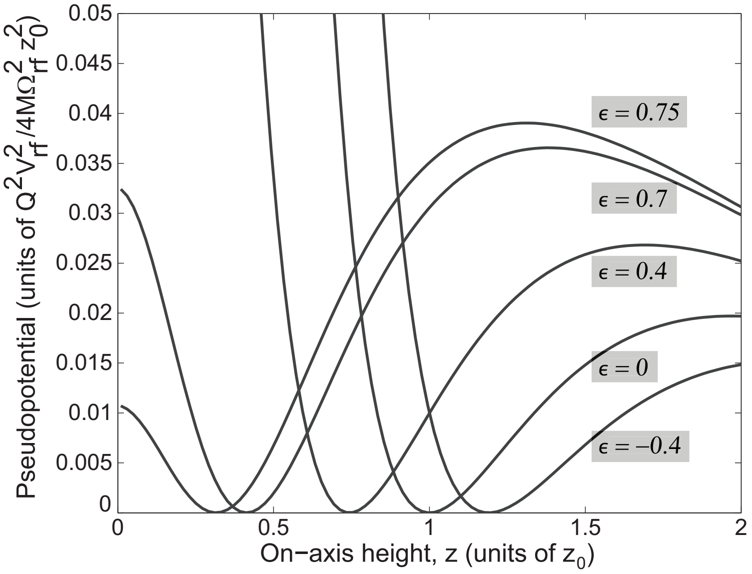

Figure 4-4: Variation in the on-axis pseudopotential Ψ with the addition of secondary RF at various values of ϵ. The trap dimensions a and b are as found in Table 2.1.

where $V(z,\rho,t) = V\cos(\Omega t)\kappa(z,\rho)$ as in our work in Chapter 2. As before, we focus on the case of $\rho = 0$ which yields a closed-form expression for $\kappa(z,0)$:

$$\kappa(z,0) = \frac{1}{\sqrt{1+(\frac{a}{z})^2}} - \frac{1}{\sqrt{1+(\frac{b}{z})^2}} + \epsilon\left(1 - \frac{1}{\sqrt{1+(\frac{a}{z})^2}}\right), \tag{4.3}$$

where $\epsilon > 0$ and $\epsilon < 0$ correspond to the in-phase and out-of-phase drives, respectively.

Inserting the expression for $\kappa(z,0)$ into the definition of the pseudopotential

$$\Psi(z,\rho) = \frac{Q^2V^2}{4M\Omega^2}|\nabla\kappa|^2, \tag{4.4}$$

and assuming the optimal point Paul trap geometry of Table 2.1, we plot the on-axis pseudopotential for various values of ϵ in Fig. 4-4. It is seen that, in accordance with our qualitative description, the in-phase drive ($\epsilon > 0$) lowers the trap height z_0 while the out-of-phase drive $\epsilon < 0$ increases the height.

Given the pseudopotential as a function of ϵ, the translated trap location $z_0'(\epsilon)$ and turning point $z_{\max}'(\epsilon)$ can be found analytically after much algebra, yielding:

$$z_0'(\epsilon) = \sqrt{\frac{b^2a^{4/3}(1-\epsilon)^{2/3} - a^2b^{4/3}}{b^{4/3} - a^{4/3}(1-\epsilon)^{2/3}}} \tag{4.5}$$

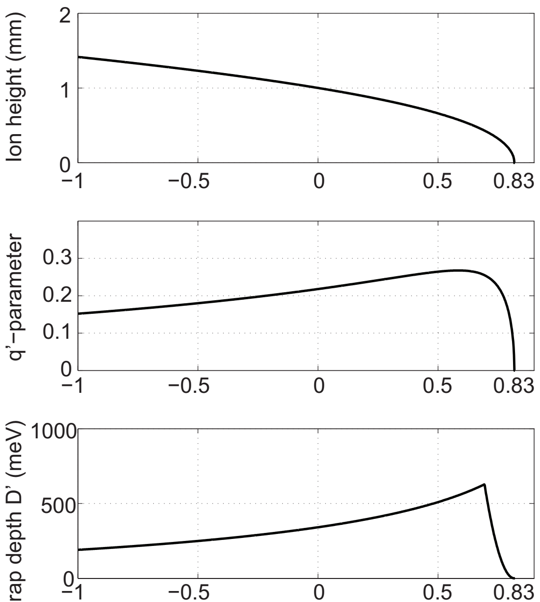

Figure 4-5: The variation in trap height, the Mathieu q-parameter and the effective trap depth as a function of the relative amplitude of the secondary RF. These parameters are computed for an optimal $z_0 = 1$ mm $^{88}\mathrm{Sr}^+$ trap (i.e. $a = 0.652$ mm and $b = 3.577$ mm), with $V = 200$ V and $\Omega = 2\pi \times 6$ MHz. (As a rough guide to interpreting D': we routinely trap atomic ions at a depth of 50 meV.)

which can be approximated to be linear for small ϵ, and

$$z'_{\max}(\epsilon) = \sqrt{\frac{b^2 a^{4/5}(1-\epsilon)^{2/5} - a^2 b^{4/5}}{b^{4/5} - a^{4/5}(1-\epsilon)^{2/5}}}. \tag{4.6}$$

We also find an expression for the Mathieu q-parameter:

$$q'(\epsilon) = \frac{2QV_{\mathrm{rf}}}{M\Omega_{\mathrm{rf}}^2}\left[\frac{3a^2 z'_0(1-\epsilon)}{(a^2+z'^2_0)^{5/2}} - \frac{3b^2 z'_0}{(b^2+z'^2_0)^{5/2}}\right]. \tag{4.7}$$

Note that, in addition to the height variation, the presence of a second RF modifies the overall shape of the pseudopotential and also the effective trap depth, as evidenced in Fig. 4-4. Namely, the out-of-phase regime is limited by a diminishing barrier on the side further away from the trap, and the in-phase drive causes a lowering of depth on the side towards the trap plane. For an ideal $z_0 = 1$ mm point Paul trap, Fig. 4-5 summarizes the variation in ion height z'_0, the Mathieu q'-parameter, and overall trap depth D' as a function of ϵ. In particular, note the cusp in trap depth at $\epsilon \approx 0.7$, which owes to the rapidly diminishing

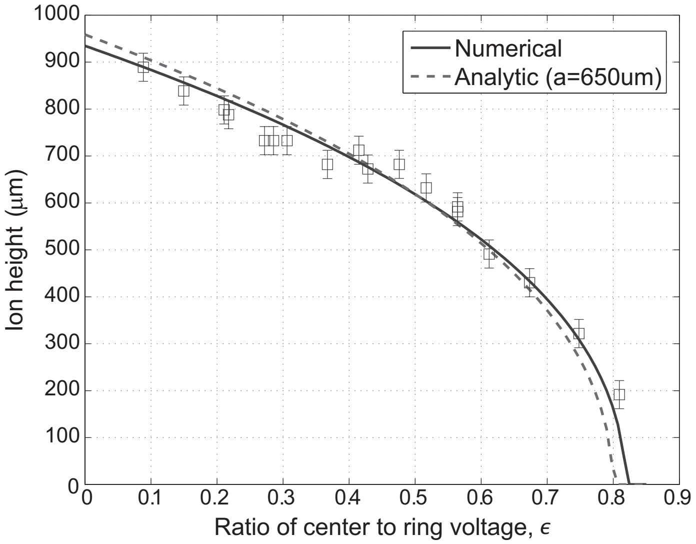

Figure 4-6: Measured variation in ion height with the addition of the second RF on the innermost electrode of the symmetric point Paul trap. Solid curve shows the height variation curve based on a numerical boundary element analysis for the field profiles, while the dashed curve shows the height as predicted by Eq. 4.5. The accuracy of the height measurement is limited by the finite waist of the laser beams.

trap barrier on the side towards the trap. Beyond $\epsilon > 0.83$, the quadrupole field is no longer defined as the superposed field is dominated by the central electrode which does not by itself produce a quadrupole node. Conservatively, a range of $0 < \epsilon < 0.7$ leads to a vertical range of $0.6 \cdot z_0$ that is achievable without suffering any decrease in trap depth from the single-RF configuration. Of course, a reduction in trap depth due to this technique may be compensated by varying the magnitude of the RF voltage and the RF frequency.

The height variation model in the symmetric point Paul trap has been experimentally validated in the in-phase $\epsilon > 0$ parameter space. Fig. 4-6 shows the results, where the vertical ion position has been accurately calibrated by a translation stage that controls the height of the ion detection laser with sub-micron precision. The solid line is the theoretical translation curve, which is based on numerically computed fields corresponding to the exact electrode geometry (e.g. with gaps between electrodes, and finite DC pads) that was shown in Fig. 4-2. In experiment, we found that stable trapping was straightforward to achieve even with two RF sources. Single ions and many-ion crystals were trapped as close as 200 μm from the trap surface, although the initial design height (with single RF) was 940 μm. Further approach to the trap plane was only prevented by scattering of the incident laser beams by the trap surface, which interfered with ion detection.

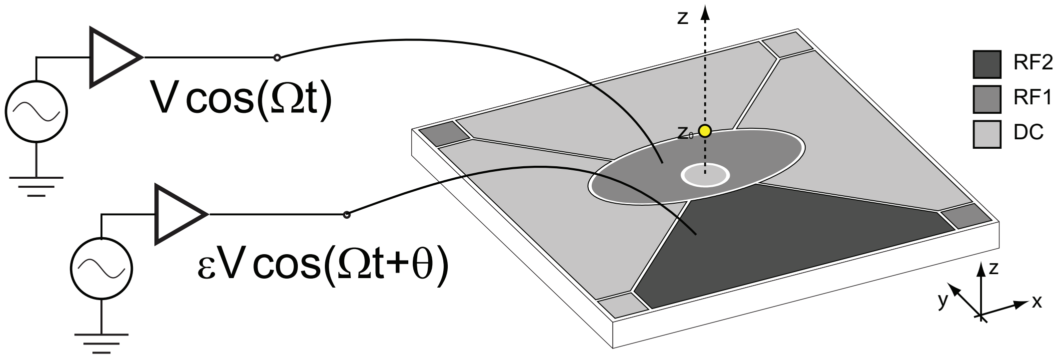

Figure 4-7: Configuration of two RF sources on the asymmetric point Paul trap that effects node translation along the radial direction. Exact dimensions of the trap are given in Section 2.5. The original RF electrode is the shifted ellipse; we apply a secondary RF to the side, formerly-DC electrode on the narrow-side of the minor axis. The combination of these electrodes will produce quadrupole node in the yz-plane that may be translated as a function of ϵ.

4.2.2 Radial translation in the asymmetric trap

In the context of this thesis work, the primary motivation for *in situ* ion positioning is due to the exponential fall-off in intensity along the transverse plane of a Gaussian fiber mode. Here, we analyze translation of the trapped ion in the horizontal plane of the fiber-integrated asymmetric point Paul trap.

Since RF translation is fundamentally based on electric field superposition, in order to translate the quadrupole node in the radial plane, we must utilize a secondary RF electrode that possesses significant radial field components. In this discussion, we use as the two RF electrodes: (1) the elliptical electrode, and (2) the side, formerly-DC electrode on the narrow side of the minor axis. The centermost electrode is grounded. The configuration is shown in Fig. 4-7. By inspection of the trap layout, we conclude that the resultant RF translation must occur in the yz-plane, over which the relevant electric field configurations can be obtained from a boundary-element electromagnetic simulation. It is then a simple numerical exercise to derive the node translation curve, the variation in trap depth and Mathieu q-parameter, etc. as we have previously done for the symmetric point Paul trap.

In Fig. 4-8 we show how the node translation is correlated with the rotation of the trap axes in the yz-plane. The series of axes corresponding to $\epsilon = 0.0, 0.1, \cdots, 0.9$ indicate the trap axes as the node is translated in the lab yz-frame. The background contour lines show the original pseudopotential at $\epsilon = 0$ which, in conjunction with the node translation curve, implies a significant reconfiguration of the trapping fields as ϵ is increased from 0 (single RF) to 1 (equivalent to shorting the two electrodes). Detailed deformation of the harmonic well is further illustrated in Fig. 4-9 where the variation in secular frequencies as a function of ϵ is shown.

We emphasize that the introduction of additional RF sources modifies the shape of the global pseudopotential, and thus all trapping parameters are expected to vary as a function of ϵ. The optimization of the electrode layout with the intent of decoupling node translation and other relevant trap parameters is likely to be experiment-specific. In the case of the fiber-trap system, the trap design is chosen such that all trap axes retain a nonzero tilt with respect to the xyz-frame over the translational range of interest, which guarantees proper laser cooling of the ion in 3D. More specifically, for $0 < \epsilon < 0.6$ which corresponds to a translational range of $\Delta y \approx 200\ \mu\text{m}$, the trap axes remain nondegenerate and each maintain a nonzero projection on the horizontal xy-plane.

Unfortunately, because the actual translation trajectory lies along $\hat{e}_y + \hat{e}_z$ and because the relevant displacements for ion-fiber modematching involve only tens of microns, it is difficult to confirm experimentally the predicted translation curves of Fig. 4-8. Aside from verification, operating the trap with multiple RFs for radial translation (e.g. in the configuration of Fig. 4-7) is as straightforward in practice as the case of height variation. We postpone the experimental validation of multiple RF radial translation until Chapter 6, where it is used to reproduce the Gaussian mode shape of the integrated fiber.

4.3 Modeling of RF errors

As the primary advantage of RF-based translation over DC offsets is the avoidance of induced micromotion, it is important to assess the sensitivity of the ion motion to the additional degrees of freedom that are introduced by the use of multiple RF sources. For example, two immediate sources of error include imperfect control of the relative amplitude ϵ and the phase offset θ. Following a qualitative discussion of the these control errors (Section 4.3.1), we precisely formulate the numerical simulation for assessing their effects (Section 4.3.2) and present the results, i.e. the susceptibility of ion motion to noise in ϵ and θ (Section 4.3.3). Our error analysis will be valuable in the design of instrumentation that will eventually control multiple RFs actively [KBB11].

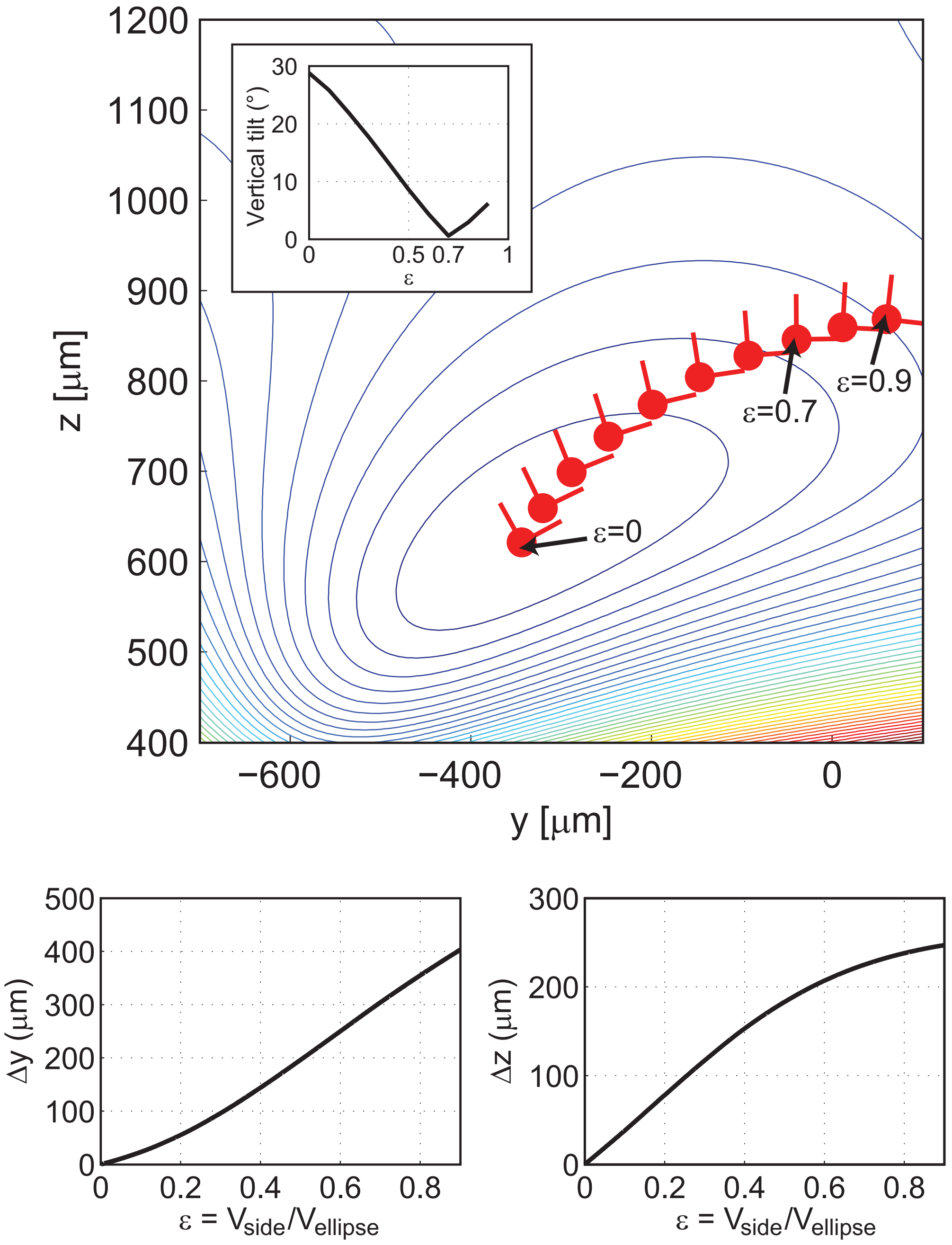

Figure 4-8: Translation of the quadrupole node in the yz-plane in the asymmetric trap using the configuration of Fig. 4-7. The zero of the y-axis represents the center of the center, grounded electrode. The contour lines indicate the pseudopotential at $\epsilon = 0$. The translated node position is indicated by a red dot whose associated vectors indicate the trap axes. Note that the tilt of the trap axes with respect to the lab frame is "undone" by increasing ϵ as indicated in the inset. The two graphs on the bottom show the ion displacements Δy and Δz from the original trapping location as a function of ϵ.

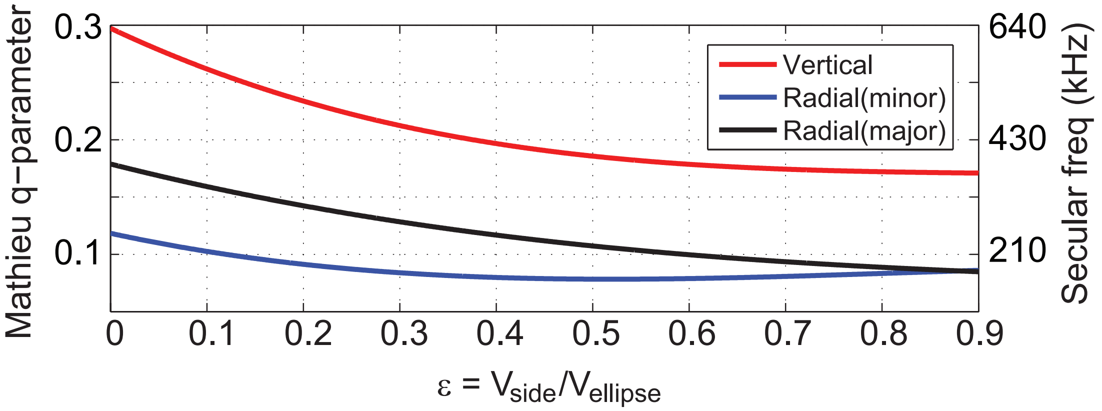

Figure 4-9: The variation in Mathieu q-parameter and the trap frequency as a function of ϵ at $V = 200$ V and $\Omega = 2\pi \times 6$ MHz in the asymmetric point Paul trap. The change in secular frequencies indicates deformation of the harmonic well. Note, in particular, the degeneracy of the two radial modes at $\epsilon \approx 0.9$, i.e. "undoing" of the built-in asymmetries of the trap.

4.3.1 Qualitative description and approach

We begin with a qualitative description. Consider the case of a time-varying $\epsilon(t)$ which represents voltage "jitter" due to imperfect amplitude control about the desired ratio ϵ_0. If the variation in $\epsilon(t)$ is sufficiently slow, and the ion is continuously Doppler cooled, it is reasonable to expect the ion to follow the node adiabatically as given by the translation curve of Fig. 4-8. On the other hand, if the jitter is fast, we expect the ion to lag behind the node position due to inertia. (The timescale determining "slow" and "fast", as well as any resonances, is of course governed by the dynamics of the ion, i.e. the damped Mathieu equation.) Note that this is in contrast to the conventional single RF configuration, where amplitude jitter on the RF will result in time modulation of the q-parameter but not spatial translation of the quadrupole node.

The stability of the node location is also jeopardized by a static phase error, i.e. when θ is neither in-phase ($\theta = 0$) nor out-of-phase ($\theta = \pi$). This is evident by considering again the basic notion of superposing two RF fields

$$\begin{aligned} \vec{E}(\vec{r},t) &= \vec{E}_1(\vec{r})\cos(\Omega t) + \vec{E}_2(\vec{r})\cos(\Omega t + \theta) && (4.8) \\ &= \left(\vec{E}_1(\vec{r}) + \cos(\theta)\vec{E}_2(\vec{r})\right)\cdot\cos(\Omega t) + \sin(\theta)\vec{E}_2(\vec{r})\cdot\sin(\Omega t) && (4.9) \end{aligned}$$

where it is shown that unless $\theta = 0$ or π, the overall field is the superposition of two spatial fields with opposite time-dependent quadratures. Given the orthogonality of $\cos(\Omega t)$ and $\sin(\Omega t)$, it follows that a time-independent quadrupole node can exist at $\vec{r}_0$ only when both $\vec{E}_1(\vec{r}_0) = 0$ and $\vec{E}_2(\vec{r}_0) = 0$, i.e. a restrictive scenario that precludes node translation. In general, the superposed node will be time-varying, and, at certain points of the RF phase, may even cease to exist.

While it is possible to perform an analytic, first-order perturbative study of the dynamics [BMB+98], we opt for a Monte Carlo-type numerical analysis. This way, we are able to explore the effects of large-magnitude errors as well as subjecting the ion to both amplitude and phase effects simultaneously.

4.3.2 Details of the numerical study

We simulate the classical dynamics of a trapped ion in the yz-plane of the asymmetric point Paul trap under two RF sources at the operating point $\epsilon_0 = 0.25$, which is a representative value for the fiber-trap experiment described in Chapter 6. The relevant equation of motion resembles the damped Mathieu equation, except that the q-parameter cannot be conveniently defined:

$$\begin{bmatrix} y'' \\ z'' \end{bmatrix} = -b \begin{bmatrix} y' \\ z' \end{bmatrix} - 2\left(\frac{2QV_1}{M\Omega^2}\right)\left\{\vec{E}_1(y,z)\cdot\cos(2\tau) + \epsilon(\tau)\vec{E}_2(y,z)\cdot\cos(2\tau+\theta)\right\}. \quad (4.10)$$

Here, the primes indicate a derivative with respect to τ. The quantity $\frac{2QV_1}{M\Omega^2}$, where V_1 is the voltage applied to the elliptical electrode RF1, is closely related to the Mathieu q-parameter, and b is the nondimensional damping constant which we take to be 1/3 of the optimum Doppler cooling value of 0.0021. The vector fields $\vec{E}_1(y,z)$ and $\vec{E}_2(y,z)$ represent the electric field profiles corresponding to each electrode at a bias of 1 V. Finally, the variables $\epsilon(\tau)$ and θ represent the errors that we seek to model. We neglect stray fields.

We implement "jitter" in the RF ratio $\epsilon(\tau)$ as follows. At every 1 μs, we sample from a normal distribution $\epsilon_0 \cdot N(1,\sigma^2)$ where ϵ_0 represents the desired ratio and σ is the standard deviation of the distribution that, in the current context, is also the fractional error in ϵ. This sampling yields a sequence which may then be connected by linear segments to produce a random continuous time function $\epsilon(\tau)$ that represents imprecision in the control of RF amplitudes. Note that, in our scheme, the variation in $\epsilon(\tau)$ is slow with respect to the RF period [$T = 1/(6\text{ MHz}) = 0.17\ \mu\text{s}$]. As a result, we are modeling the variations in the amplitudes between successive RF peaks rather than a sudden perturbation in voltage within a single period. Another way to interpret the model is that we are injecting white-noise error into the dynamic model with a bandwidth of 1 MHz. In contrast, we model phase errors straightforwardly as a static θ term in Eq. 4.10. The RF error configuration can thus be characterized by the pair (σ, θ). Given the randomness of $\epsilon(\tau)$, the simulation at every configuration is repeated ten times. Each run evolves the ion for 1 ms, which is sufficient damping time for the steady-state trajectory to emerge.

We characterize the resultant ion amplitude by computing the two-dimensional standard deviation of the steady-state orbit in the yz-plane. The motivation for choosing this measure comes from the conventional characterization of trapped atomic wavepackets in terms of their full-width-half-maximum (FWHM), which is mathematically equivalent to a standard deviation. A typical length scale for a laser-cooled ion is the Doppler-limited FWHM of some 100 nm, which serves as a convenient metric for interpreting the results of the simulation with regards to QIP applications.

4.3.3 Results

Fig. 4-10 shows the increase in ion amplitude in steps of 50 nm as the ion is subject to increasing errors in (σ, θ). The simulation corresponds to the asymmetric point Paul trap of Fig. 4-7 at the operating point of $\epsilon_0 = 0.25$. In order to maintain ion confinement near the Doppler limit ($\sim$ 100 nm), it is observed that the RF amplitudes must be stable to a fractional error of $\sigma = 0.01\%$ and the sources phase-locked to less than a degree. When the elliptical RF1 is operated at $V_1 = 200$ V (a representative number for the fiber-trap experiment), the requirement on σ implies a control of $\Delta V_2 = 20$ mV on RF2, a rather strict requirement! In our experiment, we meet this criterion by relying on a passive capacitive network for generating in-phase RF1 and RF2, which bounds the amplitude error at $\sigma = 0.005\%/\text{C}^\circ$ and provides essentially perfect phase control. Our implementation is described in Section 5.4. Note also that the sensitivity to RF control is trap-design and operational-point dependent, and may be reduced at the cost of total translational range.

What is also emphasized in this analysis is the extreme sensitivity of the trapped ion to electric field noise. One can interpret the results of Fig. 4-10 generally as being that all trap electrodes in the asymmetric point Paul trap must be controlled absolutely to within 10 mV

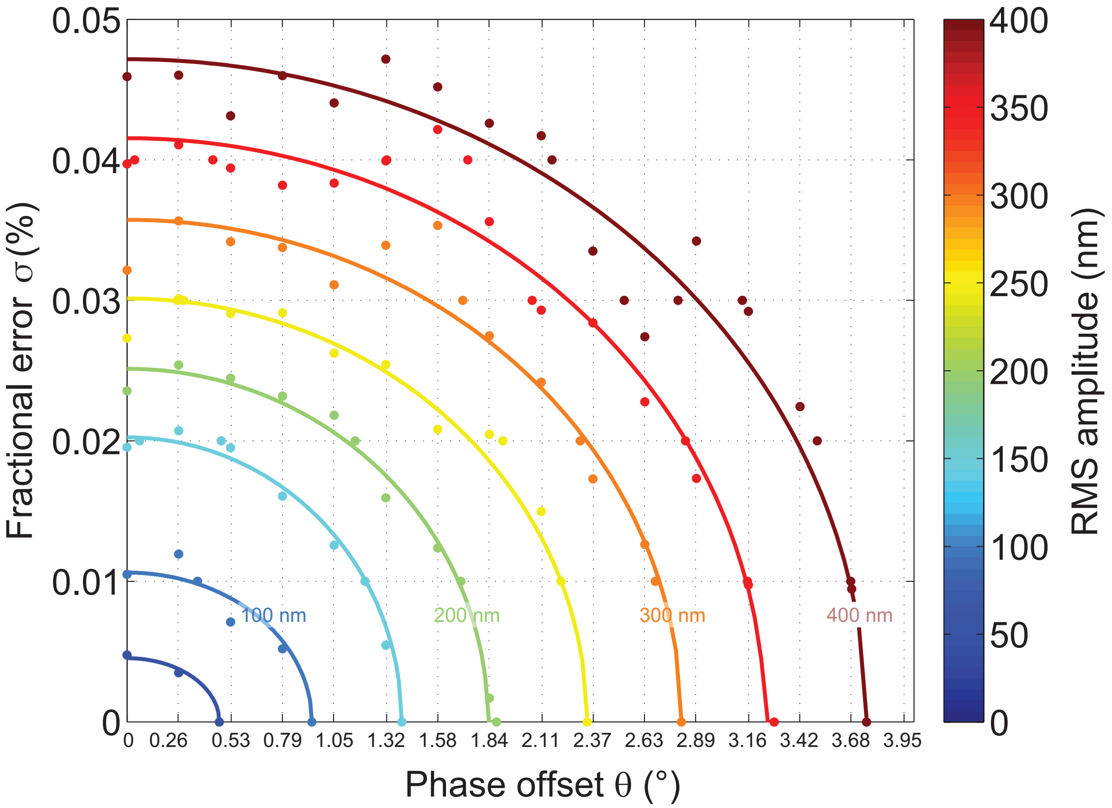

Figure 4-10: Results of a Monte-Carlo simulation showing the amplitude of ion trajectory as a function of RF errors (σ, θ). Isocurves come in steps of 50 nm. A set of 10 simulations are performed at every intersection of the dashed grid, and the desired isolevel is computed by interpolating between each edge of the simulation grid for the isovalue, which yields the colored points. Ellipses are fit as a guide to the eye. The contour line corresponding to 100 nm RMS amplitude can be considered the Doppler cooling limit.

in order to avoid significant perturbation (i.e. 100 nm) of the ion. Note that the ion height in the asymmetric point Paul trap at $\epsilon_0 = 0.25$, which we have analyzed, is $z_0' \approx 770$ μm. The sensitivity to trap electrode noise is expected to increase as the ion is brought closer to the trap plane, emphasizing the level of control over electronic noise that is required for trapped-ion QIP.

4.4 Summary and outlook

In this chapter, we have introduced the use of multiple RF sources in a single ion trap and analyzed the resultant translation of the quadrupole node in both the symmetric and asymmetric point Paul trap designs. RF-based radial translation of the ion in the asymmetric point Paul trap is highly important to fiber-integration as it provides a mechanism to mode-match the ion and the integrated mode *in situ*, without the necessary penalty of excess micromotion associated with DC-based translation. We have emphasized the coupling between node translation and various trap parameters, which must be appropriately decoupled for the given experimental requirements. Finally, we have presented a Monte-Carlo simulation of the amplitude susceptibility to the additional degrees of freedom generated by the use of two RF sources: the fractional error in amplitude control σ, and the phase offset θ. We use the numerical result to suggest that our experimental implementation of RF translation is compatible with requirements for QIP. However, the ultimate experimental verification of this claim – the confirmation of ground-state ion cooling and a measurement of multiple RF heating rate that is consistent with single RF – remains to be demonstrated.

One extreme implementation of RF translation is to use a digital "on-off" connection to multiple electrodes from a single RF source – i.e. a reconfigurable trap array. For example, in the N-electrode ideal point Paul trap, there are 2^{N-2} possible digital configurations that will generate a quadrupole node, each at a different height. In this scheme, in exchange for the loss of analog height control, one eliminates the errors σ and θ.

With the advent of multiple RF control in a single surface-electrode trap, it is possible to engineer new trap designs for specific translational functionality. For instance, the ability of the point Paul trap to vary the ion height without incurring micromotion is expected to be of tremendous value in the search for the origin of anomalous heating in ion traps [DOS+06, LGA+08]. Anomalous heating is believed to originate from fluctuating patch potentials on the electrodes. The model describing this effect predicts a scaling of the heating rate of $1/z_0^4$; however, only one experiment has thus far been able to conduct a systematic study to confirm this in a single trap geometry [DOS+06]. Previous work on this problem have either used a technically challenging setup in which the trap electrodes were moved *in situ* [DOS+06] or has relied on systematic testing of traps of identical geometry but at different scales, which has the disadvantage of random errors associated with the fabrication of the individual samples [LGA+08]. As the suggested scheme for the point Paul trap in principle allows for *in situ* variation of the ion height by almost an order of magnitude, it provides for an extremely sensitive test of the patch potential model without complications associated with physically moving the trap electrodes and without the errors and difficulty in obtaining good statistics associated with the use of individual traps for each value of z_0.

Chapter 5

Experimental setup

All work presented in this thesis were conducted in a unique experimental configuration, known as *cryogenic ion trapping*, based on a 6 Kelvin closed-cycle cryostat apparatus similar to the one presented in Ref. [ASA$^+$09]. The cryogenic environment offers several advantages for ion trapping (and also challenges) that have been explored by the trapped-ion QIP community, such as (1) the thermal deactivation of anomalous ion heating [LGA$^+$08], (2) the development of superconducting surface-electrode ion traps [WGL$^+$10], and (3) the dramatic suppression of material outgassing that allows ultra-high vacuum (UHV) pressures of sub-10^{-9} torr to be reached in 12 hours or even less. The latter point, namely the rapid turn-around time for trap deployment, was crucial for the fiber-integration project where it enabled in a span of just two years over fifteen trap instances of various designs to be tested. With each iteration and misstep, the requirements and techniques for fiber-ion integration were illuminated, which make up the contents of Chapters 2-4.

In this chapter, we describe the experimental setup in which the fiber-trap system was implemented. Through the numerous iterations, we have learned that the four “pillars” for successful ion trapping in the cryostat consist of (1) vacuum, (2) ion source, (3) electronics and (4) laser light. The discussion here is organized around this conceptual division. Following a high-level overview of our experimental setup (Section 5.1), we provide a detailed description of the cryogenic apparatus (Section 5.2) that provides UHV vacuum. We then cover “electronics,” i.e. the construction of the surface-electrode trap (Section 5.3) and electronic instrumentation (Section 5.4). Finally, we discuss light delivery and ion imaging (Section 5.5). All work presented here is my own, unless otherwise noted.

5.1 Overview

The main experiment chamber of the closed-cycle cryostat, containing the ion trap chip in its center, is shown in Fig. 5-1. The figure highlights the four requirements that we have come to appreciate for successful trapping in the cryostat system:

1. **Vacuum**: Is the pressure maintained in the experiment chamber sufficiently low to enable ion trapping (i.e. to reduce the collision rate of the trapped ion to background gas)? In the closed-cycle cryostat, the question of pressure is intimately tied to the thermal performance of the cryostat.

2. **Ion source**: Is there a functional source of $^{88}\mathrm{Sr}^+$ available for the ion trap? In the course of the fiber-trap implementation, we have explored both photoionization of an atomic strontium beam from a thermal oven [BLW+07] and ablation loading from a strontium titanate ($\mathrm{SrTiO_3}$) crystal [LCL+07]. We ultimately settled on the former as it produces significantly less contamination (i.e. generation of stray charge) during the loading process. Our thermal oven implementation is a good example of the type of heat load-conscientious design that is relevant for cryostat operation.

3. **Electronics**: Is the trap design implemented properly, i.e. does the final, fabricated product accurately reflect the intended design? Are the electrical sources – both high-voltage RF and DC compensation lines – functional and brought to the ion trap?

4. **Laser light**: Are the relevant lasers on-color and intersecting at the trap location with sufficient intensity? For the basic ion signal, one requires a minimum of two photoionization lasers (461 nm and 405 nm) and two lasers for ion detection and cooling (422 nm and 1092 nm). How can the atomic ion be detected?

In reality, the various subdivisions are interrelated. A direct verification of the ion source, for instance, may be performed only when the system has reached sufficiently low pressure (10^{-4} torr) so that photoionization fluorescence may be observed. Photoionization also requires two spatially-overlapped lasers that must be frequency-tuned and properly intersecting the neutral strontium beam. However, the conceptual division of the overall experiment into these subsystems has been particularly useful for the development and maintenance of the experimental apparatus.

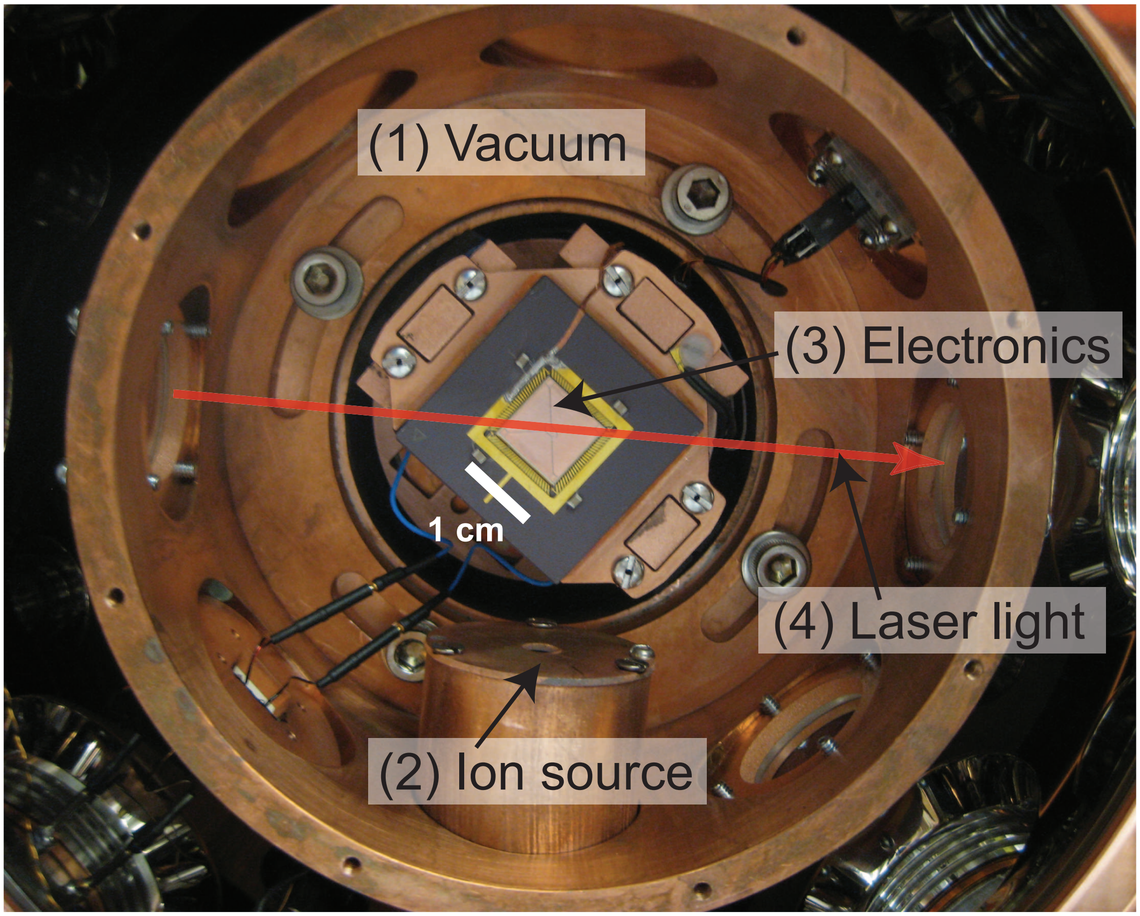

Figure 5-1: The main experiment chamber of the closed-cycle cryostat apparatus where the fiber-trap system is implemented. The stainless steel chamber (visible at the edges of the photograph) is the UHV vacuum chamber. The inner, 5-inch diameter copper tube is part of the cryostat and is cooled to 40 K during operation. The ion trap chip sits at the center of the apparatus and is cooled to, typically, 6-8 K. Following trap install, the intermediate 40 K chamber is closed by a lid that holds an imaging lens over the trap along the normal to the page. The intermediate shield is not hermetically sealed. We highlight the four "subsystems" that comprise the ion trap experiment: (1) vacuum, (2) ion source, (3) electronics, and (4) laser light.

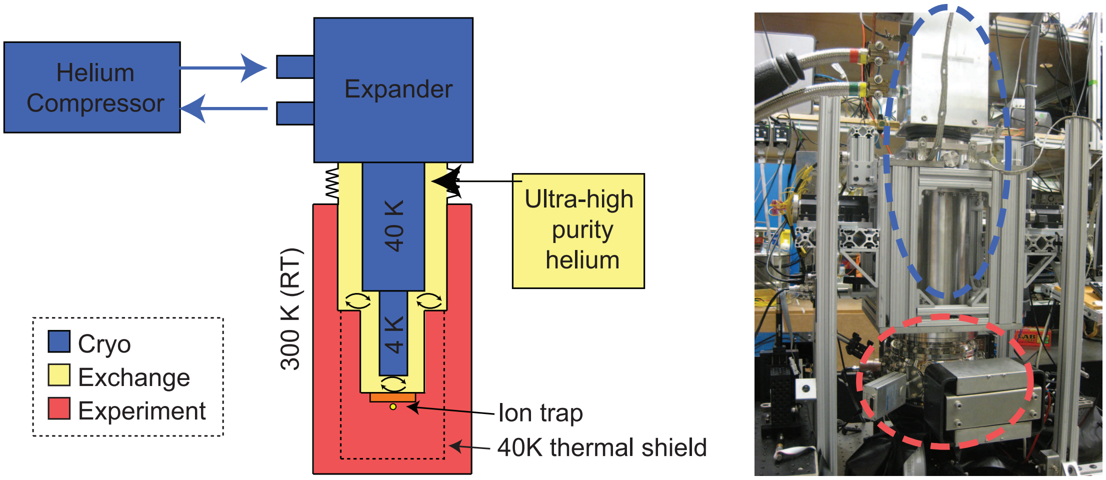

Figure 5-2: Photograph of the closed-cycle cryostat, and its physical division into three compartments: the "cryo" segment (blue) which provides 40 and 4 K stages, the "exchange" space (yellow) for convective cooling, and the "experiment" chamber (red) that contains the ion trap. The three are physically separated as indicated in the schematic. The separation of the cryo and experiment compartments is motivated by the need to isolate vibrations arising from the cryo expander from affecting trap operation. Instead of direct contact, the thermal exchange between cryo and experiment is performed by convective cooling in the exchange compartment, as indicated by the circulating arrows. The dashed lines in the experiment compartment indicate the 40 K thermal shield shown previously in Fig. 5-1. The entire apparatus is approximately 1 m tall.

5.2 The closed-cycle cryostat

In a cryogenic system, the discussion of vacuum and cryogenic cooling are synonymous as the necessary UHV pressures are achieved by thermal suppression of outgassing. We now present the basic principle of cryostat operation and its measured performance (Section 5.2.1); its mechanical construction (Section 5.2.2) and instrumentation (Section 5.2.3); and the design of the thermal ion source (Section 5.2.4).

5.2.1 Basic principles

We begin with the cryostat (also referred to as a "cryo") principle of operation. The low-vibration closed-cycle cryostat (Model: DE-210SF) is manufactured by Advanced Research Systems (ARS), and the discussion here is based on the ARS literature.

The cryostat consists of three separate compartments

The most basic concept for cryo operation is to recognize that the apparatus consists of three completely distinct compartments, which we call the "cryo", "exchange" and "experiment" compartments as shown in Fig. 5-2. These are physically separated in the apparatus. During normal operation, the cryo compartment can be considered a "black-box" instrument that provides two-stage cooling at 40 K and 4 K as indicated in the figure. (Notes from the initial assembly can be found in Refs. [Cla09] and [Ant11].) During experiment, we typically need to access only the experiment compartment, which is independently vacuum-sealed and was shown in the photograph of Fig. 5-1. The physical separation of the cryo and experiment by the exchange compartment is motivated by the desire to achieve isolation of the mechanical vibrations associated with cryo action. According to ARS, the cryo compartment shows typically 10-30 micron vibrations, whereas we measure 100 nm displacements on the experiment side [ASA$^+$09]. Due to the avoidance of direct contact, convective cooling (as indicated by the circulating arrows of Fig. 5-2) is used instead for thermal conduction between the cryo and experimental compartments. Hence, the cost of vibration isolation is that the ion trap will sit 1-2 K higher than the 4 K cold spot generated at the tip of the cryo coldfinger, since convective cooling is not as efficient as contact cooling.

In order to decouple the mechanical motion, the exchange compartment is enclosed by a flexible rubber bellow. It is absolutely crucial that these bellows be protected against bursting and the exchange space against general contamination, since the exchange compartment is directly exposed to the cryogenic surfaces of the apparatus. For example, if water or nitrogen were to get into this space, it can freeze and thermally short the experiment and cryo compartments by direct contact. The cryostat would then attempt to cool down the vacuum chamber walls from room temperature to its operating temperature. An instance of a thermal short is shown in Fig. 5-3. Obviously, the cryostat will fail in its cooling mission and possibly damage itself in the attempt.

There are two independent helium loops

As shown in Fig. 5-2, there are two circulating helium paths present in the apparatus: pressurized helium in the cryo compartment, and ultra-high purity (99.9999%) helium in the exchange compartment. The compressor provides high pressure helium to the head of

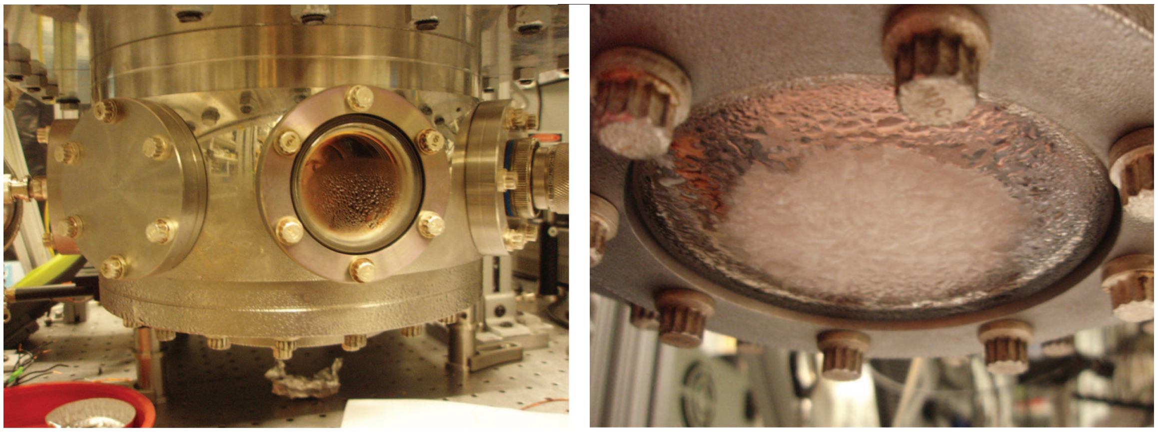

Figure 5-3: An instance of a thermal short in a closed-cycle cryostat (identical model, but not the one used in the current fiber-integration work). The cause of the the thermal short was the formation of an ice bridge between the 40 K and room-temperature portions of the experiment. The cryostat then attempts to cool the entire apparatus to cryogenic temperatures, leading to severe condensation and formation of ice on the room-temperature vacuum walls. The correct procedure, in such a short, is to immediately shut off the cryostat. The viewports are 2.75" (left panel) and 4" (right).

the cryostat, where there is a rotary motor that connects a diaphragm in the cryo body alternatingly to the high-pressure feed and then to the low-pressure exhaust. The expansion of compressed helium in the cryo body comprises the refrigeration cycle. The depressurized gas is then recirculated to the compressor, hence the description "closed-cycle".

In addition, we require an independent helium source which is used as the convective medium in the exchange compartment. This secondary helium is also extremely crucial for the cryostat operation, since it is entirely responsible for the heat exchange between the cryo and experiment compartments. If the pressure of exchange helium is not set properly, the overall cryostat performance is degraded. Namely, with too low a pressure, there is no helium in circulation and we will simply not be cooling the experiment; with too high a pressure, a valve will automatically open in the exchange compartment (which serves to prevent bursting of the bellow), and the gas will be flushed out of the compartment rather than partaking in heat circulation. These remarks are in qualitative agreement with experimental observations that the in-chamber pressure in the experiment compartment is sensitive to the exchange helium pressure being too low or too high.

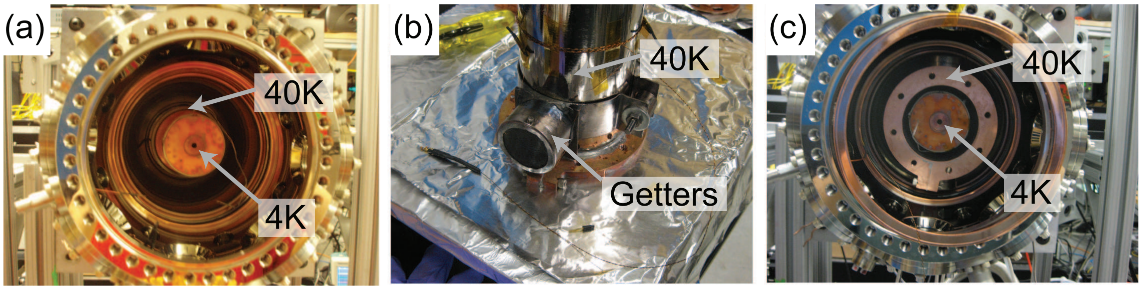

Figure 5-4: The mechanical foundations of the experiment chamber. (a) A view of the empty experimental compartment. The inner diameter of the outer vacuum shield is 8". (b) A 2'-long copper tube that extends the 40 K surface from the rear of the chamber to the 4 K coldfinger plane. Cups containing activated charcoal getters are also shown. (c) The experimental chamber after the tube has been installed.

Cryostat turn-on procedure

With this general background, we now give the standard start-up procedure for the closed-cycle cryostat. We assume that the experimental compartment has been vacuum-sealed and evacuated to moderate pressures (e.g. 10^{-6} to 10^{-5} torr) by the turbo/roughing pump station ("Turbopack", Adixen-Alcatel) and the 20 L/s ion pump.

1. Inject ultra-high purity helium into the exchange compartment. Flush the compartment several times with fresh helium by manually controlling the exhaust valve.
2. Turn on cold water flow (both source and return) that provides cooling to the helium compressor.
3. Power on the helium compressor. The compressor then provides high-pressure helium to the cryo head and actuates the expander.

In cryo shutoff, undo the above tasks in reverse order.

Experimental compartment cooldown and pressure

From this point, our discussion focuses entirely on the experimental compartment as the cryostat is, for us, simply a commercial equipment much like a vacuum pump. The 40 K and 4 K surfaces in the cryo compartment are brought, through convective cooling, into the experimental chamber as shown in Fig. 5-4, where panel (a) shows the empty interior of the experiment compartment from below, indicating the points that are cooled to 40 K and 4 K. Panel (b) shows a 2'-tall copper tube that extends the 40 K stage from rear of the

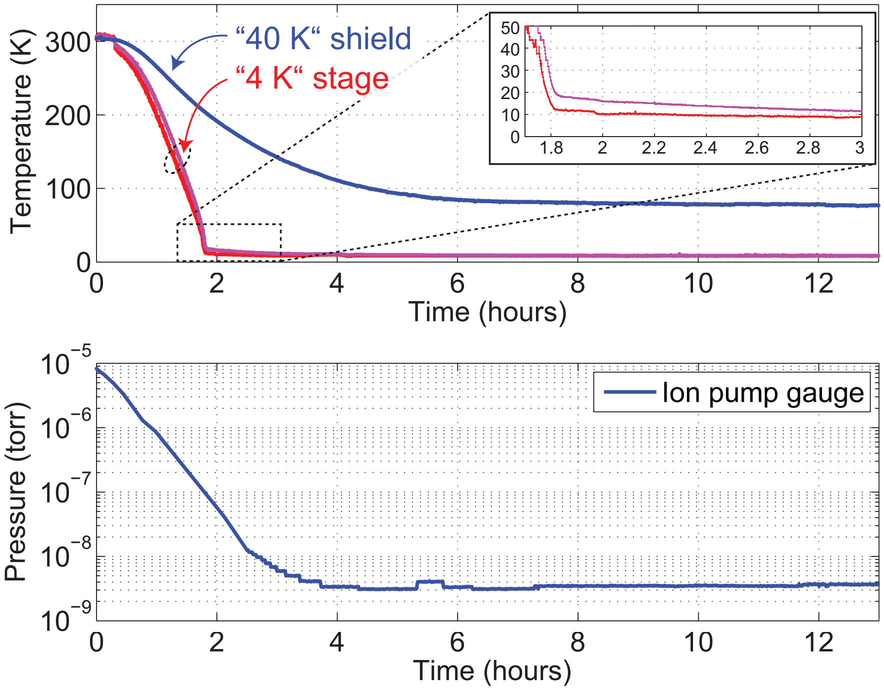

Figure 5-5: Thermal and vacuum performance of the cryostat. (Top) Cryo temperatures measured by Lakeshore DT-670 diode sensors. Two are mounted at different spots of the final ("4 K") stage and a third sensor is mounted on the "40 K" intermediate thermal shield. Owing to its large thermal mass, the shield has the longest equilibriation time, and settles to roughly 60 K after few days of pumping. (Bottom) In-chamber pressure measured by an ion pump gauge. The measurement is taken exterior to the cryogenic surfaces of the experiment. The local pressure near the coldfinger and the trap is expected to be a few orders of magnitude lower than what is indicated here. Note that the pressure correlates with the intermediate shield temperature, which is consistent with the fact that the shield offers the largest surface area for cryosorption.

chamber to roughly the same plane as the 4 K finger. A pair of copper cups (constructed by Paul Antohi) containing activated charcoal is mounted on the outside of the 40 K tube. The purpose of the charcoal getter is to improve final steady-state pressure by increasing the surface area available for cryosorption. Lastly, panel (c) shows the experiment chamber once the tube has been installed. Thus, the 40 K and 4 K temperature stages of the cryo are brought conveniently into the working area of the experiment space.

Fig. 5-5 shows the typical decrease in temperature at both "4 K" and "40 K" stages (in the experiment compartment) where $t = 0$ corresponds to turning on of the cryostat. It is immediately evident that the final temperatures are not necessarily as advertised, which owes to finite heat loads and is discussed in the following section. A typical pressure log, measured by an ion pump that is located exterior to the cryogenic stages, is also given. It is seen that the final ("4 K") stage temperature, where the ion trap sits, rapidly approaches its steady-state value of 8 K in the span of a few hours, while the intermediate ("40 K") shield has a significantly longer time constant – finally settling below 60 K after a few days of cooling. We also observe that the chamber pressure correlates best with the intermediate stage temperature. These observations are consistent with the notion that the intermediate shield has the largest thermal mass in the system (leading to its slow equilibriation time) and also has the largest surface area for cryosorption (hence the pressure correlation with shield temperature). The typical schedule that we followed after a new trap install was to allow the system to continue cooling and pumping for at least two days prior to beginning the trapping experiment, despite the relatively fast cooldown of the final ("4 K") stage. Based on this cryovacuum schedule, we never observed in this system any clear evidence of trapped ion collisions against in-chamber residual gases (e.g. generation of dark ions, charge exchange, etc.).

Lastly, we remark that the pressure log of Fig. 5-5 was taken by a room-temperature gauge. It is expected that the local pressure near the final stage coldfinger is lower by a few orders of magnitude. In Ref. [ASA$^+$09], an upper bound pressure at the ion trap is estimated based on typical trapped ion lifetimes to be 10^{-12} torr.

Details of two-stage cooling, i.e. the heat load map

Ultimately, we are interested in the steady-state temperatures of the "4 K" and "40 K" stages of the cryostat during operation. This information is given by the heat load map of Fig. 5-6. This is a slightly busy diagram, but its purpose is to give the steady-state temperatures of the first ("40 K") and second ("4 K") cryo stages as a function of heat load (Q_1 and Q_2 respectively). Temperatures are given in Kelvin, and the heat loads are measured in Watts. For example, if the first stage has a load of $Q_1 = 5$ W and the second stage a load of $Q_2 = 1$ W, one finds the intersection of the two corresponding isocurves to yield final steady-state temperatures of $T_1 \approx 44$ K and $T_2 \approx 6$ K. Our main interpretation of Fig. 5-6 is that the final stage temperature is quite sensitive to its load, but is rather tolerant of loads at the intermediate shield, as one might intuitively expect. The intended design of the two-stage cryostat is thus that the first stage is used as a sacrificial thermal shield for the second stage.

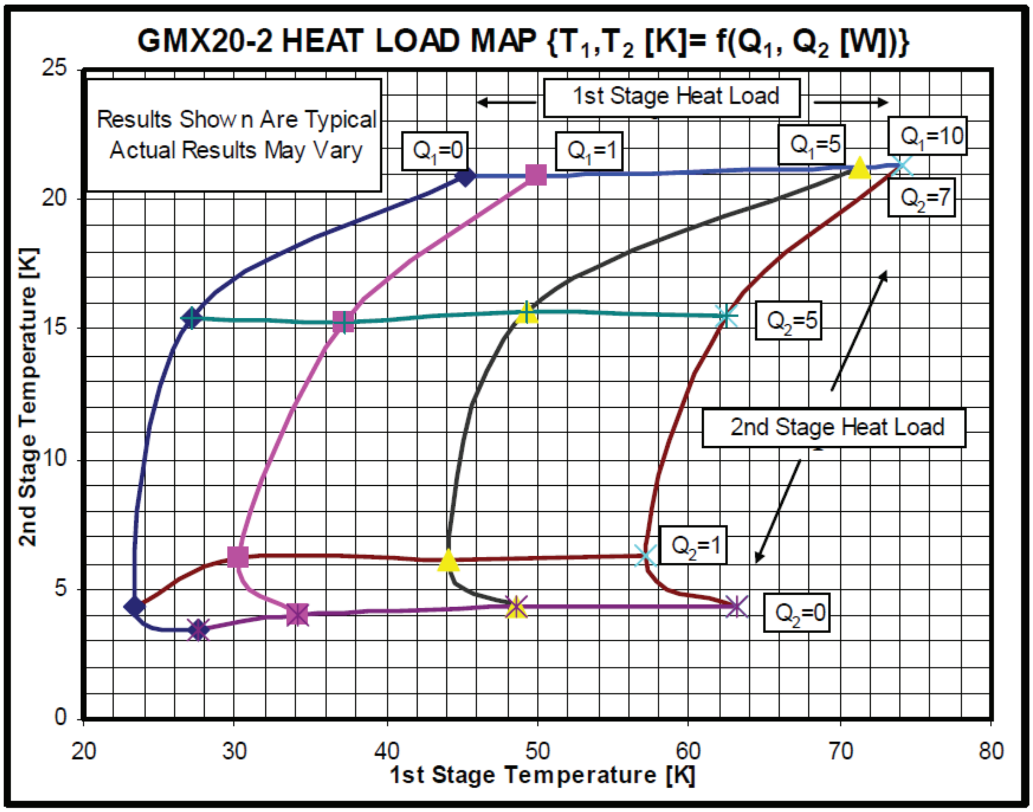

Figure 5-6: The heat load map for the ARS closed-cycle cryostat (DE-210SF) with the "ultra-low vibration interface" (GMX20-2). The cryostat provides two thermal stages, nominally at 40 K (stage 1) and 4 K (stage 2). The heat load map shows the actual steady-state temperature as a function of heat loads on the stages of the cryostat. (Diagram taken from the ARS literature.)

As an initial estimate of the load during operation, we may ask about the typical heat load in the general configuration of Fig. 5-1, before any electrical connections between the stages are made. Assuming no conduction losses and negligible convection (as expected in a UHV environment), the sole contributor to this "baseline" heat load comes from blackbody radiation exchange between nearby thermal bodies. The radiative energy flux j is given by the Stefan-Boltzmann equation

$$j = \epsilon\sigma T^4, \tag{5.1}$$

where $\sigma = 5.67 \times 10^{-8}$ W/m^{2}K^4 is the Stefan-Boltzmann constant, and ϵ is a material property known as emissivity, which is $\epsilon_{ss} = 0.28$ for type-316 stainless steel (which make up the outer vacuum walls) and $\epsilon_{cu} \approx 0.1$ for roughly-polished copper. Using these parameters, we find the radiant flux per unit area:

- Room-temperature (300 K) stainless-steel: $j_{300} = 129$ W/m^2,
- First-stage (40 K) copper: $j_{40} = 0.014$ W/m^2, and
- Second-stage (4 K) copper: $j_4 = 1.45 \times 10^{-6}$ W/m^2,

demonstrating the dramatic T^4 dependence. It is clear that the only nonnegligible contribution comes from the room-temperature vacuum walls. Estimating the outer vacuum chamber dimensions (Kimball Physics, Extended Octagon MCF800-EO200080) to be 7.1" diameter and 4.18" height, the total surface area comes to 0.088 m^2 (including the side cylinder surface and the bottom flange) which may be multiplied with the unit flux j_{300} to yield a total radiative power of 11.4 W from the room-temperature vacuum walls! While the result is only approximate in that the detailed geometry and exact material parameters have not been considered, our general conclusion is that the first thermal stage is likely to be taxed from just the radiative background. Nevertheless, since the most important experimental criterion is to cool the ion trap on the second stage, we use the first stage as a sacrificial shield against room temperature radiation, as well as other heating sources. For example, the in-vacuum 1"-diameter windows (Thorlabs, WG41050-A) on the 40 K shield of Fig. 5-1 absorb the 160 mW of predominantly-IR blackbody radiation that otherwise would strike the 4 K stage. In actual operation, we have routinely measured the temperature of the first shielding stage to be around 60 K, consistent with the current analysis and the heat load curve of Fig. 5-6.

Given this baseline load, we set a target operating point of $Q_1 \approx 10$ W and $Q_2 = 1$ W which corresponds to $T_1 \approx 60$ K and $T_2 \approx 6$ K, as we continue to consider other loading factors.

5.2.2 Experimental chamber

In this section, we give some details regarding the mechanical construction of the experiment chamber. As shown in Fig. 5-7, the components have been designed with significant modularity. Combined with the fast turnaround time of a cryogenic system, many components have been redesigned numerous times, which explains why the system appears slightly differently in the various figures of this text. The side flanges in the intermediate shield, for instance, are easily swappable to realize specific instrumentation required for a given experiment. In the fiber-integration work, for example, we required a feedthrough in the intermediate shield for the optical fiber as well as an RF-capable electrical connection to each of the six electrodes of the point Paul trap (since it was not known *a priori* along which spatial direction the ion had to be RF-translated for fiber-ion modematching). The experimental configuration for the fiber-integrated trap is shown in Chapter 6. The side flanges on the intermediate shield are held by a mechanical press fit and a light application cyanoacrylate adhesive (KrazyGlue) which can be easily removed by an acetone soak.

Despite this flexibility, any additions to the experimental chamber must be carefully engineered to satisfy the cryo load constraint. The key principle for achieving load compliance is to utilize a proper choice of materials that gives thermal uniformity at a given temperature stage, and good insulation between the stages. The material choice should also reflect its general robustness, since the cryogenic experiment will naturally be subject to repeated mechanical handling and severe temperature cycles.

In the course of developing the cryo apparatus, we have extensively explored the use of many different engineering materials, such as copper, stainless steel, bronze, MACOR (a machinable ceramic), Stycast 2850-FT epoxy (glass epoxy touted for its thermal conduction), etc. Based on such experience, our ultimate recommendation is to rely exclusively on copper and stainless steel for the general construction, as reflected in the numerous photographs of the experiment chamber. Copper is an obvious choice for thermal sinking due to its remarkable conduction properties (at temperatures below 50 K, the thermal conductivity of copper exceeds $\sigma = 1000$ W/m·K [NIST10]), and is thus used extensively in the chamber design within a given temperature stage. As a point of comparison, Stycast has significantly poorer thermal conduction of $\sigma = 0.064$ W/m·K at $T = 4$ K despite its advertising. (However, the epoxy is mechanically very robust and, as seen in Fig. 5-7(a), was frequently employed to entomb mechanically fragile points of the assembly.) On the other hand, stainless steel is a very competitive thermal insulator (its thermal conductivity being $\sigma = 5$ W/m·K at $T =$ 40-60 K and below $\sigma = 1$ W/m·K at $T < 10$ K) that is also structurally and thermally robust. For instance, stainless steel may be contrasted with MACOR, which has a relatively temperature-independent conductivity of $\sigma = 1.5$ W/m·K but is not mechanically robust against repeated handling. Plastics have excellent insulation properties, but have limited thermal tolerance especially when the system is baked to higher temperatures (80°C) prior to chamber pumpdown. In conclusion, copper and stainless steel are excellent choices for thermal and mechanical engineering in the current context.

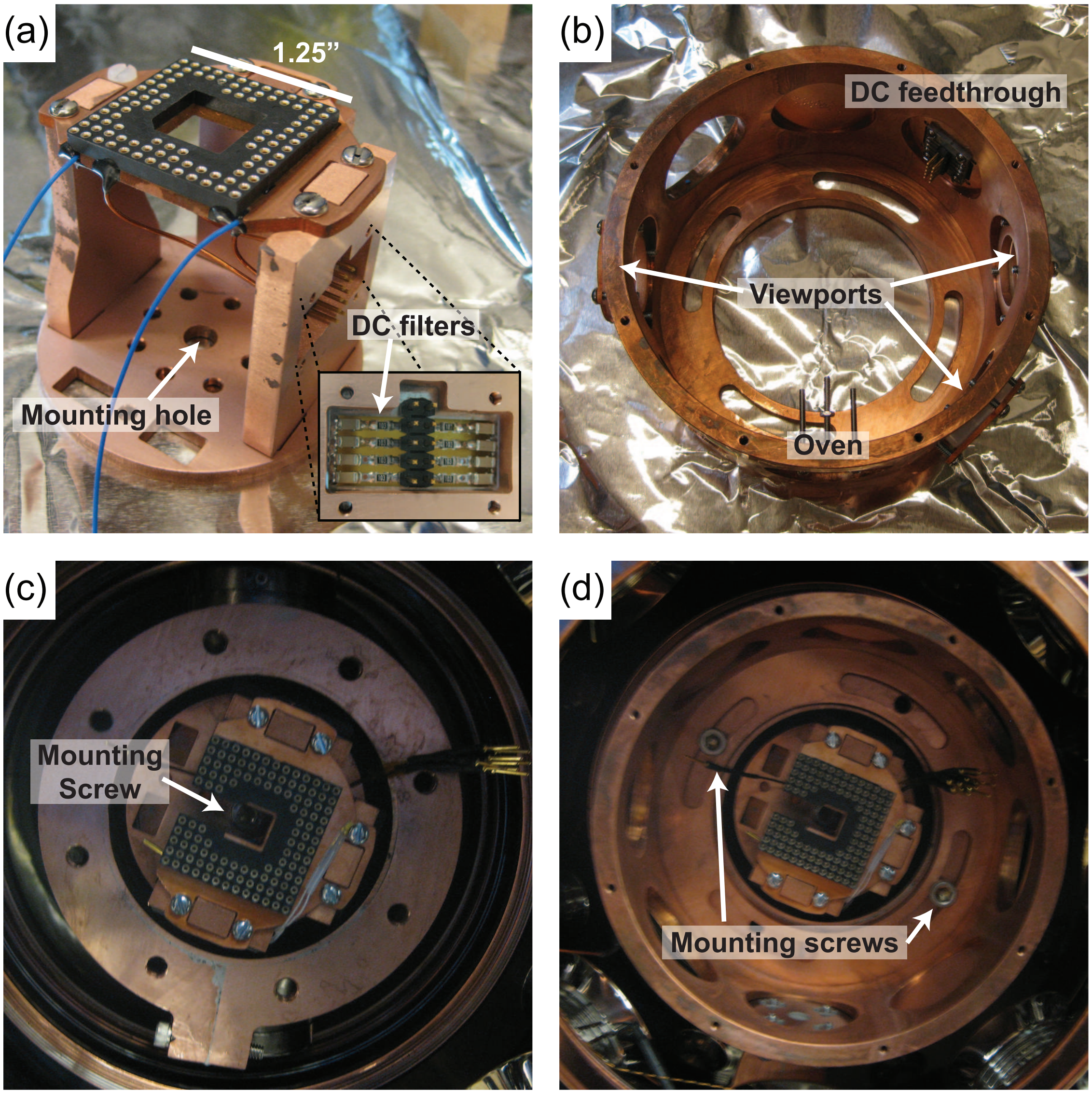

Figure 5-7: Mechanical components that make up the experiment chamber. (a) The ion trap holder and pedestal, which is mounted on the 4 K surface. Relatively large rear space (height of 2") behind the chip was required for the inclusion of an optical fiber. Stycast (black epoxy) encases fragile points such as wire contacts for mechanical robustness. The electrical interface for trap DC connections is also shown. (b) The intermediate 40 K shield, illustrating the easily-reconfigurable side flanges (1.48" diameter) for trap instrumentation. (c) The trap holder installed on the 4 K surface of the cryostat. (d) Both the trap holder and the 40 K shield installed.

5.2.3 Wiring

Once the structural members are in place, electrical connections to the trap and other instrumentation must be made through the various temperature stages. We make extensive use of copper wires for their low resistance, and phosphor bronze "cryogenic wires" (LakeShore Cryotronics) due to their high thermal insulation. Two heating mechanisms were considered:

1. Thermal conduction: When two points of an object are held at different temperatures, there will be steady-state heat flow from the hotter to the colder spot. The magnitude of the flow is geometry-, material-, and temperature gradient-dependent. For a wire of length L and cross-sectional area A, the heat flow Q is given by

$$Q = \frac{\sigma A}{L} \cdot \Delta T \tag{5.2}$$

   where ΔT is the temperature difference and σ is the thermal conductivity of the material, which is generally temperature-dependent [NIST10].

2. RF Joule heating: The basic operation of an ion trap requires at least one high-voltage RF source. As each trap electrode possesses a finite capacitance C, the delivery of high RF voltage V requires a finite current through the wire which will cause Joule-heating according to the formula

$$\langle W \rangle = \frac{1}{2} R C^2 V^2 \Omega^2 \tag{5.3}$$

   where the $\langle . \rangle$ denotes a time average, and $\Omega = 2\pi \times f_{\mathrm{RF}}$ is the RF frequency.

Wire	σ (W/m·K)	Conductive load (W)	R (ohm/inch)	RF load (mW)
PB (32 AWG)	50	0.017	0.10	28
PB (36 AWG)	50	0.007	0.25	71
Cu (22 AWG)	1100	3.7	0.001	0.28

Table 5.1: Thermal conductivities σ and electrical resistances R of commonly used wire types in the closed-cycle cryostat. PB stands for phosphor bronze; Cu is copper. Data is taken from LakeShore Cryotronics literature. When σ or R is temperature-dependent, the worst-case scenario over T = 4-300 K (i.e. the largest value) is cited. Conductive heating load is calculated for a 1"-long wire segment carrying a temperature differential of ΔT = 300-40 K. RF Joule heating is given for the same 1"-segment when driving a trap electrode of C = 30 pF capacitance with RF at V = 500 V and $\Omega = 2\pi \times 8$ MHz.

Table 5.1 indicates the amount of heat conduction by a 1”-segment of wire from room temperature (300 K) to the cryogenic environment (40 K), and also the RF heating of the same segment assuming a $C = 30$ pF trap capacitance and a $V = 500$ V, $\Omega = 2\pi \times 8$ MHz RF source. These values can be interpreted with respect to the heat load map as follows: (1) direct copper contact between temperature stages must absolutely be avoided; (2) but, just an inch of phosphor bronze wire serves as a sufficient thermal break between stages; (3) and, with RF heating in mind, 36 AWG phosphor bronze is not necessarily superior to 32 AWG in thermal performance. We followed these principles rigorously in the instrumentation of the cryostat, where every electrical connection is thermally broken by short (usually 1”) segments of 32 AWG phosphor bronze. We especially advise the use of 32 AWG wire over 36 AWG, as the latter is remarkably brittle.

In contrast to thermal requirements, electrical performance demands the use of short, low-resistance wire segments. For instance, one consideration is to minimize differential resistances between the various wire pairs that, when the trap is driven with multiple RF sources, may introduce static phase offsets between the drives (see Section 5.4.1). Low differential resistance motivates the use of short wire segments to deliver RF, which will also minimize the potential for crosstalk and stray capacitances to ground. On that note, resist the urge to introduce copper wire in addition to the phosphor bronze thermal break when the latter segment alone can make the connection! Less wire is better.

5.2.4 Ion source

The implementation of a successful thermal “oven” (i.e. a source of strontium atom flux) in a cryogenic environment represents the typical type of heat load-conscientious design that is required for working in the closed-cycle cryostat. The requirements are as follows:

1. A sample of strontium metal must be heated in an oven to over several 100°C in order to generate a flux of strontium atoms over the ion trap, which may then be photoionized by 461 nm and 405 nm lasers to produce $^{88}\mathrm{Sr}^+$.

2. The oven must be mechanically secured with respect to the trap. In particular, cryostat cooldown can cause thermal contractions as large as 1 mm, and the rapid temperature cycling may also cause severe deflections of the oven structure if it is not rigidly secured. Both effects have been observed.

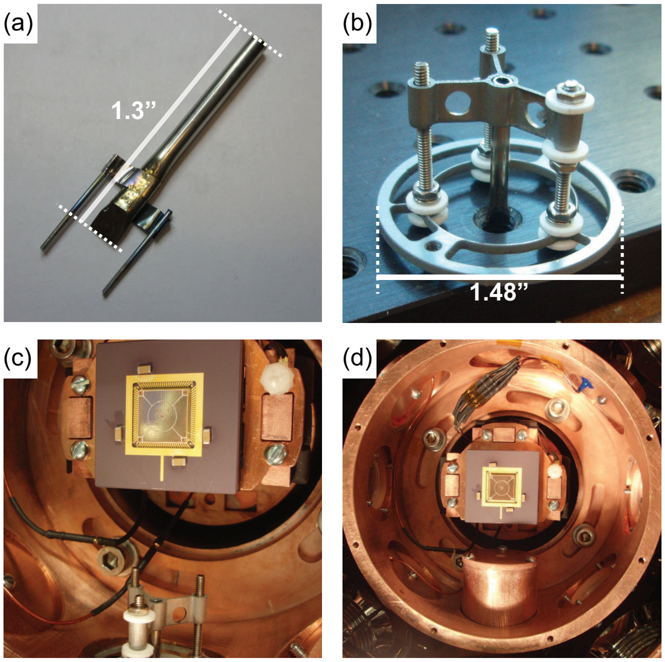

Figure 5-8: The thermal ion source. (a) The stainless steel oven for producing flux of strontium atoms. The strontium metal is contained at the rear of the tube where it is heated by Joule heating of the stainless steel flaps. The leads are connected to vacuum feedthroughs via barrel connectors. (b) A mechanism for rigidly holding the oven at the intermediate 40 K shield. (c) The oven holder shown with respect to a mounted trap in the cryo experiment. (d) The oven assembly with a copper cup that shields the cryogenic surfaces from thermal radiation.

We heat a tubular, stainless steel oven containing strontium metal by flowing a large DC current (typically 2-4 A) through a strip of stainless steel foil that is spot-welded to the rear of the tube. Fig. 5-8(a) shows a typical oven sample. The tube length is approximately 1.3” with an outer diameter of 0.11” with 0.01”-thick walls. The stainless steel foils are 0.003” thick, and the stainless wire is 0.03” in diameter. A roughly (2 mm)^3 piece of strontium metal is inserted into the rear of the tube and crimped in order to establish efficient thermal contact between the oven and strontium piece. Following the insertion of strontium, the oven must be quickly placed under vacuum (30 minutes is safe) since strontium will otherwise oxidize in air, making it unsuitable for ^{88}Sr$^+$ photoionization. It is advised that future oven implementations in the cryostat adhere to the parameters presented here, as the oven operation is sensitively controlled by its physical dimensions. Despite the high operating temperatures of several 100°C, the tube is directly held by a fixture on the intermediate 40 K shield in order to maintain rigid mechanical alignment with respect to the cryogenic trap.

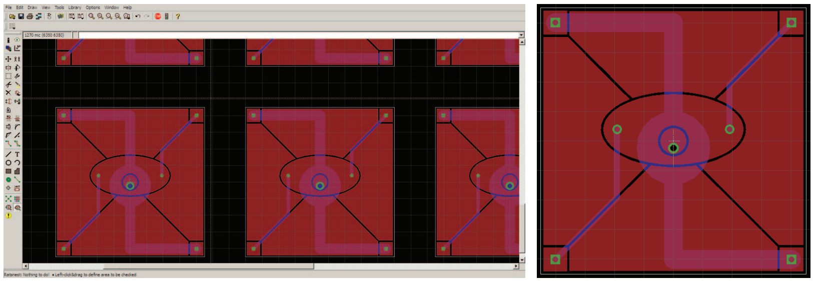

Figure 5-9: Design of PCB-based asymmetric point Paul traps in EAGLE (CadSoft). The trap is implemented as a two layer 1.1 cm × 1.1 cm board, where the red pads indicate the copper electrodes on the top plane, blue traces are in the rear plane, and vias are indicated by green dots. The corner pins allow electrical contact to the enclosed electrodes of the point Paul trap through vias. The large 400 μm-diameter via that is offset in the center electrode is used for the insertion of an optical fiber and ferrule.

The remainder of Fig. 5-8 shows the cryogenic oven holder – constructed of stainless steel – that provides excellent thermal insulation despite the presence of extreme temperature gradients. The steel assembly is encased (direct contact only at the base) by a copper cup that limits the exposure of the 4 K cryo stage to radiant energy from the glowing oven and the room temperature background.

5.3 Surface-electrode trap

Given its planar electrode structure, surface-electrode ion traps can be constructed using conventional techniques of electronic fabrication. As described in this section, the fiber-trap project can be implemented by printed circuit board technology (Section 5.3.1), as well as by semiconductor microfabrication techniques (Section 5.3.2).

5.3.1 Printed circuit board (PCB) implementation

An important aspect of the current work was the rapid iterations of the point Paul trap design, which incrementally identified the components for successful fiber-integration, e.g. the absolute necessity of trap axis engineering with respect to the lab frame as discussed in Chapter 3. We achieve short design turnaround time (typically 1 week) by implementing our surface-electrode ion traps as a printed circuit board (PCB) [PLB+06, BCL+07]. The production of point Paul trap PCBs has been automated, so that a set of design parameters such as ring electrode position, minor- and major radii, etc. computationally generate EAGLE-compatible (CadSoft) scripts that may then be sent to the PCB manufacturer, as shown in Fig. 5-9. An additional advantage is that PCB manufacturing routinely implements through-layer electrical vias, so that connections to enclosed electrodes of the point Paul trap (i.e. the annular rings) may be easily made without directly altering the trapping half-space $z \geq 0$.

Our PCBs are manufactured by Hughes Circuits Inc., with bare copper electrodes on a Rogers 4350B substrate which is a commonly used high-frequency laminate in RF designs. We have typically found large variations in copper surface quality and oxidation level of the samples on arrival. Thus, immediately prior to install, the trap is mechanically polished using a Dremel and subsequently washed in a particularly efficient solvent (Branson OR) that removes the abraded remains.

The most crucial disadvantage of the PCB implementation is, however, the lack of precision in electrode definition. Nominally, the typical limitation (such as the "Advanced" fabrication option at Hughes Circuits) is 75 μm spacing between electrodes and 100 μm via sizes, and ± 50 μm tolerances on electrode definition. In practice, however, the situation is considerably worse, as the manufacturer cited tolerances are further degraded as additional features in the design are requested (such as mechanical vias). Fig. 5-10 shows typical discrepancies between design specification and measurements of received PCB samples. It is seen that electrode dimensions are consistently off-target, sometimes by even 50% (e.g. the electrode gaps), and that the drilling of the central via has morphed the shape of the central electrode. The measured dimensions of the trap vary from sample to sample even within the same batch. Recall that, in the context of fiber integration, one must be able to predict the location of the quadrupole field node to a few micrometers; it then follows that one cannot rely on the precision of PCB technology in order to guarantee the fiber-ion overlap. Furthermore, deviations between design and implementation make it difficult to rely on trap simulations to predict actual performance, such as the exact translation curve under multiple RF operation (e.g. Fig. 4-8). While it is possible to model the particular trap instance following measurement (rather than the intended design), this process is quite cumbersome since the measured layout invariably lies outside of the initial design space due to its irregular features, such as the bulge of the center electrode in Fig. 5-10.

These limitations in electrode definition highlight the crucial importance of *in situ* RF translation for successful fiber-integration. Given our PCB implementation, it is impossible to attain "perfect construction" of the fiber-trap system. Instead, we rely on the RF

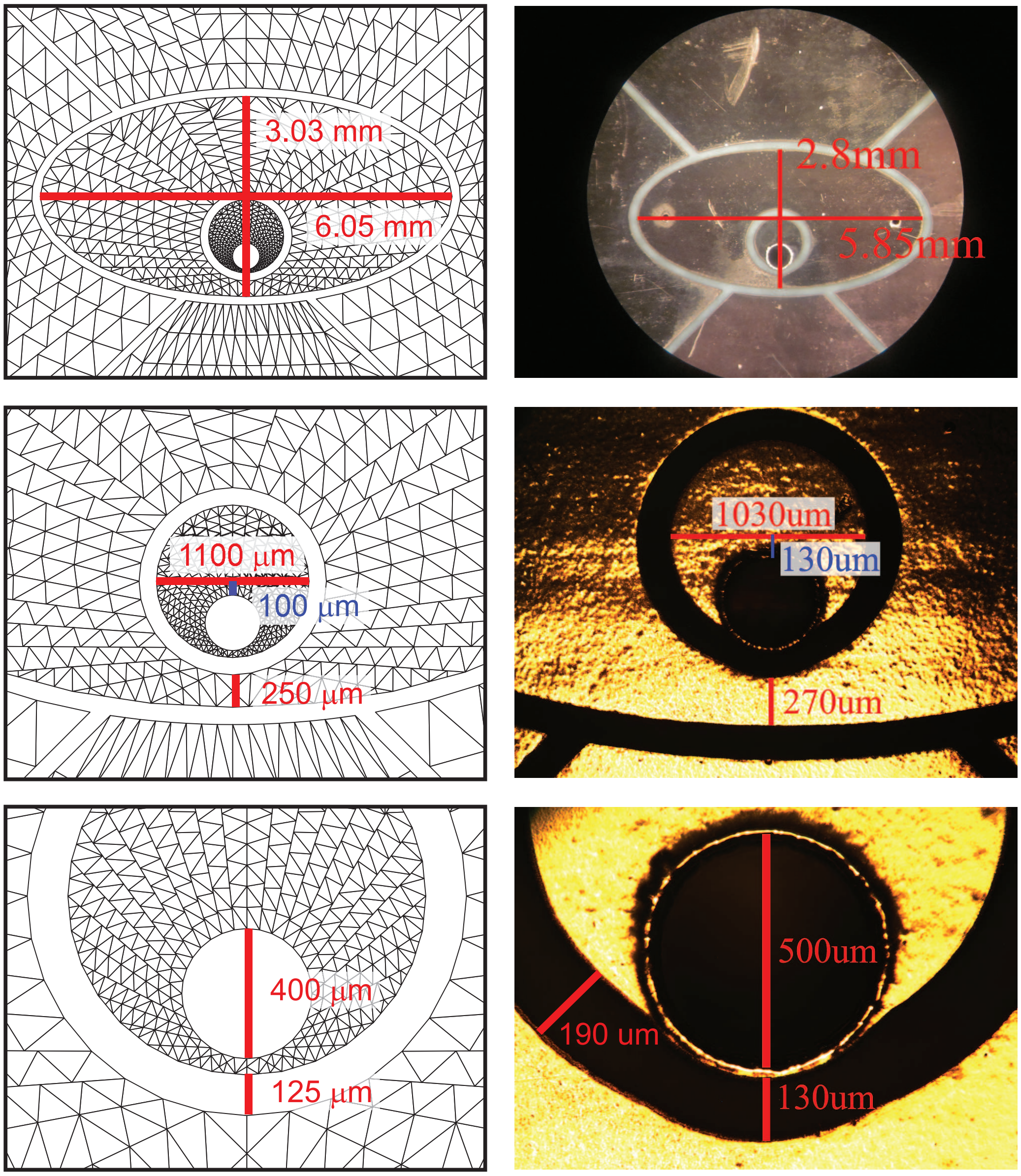

Figure 5-10: Deviations between the numerically simulated trap design and measured PCBs (fabricated by Hughes Circuits). The design corresponds to the asymmetric point Paul trap shown in Fig. 5-9. The large via (400 μm-diameter by design) in the central electrode is for the insertion of an optical fiber and ferrule. Note that the electrode gaps are 50% larger than the specification, and that the drilling of the central via has morphed the shape of the center electrode.

translation technique to correct for any errors arising from fabrication. While one can advance the technical toolbox – for example, by utilizing microfabrication techniques for the construction of the trap – the corresponding scientific push [GKH$^+$01] towards even further microscopic elements underscore the general usefulness of RF-based positioning.

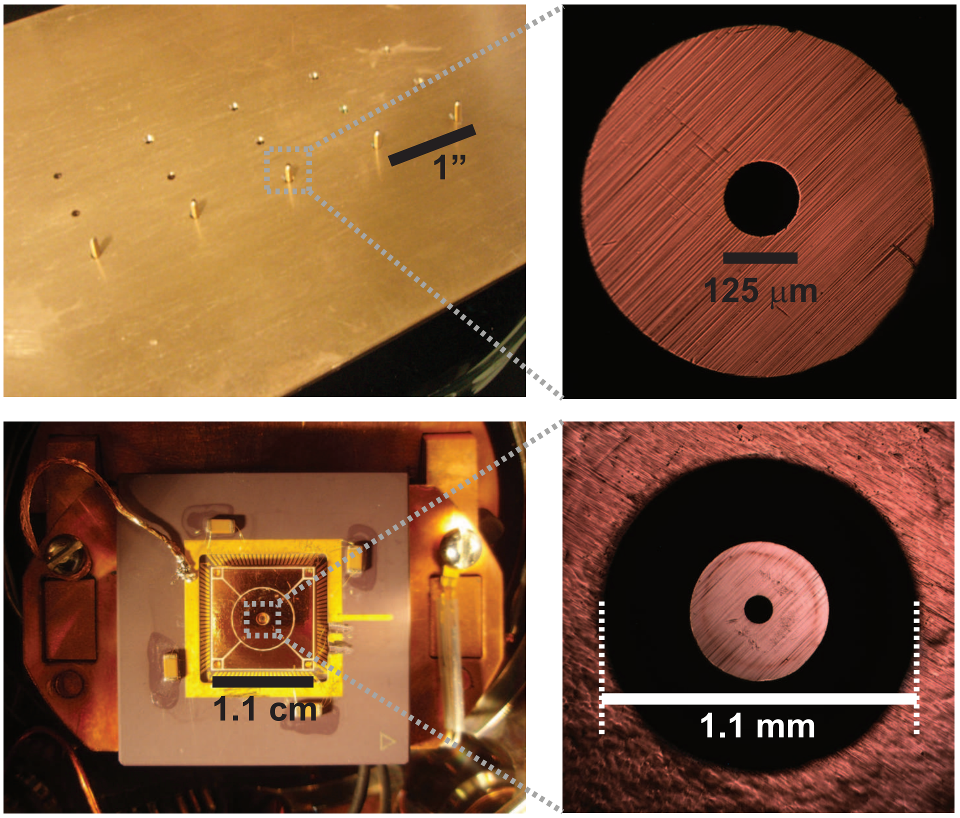

Figure 5-11: Metallization of ceramic optical ferrules. (Top row) Metallization of ceramic optical ferrules in an e-beam evaporator. A 450 nm layer of copper is deposited on the ferrule, with 10 nm of titanium as an adhesion layer. The striations on the ferrule face owe to the original surface quality of the ferrules. (Bottom row) Fiber-integrated point Paul trap, where a fiber-embedded center electrode is implemented by a metallized optical ferrule. Electrical connection to the metallized ferrule is made by a conductive epoxy (H20E) that shorts the ferrule to a ground trace in the rear plane of the PCB. A "cone"-shaped ferrule was chosen in order to decrease the possibility of shorting between the evaporated ferrule and the PCB.

5.3.2 Microfabrication

In the current work, we utilize microfabrication techniques for two purposes. Firstly, as one approach for embedding an optical fiber in the trap substrate, we metallize the tip of a commercial optical ferrule that is then used as the center electrode in the point Paul trap. Secondly, we are working towards general, in-house microfabrication of the point Paul trap. The latter effort is led by Yufei Ge.

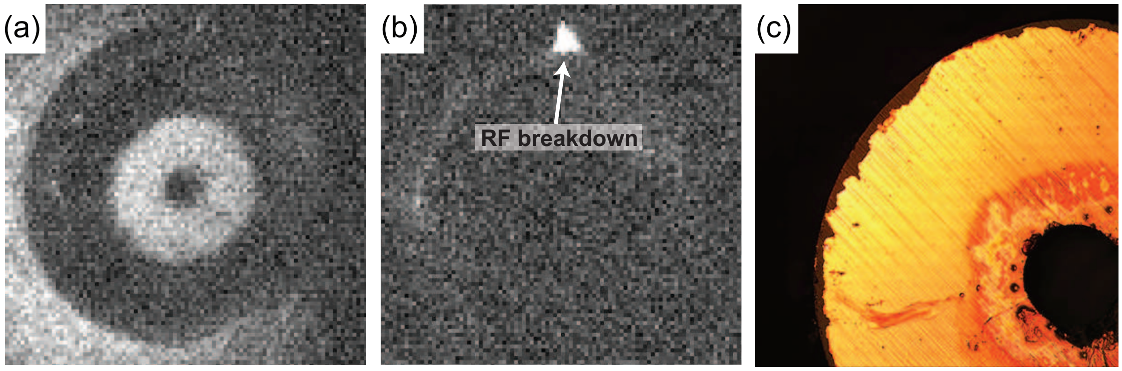

Figure 5-12: RF breakdown of the evaporated ferrule. (a) A CCD image of the ferrule-trap under illumination. Dimensions are given in Fig. 5-11. (b) General glow in the ferrule-PCB gap and a bright arc spot indicating RF breakdown at 1 kVpp RF voltage. (c) Post-breakdown examination of the ferrule. It is observed that the sharp corners of the ferrule are particularly susceptible to electrical breakdown.

Metallization of ferrule for Fiber-trap

The first row of Fig. 5-11 shows the evaporation of copper onto a standard, ceramic (zirconia) LC-type ferrules (Precision Fiber Products, SM-FER1010C-1260). The striations on the ferrule face owe to the original surface quality of the ferrules. The metallization of ferrules is performed at MIT Exploratory Materials Laboratory by electron-beam evaporation, where 10 nm of titanium layer is initially deposited as an adhesion layer, followed by 450 nm of copper. The evaporation is performed without an optical fiber in the ferrule.

Following metallization, the ferrule is inserted into an appropriately-sized via in the point Paul trap PCB, as shown in the second row of Fig. 5-11. We originally intended to apply a press-fit of the ferrule into the via, but found that the evaporated copper easily delaminates from the mechanical friction. Instead, the via was enlarged so that the ferrule could be inserted without force, at the increased risk of misalignment. Electrical connection to the metallized ferrule, as well as mechanical rigidity, was established by curing a conductive epoxy (Epo-Tek, H20E) to a ground trace in the rear of the PCB. The insertion of a pre-cleaved optical fiber is the last step in the assembly. While we succeeded in trapping $^{88}\mathrm{Sr}^{+}$ in such a fiber-trap system, we did not demonstrate fiber-ion interaction due to radial misalignment of a a few 100 microns. (At this point in time, we had not yet implemented RF translation.)

The combination of microfab and "macroscopic" PCB techniques was replete with tech-

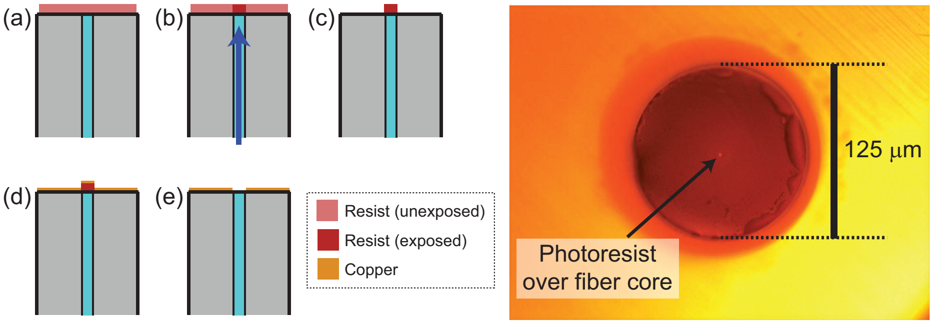

Figure 5-13: Fabrication recipe for metallizing an optical fiber. [Left] Intended recipe for patterning of metal on the fiber face: (a) A negative resist (e.g. NR9-3000P) is transferred onto the fiber surface; (b) The resist is exposed by light through the fiber; (c) The undeveloped photoresist is removed; (d) Metal layer is deposited; (e) Liftoff. [Right] Photograph of a fiber sample where resist has been applied over the fiber core, corresponding to step (c) of the process. Liquid residue on the surface is a mixture of RD6 (resist developer) and deionized water.

nical challenges. As already mentioned, the delamination of copper from the ferrule during insertion resulted in several failed instances. The metallized ferrule was also highly prone to electrical breakdown, as shown in Fig. 5-12. Panel (a) is a CCD image of the metallized ferrule under flashlight illumination. Panel (b) shows a slight glow in the gap between ferrule and PCB, as well as a bright arc discharge spot under a 1 kVpp RF drive. A post-examination of a ferrule-trap that suffered breakdown is shown in panel (c), where it is revealed that the sharp corners of the ferrule were particularly susceptible. Furthermore, the use of metallized ferrules precluded the possibility of fiber preparation by optical polishing, which is desirable for its mechanical robustness and fiber face planarity (cf. inserting and gluing a cleaved fiber). For these reasons, we abandoned ferrule metalization and opted instead for the use of stainless steel optical ferrules, which is discussed in Chapter 6.

Metallization of fiber

In addition, we also pursued metal evaporation on the fiber surface. This work was done in collaboration with Yufei Ge. The fabrication process is slightly more complicated, as one must pattern the evaporated metal so that it does not block the propagation of fiber light. Our strategy was to perform liftoff lithography. We begin by transferring negative photoresist (NR9-3000P) to the fiber surface by stamping the fiber against a resist-spun wafer. Subsequently, we deliver UV exposure light through the fiber itself, which leaves an

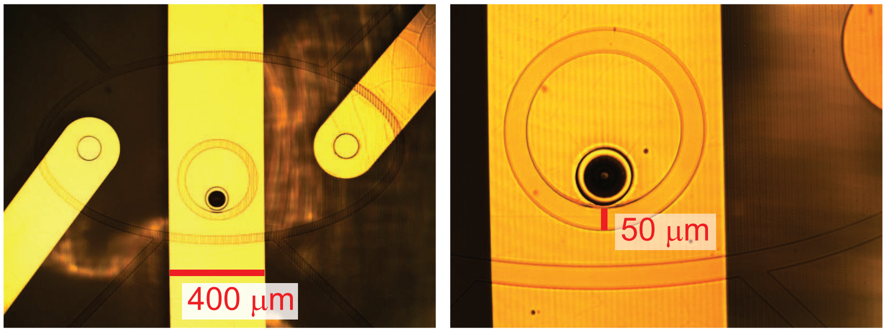

Figure 5-14: Photographs of the microfab point Paul trap, currently under development. SU-8, a commonly-used transparent photoresist for microelectromechanical devices [LBW+05], is used as the insulating medium between top and bottom layers. Striations owe to the raster-like exposure of the Heidelberg uPG 101 maskless-lithography system.

island of resist over the fiber core that may be used for liftoff of deposited metal. Fig. 5-13 shows the intended process. The figure also shows a sample – in which the fiber was epoxied (Thorlabs, F112) in the ferrule and polished prior to fab – with an exposed photoresist over the fiber core. The image corresponds to step (c) of the intended process.

In the end we did not extensively pursue fiber patterning due to our low success rate of resist transfer and exposure, and also because the primary motivation for fiber fab was to yield a point Paul trap with microscopic dimensions (ion height of $z_0 \approx 200$ μm), which was ultimately achieved regardless of electrode size by multiple RF height variation. However, the basic notion of fiber metallization may still be useful for the intent of minimizing dielectric surfaces in an integrated Paul trap that could otherwise contribute to stray charge accumulation.

The microfab point Paul trap

The imprecision of PCB fabrication, as well as a general desire to miniaturize the point Paul trap in order to manipulate the ion in the Lamb-Dicke regime [Roo00], initiated efforts to implement the design entirely using microfabrication processes. The fabrication project is credited entirely to Yufei Ge, whereas I have provided the target trap design, namely the asymmetric point Paul trap. The combination of wide material selection in microfab, along with the demonstrated ability to perform height variation, makes the microfab point Paul trap a compelling platform for studying the material-dependence of anomalous heating, among others. A photograph of this work-in-progress is shown in Fig. 5-14.

5.4 Electronics

The operation of the point Paul trap requires a minimum of one high-voltage RF source and four DC compensation sources. We begin with a discussion of the RF instrumentation, emphasizing a lumped circuit model for the network that will allow us to effect multiple RF drives through passive coupling (Section 5.4.1). We then describe the DC system, including our ongoing efforts to deploy DAC circuitry at cryogenic temperatures (Section 5.4.2).

5.4.1 RF

The basic signal chain to produce high-voltage RF is shown in the left side of Fig. 5-15(a). A function generator (Agilent 33250A) provides a sinusoidal signal of a few 100 mVpp, which is provided to a 4 W amplifier (Mini-Circuits TIA-1000-1R8) that has a maximum output voltage of about 50 Vpp (high-Z measurement) before noticeable distortions, i.e. clipping, affect the waveform. A distributed LC tank – known as a helical resonator [Fis76] – further amplifies the signal at the resonator frequency with a typical gain of 10-30×, and filters nonresonant components such as the harmonic distortions from the active amplifier.

The lumped approximation

Fig. 5-15(a) shows all electrical connections that are made to the trap where, for clarity, only one of the DC electrodes is shown in full detail. Panel (b) shows a lumped element approximation for the network that captures much of the system's qualitative behavior in the vicinity of the resonator's fundamental frequency. For example, with added load capacitance as seen by the resonator, the overall resonance frequency and peak gain are lowered; and, by increasing the strength of the coupling capacitor C_{in} one can obtain higher gain at the cost of lower operating frequency. We leave the verification of such details as a task for the reader. On the other hand, we emphasize the presence of stray capacitances, such as C_1, C_2 and C_{12} that arise intrinsically from wiring capacitances to ground and electrode-electrode coupling. Stray capacitances can be especially large (few 10 pF) in the cryostat system, due to the requirement of thermal sinking that necessitates the arrangement of signal wires near large bodies of grounded copper. The lumped element model with stray capacitances is useful for predicting the dynamics of more complicated RF configurations, such as the use of multiple (coupled) resonators for effecting a pair of out-of-phase RFs.

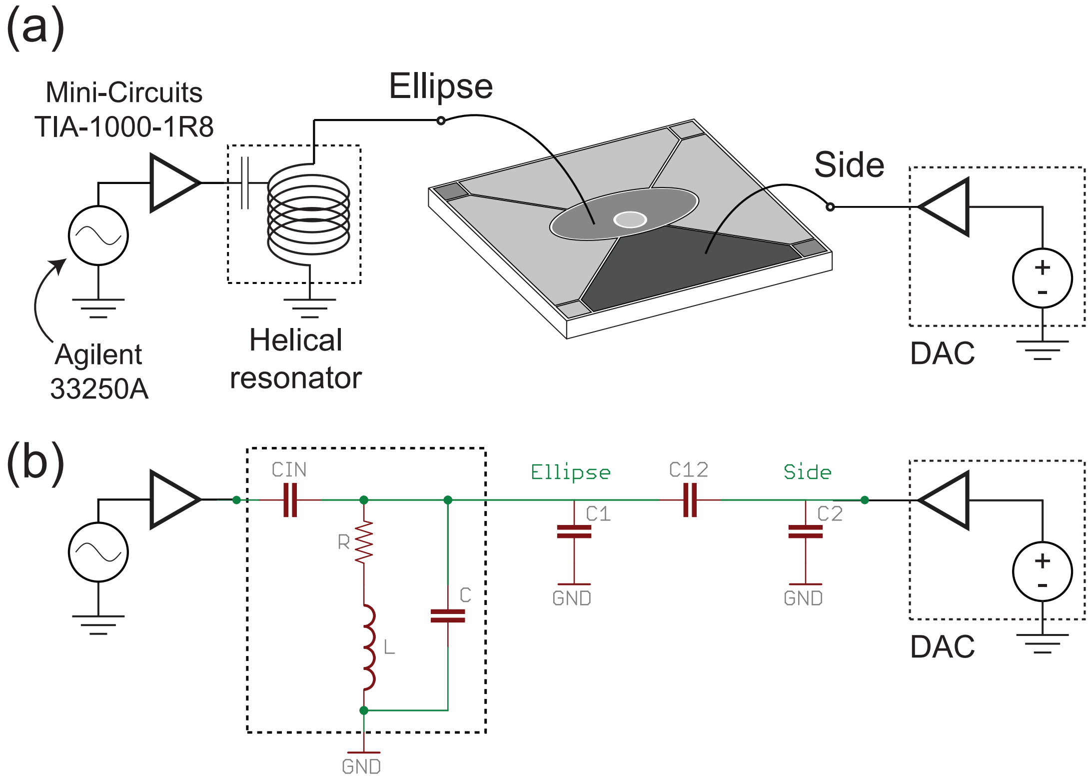

Figure 5-15: Physical and lumped models for electronic instrumentation of the point Paul trap. (a) A schematic showing all physical electrical connections made to the ion trap. For clarity, only one of the DC electrodes is shown in detail; in reality, all four side electrodes are instrumented identically. The RF signal is generated by an Agilent function generator, which is actively amplified by an RF amplifier. The helical resonator (indicated in dashed lines) provides further gain of approximately 20× and filters out nonresonant components, such as the high frequency distortions due to the active amplifier. On the other hand, the DC electrodes are driven by a home-made DAC system described in Section 5.4.2. (b) A lumped-model representation of the physical circuit. The helical resonator may be approximated by an RLC tank (typical parameters, obtained by fitting a measured transfer function, are $R \approx 1$ ohm, $L \approx 10^{-6}$ H, $C \approx 10$ pF) in the vicinity of its fundamental resonance. The coupling capacitor C_{in} is implemented by a variable capacitor ($C_{\text{in}} =$ 1-10 pF, Voltronics Corp.). Note the inclusion of stray capacitances: $C_1 \approx C_2 \approx 30$ pF are trap electrode capacitances to ground (which are relatively large in the cryogenic system due, for instance, to the thermal sinking of electrical lines at the intermediate shield) and $C_{12} \approx 3$ pF is the intrinsic coupling between the electrodes. The latter can be approximated by measuring the RF pickup on the side electrode when it is left floating.

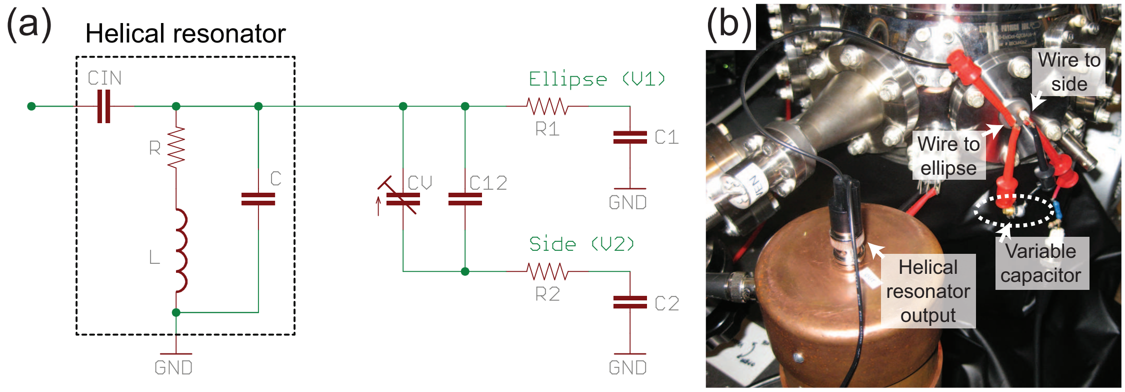

Figure 5-16: Implementation of in-phase multiple RFs. (a) Capacitive network for implementing two in-phase RF drives V_1 and V_2 on the ellipse and side electrodes of the asymmetric point Paul trap. The main output of the helical resonator is connected to the ellipse electrode. A variable capacitor C_v, typically ranging from 1-30 pF, is connected between the ellipse and side electrodes (where the DC connection has been removed). Resistors R_1 and R_2 represent residual resistances of the wiring, which are negligible in comparison to the capacitive impedances at our RF frequencies. Thus, a capacitive divider is formed for V_2 with divider ratio $\epsilon = V_2/V_1 \approx C_v/C_2$. (b) Photograph of the experimental configuration showing the variable capacitor attached at the vacuum electrical feedthroughs.

Multiple RFs by a capacitive network

A particularly simple mechanism to implement multiple RF drives in a single trap is to purposely increase the capacitive coupling between the target electrodes and thereby "leak" a controllable RF amplitude onto the secondary electrode. The design is shown schematically in Fig. 5-16(a), where the DC connection to the side electrode has been removed, and a variable capacitor C_v has been installed instead between the ellipse and side electrodes. The resistances R_1 and R_2 represent residual resistances of the wiring that leads to the trap, which may be ignored in the initial discussion. (They are especially negligible given the large capacitive impedances at the RF frequency of $\Omega = 2\pi \times 6$ MHz.) The physical realization of this network is shown in Fig. 5-16(b), where a variable capacitor (1-30 pF, Voltronics Corp.) is connected between the two electrical feedthroughs corresponding to the ellipse and side electrodes. In this configuration, a capacitive voltage divider is formed for the side electrode, yielding a ratio of RF amplitudes given by

$$\epsilon = \frac{V_2}{V_1} = \frac{C_{12} + C_v}{C_{12} + C_2 + C_v} \approx \frac{C_v}{C_2}, \tag{5.4}$$

where the last approximation is valid under our usual operating parameters, i.e. the situation where the secondary RF pickup is used only to trim the quadrupole field (as in the case of fiber-ion modematching), rather than large-magnitude rearrangement of the relative amplitudes. On the latter point, note that the capacitive network can be "flipped", so that the main output of the resonator directly drives the side electrode, and the ring electrode is capacitively coupled to the former. In that case, we operate in the regime $\epsilon = V_2/V_1 > 1$. Note, however, that capacitive coupling is restricted in all scenarios to in-phase RF drives, i.e. $\epsilon > 0$. In exchange, the advantage of the capacitive coupling mechanism is that only a single RF generator and a single helical resonator are needed for the implementation.

Despite its simplicity, the capacitive network may nevertheless suffer RF errors (σ, θ), of the type discussed in Chapter 4, that contribute to increased amplitude of the ion trajectory. We assess how the physical parameters of Fig. 5-16 yield the fractional error (σ) in the RF ratio, and phase offsets (θ) between V_1 and V_2. From Eq. 5.4, it follows that

$$\sigma = \frac{\Delta\epsilon}{\epsilon} = \frac{\Delta C_v}{C_v}, \tag{5.5}$$

where we have assumed that the intrinsic capacitances are not time-varying. In this case the fractional error in the RF ratio is, as expected, identical to that of the variable capacitor. Given a commonly-available temperature coefficient of 50 ppm/C° in air-gap trimmer capacitors (Voltronics Corp.) and a conservative temperature control of 1°C, we find an error of $\sigma = 0.005\%$, which implies a sub-100 nm ion jitter according to the Monte-Carlo simulation presented in Section 4.3. We also consider the possibility of phase offsets between V_1 and V_2. In the network of Fig. 5-16(a), a possible phase offset may arise if the wires leading from the vacuum feedthrough to the trap have differential RC products. Assuming $C_1, C_2 = 30$ pF and an operating frequency of $\Omega = 2\pi \times 6$ MHz, we find that a phase error arises at a rate of 0.06° per differential ohm $\Delta R = |R_2 - R_1|$. However, the differential resistance is bounded at much less than 1 ohm, as the overall wire lengths leading up to the trap have been purposely kept short. Given that all RF wiring is performed by sub-6"-segments, Table 5.1 bounds the total resistance per connection to be less than 0.6 ohm (assuming 32 AWG phosphor bronze). Thus, the phase error contribution to ion amplitude is also quite negligible. In conclusion, we predict no appreciable (σ, θ)-induced errors on ion trajectory under the current scheme, and indeed found no additional difficulties in trapping,

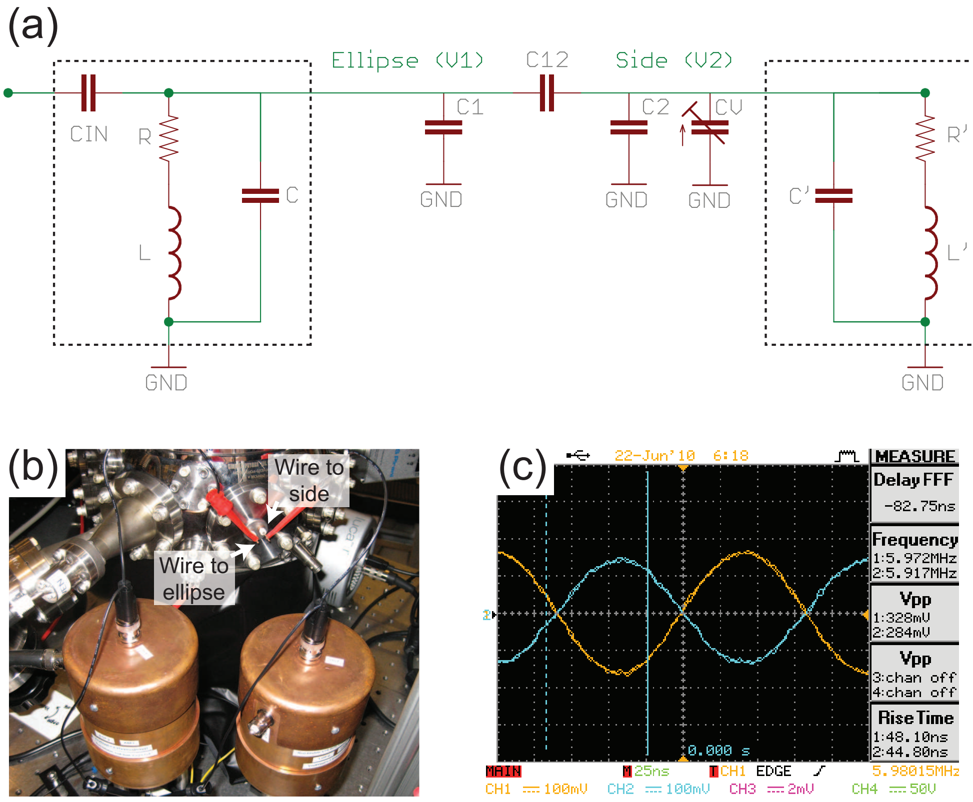

Figure 5-17: Implementation of out-of-phase multiple RFs. (a) Implementation of two out-of-phase RF drives by the use of two helical resonators that are coupled through the stray capacitance C_{12}. The coupling causes the two resonators to split into symmetric and antisymmetric modes, and the network is driven at the antisymmetric resonance. A variable capacitor C_v is used to mismatch the two resonators, thereby effecting different antisymmetric ratios $\epsilon < 0$. (b) Physical implementation of the coupled resonators in experiment. (c) An oscilloscope trace showing the antisymmetric phase relationship between V_1 and V_2 (amplitude in arb. units).

in comparison to the single RF configuration. Due to this robustness, all of our work on RF-based ion translation (e.g. height variation and fiber-ion modematching) was performed in the in-phase regime using the capacitive method.

Multiple RFs by a coupled resonator pair

At the same time, we also explored implementations for the out-of-phase regime, $\epsilon < 0$. One idea, as shown in Fig. 5-17, is to attach two helical resonators (that are identically constructed and thus similar in value) to the ellipse and side electrodes, and to allow the two nodes V_1 and V_2 to interact through the intrinsic coupling capacitance C_{12}. The coupling of two LC resonators by C_{12} yields a diagonalization of the overall system into symmetric and antisymmetric coupled modes. Once again, we control the relative amplitude ϵ by the use of a variable capacitor C_v which, in this case, causes a mismatch of the two resonant circuits that adjusts the relative weightings of the antisymmetric mode.

In experiment, we implement the coupled resonator structure as shown in Fig. 5-17(b), and effect out-of-phase oscillations as shown in the oscilloscope trace in panel (c). While we have successfully trapped ions as far as $\epsilon = -0.2$ using this mechanism (yielding an ion position in agreement with theory), the computation of the exact transfer functions V_i/V_{in} for $i = 1, 2$ reveals that in the case of finite resistances ($R, R' \neq 0$) the antisymmetric mode can deviate by a few degrees from the ideal 180° phase relationship. In practice, we encountered noticeable difficulties in trapping and compensating the trapped ions under this scheme. It is not known definitively whether nonideal phase slip or simple stray field miscompensation caused our trapping difficulties. In any case, the remarkable success of in-phase capacitive coupling motivated us to forego the out-of-phase regime and to focus entirely on in-phase RF ion translation.

5.4.2 DC compensation

The DC pads of the point Paul trap are driven by a home-made DAC system, which is based on an original design by Jarek Labaziewicz. Notable features of the hardware design include: (1) USB interface to the experiment PC by an Attiny861 microcontroller (Atmel) that implements V-USB (a software USB port, Objective Development); (2) 4-channels of 16-bit DAC outputs (LTC1592); and (3) an isolating digital-analog boundary (ADuM1400) following the microcontroller. The first assembly of this system for the closed-cycle cryostat was provided by Shankari Rajagopal who also wrote the firmware under my supervision. One useful feature in the system user-interface is the ability to drive compensation electrodes in an arbitrary combinational basis. The basis in which the resultant DC fields coincide with the trap axes is particularly convenient for micromotion minimization.

The DAC outputs are passed through two in-vacuum RC filters before they reach the trap electrodes. The RC filters are implemented on a PCB and mounted on the 40 K ($f_{\text{3dB}} = 20$ kHz) and 4 K stages (20 Hz) of the experiment, where they do triple duty in: (1) noise filtering, (2) convenient electrical connection interface between stages, and (3) thermal sinking of the wires.

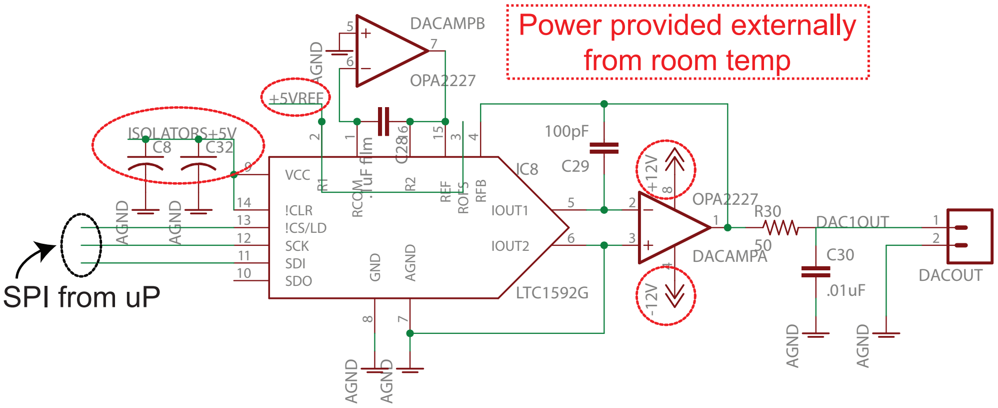

Figure 5-18: Electrical schematic for a single-channel 16-bit DAC output based on LTC1592. When the circuit power (marked in red) is provided from room temperature sources, the DAC circuit functions even when completely submerged in liquid nitrogen ($T = 77$ K).

5.4.3 Cryogenic instrumentation

The work by Shankari Rajagopal and myself on the 4× DAC system led to an exploration of whether electronic instrumentation can be operated in-vacuum at cryogenic temperatures. More specifically, our goal was to deploy the entire DAC system in a cryogenic environment. There are several motivations for this investigation.

- First, as a pure technical issue, the installation of an in-chamber microcontroller enables sensor fanout without incurring heat load costs of individual wiring.
- Second, as surface-electrode ion trap designs scale to hundreds and thousands of electrodes [KMW02], tight integration of the trapping electrodes and control electronics is expected. The demonstration of an in-vacuum DAC system proves the viability of direct electronic integration for cryogenic ion trapping.
- Thirdly, the motion of the trapped ion in the ion trap is adversely affected by voltage noise in the electrodes, such as Johnson noise, that may be suppressed by cooling of the instrument.

We test empirically the viability of a "CryoDAC", by submerging a single channel of our DAC system in liquid nitrogen ($T = 77$ K). In doing so, we have identified specific components of our hardware that fail at cryo, namely: voltage regulators (e.g. 78xx and 79xx series), a voltage reference (MAX6035), and numerous surface-mount 12 MHz resonators (e.g. ZTT-12.00MT). Our generalization from this experience is that diode-based power devices are generally unreliable for low-temperature operation, presumably due to the temperature-dependence of the diode thermal voltage [Pie88]. With the circuit power provided externally and the use of an alternate 12 MHz crystal (of a non-SMT package, ATS120), we demonstrated the 77 K operation of a USB-enabled Attiny861 microcontroller with a single-channel DAC based on LTC1592 (schematic shown in Fig. 5-18). The deployment of a complete 4× CryoDAC in the closed-cycle cryostat is, however, a task that remains for the future.

5.5 Light

Given a surface-electrode ion trap under UHV vacuum driven with appropriate RF and DC potentials, the final requirement for ion trapping is to provide laser light at the quadrupole node, which is responsible for ion loading (along with the neutral flux), cooling and detection. In this section, we describe our setup for light delivery (Section 5.5.1) as well as the detection system that is capable of resolving individual atomic ions (Section 5.5.2).

5.5.1 Light delivery

In order to produce a trapped $^{88}\mathrm{Sr}^+$ signal, the minimal set of lasers that must be provided to the experiment are:

- Photoionization lasers for ion loading: 461 nm and 405 nm. These two beams, when intersecting the neutral strontium flux, generate $^{88}\mathrm{Sr}^+$ by two-step photoionization [BLW+07] which can then interact with the RF trap.

- Dipole lasers for ion cooling and detection: 422 nm and 1092 nm. The scattering of 422 nm photons by trapped $^{88}\mathrm{Sr}^+$ ions along the $5\mathrm{S}_{1/2} \leftrightarrow 5\mathrm{P}_{1/2}$ transition provides both Doppler cooling and ion detection as discussed in Chapter 3. The 1092 nm laser is required to prevent occupation of the dark $4\mathrm{D}_{3/2}$ state [Lab08].

Additional details regarding the construction and characterization of these laser systems may be found in Ref. [Lab08]. For the current experiment, we cite in Table 5.2 the proper laser frequencies as monitored during successful runs by a wavemeter with 10 MHz precision

(High-Finesse WS-7). The table also lists typical power levels at the experiment, and the $1/e^2$-intensity beam waists at the ion location.

With the lasers on-color, the objective of the light delivery system is to intersect all required laser beams at the location of the ion (i.e. at the trap quadrupole node) with sufficient intensities. The delivery of laser light at the closed-cycle experiment is particularly simple due to an elaborate laser distribution system located upstream, which was implemented for the Quanta group by Peter Herskind. Specifically, the closed-cycle experiment receives all required lasers from the distribution system through just two optical fibers, where the "blue" fiber carries simultaneously 461 nm, 405 nm and 422 nm light, and the "IR" fiber carries 1092 nm and 1033 nm light as shown in Fig. 5-19. (The 1033 nm light is used to repump the ion from the $4D_{5/2}$ state, which is not discussed here.) Because the two delivery fibers are single-mode, each set of these lasers are automatically coaligned.

We further simplify the laser-ion alignment task at the experiment table by spatially overlapping the blue and IR lasers by the use of a dichroic element. Following blue-IR coalignment, we take the overlap of all lasers for granted, and a typical search for ions involves the scanning of the combined beam over the lab XY-frame using computer-controlled translation stages. Note that, although only a single axis of Doppler cooling is provided, the rotated arrangement of the trap in the lab frame [Fig. 5-19(a)] as well as our engineering of the trap axes results in a finite projection of the cooling beam on all intrinsic axes of the trap. We thereby achieve three-dimensional Doppler cooling and the capability for micromotion minimization along every axis.

Laser	WS-7 frequency (THz)	Power at experiment (μW)	Waist (μm)
461 nm	650.50386	200	50
405 nm	N/A	200	50
422 nm	710.96300	15	50
1092 nm	274.58920	20	100

Table 5.2: Typical laser parameters for trapping in the closed-cycle cryostat. Laser frequencies (vacuum) are measured by the WS-7 wavemeter. The 405 nm frequency is not cited because it is usually not under continuous observation due to the large 0.5 nm bandwidth of that transition. Note that the frequencies cited here may deviate from the absolute atomic frequencies due to frequency-shifting elements located downstream, e.g. acousto-optic modulators. Laser power is measured at the experiment at the spot indicated by a red triangle in Fig. 5-19. The $1/e^2$-intensity beam waist is given at the ion location.

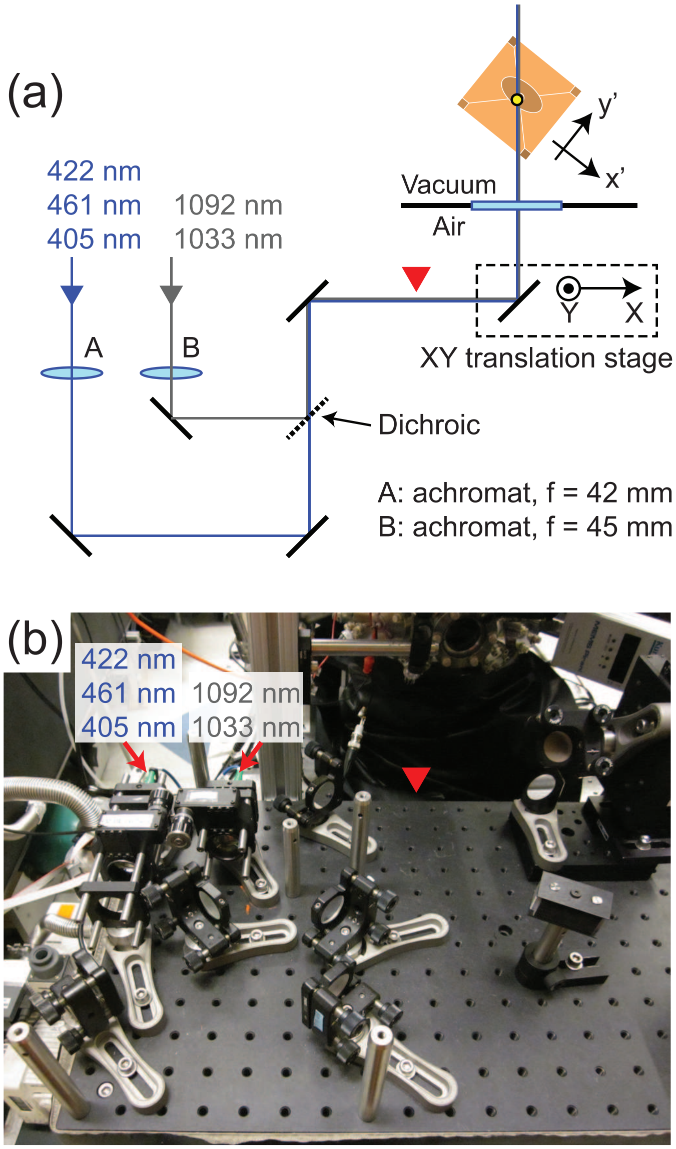

Figure 5-19: Light delivery to the ion at the closed-cycle cryostat experiment. The setup is particularly simple because all required lasers are brought to the experiment in just two single-mode optical fibers. The "blue" fiber carries 422 nm, 461 nm and 405 nm light, and the "IR" fiber carries 1092 nm and 1033 nm. (a) Schematic for the optics setup. The blue beams are focused by a $f = 42$ mm fast achromat (Thorlabs FAC1040-A1) and the IR beams by a $f = 45$ mm achromat (Thorlabs AC254-045-C). The blue and IR lasers are combined by a dichroic element, so that a single spatially overlapped beam is delivered to the ion. The beam can be scanned in the lab XY frame by computer-controlled translation stages. The red triangular marker denotes where the typical optical powers of Table 5.2 are measured. Note that the trap is arranged with respect to the optical path so that the cooling beam has a projection along all trap axes. (b) Photograph of the laser delivery setup.

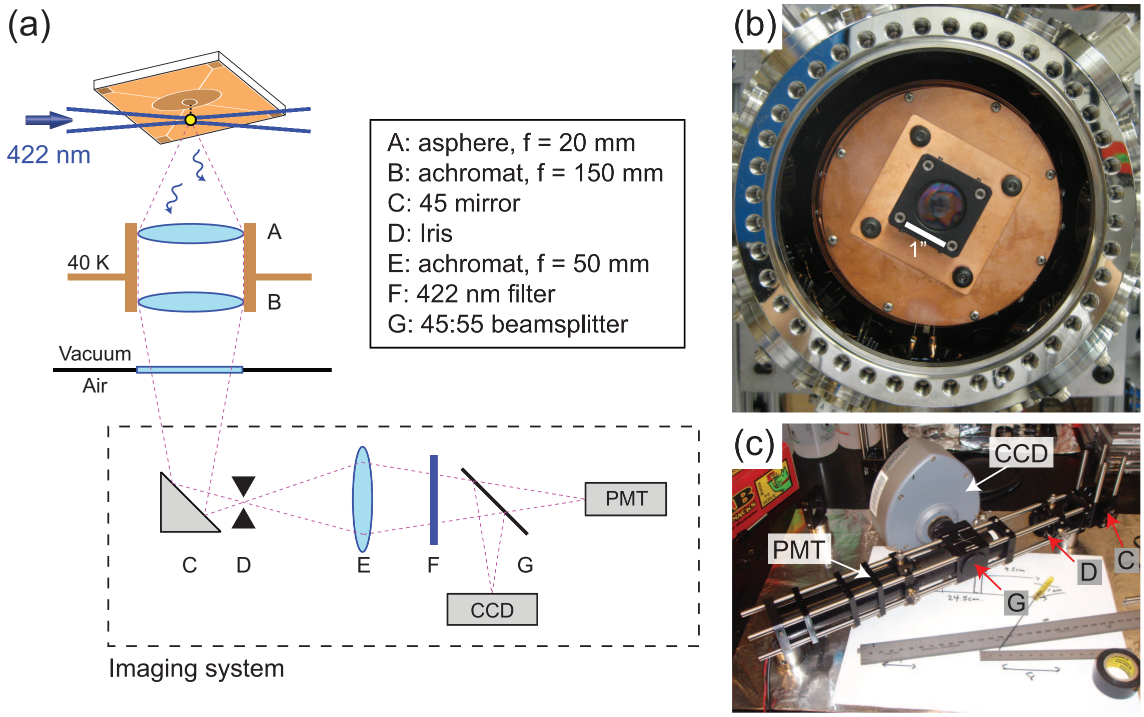

Figure 5-20: Design and implementation of the main imaging system in the closed-cycle cryostat. Schematic of the (axial) imaging system (figure not to scale) is given in panel (a). The overall goal is to image the trapped ion onto the CCD camera (Andor Luca R) and the PMT (Hamamatsu H7360-02). In order to capture a large solid angle of the ion fluorescence, two lenses A and B are mounted inside the vacuum chamber on the 40 K thermal shield and are a fixture of the experiment as shown in panel (b). All optics are 1"-diameter, and the aspheric objective A provides a numerical aperture of 0.5. The in-vacuum lenses form an intermediate image of the ion outside of the chamber. The imaging assembly, delineated by a dashed box, is then constructed to re-image the intermediate plane. The cited parameters correspond to our "high-magnification" imaging system which is also shown in panel (c).

5.5.2 Ion detection

The detection of trapped $^{88}\mathrm{Sr}^{+}$ ions is based on the collection of scattered 422 nm photons. Fig. 5-20(a) shows the general schematic for the imaging setup at the closed-cycle experiment, where it is seen that the overall system consists of two parts: (1) two in-vacuum lenses mounted on the 40 K shield, and (2) the external assembly. As the in-vacuum lenses are a fixture of the experiment [as seen in Fig. 5-20(b)], we refer to only the external part as an instance of an "imaging system".

The basic design principle is as follows. The in-vacuum lenses form an intermediate image of the ion outside of the vacuum. The exact location of the intermediate image tends to vary as different trap instances have different substrate thicknesses, ion height,

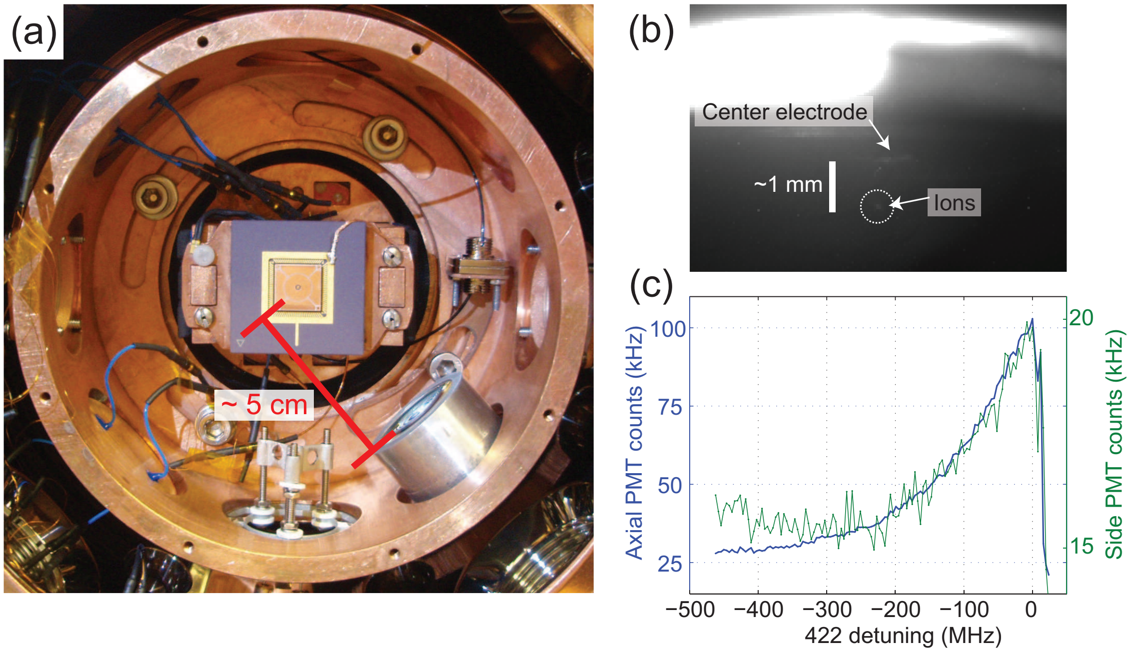

Figure 5-21: Implementation of a side-imaging system. (a) Photograph of the side-imaging system where an objective is mounted on one of the flanges of the 40 K shield (ion-lens distance ∼ 50 mm). (b) A CCD image of the trap from the side, showing both the electrodes and a large ion cloud. (c) Single ion spectroscopy of the 422 nm transition as collected by the side and axial systems. The on-resonance counts may be compared, yielding a side-to-axial efficiency of about 0.06.

etc. that affect the ultimate ion-objective distance. Once the intermediate image plane has been located, we design an imaging system (e.g. Fig. 5-20(c), not necessarily single-lens) to re-image the intermediate ion with desired performance characteristics, i.e. physical magnification, field of view (FOV), depth of field (DOF), etc. In the course of the point Paul trap experiments, we have found it useful to develop two independent imaging systems: a low-magnification/high-FOV/high-DOF system for use in the initial search for ions; and a high-magnification/low-FOV/low-DOF system to obtain individual ion resolution once the experiment is underway.

The natural metric for the overall performance is the ion signal-to-noise (SNR) ratio. There are several factors that enter into the overall SNR, such as imaging geometry, optical filtering, and detector quantum efficiency and dark noise.

The maximum achievable ion signal is largely determined by the geometry of the imaging optics, where the two most important parameters are the lateral size of the optics, and the numerical aperture (NA) of the system. We use 1”-diameter optics throughout. The NA is then determined by the placement of the objective lens [element A in Fig. 5-20(a)] which is located in-vacuum at a focal length ($f = 20$ mm) distance from the ion. The corresponding NA is 0.5 and, equivalently, the lens captures 8% of the full 4π solid angle about the ion. Given a maximum 422 nm scattering rate of $\Gamma/2 = 63.5$ MHz, the given NA yields a theoretical bound for single ion detection at 5×10^6 photons/s. This performance may be contrasted with an alternate imaging configuration, namely "side" imaging, that has been implemented on numerous occasions during the fiber-integration work. In this scenario, as seen in Fig. 5-21, one of the side 40 K flanges has been replaced with an imaging objective at a distance of ~ 50 mm from the ion, in order to image the ion along the plane of the trap. Based on the geometry alone, we expect a signal reduction factor of $\left(\frac{20}{50}\right)^2 \cdot \frac{1}{2} = 0.08$ compared to the axial system, where the factor $\frac{1}{2}$ originates from clipping of the line of sight by the trap substrate. Experimentally, we found a side-to-axial performance ratio of 0.06.

Note that, in using the objective lens to define the system NA, we are making the assumption that all light within the initial acceptance cone defined by the objective is ultimately collected by the detectors. In practice, this assumption must be explicitly verified by performing a ray-trace analysis of the candidate system that takes into account the finite sizes of the optical elements involved. During our work, we have debugged several particularly poor-performing imaging systems by performing such verification.

Subsequently, the ion SNR may be optimized by optical filtering, as shown in Fig. 5-20: namely, spatial filtering by an iris mounted on a translation stage (element D) and spectral filtering by a 422 nm notch filter (element F; Semrock, FF01-427/10-2, 98% transmission at 422 nm). The iris is placed at the intermediate image plane, where it isolates the scatter originating from the ion. Meanwhile, the notch filter effectively negates all contributions from non-422 nm lasers involved in the experiment.

Finally, the ion signal is collected by the detectors. We use a combination of a CCD camera (Andor Luca R) and a photomultiplier tube (PMT; Hamamatsu H7360-02), which have quantum efficiencies at 422 nm of 50% and 20% respectively. The ratio of optical power between the two detectors is set by a beamsplitter, which is 45 : 55 in the case of the system presented in Fig. 5-20. Taking into account the NA of the (axial) objective, the beamsplitter ratio and the detector quantum efficiency, we expect to observe on the PMT 5×10^5 photons/s from a single ion on resonance. In practice, we routinely observe

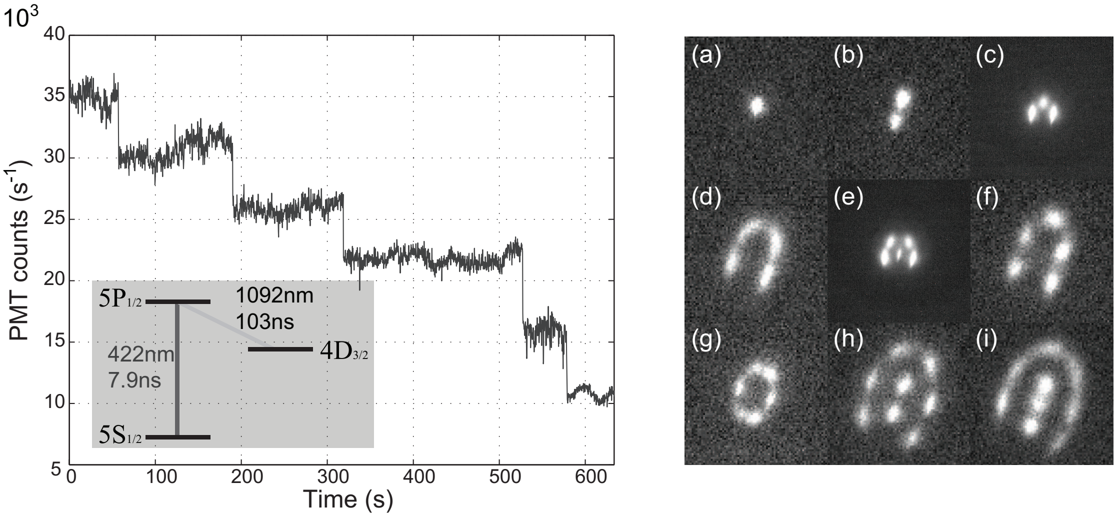

Figure 5-22: Single ion resolution in both the PMT and the camera. (Left) The PMT output as a function of time shows the discrete loss of five ions from the trap. Inset shows the $^{88}\mathrm{Sr}^+$ structure that gives rise to scattering of 422 nm photons. (Right) Ion crystals observed in the symmetric point Paul trap. Panels (c) and (e) correspond to a field of view of 70×70 μm; the remaining panels are 40×40 μm.

peak single ion scatter of 1×10^5 photons/s. Hence, the experimental scatter is on the right order-of-magnitude. The remaining discrepancy may be explained by elaboration of the Doppler cooling model (in a three-level system), nonoptimal ion cooling, optical losses at surfaces, aberration losses at the edges of the optical elements (which can, for instance, lead to imperfect spatial filtering), and so on.

Both the PMT and the camera (in the high magnification system) have individual ion resolution, as shown in Fig. 5-22. The PMT trace shows the discrete loss of five trapped ions, where the discrete steps provide a calibration of the scale to distinguish a single ion from two or more. (This rapid loss of ions was observed prior to compensation of stray fields and optimization of Doppler cooling.) In addition to the discrete PMT logs, we have been able to directly resolve individual ions in 2D crystals in the point Paul trap involving up to nine ions.

5.6 Summary and outlook

In this chapter, we have given a broad overview of cryogenic ion trapping as enabled by the closed-cycle cryostat. In particular, we discussed in detail the thermal requirements of the apparatus, the implementation of surface-electrode ion traps by PCB manufacturing, and the implementation of multiple in-phase RFs by the use of a capacitive network.

The closed-cycle experiment described here has been engineered with significant flexibility, and it reliably enables ion trapping after a short cooldown period of a few days. Furthermore, in the pursuit of fiber-integration, we have optimized the experimental layout for three-dimensional ion cooling and micromotion compensation, and also developed the infrastructure for ion translation by the use of multiple RF drives in a single trap.

The next logical step for the closed-cycle experiment is to demonstrate coherent operations based on the 674 nm qubit transition. This objective provides a clear organizing principle for the continuation of the efforts described in this chapter:

- **Firstly**, the target of QIP requires the miniaturization of traps to reach the resolved-sideband regime of the 674 nm qubit transition [Roo00], which can be achieved by the microfabrication of the asymmetric point Paul trap. To facilitate the trap development process, the workflow from trap design to lithography (using the in-house Heidelberg exposure system, for example) should be automated as much as possible, as was done for PCB fabrication.

- Along with trap miniaturization, the operating RF frequency must also be increased to reach the resolved-sideband regime: $\Omega > 2\pi \times 20$ MHz. In early explorations of miniature, high-frequency trap designs at the closed-cycle experiment, I have learned that various electronic equipment (e.g. DAC outputs, CCD camera) must be reinforced to overcome increased RF pickup at higher frequencies. Thus, in conjunction with trap development, further work in robust instrumentation and electrical isolation is needed.

- The implementation of multiple RFs at higher operating frequencies is also likely to require additional effort.

- **Secondly**, the demonstration of ground-state cooling and coherent operations requires the identification and resolution of noise sources at a level beyond what was necessary for Doppler cooling. With ground state cooling, noise sources can be quantified with exquisite sensitivity (whether one wants it or not). Points for immediate improvement include: better mechanical vibration isolation between the experiment table and the cryo head; secure and rigid layout for the two optical fibers (from the laser distribution system) in order to minimize polarization noise; aggressive electrical grounding of the experiment, especially the cryo head which emits electronic noise at ~ 100 kHz repetition rate.

- Furthermore, the temperature performance of the closed-cycle cryostat needs to be better characterized: what is the exact temperature profile – spatial and temporal – within the apparatus? Is it truly steady-state or does it suffer from instabilities? Recall, from the previous chapter, our requirement of sub-10 mV electronic noise for reaching the Doppler cooling limit. Thermal instabilities may lead to mechanically-induced RF and electronic noise (e.g. variations in stray capacitances) that can contribute to ion heating. Questions regarding cryostat performance could be effectively addressed with the deployment of an in-vacuum measurement system with large fanout (i.e. the CryoDAC-ADC infrastructure).

- **Thirdly**, beyond the correction of currently existing noise sources, there is an opportunity to explore novel options for system isolation as enabled specifically by the cryogenic environment. These include a superconducting shield for magnetic field noise [KWN04] and cryo cooling of electronic instrumentation.

The exploration of coherent operations in the resolved-sideband regime is the soul of trapped-ion QIP. The foundational work of the past two years has led to a reliable ion trapping machine, which can now employed as a vehicle for quantum information science proper. I predict that there will be exciting challenges and opportunities to come with this experimental system!

Chapter 6

Surface-electrode ion trap with an integrated light source

An array of trapped ions in optical cavities, connected by a network of optical fibers, represents a possible distributed architecture for large-scale quantum information processing (QIP) [CZKM97]. The vision of an ion-photon quantum network, at the level of tens and hundreds of qubits, is a technological challenge that requires the simultaneous large-scale integration of electronic [KMW02, AUW$^+$10, HHJ$^+$10] and optical components [KPM$^+$05, KK09] which is, in principle, compatible with the surface-electrode paradigm as enabled by existing fabrication technology for integrated circuits.

In this chapter, we report on the design (Section 6.1), fabrication (Section 6.2), and experimental demonstration of a surface-electrode ion trap with an integrated single-mode optical fiber for driving the 674 nm quadrupole transition of $^{88}\mathrm{Sr}^+$ (Section 6.3.1). The 674 nm transition is of particular interest in QIP with trapped ions, where it serves as the optical qubit [BW08], as well as in metrology, where it constitutes an optical frequency standard [MBH$^+$04]. The ion-fiber spatial overlap is optimized *in situ* by micromotion-free translation of the ion using multiple RF electrodes. We use this technique to map out the Gaussian profile of the fiber mode along a single transverse axis (Section 6.3.2). With the ion over the center of the mode, we quantify the magnitude and timescale of light-induced self-charging of the fiber (Section 6.3.3), which may be considered a fundamental lower bound in trap perturbation introduced by the fiber. The fiber-trap system described here is my own work, and has been published in Ref. [KHC11].

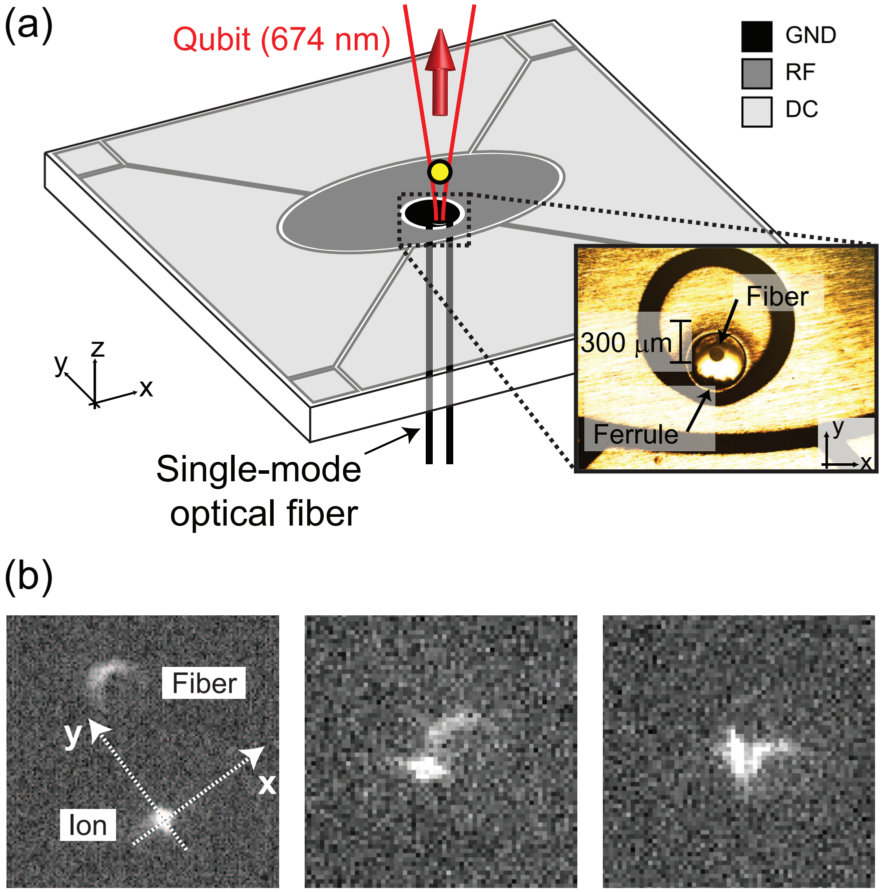

Figure 6-1: An overview of the fiber-integrated point Paul trap system. (a) A single-mode optical fiber is integrated in the substrate of a surface-electrode trap, and the ability of the integrated-fiber to drive the 674 nm qubit transition of $^{88}\mathrm{Sr}^{+}$ is demonstrated. Asymmetries in the trap design facilitate three-dimensional localization of the ion in the optical mode. (b) Using multiple RF sources, the ion is positioned *in situ* with respect to the 10 μm-scale integrated Gaussian mode despite an initial 160 μm ion-fiber offset along $\hat{e}_y$ (leftmost panel) arising from errors in trap fabrication.

6.1 Fiber-trap design

In this section, we describe the design principles underlying our surface-electrode ion trap with an integrated single-mode fiber. As summarized in Fig. 6-1, we achieve ion localization in all three-dimensions with respect to the center of the 10 μm-scale integrated Gaussian mode, and access the 674 nm qubit transition of trapped $^{88}\mathrm{Sr}^{+}$ through the fiber. Underlying this demonstration are the following basic questions regarding optics-integration in surface-electrode ion traps:

- What fiber geometry relative to the surface-electrode trap minimizes electromagnetic perturbations due to the fiber dielectric (Section 6.1.1)?
- How can the trap design be optimized to facilitate three-dimensional ion localization in the fiber output (Section 6.1.2)?
- Given the sub-micron length scale of a trapped ion and typical technical constraints in trap fabrication, how can the precise spatial overlap between the ion and the integrated mode be guaranteed (Section 6.1.3)?

We now present our design choices that address each of these questions, and arrive at the integrated system illustrated in Fig. 6-1(a).

6.1.1 The prior art, and geometry for fiber integration

We begin with a review of the prior art in fiber-integration. The fundamental challenge in this effort – and, in general, the integration of optical elements into ion traps – has been the adverse interaction between large bodies of dielectric such as the fiber body and the RF trapping mechanism. Namely:

1. The presence of dielectrics distorts the electric field from the free-space configuration, leading to displacements in the quadrupole node position and shifts in important trapping parameters such as the Mathieu q-parameter and the trap depth. While undesirable, such "static" perturbations can be compensated by trap design that explicitly models the electromagnetic presence of the dielectric material.
2. At the same time, dielectrics in the vicinity of the trap provide electrically insulated surfaces where charges (such as those generated during ion loading) may deposit. In

contrast to dielectric distortion, dynamic accumulation of charge is difficult to predict *a priori*; yet, it can contribute to excess motional heating of the ion [DNM+11] and even generate sufficiently large stray fields as to prevent trapping entirely. Dielectric charging is especially hazardous in the current context, given short ion-fiber proximities that are desired (usually a few 100 μm) and shallow trapping potentials characteristic of surface-electrode designs.

3. Finally, the physical presence of fibers in the trapping space can occlude free-space optical access to the ion that contributes to increased background scattering. In turn, a degraded ion SNR limits the fidelity of quantum state readout which affects the system's capability for QIP protocols.

Despite these difficulties, early attempts at fiber-optics integration in surface-electrode ion traps [Geo08] sought to introduce a bare fiber directly in the trapping half-space, $z > 0$, as shown in Fig. 6-2(a). A similar geometry was also pursued in Ref. [Zae07], but where a preemptive countermeasure was taken by applying a copper coating over the fiber body [Fig. 6-2(b)]. However, as the metallized fibers pull the RF field lines away from the surface-electrode trap, the fibers were forced to carry high-voltage RF potentials instead, making the overall system akin to a three-dimensional "endcap" trap [SPSW93] rather than the originally-intended surface-electrode design. Ultimately, with such complications due to the fiber dielectric, no trapped ions were produced in these early investigations where the fiber was delivered directly through the trapping half-space of a surface-electrode trap.

More recently, and concurrent with the work described in this thesis, an alternative geometry for integration emerged where the bulk of the fiber is naturally shielded from the trapping space. This approach avoids the above-mentioned difficulties associated with trapping near dielectrics, and allows the fiber to remain decoupled from the electrical mechanism for RF trapping. The scheme was first successfully demonstrated in Ref. [VCA+10], where a multimode optical fiber is installed underneath the trapping space of a surface-electrode design [Fig. 6-2(c)]. The integrated fiber samples $^{24}\text{Mg}^+$ fluorescence through a 50 μm light-collection hole in the trap substrate. Notably, trapped ions are obtained despite a relatively short ion-dielectric distance of 100 μm. A similar setup was also achieved in Ref. [BEM+11]. And, in Ref. [WTRW+11], two multimode fibers collect $^{40}\text{Ca}^+$ fluorescence through hollow coaxial RF electrodes that make up a three-dimensional endcap trap [Fig.

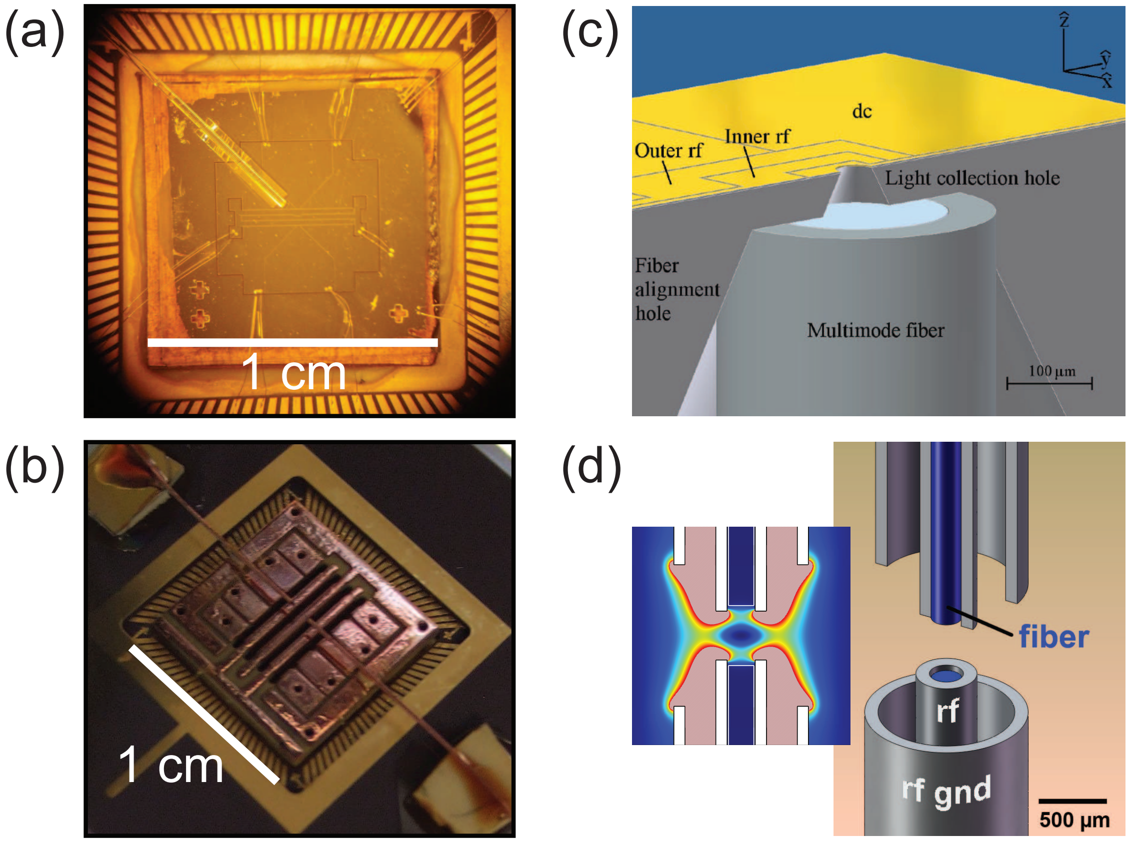

Figure 6-2: Prior art (a,b) and concurrent efforts (c,d) in fiber-optic integration into ion traps. All systems here are based on multimode fibers for fiber-optic detection of trapped ion fluorescence. (a) A bare multimode fiber with a core diameter of 200 μm is brought to $\sim$ 500 μm of the predicted quadrupole node in a surface-electrode trap, directly through the trapping half-space $z > 0$. The system is believed to have suffered from dielectric charging of the fiber that prevented trapping [Geo08]. (b) Two multimode fibers with a core diameter of 200 μm is each brought to 500 μm of the predicted trap location. The fibers have been metallized with a layer of copper, and are utilized as the RF electrodes in an "endcap" trap geometry. No ions were produced in this system due to external technical difficulties [Zae07]. (c) A 220 μm-core multimode fiber is brought to within 100 μm of a trapped ^{24}Mg^{+} ion in a surface-electrode design, but is shielded from the trapping space. Fiber-based ion detection is demonstrated with a NA of 0.37 [VCA^{+}10]. (d) Multimode fibers with 200 μm core are incorporated into a three-dimensional endcap trap, and fiber-based ^{40}Ca^{+} detection is demonstrated. The NA of each individual fiber is comparable to the system in (c) [WTRW^{+}11].

6-2(d)]. A notable feature of the latter system, in addition to its aggressive shielding of the fiber dielectric, is the use of cylindrical symmetry in trap design, which is motivated by the compatible symmetry of the optical fiber. For example, the RF electrode may thus be bored for the insertion of an optical fiber without displacing the ion from the symmetry axis of the overall assembly.

These same principles, i.e. the electrical shielding of the fiber dielectric and the use of compatible (cylindrical) symmetry, also identify the surface-electrode point Paul trap as a good candidate for fiber-integration, where the optical fiber is embedded directly beneath the ion within the center electrode and is situated at a normal to the trap plane. Our suggested geometry is illustrated in Fig. 6-1(a), based on the elliptical variant of the point Paul trap. Experimentally we find, with and without the fiber, comparable secular frequencies and trapped ion lifetimes (several hours under Doppler cooling) and similar stability of the compensation voltages during continuous trap operation. Thus, the point Paul design allows direct fiber-access to the ion in a surface-electrode trap while eliminating the major perturbative effects of the fiber dielectric.

6.1.2 Trap engineering for three-dimensional ion localization

The requirement of three-dimensional ion localization necessitates a projection of the cooling laser on all intrinsic axes of the trap. In principle, this may be achieved by multiple non-colinear beams that intersect at the ion position. However, the demand for experimental simplicity and practical geometric considerations (namely that, in a surface-electrode design, free-space optical access is constrained to the radial plane) motivate the optimization of trap axes in order to facilitate three-dimensional ion localization.

As previously noted, absolute cylindrical symmetry in fiber-integration (e.g. the symmetric point Paul trap) is conceptually attractive. Such a design has the consequence that the intrinsic axes of the trap are coaligned with respect to the xyz reference frame of the trap as defined by the fiber axis and the trap plane, as shown in Fig. 6-3(a). In the figure, the large blue arrow denotes a single axis of Doppler cooling, and the set of smaller orthogonal arrows indicates the orientation of the trap axes with respect to the xyz-frame. In panel (a), given the degeneracy of the radial potential, we diagonalize the radial axes along the direction of the cooling beam ($\hat{e}_x$) without loss of generality. In contrast, Fig. 6-3(b) shows the orientation of the trap axes in the asymmetric point Paul trap, where the shift

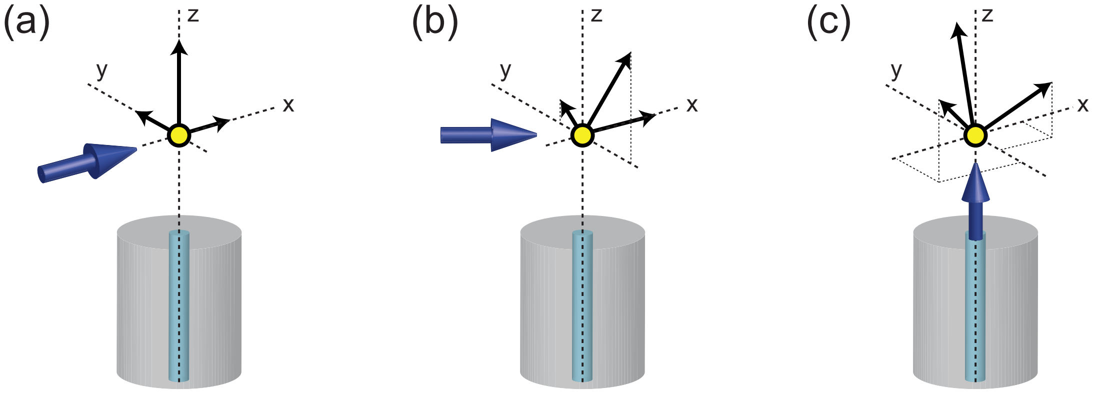

Figure 6-3: The engineering of trap axes over the integrated fiber. The xyz reference frame is defined by the axis of the fiber and the plane of the surface-electrode trap (not shown). The large blue arrow denotes a single axis of Doppler cooling, and the orthogonal triad at the ion indicates the orientation of the trap axes. (a) Trap axes in a cylindrically symmetric design, where the radial axis $\hat{e}_x$ may be defined without loss of generality by the cooling laser. In this configuration it is seen that, in order to achieve projection on all three axes, two free-space and one fiber-delivered beams are required. (b) The orientation of the trap axes in the asymmetric point Paul trap, where the trap axes is rotated by 30° in the yz-plane about $\hat{e}_x$. By a suitable arrangement of the Doppler beam (e.g. $\hat{e}_x - \hat{e}_y$), a single radially-delivered beam can cool all three axes of motion. (c) The arrangement of trap axes which is required for three-dimensional cooling of the ion by a fiber-delivered Doppler beam.

of the elliptical electrode along $\hat{e}_y$ removes radial degeneracy and yields a 30° rotation of the trap axes in the yz-plane about $\hat{e}_x$.

Thus it is observed that, by breaking absolute cylindrical symmetry, an arrangement of trap axes emerges where the trapped ion may be localized in three-dimensions with a single, radially-delivered (e.g. $\hat{e}_x - \hat{e}_y$) cooling beam. This may be contrasted with the symmetric system of (a), where three cooling beams (two free-space and one fiber-delivered) are required for the same result. In our fiber-trap design, we opt for the experimental simplicity afforded by configuration (b) at the cost of breaking absolute cylindrical symmetry in trap layout. (Note, however, that further rotation of the trap axes [e.g. Fig. 6-3(c)] is needed in order for a single fiber-delivered beam to achieve three-dimensional cooling.)

6.1.3 *In situ* modematching of the ion to the integrated element

A key contrast between the concurrent efforts of Fig. 6-2 [VCA$^+$10, BEM$^+$11, WTRW$^+$11] and this thesis work is in the function of the integrated fiber. In the former systems, multimode fibers with relatively large core diameters (~ 200 μm) are employed to collect the isotropic fluorescence of a trapped ion. This thesis, on the other hand, complements such efforts by demonstrating light delivery to the ion through an integrated single-mode fiber. As a consequence, our system generally deals with significantly smaller dimensions: a single-mode fiber has a typical core diameter of ~ 3 μm, and the optical output is a highly directional Gaussian beam with a mode waist of some 10 μm at an ion height of ~ 500 μm. As such, the current light-delivery system demands greater precision in trap fabrication in order to observe even basic ion-fiber interaction.

Hence, a major feature of our design is the use of multiple RF electrodes that permits *in situ* modematching of the ion relative to the Gaussian output of the single-mode fiber. This technique can be used in general to defray a part of the precision requirement in integrated trap fabrication. Here, we demonstrate correction of the ion-fiber spatial overlap despite an initial 160 μm offset, which is over three times the mode waist at the ion height. With this functionality, we obtain a technically simple and mechanically robust (though imprecise) procedure for fiber-trap assembly, which is presented in the following section.

6.2 Experimental realization

The general infrastructure for cryogenic ion trapping is described in Chapter 5. In this section, we focus on the construction of the fiber-trap system (Section 6.2.1), and the experimental configuration unique to the integration project: our custom vacuum fiber feedthrough (Section 6.2.2) and the polarization analyzer for the fiber output (Section 6.2.3).

6.2.1 Fiber-trap construction

The target geometry for fiber integration is to embed the fiber within the trap substrate. Fig. 6-4 shows a photograph of our fiber-trap implementation, which consists of two parts: (1) a PCB chip (i.e. the asymmetric point Paul trap) with a 400 μm plated via in the center electrode for the insertion of fiber and ferrule; and, (2) a single-mode optical fiber connectorized in a stainless steel optical ferrule that has an appropriately machined nipple for mating with the PCB. In the final assembly, the metallic ferrule is electrically shorted to the center (ground) electrode and spatially fills the via.

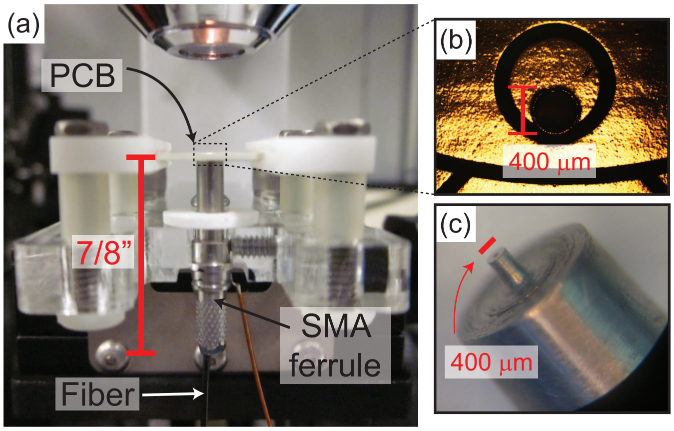

Figure 6-4: Assembly jig for the construction of the fiber-trap. (a) Side profile of the fiber-trap system mounted in the microscope assembly jig. The system consists of two parts: the point Paul trap PCB, and an optical ferrule containing the desired fiber, e.g. a polarization-maintaining single-mode fiber for 674 nm. The PCB is held by grooves in the jig, while the ferrule is held by a setscrew from the side. This arrangement allows the ferrule to be rotated with respect to the PCB. (b) Photograph of the PCB, emphasizing the large 400 μm plated via in the central electrode for the insertion of ferrule and fiber. (c) An angled view of the stainless steel ferrule, showing the 400 μm-diameter nipple for mating with the PCB via. In the final assembly, the metallic ferrule is electrically shorted to the center electrode and spatially fills the via.

Asymmetric point Paul trap PCB

A detailed discussion of trap design can be found in Chapter 2. Here, we summarize the trap layout for completeness. The center, grounded electrode has a diameter of 1.1 mm. The elliptical RF pad has major- and minor-axis diameters of 5.9 mm and 2.8 mm, respectively, and is shifted by 500 μm along the minor-axis relative to the center of the ground electrode. Electrode gaps are 100 μm. This design achieves an ion height of 670 μm and the electrode asymmetries uniquely define the principal axes of the trap, which are tilted by 30° in the yz-plane for achieving projection of the cooling beam on all principal axes. The side electrodes are used for DC compensation of stray fields, as well as radial translation of the quadrupole node by the use of additional RF sources. The trap is defined on a PCB, with copper electrodes on a low RF-loss substrate (800 μm-thick Rogers 4350B, fabricated by Hughes circuits). The PCB includes a 400 μm diameter plated via in the central ground electrode for the insertion of an optical ferrule. The via is offset by 300 μm with respect to the center of the ground electrode to account for the displacement of the trapping point that accompanies the shift in the elliptical RF electrode.

Optical fiber and ferrule

Our optical fiber (OZ Optics, PMF-633-4/125-3-L) is single-mode for 674 nm and is mechanically protected by a 250 μm-diameter acrylate buffer and a tight-fitting 900 μm-diameter plastic jacket (Hytrel PVC). We prepare a fiber of length 1-2 m by conventional fiber connectorization: the sample is cured in a stainless steel SMA-905 optical ferrule (Thorlabs, 10125A) using fiber epoxy (Thorlabs, F112), and is flat polished on lapping film.

The subsequent task is to machine a 400 μm-diameter mating nipple on the ferrule. This is performed on a standard lathe, where the length of the fiber is funneled through the central (hollow) axis and is free to rotate. The machining of the ferrule with an internal fiber is surprisingly robust: in half-dozen instances of this process, we have never caused any damage to the optical fiber through turning. This attests to the mechanical robustness of the stainless steel ferrule approach, which is in stark contrast to the copper-evaporated ceramic ferrule. Instead, the primary limitation of this approach is the machining imprecision: as a rule, we have not achieved fiber-nipple concentricity better than 50 μm. The nipple may also be tilted (sub-1°) relative to the ferrule body. However, we are able to compensate for such errors in the final system by RF translation. Following the machining step, the sample is subject to a typical UHV wash [i.e. soap, rinse, isopropyl alcohol (IPA)] in an ultrasonic bath in order to remove oils and other residues. Finally, we attach a wire to the body of the ferrule [visible in Fig. 6-4(a)] using a conductive epoxy (Epo-Tek, H20E), which serves as a redundant grounding connection for the ferrule.

Note: we opt to machine the nipple after fiber connectorization rather than vice versa, due to the tight tolerance of the ferrule hole that provides only a few microns of clearance for the fiber. Even the slightest deformation of the ferrule hole during turning can make subsequent fiber insertion practically impossible.

PCB-ferrule attachment

The attachment of the PCB and ferrule is performed under an optical microscope, using a simple assembly jig which is illustrated in Fig. 6-5. The basic usage of the jig is explained in the figure caption.

Our strategy for PCB-ferrule alignment is as follows: while general RF-based translation can achieve arbitrary ion positioning, we have chosen to concentrate as much as possible all

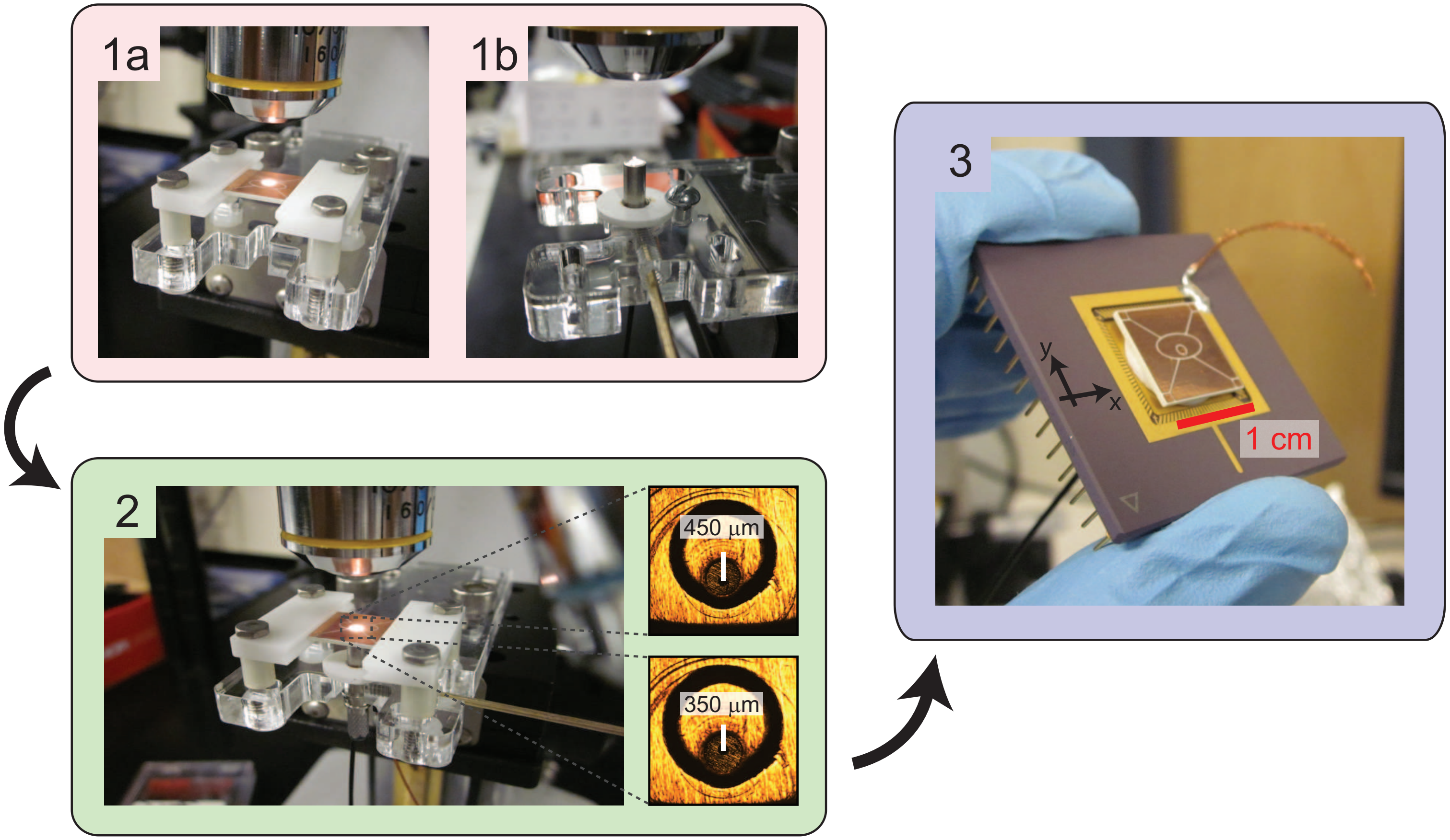

Figure 6-5: Illustration of the PCB-ferrule attachment process. The scale is given by the dimensions of the PCB, which is 1 cm × 1 cm. (1a) The PCB is firmly held in place in the grooves of two elevated grabber pieces. (1b) The ferrule is rigidly held in place by a setscrew from the side. A ceramic washer is fit over the ferrule, which serves as a spacer in the final assembly. (2) With the ferrule inserted in the PCB via, both components are secured independently. By loosening the ferrule setscrew, the ferrule can be rotated. The microscope pictures show two orientations of the ferrule, where the fiber hole is aligned to the minor-axis of the trap but with a different fiber-center offset due to the nonconcentricity of the nipple. Once the desired orientation is achieved, the ferrule setscrew is applied. The entire structure can now be rigidly detached from the microscope stage, so that cyanoacrylate adhesive may be conveniently applied. (3) The assembled PCB and ferrule (and washer) are "front-loaded" through a hole in the CPGA chip carrier and glued in place. Subsequently, the PCB pads are wirebonded to the CPGA bonding pads.

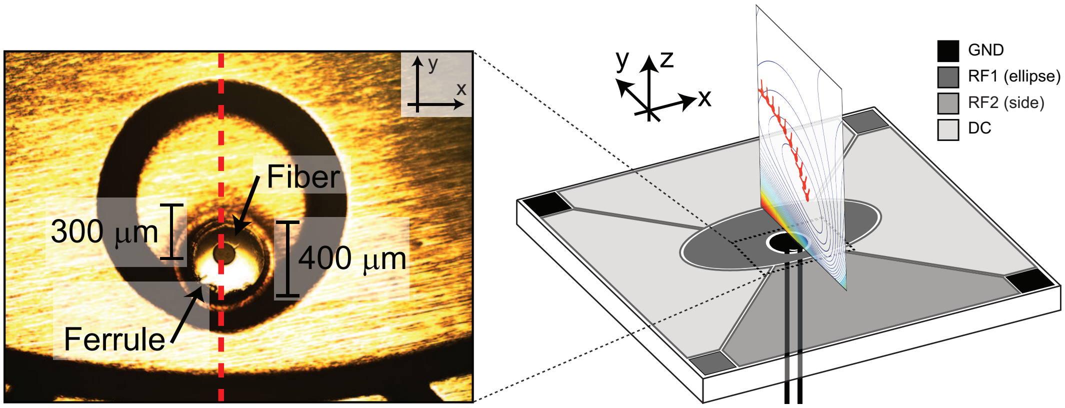

Figure 6-6: General strategy for the alignment of the ferrule and fiber in the PCB. We seek to concentrate fiber-ion displacement (as much as possible) along the y-axis of the trap, which lies in the translational span of ellipse and (minor-axis, narrow-end) side RF electrodes. [Left] Despite the asymmetries of the elliptical point Paul trap, the PCB maintains a mirror plane along the y-axis (indicated by dashed red lines) which is a convenient guide-to-the-eye. The ferrule is rotated in the PCB via until the fiber is aligned with respect to the mirror axis. Machining imprecision of the ferrule is clearly evident in the form of $\sim 100\ \mu$m nonconcentricity between the fiber and ferrule. [Right] Illustration of the RF translation curve (Fig. 4-8) spanned by the ellipse and side electrodes in relation to the trap. The ion is translated along $\hat{e}_y + \hat{e}_z$ as a function of $\epsilon = V_{\text{side}}/V_{\text{ellipse}}$. The figure is not to scale.

fabrication errors along the y-axis of the trap, which lies in the locus of quadrupole nodes spanned by the ellipse and side (minor-axis, narrow-end) electrodes as shown in Fig. 6-6. The motivation for this choice is twofold. Firstly, despite the asymmetries of the elliptical point Paul trap, the PCB maintains a mirror plane about the y-axis, which is therefore a natural guide to the eye (dashed red line in Fig. 6-5) during PCB-ferrule attachment. Secondly, the chosen side electrode is, among the four compensation electrodes, physically the closest to the original quadrupole node and thus yields a relatively strong translation effect even for moderate RF ratios (e.g. $\Delta y = 200\ \mu$m for $\epsilon = V_{\text{side}}/V_{\text{ellipse}} = 0.5$). In other words, we have chosen *a priori* to utilize the two RF electrodes that yield a large translational span along the y-axis; accordingly, we orient the ferrule so that the fiber lies on the same axis but not necessarily at the correct location.

Once the desired ferrule orientation is achieved, the two parts are glued together with cyanoacrylate adhesive (KrazyGlue). Next, the entire structure is loaded onto a ceramic pin grid array (CPGA) chip carrier that has a machined hole (made using a waterjet) in its die attach area to permit the routing of fiber and ferrule. Finally, the PCB electrodes are wirebonded to the CPGA bonding pads.

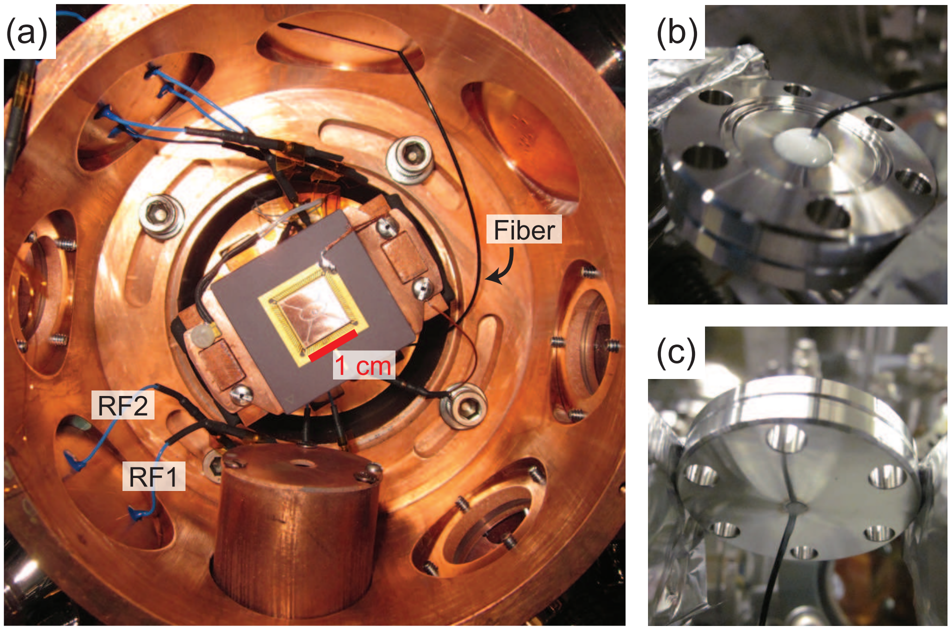

Figure 6-7: Routing of the integrated fiber in vacuum. The fiber-trap system is mounted on a CPGA and installed on the 8 K baseplate of the closed-cycle cryostat. The fiber is routed through a slit in the 40 K intermediate shield, and exits the vacuum chamber through a 1 mm hole in a 1.33"-diameter CF blank where it is sealed in place with TorrSeal UHV epoxy. The epoxy is cured for 24 h at room temperature (rather than 1.5 h cure at 60°C), in order to avoid heat damage to the plastic jacket of the fiber.

6.2.2 Vacuum feedthrough for the fiber

The assembled fiber-trap system is installed in the working chamber of the closed-cycle cryostat, as shown in the photograph of Fig. 6-7(a). A slit-like feedthrough port in the intermediate shield permits the fiber to exit the cryogenic chamber with minimal mechanical stress. Following the 40 K slit, the fiber is fed through a 1 mm-hole in a standard 1.33" ConFlat (CF) blank, where it is sealed in place with TorrSeal UHV epoxy as seen in Fig. 6-7(b,c). Our typical in-vacuum fiber length is 0.5 m, which makes heat conduction through the fiber negligible. Note: while TorrSeal can be cured more rapidly at elevated temperatures (e.g. 60°C), we utilize a 24 h room-temperature cure, since the PVC jacket of the fiber is susceptible to softening when heated. Also, the jacket must be washed thoroughly (ultrasonicated in IPA) prior to TorrSeal application, in order to remove contaminants that can affect the vacuum seal. With such precautions, we did not encounter pressure degradations in the cryostat (at the 10^{-9} torr level) correlated with our custom fiber feedthrough.

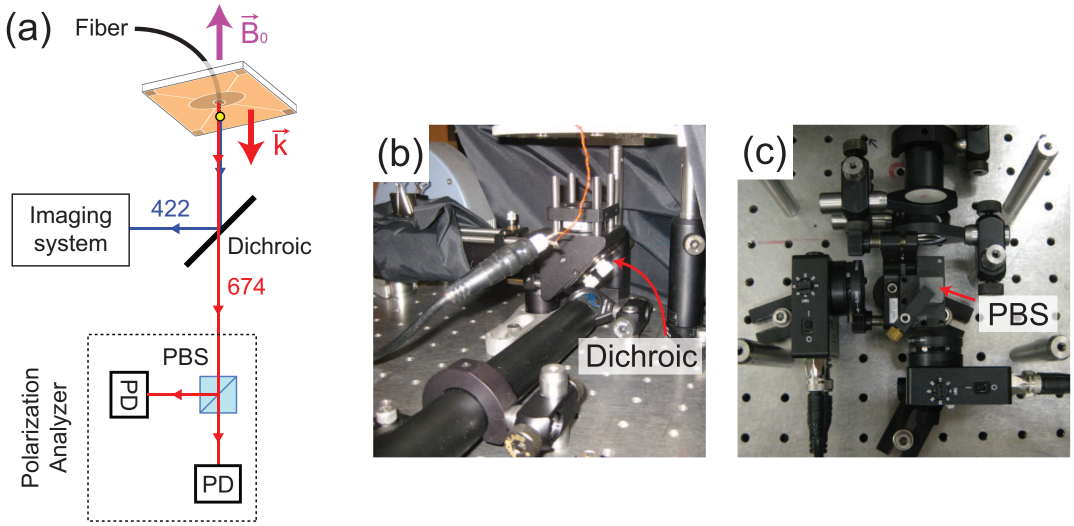

Figure 6-8: The orientation of magnetic bias $B_0 \approx 3$ gauss and the wavevector ($\vec{k}$) and polarization (not shown) of the fiber output. (a) The bias field $\vec{B}_0$ is oriented parallel to the fiber wavevector. In such a configuration, the quadrupole transition coupling strength is invariant with respect to 674 polarization which is constrained to lie in the trap plane [Roo00]. Nevertheless, we install a dichroic mirror (Thorlabs, DMLP505) that allows the 674 nm fiber light to be transmitted to a polarization analyzer setup. (b) Photograph of the dichroic mirror placement in the imaging axis. (c) A standard polarization analyzer based on a polarizing beamsplitter (PBS) and two photodiodes (PD). Using the analyzer, we continuously monitor both polarization and power of the integrated fiber output.

6.2.3 Polarization analyzer for fiber output

Our main goal for the fiber-trap system is to access the 674 nm quadrupole transition of $^{88}\mathrm{Sr}^+$ through the integrated fiber. However, the response of $^{88}\mathrm{Sr}^+$ to 674 nm illumination depends not only on the beam intensity, but also the orientation of the 674 nm wavevector and polarization relative to the quantization axis set by the bias magnetic field $\vec{B}_0$.

As shown in Fig. 6-8, the bias field in our experiment is oriented normal to the trap plane or, equivalently, parallel to the fiber wavevector $\vec{k}$. In such a configuration, the quadrupole transition coupling strength is invariant to rotations of the 674 nm polarization in the trap plane [Roo00] which is desirable since we seek to image the intensity profile of the fiber mode without being affected by polarization drifts.

Nevertheless, we modified our imaging system to permit the fiber-delivered 674 nm light to be extracted [Fig. 6-8(a,b)] and propagated to a polarization analyzer setup [Fig. 6-8(c)]. Using the analyzer, we maintain the fiber polarization along $\hat{e}_x + \hat{e}_y$ in the trap frame (Fig. 6-9), and continuously monitor the optical power emerging from the trap fiber.

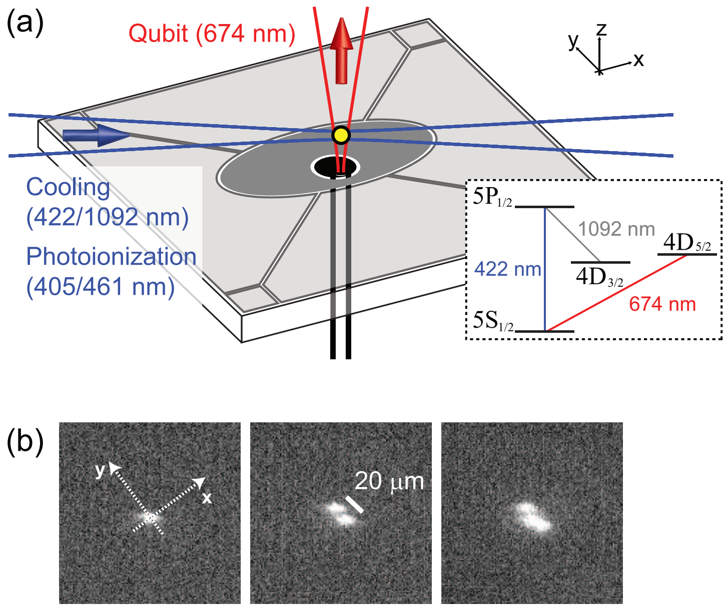

Figure 6-9: Basic operation of the fiber-integrated point Paul trap. (a) Illustration of all light delivery to the ion: photoionization (405,461 nm) and cooling/detection (422,1092 nm) lasers are delivered radially, as in conventional surface-electrode ion trap experiments; the 674 nm qubit laser is delivered normal to the trap plane. Inset shows the level structure of $^{88}\mathrm{Sr}^{+}$. (b) One, two and three-ion $^{88}\mathrm{Sr}^{+}$ crystals in the fiber-integrated point Paul trap. The ions align along the y-axis, which is the weakest-confining trap axis in the design. The operating RF parameters are: $\Omega = 2\pi \times 6.26$ MHz, $V_{\mathrm{ellipse}} = 230$ Vpp, $V_{\mathrm{side}} = 60$ Vpp, $\epsilon = V_{\mathrm{side}}/V_{\mathrm{ellipse}} = 0.26$.

6.3 Demonstration of the fiber-trap system

The fiber-trap is operated at a typical RF frequency of $\Omega = 2\pi \times 6$ MHz and 250 Vpp amplitude, achieving secular frequencies of $\omega_{z'} = 2\pi \times 410$ kHz, $\omega_x = 2\pi \times 240$ kHz, and $\omega_{y'} = 2\pi \times 170$ kHz. We produce $^{88}\mathrm{Sr}^{+}$ ions by resonant photoionization [BLW⁺07], which are Doppler cooled on the $5S_{1/2} \leftrightarrow 5P_{1/2}$ transition at 422 nm while simultaneously driving the $4D_{3/2} \leftrightarrow 5P_{1/2}$ transition at 1092 nm [see inset of Fig. 6-9(a)]. The photoionization and cooling beams are delivered radially [Fig. 6-9(a)], as in conventional surface-electrode trap experiments, and ion fluorescence at 422 nm is collected by a 0.5 NA lens inside the chamber and imaged onto a CCD camera and a photomultiplier tube. Fig. 6-9(b) shows one, two, three-ion crystals loaded along the y-axis of the trap, which is the weakest-confining axis. In comparison to point Paul traps without the fiber, we do not encounter additional difficulties in trapping with the integrated fiber (e.g. shorter ion lifetimes, instability of compensation voltages for micromotion compensation, etc.).

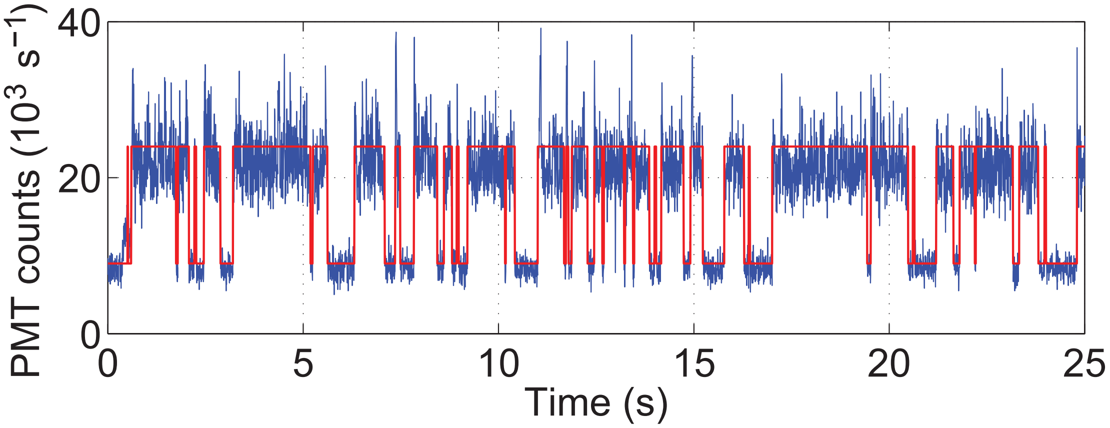

Figure 6-10: Telegraph log showing the interaction of ion with 674 nm light. The blue curve is the raw stream from the photomultiplier tube, whereas the red curve has been digitized and debounced for further analysis. The ion is "dark" when its valence electron is shelved into the $4D_{5/2}$ state where it cannot scatter detection (422 nm) photons. The ion remains dark until it decays spontaneously back to the "bright" $5S_{1/2}$ state. The telegraph log highlights the randomness inherent in the quantum dynamics of a single atom i.e. random quantum jumps between the $5S_{1/2}$ and $4D_{5/2}$ states. The fiber-ion interaction strength can be quantified in the form of an effective shelving rate, computed by counting the number of bright-to-dark transitions per total bright time. This analysis is performed on telegraphs of 1 min duration.

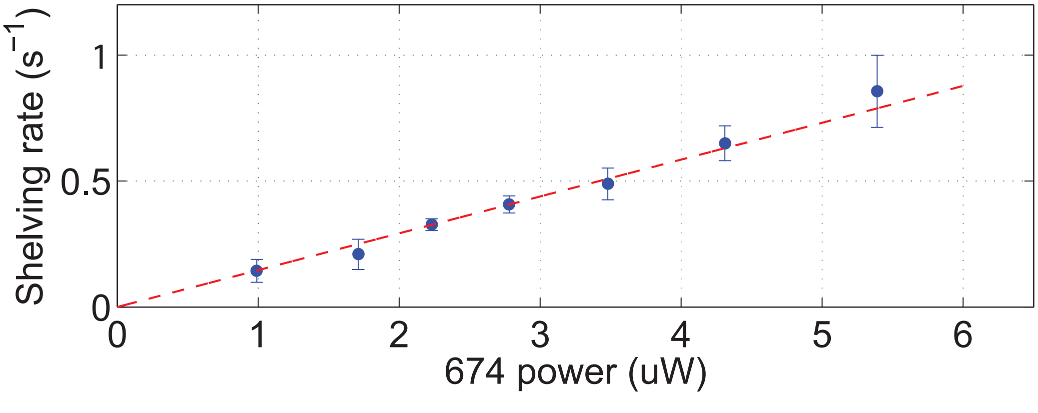

Figure 6-11: Linear increase in the $5S_{1/2} \leftrightarrow 4D_{5/2}$ shelving rate as a function of the 674 nm power delivered to the ion, as expected for the weakly-coupled regime. The linear relationship justifies the use of the $^{88}Sr^{+}$ ion as a probe for the local 674 nm intensity. The 674 nm beam waist at the ion is approximately 50 μm, and intensities were purposely kept low, in order to simplify the counting of bright-to-dark transitions necessary for the computation of the shelving rate.

6.3.1 Measurement of fiber-ion interaction

Interaction between the ion and the 674 nm fiber mode is demonstrated using the electron shelving method [Deh75]. In this scheme, the $^{88}\mathrm{Sr}^+$ ion is driven on the $5\mathrm{S}_{1/2} \leftrightarrow 4\mathrm{D}_{5/2}$ transition by 674 nm light from the fiber, while being simultaneously illuminated by the 422 and 1092 nm beams. Upon shelving to the $4\mathrm{D}_{5/2}$ state, no 422 nm photons are scattered and the ion remains dark until it decays spontaneously back to the $5\mathrm{S}_{1/2}$ state, as illustrated by the single ion telegraph signal in Fig. 6-10. The fiber-ion interaction strength can be quantified in the form of an effective shelving rate by counting the number of bright-to-dark transitions per total bright time. In Fig. 6-11, we show the linear relationship between shelving rate and 674 nm power coupled to the fiber as expected for a weak driving field. The linear proportionality between shelving rate and illumination power justifies the use of the trapped ion as a probe for the local 674 nm intensity.

6.3.2 Imaging of the fiber mode by RF translation

Because of the exponential fall-off in intensity along the transverse plane of a Gaussian mode, a method for *in situ* control of the ion position is highly desired. While DC fields may achieve ion translation, the resultant displacement of the ion from the RF node incurs excess micromotion that broadens atomic transitions [BMB+98], which limits the range and usefulness of DC translation. In the current system, we achieve micromotion-free translation along the y-axis of the trap by using multiple in-phase RF voltages on the ellipse and side electrodes, which effects node translation along $\hat{e}_y + \hat{e}_z$. The exact translation curve is given schematically in Fig. 6-6 and in detail in Fig. 4-8. With an initial height of 670 μm, the intensity variation is dominated by the displacement along y.

Fig. 6-12 shows the change in shelving rate as the ion is translated along the y-axis, across the mode of the fiber. The dashed line represents a Gaussian beam shape indicating good qualitative agreement with the shelving rate profile. The beam waist ($1/e^2$-intensity) at the ion height of 670 μm has been measured independently using an identical fiber to be 50 μm, which is used to calibrate the y-axis in Fig. 6-12 assuming a linear relationship between y-displacement and $\epsilon = V_{\mathrm{side}}/V_{\mathrm{ellipse}}$. We use a linear fit rather than the computed translation curve, due to the deviations in electrode layout between our simulated design and the PCB realization. In units of the measured mode waist, the ion is brought to within

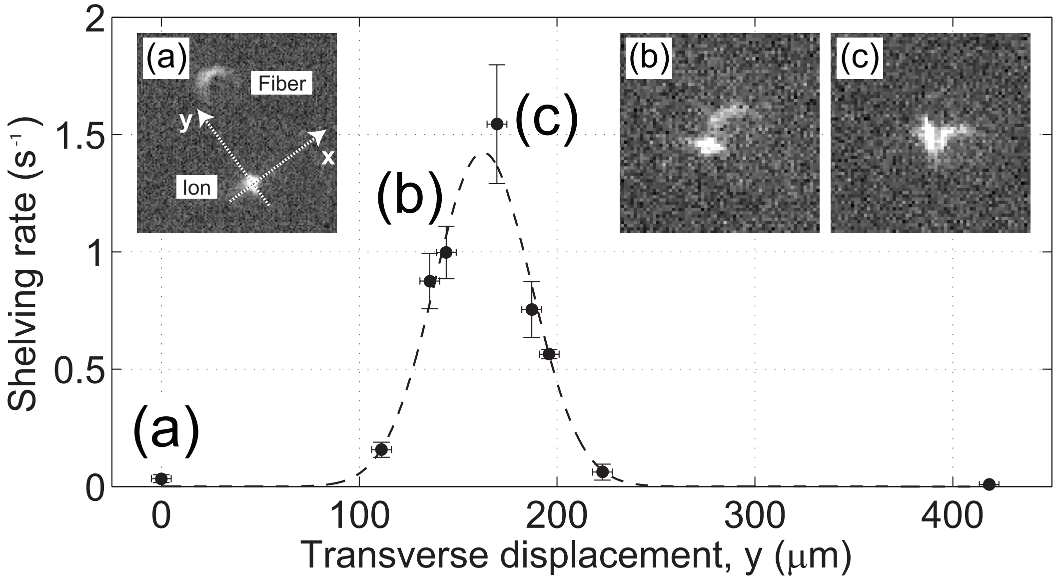

Figure 6-12: Measurement of the mode profile of the integrated fiber using the ion as a probe. The dashed line is a fit to a Gaussian profile showing good qualitative agreement with the expected profile. Calibrating the transverse displacement by an independent measurement of the fiber mode, the initial fiber-ion offset is roughly 160 μm along the y-axis. Images show the relative position of a single ion and an unfocused image of the fiber, where residual ion-fiber offset along $\hat{e}_x$ is evident.

0.13 ± 0.10 of the mode center, despite an initial displacement of 3.34 ± 0.10 arising from trap construction. CCD images show the ion displaced relative to the (unfocused) image of the fiber. In all measurements, the ion was positioned at the RF node by eliminating micromotion amplitude according to the photon correlation technique [BMB$^+$98].

The ultimate precision of RF translation is limited by the stability and control of the relative amplitudes, and phase offsets between the multiple sources. The position uncertainty indicated in Fig. 6-12 is limited by the typical resolution of our imaging system to ±5 μm and is not fundamental to the RF node translation method. The numerical simulation of the ion trajectory under RF errors that was presented in Section 4.3 corresponds to the current scenario of y-axis translation. According to the numerical result, we expect a Doppler-limited ion confinement throughout RF-based translation, based on typical parameters characterizing our passive implementation for two in-phase RF drives (i.e. the capacitive network). In contrast, a DC translation of 160 μm would result in a peak-to-peak micromotion amplitude over 30 μm, which is well beyond the Doppler limit and would be clearly visible given our imaging resolution.

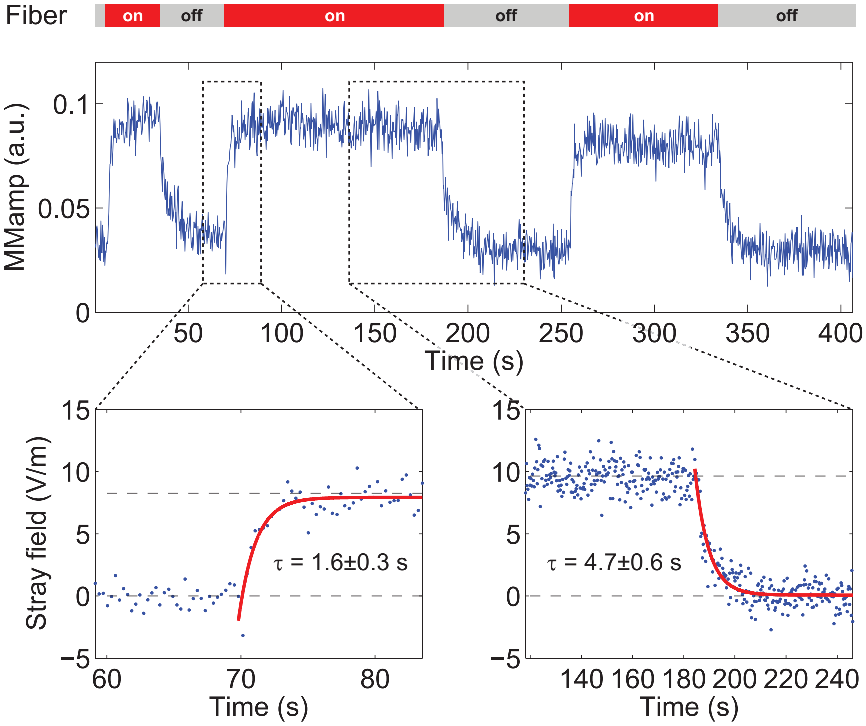

Figure 6-13: Detection of light-induced self-charging of the fiber by ion micromotion. The micromotion amplitude (MMamp) is recorded over several minutes while 125 μW of 674 nm light is coupled to the fiber, revealing a clear correlation between turning on and off of the fiber and ion MMamp. The micromotion amplitude is converted into a stray electric field at the ion location by applying a DC mis-compensation field of known magnitude and noting the change in MMamp. Exponential fits to charging and discharging processes are shown in the two insets. We observe induced fields of $\sim$ 10 V/m by the fiber, with charging and discharging time constants of $\tau = 1.6 \pm 0.3$ s and 4.7 ± 0.6 s respectively. Following initial generation, the MMamp signal remains constant for minutes, indicating stable saturation of fiber-induced charge.

6.3.3 Light-induced self-charging of fiber

The general geometry for fiber integration, where the fiber is embedded in the trap substrate of a surface-electrode trap, minimizes perturbations of the trapping fields by the fiber dielectric. However, given light-induced charging of dielectrics [HBHB10], there is an unavoidable disturbance of the trapping fields as light is coupled to the trap fiber, which leads to self-charging of the fiber core. Given a particular type of fiber and its properties (e.g. step-index, fused-silica core, etc.), light-induced self-charging of the fiber may thus be considered a fundamental limit in trap perturbation introduced by fiber integration.

With the ion centered in the mode (operational point (c) of Fig. 6-12), we looked for evidence of light-induced fiber self-charging. In these tests, 125 μW of 674 nm light is coupled into the fiber while the amplitude of ion micromotion is recorded for several minutes to detect any dynamic shifts in the ion position due to a possible fiber-induced generation of charge. A typical charging run is demonstrated in Fig. 6-13, where ion micromotion amplitude (MMamp) clearly correlates with the turning on and off of the fiber. The MMamp to field strength conversion factor is determined experimentally by applying a known DC mis-compensation field and noting the corresponding change in ion MMamp. Through this calibration, we observe induced fields of $\sim$ 10 V/m by the fiber, with charging and discharging time constants of 1.6 ± 0.3 and 4.7 ± 0.6 s. Following initial generation, the micromotion amplitude remains constant for minutes, indicating stable saturation of fiber-induced charge.

We interpret the charging results as follows: for our typical operating RF parameters and a Mathieu q-parameter of 0.2, an induced field of $\sim$ 10 V/m corresponds to a ion-node displacement of $\sim$ 5 μm and a peak-to-peak micromotion of $\sim$ 1 μm, which are significant disturbances in the context of trapped ion QIP. On the other hand, the timescale of fiber self-charging is many orders of magnitude slower than typical optical π-pulse times ($\sim$ 10 μs). Self-charging of the fiber is therefore not expected to be entirely prohibitive for QIP applications. Nevertheless, the magnitude of fiber self-charging may be mitigated by further elaborations on the fiber-trap design: for example, a coating of transparent electrodes over the fiber facet may help dissipate the light-generated charge, and the use of hollow-core fibers (which propagate optical power through a free-space core) is expected to significantly reduce the charging effect.

6.4 Summary and outlook

In conclusion, we have demonstrated an ion trap with an integrated single-mode fiber for light delivery, and an *in situ* micromotion-free optimization of the ion-fiber spatial overlap. The fiber has been used to directly address the qubit transition of a single ion in the trap and, as such, the fiber-trap system represents a step forward in optics-integration for large-scale QIP in surface-electrode designs. The work is, however, only a first-order demonstration of both fiber-integration and RF translation. Below, we propose a few possible opportunities based on the current work.

6.4.1 Scalable ion-trap technology

One inspiring vision for large-scale quantum computing is based on a planar "CCD" architecture [KMW02], in which hundreds of atomic ions are trapped in a large connected array, and a multitude of laser beams are utilized for ion cooling, detection and qubit manipulation. In the current work, we have demonstrated a trap primitive with an integrated single-mode fiber for site-specific light delivery. On the other hand, we have not entirely removed the use of free-space optical beams, as was seen in Fig. 6-9 where four lasers are delivered radially in addition to a single fiber-delivered qubit beam. However, the fiber-integrated point Paul trap design and the assembly process presented in this chapter are compatible with more advanced fiber systems.

For one example, the commercial availability of "endlessly single-mode" photonic crystal fibers (e.g. NKT Photonics) offers the tantalizing opportunity to develop a variant of the current system in which all relevant $^{88}\mathrm{Sr}^+$ lasers (405, 422, 461, 674, 1033, 1092 nm) for all functions (photoionization, cooling, detection, qubit control) are propagated through a single, wide-bandwidth optical port. Such a system would be the first demonstration of an ion trap for QIP that operates entirely without free-space optical beams, thereby representing a fully integrated node for ion trapping and internal state manipulation in a large trap array. Additionally, in a cryogenic environment, the elimination of the need for optical access greatly reduces the heat load, which may enable sub-Kelvin trap operation in a dilution refrigerator. The pursuit of milli-Kelvin operation could provide insights with regards to the physics of anomalous ion heating and further suppression of decoherence rates [LGA+08] that may assist in the realization of large-scale systems such as the CCD architecture.

Another proposition is to use lensed fibers [Gra08] or microscopic lenses [BEM+11, SNJ+11] that focus the fiber beam at the ion location, and thereby attain higher optical intensities and faster gate times. Given the diffraction limit, however, it is not expected that the lensed fiber will greatly outperform existing free-space systems [BHR+04] that are used for individual qubit addressing in ion chains. On the other hand, because of the steep divergence of strongly focused beams, our axial fiber-integration geometry offers a unique possibility of delivering diffraction-limited intensities to trapped ions in a large surface-electrode chip without having the optical beam obscured by the trap bulk.

At the same time, it is obviously clear that our assembly process does not lend itself to scalable microfabrication. Here, a natural path is to pursue on-chip waveguides – as has been demonstrated in neutral atom chips [KSP$^+$11] – with vertically-oriented output couplers such as waveguide gratings. For this pursuit, our validation of the general geometry for fiber-integration may provide a useful design target.

6.4.2 Towards QIP and novel systems

In addition to scalable trap technologies, there are extensions of the fiber-trap system towards QIP protocols. For instance, there is a natural analogy between the 50 μm-waist Gaussian mode of our single-mode fiber to the 10 μm-scale cavity modes of microfabricated [HWS$^+$11] and fiber-based [HSC$^+$10] optical cavities, which are proposed for achieving single-ion to single-photon qubit transfer in the framework of cavity quantum electrodynamics. An integrated trap that utilizes the fiber facet as one of the mirrors in an optical cavity could serve as a node in a distributed QIP architecture where the photon state can be extracted through the fiber [CZKM97, KK09]. For such pursuits, the demonstration of RF-based, micromotion-free translation for ion-mode modematching will be a crucial technique to achieve optimal alignment of the ion with respect to the cavity mode, as has already been demonstrated in a three-dimensional linear Paul trap for realizing collective strong-coupling between many ions and an optical mode [HDA$^+$09]. Our observation of light-induced self-charging of the fiber may also guide the material design of integrated-cavity systems.

The optical fiber also represents a novel interface for studies involving both ions and neutral atoms – such as those investigating ultracold atom-ion collisions [GCOV09, ZPSK10], sympathetic cooling of the trapped ion by immersion in a superfluid [DFZ04], charge transport [Cot00], etc. – where ions are trapped at one end of a hollow-core fiber, in a system similar to that described here, and neutral atoms are loaded at the other end into the hollow-core and transported by the optical tweezer effect [CWS$^+$08, BHB$^+$09]. An early effort along these lines could focus on the transport of neutral ^{88}Sr through the fiber which are then ionized at the ion trap. Such confined transport of neutral atoms may also offer a clean and integrated mechanism for ion loading [CGC$^+$07] for use in large-scale architectures.

Chapter 7

Outlook

The vision of a quantum network, possible in principle through the simultaneous integration of electronic and optical functionalites in a single microfabricated device, guided my efforts in this work. To this end, the current thesis makes two primary contributions:

1. **A surface-electrode ion trap with an integrated fiber for single-mode light delivery** was demonstrated, which successfully resolves the fundamental difficulties regarding fiber-integration at a single trap node. The demonstration of the integrated design is a foundation for future work in advanced microfabrication methods and the realization of trap arrays and networks for large-scale quantum computing.

2. **The design and implementation of multiple RF drives in a single ion trap** was shown, which achieves *in situ* ion translation without incurring excess micromotion. Our use of this technique to correct a macroscopic 160 μm fabrication error in fiber-ion alignment is a prototype example of how RF-based translation is an enabling tool for integrated trap development, with direct implications for ion-microcavity systems proposed for implementing quantum ion-photon interfaces [HWS$^+$11].

The immediate future work continuing the results of this thesis – such as the microfabrication of the point Paul trap, instrumentation of multiple RF control, the verification of ground-state cooling with multiple RFs, the integration of more advanced fiber systems – have already been outlined throughout the individual chapters. Here, we consider a new direction made possible by our demonstrated ability for arbitrary ion positioning.

The topic of anomalous ion heating, i.e. decoherence of the trapped ion motional state, has attracted significant attention in the trapped-ion QIP community as it represents a

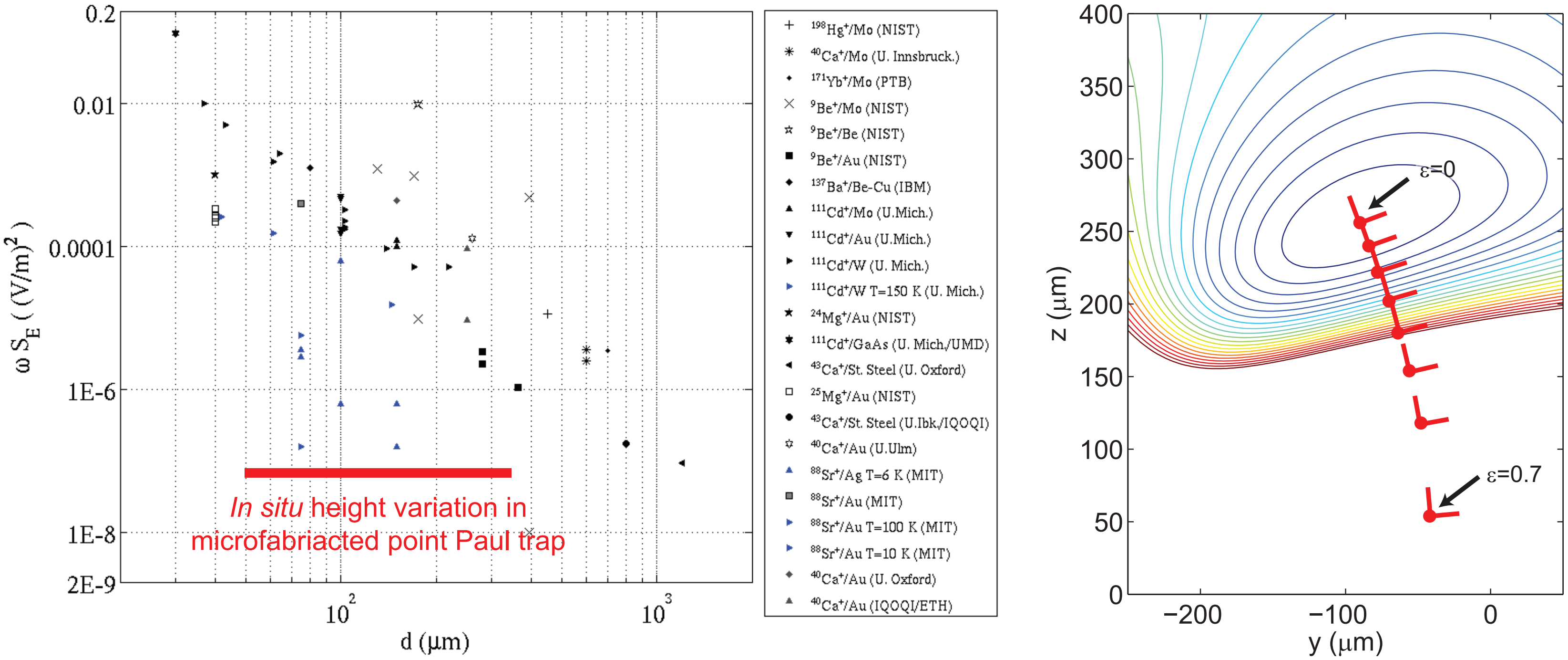

Figure 7-1: The microfabricated point Paul trap as a platform for studying the dependence of anomalous heating on the ion-electrode distance d. [Left] A compilation of heating rates – quantified as field noise spectral density $S_E(\omega)$ – from numerous ion trap samples as presented in Ref. [DNM$^+$11] (with additional references therein). In contrast, the red bar indicates a range of d that is accessible in a *single* microfabricated point Paul trap. Of the measurements taken at room temperature (black markers) the dominant diagonal suggests a d^{-4} scaling law for ion heating, which represents a challenge for the development of large-scale microfabricated quantum processors. [Right] The *in situ* variation in ion height in the microfabricated point Paul trap (currently under development; see Fig. 5-14) under the in-phase regime of dual-RF. This system provides an extremely stringent test of the scaling law, with a predicted variation of the decoherence rate over two orders of magnitude ($5^4 = 625$). The corresponding range is shown in the heating rate plot as a red bar. (Contour lines indicate the pseudopotential at $\epsilon = 0$.)

source of error that limits the performance of QIP systems. Fig. 7-1 shows a compilation of heating rates [DNM$^+$11] in numerous ion trap systems collected in the last twenty years, organized by a characteristic length scale d which is the ion-to-electrode distance. Given the electromagnetic nature of ion perturbation, the decoherence rate is cited in terms of $S_E(\omega)$, the spectral density of electric-field fluctuations at the ion location [TKK$^+$00]. The figure embodies our current empirical understanding of anomalous heating. Based on the subset of measurements taken at room temperature, the prevailing view is that the heating rate scales as d^{-4}, which constrains the various physical models that have been proposed to explain the phenomenon. In this respect, *in situ* RF translation offers a remarkable opportunity to observe the scaling law without being affected by random errors arising from individual trap samples and varying experimental conditions as has been hitherto explored. For example, we show in Fig. 7-1 the height translation curve using the center and ellipse electrodes in the microfabricated point Paul trap currently under development (Fig. 5-14). Our technique of RF-based ion translation may thus enable an ideal platform for elucidating the mechanism underlying anomalous heating.

The study of ion decoherence is fascinating – not only to eventually reduce the effect in the context of large-scale QIP in a $d < 1$ μm microfabricated chip – but also as a source of information on its own right. Here, let me make an analogy to the field of magnetic resonance imaging (MRI). Among its many achievements, the development of MRI has profoundly transformed the practice of medicine and is a basis for today's investigations into the understanding of the human mind. Yet, the fundamental physical mechanism underlying such a far-reaching technology is the measurement of decoherence in an ensemble of hydrogen nuclei in water. Thus, I pose the following questions regarding trapped-ion decoherence:

1. Is there sufficient contrast in the measurement of decoherence as to yield usable and reliable information regarding its sources?

2. Does the physical mechanism provide a unique opportunity to collect that information, or is it obsolete in comparison to existing mechanisms?

3. And lastly, is the information sufficiently interesting as to justify the development efforts for its acquisition?

In the case of MRI, with the luxury of hindsight, these three questions each yield an affirmative response. In addition, the discovery of a beautiful mathematical scheme for encoding spatially-specific contrast information into the free induction decay signal enabled the technology to be fully realized. Further elaborations on such techniques – both physical control and mathematical methods – even allow one to measure the preferred direction of decoherence in space, which has led to the recent development of diffusion-weighted MRI that provides an entirely new layer of information beyond basic tissue-based contrast originally envisioned by the field's pioneers.

I propose to view the investigation of anomalous ion heating as the foundational work for trapped ion-based decoherence tomography. In this context, the *in situ* translation technique developed in this thesis is an rudimentary tool for achieving spatial source selectivity. The ion is translated over a volume, and an "image" of the electromagnetic spectral density is recorded, in analogy to the measurement of the fiber mode performed in this thesis. The volumetric data may then be used to infer knowledge regarding charge dynamics in the vicinity of the ion. We return to the three previously-posed questions:

1. Contrast? Investigations towards understanding the physical mechanism of anomalous heating, especially studies that seek to correlate ion-based measurements to those by established semiconductor methods [Col11, Haf11], is the crucial effort that will address the fundamental question of contrast. The measurement of anomalous heating as a function of ion height in the point Paul trap would be a proof-of-principle demonstration for the feasibility of trapped-ion decoherence tomography.

2. Unique? A trapped ion in the ground-state of a quantum harmonic oscillator represents a physical extreme in the general notion of a sensor.

3. Interesting? Basic questions in science and technology – such as proposed mechanisms of superconductivity and the electrostatic imaging of single or few molecules [PY09] – yield electromagnetic signatures that may lend itself to trapped-ion field tomography.

The prospect of ion decoherence imaging represents a very different kind of "single atom electronics" than the large-scale quantum processors and networks which have occupied the majority of this thesis. Nevertheless, the techniques developed in this work may help generalize the notion of atomic electronics and lead to new methods for acquiring nanoscopic insights.

Bibliography

[Ant11] P. Antohi. *Cryogenic surface electrode ion traps with integrated superconducting microwave resonators for polar molecular ion spectroscopy.* PhD thesis, Massachusetts Institute of Technology, June 2011.

[AS64] M. Abramowitz and I. A. Stegun. *Handbook of Mathematical Functions With Formulas, Graphs, and Mathematical Tables.* National Bureau of Standards, 1964.

[ASA$^+$09] P. B. Antohi, D. Schuster, G. M. Akselrod, J. Labaziewicz, Y. Ge, Z. Lin, W. S. Bakr, and I. L. Chuang. Cryogenic ion trapping systems with surface-electrode traps. *Rev. Sci. Instrum.*, 80:013103, 2009.

[AUW$^+$10] J. Amini, H. Uys, J. H. Wesenberg, S. Seidelin, J. Britton, J. J. Bollinger, D. Leibfried, C. Ospelkaus, A. P. VanDevender, and D. J. Wineland. Toward scalable ion traps for quantum information processing. *New Journal of Physics*, 12:033031, 2010.

[BB84] C. H. Bennett and G. Brassard. Quantum cryptography: Public key distribution and coin tossing. *Proceedings of the IEEE International Conference on Computers, Systems, and Signal Processing*, page 175, 1984.

[BBC$^+$93] C. H. Bennett, G. Brassard, C. Crepeau, R. Jozsa, A. Peres, and W. K. Wootters. Teleporting an unknown quantum state via dual classical and Einstein-Podolsky-Rosen channels. *Phys. Rev. Lett.*, 70:1895–1899, 1993.

[BCL$^+$07] K. R. Brown, R. J. Clark, J. Labaziewicz, P. Richerme, D. R. Leibrandt, and I. L. Chuang. Loading and characterization of a printed-circuit-board atomic ion trap. *Phys. Rev. A*, 75(1):015401, 2007.

[BDCZ98] H.-J. Briegel, W. Dür, J. I. Cirac, and P. Zoller. Quantum repeaters: the role of imperfect local operations in quantum communication. *Phys. Rev. Lett.*, 81:5932–5935, 1998.

[Bel64] J. S. Bell. On the Einstein Podolsky Rosen paradox. *Physics*, 1:195–200, 1964.

[BEM+11] G. R. Brady, A. R. Ellis, D. L. Moehring, D. Stick, C. Highstrete, K. M. Fortier, M. G. Blain, R. A. Haltli, A. A. Cruz-Cabrera, R. D. Briggs, J. R. Wendt, T. R. Carter, S. Samora, and S. A. Kemme. Integration of fluorescence collection optics with a microfabricated surface electrode ion trap. *Applied Physics B-Lasers And Optics*, 103(4):801, 2011.

[Ben73] C. H. Bennett. Logical reversibility of computation. *IBM Journal of Research and Development*, 17:525–532, 1973.

[BHB+09] M. Bajcsy, S. Hofferberth, V. Balic, T. Peyronel, M. Hafezi, A. S. Zibrov, V. Vuletić, and M. D. Lukin. Efficient all-optical switching using slow light within a hollow fiber. *Phys. Rev. Lett.*, 102:203902, 2009.

[BHR+04] R. Blatt, H. Häffner, C. Roos, C. Becher, and F. Schmidt-Kaler. Ion trap quantum computing with Ca^+ ions. *Quantum Information Processing*, 3:61, 2004.

[BLW+07] M. Brownnutt, V. Letchumanan, G. Wilpers, R. C. Thompson, P. Gill, and A. G. Sinclair. Controlled photoionization loading of $^{88}Sr^+$ for precision ion-trap experiments. *Applied Physics B-Lasers And Optics*, 87(3):411–415, May 2007.

[BMB+98] D. J. Berkeland, J. D. Miller, J. C. Bergquist, W. M. Itano, and D. J. Wineland. Minimization of ion micromotion in a paul trap. *Journal Of Applied Physics*, 83(10):5025–5033, May 1998.

[BOC+11] K. R. Brown, C. Ospelkaus, Y. Colombe, A. C. Wilson, D. Leibfried, and D. J. Wineland. Coupled quantized mechanical oscillators. *Nature*, 471:196–199, 2011.

[Bra97] G. Brassard. Searching a quantum phone book. *Science*, 275:627–628, 1997.

[BW08] R. Blatt and D. J. Wineland. Entangled states of trapped atomic ions. *Nature*, 453(7198):1008–1015, June 2008.

[CBB$^+$05] J. Chiaverini, R. B. Blakestad, J. Britton, J. D. Jost, C. Langer, D. Leibfried, R. Ozeri, and D. J. Wineland. Surface-electrode architecture for ion-trap quantum information processing. *Quantum Information & Computation*, 5(6):419–439, September 2005.

[CGC$^+$07] M. Cetina, A. Grier, J. Campbell, I. L. Chuang, and V. Vuletić. Bright source of cold ions for surface-electrode traps. *Phys. Rev. A*, 76(4):041401, October 2007.

[Chi11] J. Chiaverini. Faster quantum operations and control for trapped ions. In *Workshop on Trapped-ion Technology*, Boulder, CO, February 2011.

[Cla09] R. J. Clark. *An Investigation of Precision and Scaling Issues in Nuclear Spin and Trapped-Ion Quantum Simulators*. PhD thesis, Massachusetts Institute of Technology, June 2009.

[CLSZ95] I. L. Chuang, R. Laflamme, P. W. Shor, and W. H. Zurek. Quantum computers, factoring, and decoherence. *Science*, 270:1633–1635, 1995.

[Col11] Y. Colombe. Ion traps for quantum information processing at NIST. In *Workshop on Ion Trap Technology*, Boulder, CO, February 2011.

[Cot00] R. Côté. From classical mobility to hopping conductivity: Charge hopping in an ultracold gas. *Phys. Rev. Lett.*, 85:5316–5319, 2000.

[CS96] A. R. Calderbank and P. W. Shor. Good quantum error-correcting codes exist. *Phys. Rev. A*, 54:1098–1105, 1996.

[CWS$^+$08] C. A. Christensen, S. Will, M. Saba, G. B. Jo, Y. Shin, W. Ketterle, and D. E. Pritchard. Trapping of ultracold atoms in a hollow-core photonic crystal fiber. *Phys. Rev. A*, 78:033429, 2008.

[CZ95] J. I. Cirac and P. Zoller. Quantum computations with cold trapped ions. *Phys. Rev. Lett.*, 74:4091–4094, 1995.

[CZKM97] J. I. Cirac, P. Zoller, H. J. Kimble, and H. Mabuchi. Quantum state transfer and entanglement distribution among distant nodes in a quantum network. *Phys. Rev. Lett.*, 78(16):3221–3224, April 1997.

[Deh67] H. G. Dehmelt. *Radiofrequency spectrocopy of stored ions: I storage*, volume 3 of *Advances in Atomic and Molecular Physics*, pages 53–72. Academic Press, New York, 1967.

[Deh75] H. G. Dehmelt. *Bulletin of the American Physical Society*, 20:60, 1975.

[DFZ04] A. J. Daley, P. O. Fedichev, and P. Zoller. Single-atom cooling by superfluid immersion: A nondestructive method for qubits. *Phys. Rev. A*, 69:022306, 2004.

[DLCZ01] L.-M. Duan, M. D. Lukin, J. I. Cirac, and P. Zoller. Long-distance quantum communication with atomic ensembles and linear optics. *Nature*, 414:413-418, 2001.

[DNM$^+$11] N. Daniilidis, S. Narayanan, S. A. Möller, R. J. Clark, T. E. Lee, P. J. Leek, A. Wallraff, S. Schulz, F. Schmidt-Kaler, and H. Häffner. Fabrication and heating rate study of microscopic surface electrode ion traps. *New Journal of Physics*, 13:013032, 2011.

[DOS$^+$06] L. Deslauriers, S. Olmschenk, D. Stick, W. K. Hensinger, J. Sterk, and C. Monroe. Scaling and suppression of anomalous heating in ion traps. *Phys. Rev. Lett.*, 97(10):103007, September 2006.

[DRB$^+$10] F. Dubin, C. Russo, H. G. Barros, A. Stute, C. Becher, P. O. Schmidt, and R. Blatt. Quantum to classical transition in a single-ion laser. *Nature Physics*, 6:350–353, 2010.

[EPR35] A. Einstein, B. Podolsky, and N. Rosen. Can quantum-mechanical description of physical reality be considered complete? *Physical Review*, 47:777–780, 1935.

[ES90] D. M. Eigler and E. K. Schweizer. Positioning single atoms with a scanning tunneling microscope. *Nature*, 344:524–526, 1990.

[Fis76] J. R. Fisk. Helical resonator design techniques. *QST*, page 11, June 1976.

[Gal67] A. Gallagher. Oscillator strengths of Ca II, Sr II, and Ba II. *Physical Review*, 157:24-30, 1967.

[GCOV09] A. T. Grier, M. Cetina, F. Oručević, and V. Vuletić. Observation of cold collisions between trapped ions and trapped atoms. *Phys. Rev. Lett.*, 102:223201, 2009.

[Geo08] E. M. George. Fiber optic integration in planar ion traps. S.B. thesis, Massachusetts Institute of Technology, June 2008.

[Gho95] P. K. Ghosh. *Ion Traps.* Oxford University Press, New York, 1995.

[GKH$^+$01] G. R. Guthöhrlein, M. Keller, K. Hayasaka, W. Lange, and H. Walther. A single ion as a nanoscopic probe of an optical field. *Nature*, 414(6859):49–51, November 2001.

[Gra08] D. M. Grant. Development of micro-scale ion-traps. Master's thesis, University of Århus, August 2008.

[Gro97] L. K. Grover. Quantum mechanics helps in searching for a needle in a haystack. *Phys. Rev. Lett.*, 79(2):325–328, July 1997.

[GRTZ02] N. Gisin, G. Ribordy, W. Tittel, and H. Zbinden. Quantum cryptography. *Reviews of Modern Physics*, 74:145–195, 2002.

[Haf11] H. Häffner. Trapped ions meet solid state physics. In *Workshop on Ion Trap Technology*, Boulder, CO, February 2011.

[HBHB10] M. Harlander, M. Brownnutt, W. Hänsel, and R. Blatt. Trapped-ion probing of light-induced charging effects on dielectrics. *New Journal of Physics*, 12:093035, 2010.

[HDA$^+$09] P. F. Herskind, A. Dantan, M. Albert, J. P. Marler, and M. Drewsen. Positioning of the rf potential minimum line of a linear paul trap with micrometer precision. *Journal Of Physics B*, 42(15):154008, August 2009.

[HDM$^+$09] P. F. Herskind, A. Dantan, J. P. Marler, M. Albert, and M. Drewsen. Realization of collective strong coupling with ion coulomb crystals in an optical cavity. *Nature Physics*, 5(7):494–498, July 2009.

[HHJ$^+$10] D. Hanneke, J. P. Home, J. D. Jost, J. Amini, D. Leibfried, and D. J. Wineland. Realization of a programmable two-qubit quantum processor. *Nature Physics*, 5:13–16, 2010.

[HLB$^+$11] M. Harlander, R. Lechner, M. Brownnutt, R. Blatt, and W. Hänsel. Trapped-ion antennae for the transmission of quantum information. *Nature*, 471:200–203, 2011.

[Hou08] M. G. House. Analytic model for electrostatic fields in surface-electrode ion traps. *Phys. Rev. A*, 78:033402, 2008.

[HSC$^+$10] D. Hunger, T. Steinmetz, Y. Colombe, C. Deutsch, T. W. Hänsch, and J. Reichel. A fiber fabry-perot cavity with high finesse. *New Journal of Physics*, 12:065038, 2010.

[HWS$^+$11] P. F. Herskind, S. X. Wang, Molu Shi, Y. Ge, M. Cetina, and I. L. Chuang. Microfabricated surface trap for scalable ion-photon interfaces. *Optics Letters*, 36:3045–3047, 2011.

[Jac99] J. D. Jackson. *Classical Electrodynamics*. John Wiley & Sons, Inc., USA, third edition, 1999.

[KBB11] M. Kumph, M. Brownnutt, and R. Blatt. Two-dimensional arrays of radio-frequency ion traps with addressable interactions. *New Journal of Physics*, 13:073043, 2011.

[KHC11] T. H. Kim, P. F. Herskind, and I. L. Chuang. Surface-electrode ion trap with integrated light source. *Applied Physics Letters*, 98:214103, 2011.

[KHK$^+$10] T. H. Kim, P. F. Herskind, T. Kim, J. Kim, and I. L. Chuang. Surface-electrode point paul trap. *Phys. Rev. A*, 82:043412, 2010.

[KK09] J. Kim and C. Kim. Integrated optical approach to trapped ion quantum computation. *Quantum Information & Computation*, 9:0181–0202, 2009.

[KLBK$^+$10] T. Karin, I. Le Bras, A. Kehlberger, K. Singer, N. Daniilidis, and H. Häffner. Transporting particles in three dimensions via adjustable radio frequency fields and its application to scalable quantum information processing. *arXiv:1011.6116v1*, 2010.

[KLH$^+$04] M. Keller, B. Lange, K. Hayasaka, W. Lange, and H. Walther. Continuous generation of single photons with controlled waveform in an ion-trap cavity system. *Nature*, 431(7012):1075–1078, October 2004.

[KMW02] D. Kielpinski, C. Monroe, and D. J. Wineland. Architecture for a large-scale ion-trap quantum computer. *Nature*, 417:709–711, 2002.

[KMWZ95] P. G. Kwiat, K. Mattle, H. Weinfurter, and A. Zeilinger. New high-intensity source of polarization-entangled photon pairs. *Phys. Rev. Lett.*, 75:4337–4341, 1995.

[KPM$^+$05] J. Kim, S. Pau, Z. Ma, H. R. McLellan, J. V. Gates, A. Kornblit, R. E. Slusher, R. M. Jopson, I. Kang, and M. Dinu. System design for large-scale ion trap quantum information processor. *Quantum Information & Computation*, 5(7):515–537, November 2005.

[KSP$^+$11] M. Kohnen, M. Succo, P. G. Petrov, R. A. Nyman, M. Trupke, and E. A. Hinds. An array of integrated atom-photon junctions. *Nature Photonics*, 5:35–38, 2011.

[KWN04] K. Kamiya, B. A. Warner, and T. Numazawa. Geometry dependence of superconducting shielding for sensitive detectors. *IEEE Transactions on Applied Superconductivity*, 14:1042, 2004.

[Lab08] J. Labaziewicz. *High Fidelity Quantum Gates with Ions in Cryogenic Microfabricated Ion Traps*. PhD thesis, Massachusetts Institute of Technology, September 2008.

[LBMW03] D. Leibfried, R. Blatt, C. Monroe, and D. J. Wineland. Quantum dynamics of single trapped ions. *Reviews Of Modern Physics*, 75:281–324, 2003.

[LBW$^+$05] X. Liu, K. H. Brenner, M. Wilzbach, M. Schwarz, T. Fernholz, and J. Schmiedmayer. Fabrication of alignment structures for a fiber resonator by use of deep-ultraviolet lithography. *Applied Optics*, 44:6857–6860, 2005.

[LCL$^+$07] D. Leibrandt, R. J. Clark, J. Labaziewicz, P. Antohi, W. S. Bakr, K. R. Brown, and I. L. Chuang. Laser ablation loading of a surface-electrode trap. *Phys. Rev. A*, 76:055403, 2007.

[Lei09] D. Leibrandt. *Integrated chips and optical cavities for trapped ion quantum information processing.* PhD thesis, Massachusetts Institute of Technology, June 2009.

[LGA$^+$08] J. Labaziewicz, Y. Ge, P. Antohi, D. Leibrandt, K. R. Brown, and I. L. Chuang. Suppression of heating rates in cryogenic surface-electrode ion traps. *Phys. Rev. Lett.*, 100(1):013001, January 2008.

[LJL$^+$10] T. D. Ladd, F. Jelezko, R. Laflamme, Y. Nakamura, C. Monroe, and J. L. O'Brien. Quantum computers. *Nature*, 464:45–53, 2010.

[LLVC09] D. R. Leibrandt, J. Labaziewicz, V. Vuletić, and I. L. Chuang. Cavity sideband cooling of a single trapped ion. *Phys. Rev. Lett.*, 103(10):103001, September 2009.

[LW03] D. A. Lidar and K. B. Whaley. Decoherence-free subspaces and subsystems. *Lecture Notes in Physics*, 622:83–120, 2003.

[LWW$^+$10] L. Lydersen, C. Wiechers, C. Wittmann, D. Elser, J. Skaar, and V. Makarov. Hacking commercial quantum cryptography systems by tailored bright illumination. *Nature Photonics*, 4:686–689, 2010.

[MBH$^+$04] H. S. Margolis, G. P. Barwood, G. Huang, H. A. Klein, S. N. Lea, K. Szymaniec, and P. Gill. Hertz-level measurement of the optical clock frequency in a single $^{88}\mathrm{Sr}^+$. *Science*, 306:1355–1358, 2004.

[MSB$^+$11] T. Monz, P. Schindler, J. T. Barreiro, M. Chwalla, D. Nigg, W. A. Coish, M. Harlander, W. Hänsel, M. Hennrich, and R. Blatt. 14-qubit entanglement: Creation and coherence. *Phys. Rev. Lett.*, 106:130506, 2011.

[MvdS99] H. J. Metcalf and P. van der Straten. *Laser Cooling and Trapping*. Springer, 1999.

[NC00] M. A. Nielsen and I. L. Chuang. *Quantum Computation and Quantum Information*. Cambridge University Press, 2000.

[NIST10] Cryogenics Technologies Group, NIST. Material properties NIST SRD 152. Technical report, National Institute of Standards and Technology, Accessed 2010.

[Pau93] W. Paul. *Electromagnetic Traps for Charged and Neutral Particles. Nobel lectures, Physics 1981-1990.* World Scientific Publishing Co., 1993.

[Pea06] C. E. Pearson. Theory and application of planar ion traps. Master's thesis, Massachusetts Institute of Technology, June 2006.

[Pie88] Robert F. Pierret. *Semiconductor Fundamentals, Volume 1.* Prentice Hall, 1988.

[PLB$^+$06] C. E. Pearson, D. R. Leibrandt, W. S. Bakr, W. J. Mallard, K. R. Brown, and I. L. Chuang. Experimental investigation of planar ion traps. *Phys. Rev. A*, 73(3):032307, March 2006.

[PS53] W. Paul and H. Steinwedel. Ein neues Massenspektrometer ohne Magnetfeld. *Zeitschrift für Naturforschung Section A-A Journal Of Physical Sciences*, 8(7):448–450, 1953.

[PY09] W. P. Putnam and M. F. Yanik. Noninvasive electron microscopy with interaction-free quantum measurements. *Phys. Rev. A*, 80:040902, 2009.

[Roo00] C. Roos. *Controlling the quantum state of trapped ions.* PhD thesis, Leopold-Franzens-Universität Innsbruck, February 2000.

[RSA78] R. Rivest, A. Shamir, and L. Adleman. A method for obtaining digital signatures and public key cryptosystems. *Communications of the ACM*, 21(2):120–126, 1978.

[SCR$^+$06] S. Seidelin, J. Chiaverini, R. Reichel, J. J. Bollinger, D. Leibfried, J. Britton, J. H. Wesenberg, R. B. Blakestad, R. J. Epstein, D. B. Hume, W. M. Itano,

J. D. Jost, C. Langer, R. Ozeri, N. Shiga, and D. J. Wineland. Microfabricated surface-electrode ion trap for scalable quantum information processing. *Phys. Rev. Lett.*, 96(25):253003, June 2006.

[SEHS10] C. Schneider, M. Enderlein, T. Huber, and T. Schaetz. Optical trapping of an ion. *Nature Photonics*, 4:772–775, 2010.

[SGA+05] S. Stahl, F. Galve, J. Alonso, S. Djekic, W. Quint, T. Valenzuela, J. Verdú, M. Vogel, and G. Werth. A planar Penning trap. *Eur. Phys. J. D.*, 32:139–146, 2005.

[Sho94] P. W. Shor. Algorithms for quantum computation: Discrete logarithms and factoring. *Proc. 35nd Annual Symposium on Foundations of Computer Science*, pages 124–134, 1994.

[Sho96] P. W. Shor. Polynomial-time algorithms for prime factorization and discrete logarithms on a quantum computer. *J. Sci. Statisti. Comput.*, 26:1484, 1996.

[SHO+06] D. Stick, W. K. Hensinger, S. Olmschenk, M. J. Madsen, K. Schwab, and C. Monroe. Ion trap in a semiconductor chip. *Nature Physics*, 2(1):36–39, January 2006.

[SKHG+03] F. Schmidt-Kaler, H. Häffner, S. Gulde, M. Riebe, G. Lancaster, T. Deuschle, C. Becher, W. Hänsel, J. Eschner, C. Roos, and R. Blatt. How to realize a universal quantum gate with trapped ions. *Applied Physics B-Lasers And Optics*, 77:78–796, 2003.

[SM99] A. S. Sørensen and K. Mølmer. Quantum computation with ions in thermal motion. *Phys. Rev. Lett.*, 82:1971–1974, 1999.

[SNJ+11] E. W. Streed, B. Norton, A. Jechow, T. J. Weinhold, and D. Kielpinski. Imaging of trapped ions with a microfabricated optic for quantum information processing. *Phys. Rev. Lett.*, 106:010502, 2011.

[SPSW93] C. A. Schrama, E. Peik, W. W. Smith, and H. Walther. Novel miniature ion traps. *Optics Communications*, 101:32, 1993.

[TBZ+98] W. Tittel, J. Brendel, H. Zbinden, and N. Gisin. Violation of Bell inequalities by photons more than 10 km apart. *Phys. Rev. Lett.*, 81:3563, 1998.

[TKK+00] Q. A. Turchette, D. Kielpinski, B. King, D. Leibfried, D. Meekhof, C. J. Myatt, M. A. Rowe, C. A. Sackett, C. S. Wood, W. Itano, C. Monroe, and D. J. Wineland. Heating of trapped ions from the quantum ground state. *Phys. Rev. A*, 61:063418, 2000.

[Tof80] T. Toffoli. Reversible computing. Technical report (MIT/LCS/TM-151), Laboratory for Computer Science, Massachusetts Institute of Technology, 1980.

[VCA+10] A. P. VanDevender, Y. Colombe, J. Amini, D. Leibfried, and D. J. Wineland. Efficient fiber optic detection of trapped ion fluorescence. *Phys. Rev. Lett.*, 105:023001, 2010.

[VSB+01] L. M. K. Vandersypen, M. Steffen, G. Breyta, C. S. Yannoni, M. Sherwood, and I. L. Chuang. Experimental realization of Shor's quantum factoring algorithm using nuclear magnetic resonance. *Nature*, 414:883, 2001.

[WGL+10] S. X. Wang, Y. Ge, J. Labaziewicz, E. Dauler, K. Berggren, and I. L. Chuang. Superconducting microfabricated ion traps. *Applied Physics Letters*, 97:244102, 2010.

[WJS+98] G. Weihs, T. Jennewein, C. Simon, H. Weinfurter, and A. Zeilinger. Violation of Bell's inequality under strict Einstein locality conditions. *Phys. Rev. Lett.*, 81:5039–5043, 1998.

[WMI+98] D. J. Wineland, C. Monroe, W. M. Itano, D. Leibfried, B. E. King, and D. M. Meekhof. Experimental issues in coherent quantum-state manipulation of trapped atomic ions. *Journal of Research of the National Institute of Standards and Technology*, 103:259, 1998.

[WTRW+11] A. Wilson, H. Takahashi, A. Riley-Watson, F. Oručević, P. Blythe, A. Mortensen, D. R. Crick, N. Seymour-Smith, E. Brama, M. Keller, and W. Lange. Fiber-coupled single ion as an efficient quantum light source. *arXiv:1101.5877*, 2011.

[Zae07] F. A. Zähringer. Faseroptische Detektion gespeicherter Calciumionen in einer Mikrofalle. Diplomarbeit, Universität Konstanz, July 2007.

[ZPSK10] C. Zipkes, S. Palzer, C. Sias, and M. Köhl. A trapped single ion inside a Bose-Einstein condensate. *Nature*, 464:388–391, 2010.

Appendix A

Surface-electrode point Paul trap

We present a model as well as experimental results for a surface electrode radiofrequency Paul trap that has a circular electrode geometry well suited for trapping single ions and two-dimensional planar ion crystals. The trap design is compatible with microfabrication and offers a simple method by which the height of the trapped ions above the surface may be changed *in situ*. We demonstrate trapping of single $^{88}\mathrm{Sr}^{+}$ ions over an ion height range of 200-1000 μm for several hours under Doppler laser cooling and use these to characterize the trap, finding good agreement with our model.

PHYSICAL REVIEW A **82**, 043412 (2010)

Surface-electrode point Paul trap

Tony Hyun Kim,[1,*] Peter F. Herskind,[1] Taehyun Kim,[2] Jungsang Kim,[2] and Isaac L. Chuang[1]
[1]*Center for Ultracold Atoms, Department of Physics, Massachusetts Institute of Technology 77 Massachusetts Avenue, Cambridge, Massachusetts 02139, USA*
[2]*Department of Electrical and Computer Engineering, Duke University Durham, North Carolina 27708, USA*

(Received 9 August 2010; published 12 October 2010)

We present a model as well as experimental results for a surface electrode radiofrequency Paul trap that has a circular electrode geometry well suited for trapping single ions and two-dimensional planar ion crystals. The trap design is compatible with microfabrication and offers a simple method by which the height of the trapped ions above the surface may be changed *in situ*. We demonstrate trapping of single $^{88}\mathrm{Sr}^+$ ions over an ion height range of 200–1000 μm for several hours under Doppler laser cooling and use these to characterize the trap, finding good agreement with our model.

DOI: 10.1103/PhysRevA.82.043412 PACS number(s): 37.10.Ty, 03.67.Lx, 37.10.−x

I. INTRODUCTION

Radiofrequency (rf) traps have been applied extensively in a large variety of scientific studies over the past 6 decades. Originating from mass spectrometry [1], they have then been applied in fields such as metrology [2], quantum information science [3,4], and cold molecular physics [5,6], to mention but a few.

Traditionally, such devices have been rather bulky, three-dimensional structures that required precise machining and careful assembly. Recently, however, the four-rod linear Paul trap [see Fig. 1(a)] has been transformed into a two-dimensional structure, with all electrodes in a single plane above which ions can be trapped [7]. This new class of so-called surface traps offer a tremendous advantage over their predecessors in that electrodes can be defined lithographically with extremely high precision and that construction can leverage the techniques of microfabrication, with the possibility of incorporating the technology of Complementary metal-oxide semiconductor (CMOS) for integrated control hardware [8,9]. These aspects are particularly attractive to applications in quantum information processing where limitations currently, by a large degree, pertain to the scalability of devices for trapping as well as certain elements of infrastructure such as optics, laser light delivery, and control electronics.

In this article we study a type of rf surface trap with a high degree of symmetry in its electrode geometry. The generic geometry of this trap, which we shall refer to as the point Paul trap, is shown in Fig. 1(b) and may consist of any number of concentric electrodes of arbitrary widths to which different voltages can be applied. This design originated in a study of surface electrode traps [10,11] but was subsequently strongly inspired by work on planar Penning traps [12], where a similar geometry was used to create a static electric quadrupole field that, when combined with a strong homogeneous magnetic field, gave rise to a confining potential above the surface of the electrodes. The point Paul trap also bears close resemblance to the rf ring and the rf hole traps [13]; however, it differs in that the ion is trapped above the surface of the electrodes as opposed to in between, which makes this geometry better suited for microfabrication.

A consequence of the azimuthal symmetry of the electrodes is that the rf field exhibits a nodal point rather that a nodal line as in the linear Paul trap and that the confining fields originate exclusively from the rf potential, rendering the addition of dc potentials nonessential for anything but the compensation of stray charges on the trap. This makes the point Paul trap well suited for confinement of single ions, which may then reside at the rf nodal point where the amplitude of the rapidly oscillating rf field vanishes.

The ability to fabricate these traps in a scalable fashion makes them attractive for realizing large arrays of single ions in independent traps that may be utilized for a quantum processor, provided the individual ions can be interconnected, e.g., through optical fibers [14–16]. On this aspect, the axial symmetry of the trap lends itself well to integration of such fibers and potentially other optical elements that also possess axial symmetry. The fiber, for instance, may be introduced through the electrodes directly beneath the ions with minimal perturbation of the trapping fields.

Another possible application of this trap is in the field of quantum simulation. While classical computers are unable to efficiently simulate coupled spin systems, such simulations may be implemented using a quantum mechanical system of effective spins, such as a two-dimensional lattice of interacting ions. The resulting potential of the point Paul trap provides ion crystals with exactly the requisite two-dimensional planar structure. As such, the system could be used to simulate, e.g., a frustrated spin system [17,18], as was demonstrated recently [19].

We also find that our trap design is ideally suited for realizing a scheme by which the height of a single trapped ion above the trap surface is varied *in situ*. This capability may prove extremely useful in the search for the origin of anomalous heating in ion traps: a problem currently impeding the advancement of quantum computation with trapped ions [20,21]. It also provides a general technique by which oven contamination of the trap can be minimized by loading further away from the trap surface and subsequently bringing the ion to the desired trap height.

This article is organized as follows: in Sec. II we present a model for the planar point Paul trap, derive analytic expressions for the relevant trapping parameters, present full numerical results of trap optimization, and consider a scheme

---

[*] kimt@mit.edu

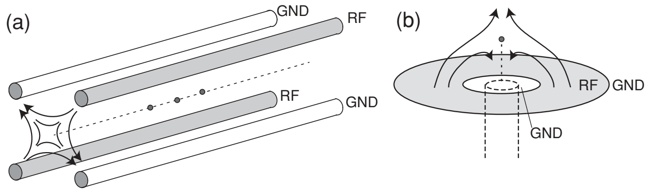

FIG. 1. Comparison of the traditional four-rod linear Paul trap (a) to the point Paul trap (b). The latter achieves quadrupole ion confinement through rf on a single, ring-shaped electrode. Dashed lines suggest how cylindrical elements, such as optical fibers, may be introduced to the point Paul geometry.

for the variation of the ion height above the trap surface. In Sec. III we describe our experimental setup used for the verification of the model; and in Sec. IV we present experimental results for trapping of single and few ions in a printed circuit board (PCB) implementation of the point Paul trap.

II. POINT PAUL TRAP MODEL

We proceed with a general treatment applicable to an arbitrary number of circular electrodes and then focus on a particular geometry that we will study experimentally later in Secs. III and IV. Further theoretical discussion can be found in Refs. [22,23]. At the end of this section we also describe a scheme for variation of the ion height above the trap surface.

A. Potential from annular planar electrodes

We begin with the general solution to the Laplace equation in charge-free space and express this in cylindrical coordinates for $z \geqslant 0$, yielding [24]

$$\Phi(z,\rho,\phi) = \sum_{m=0}^{\infty} \int_0^{\infty} J_m(k\rho) e^{-kz} \times [\mathcal{A}_m(k)\cos(m\phi) + \mathcal{B}_m(k)\sin(m\phi)]\, dk, \quad (1)$$

where $J_m(k\rho)$ are the usual Bessel functions and $\mathcal{A}_m(k)$ and $\mathcal{B}_m(k)$ are coefficients to be determined based on the boundary conditions of the problem. Based on the azimuthal symmetry of Fig. 2, Eq. (1) further simplifies to [24]

$$\Phi(z,\rho) = \int_0^{\infty} J_0(k\rho) e^{-kz} \mathcal{A}_0(k)\, dk. \quad (2)$$

In turn, $\mathcal{A}_0$ can be expressed as $\mathcal{A}_0(k) = \sum_i^n A_i(k)$, where

$$A_i(k) = k \int_{\alpha_i}^{\beta_i} \rho J_0(k\rho) V_i(\rho)\, d\rho. \quad (3)$$

All information about the electrode geometry is now included in the $\mathcal{A}_0$ coefficient, which we have in turn written as a sum of n subcoefficients, each accounting for the effect of a single annular electrode i with inner radius α_i, outer radius β_i and a voltage V_i, which we shall assume is constant across the electrode. The integral of Eq. (3) can be evaluated using the identity for the Bessel functions $\int_0^u v J_0(v) dv = u J_1(u)$ to give

$$A_i(k) = V_i[\beta_i J_1(k\beta_i) - \alpha_i J_1(k\alpha_i)]. \quad (4)$$

This completes the general treatment of the problem: The electric potential above a surface at $z = 0$ with n concentric circular electrodes, each with independent voltages V_i and inner and outer radii of α_i and β_i, respectively, is given by Eq. (2) with $\mathcal{A}_0(k) = \sum_i^n A_i(k)$, where the A_i coefficients are given by Eq. (4).

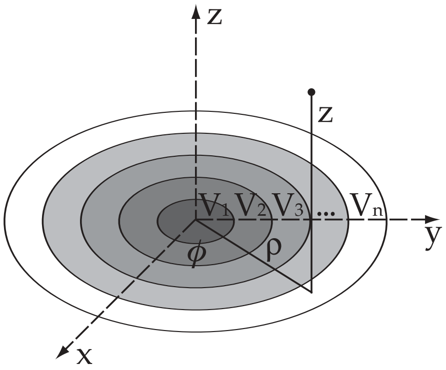

FIG. 2. The generic layout of the point Paul trap, which consists of concentric annular electrodes with arbitrary widths, illustrated in a cylindrical coordinate system.

B. The three-electrode point Paul trap

While static potentials alone may provide confinement in one or two dimensions, Earnshaw's theorem dictates that this is accompanied by a defocusing effect in the orthogonal dimensions. In the work of Ref. [12], three-dimensional confinement was achieved via the addition of a static magnetic field to realize a planar Penning trap. Here, we use a time-varying rf field to achieve charge confinement as a planar Paul trap. Namely, we consider the simple geometry of only three electrodes defined by the following boundary conditions:

$$\Phi(z=0,\rho) = \begin{cases} 0 & \text{for } 0 < \rho < a, \\ V_{\mathrm{rf}}\cos(\Omega_{\mathrm{rf}} t) & \text{for } a \leqslant \rho \leqslant b, \\ 0 & \text{for } b < \rho < \infty, \end{cases} \quad (5)$$

where V_{rf} is the amplitude of the applied voltage and Ω_{rf} is the frequency. The resulting potential then reads

$$\Phi(z,\rho,t) = V_{\mathrm{rf}}\cos(\Omega_{\mathrm{rf}} t)\kappa(z,\rho), \quad (6)$$

where

$$\kappa(z,\rho) = \int_0^{\infty} [bJ_1(kb) - aJ_1(ka)] e^{-kz} J_0(k\rho)\, dk. \quad (7)$$

In general, Eq. (7) has to be solved numerically. However, for the case of $\rho = 0$ the problem simplifies significantly and an analytic solution can be obtained. From the symmetry of the problem we can infer that if a nontrivial field zero ($\vec{E} = 0$) exists for $z > 0$, it will be located on the axis defined by $\rho = 0$ and hence this scenario is worthy of attention.

The on-axis potential is easily integrated to yield:

$$\kappa(z,0) = \frac{1}{\sqrt{1+\left(\frac{a}{z}\right)^2}} - \frac{1}{\sqrt{1+\left(\frac{b}{z}\right)^2}}. \quad (8)$$

Asserting that this potential provides for an electric field null at $z = z_0 > 0$, we expand $\Phi(z,t)$ around this point and use the resulting expansion to find the equation of motion for a particle of mass M and charge Q along the z axis:

$$\begin{aligned}\ddot{z}(t) &= -\frac{Q}{M}\frac{\partial\Phi(z,t)}{\partial z}\\ &\simeq -\frac{QV_{\rm rf}}{M}\cos(\Omega_{\rm rf}t)[f(a,b)(z-z_0)+O(z-z_0)^2]. \end{aligned}\quad (9)$$

Provided $|z - z_0| \ll z_0$, which is a reasonable assumption for a trapped ion, terms of second and higher order can be neglected, and the equation of motion takes the form of the well-known Mathieu equation. With proper rescaling of variables, Eq. (9) can be cast into the standard Mathieu form [25]:

$$\ddot{\tilde{z}}(\tau) + 2q\cos(2\tau)\tilde{z}(\tau) = 0, \quad (10)$$

where we have substituted $\tilde{z} = z - z_0$ and $\tau = \Omega_{\rm rf}t/2$, and the Mathieu q parameter has been defined as

$$q = \frac{2QV_{\rm rf}}{M\Omega_{\rm rf}^2}f(a,b). \quad (11)$$

Here, everything related to the trap geometry is collected into a single function $f(a,b)$ of unit [length]$^{-2}$ given by

$$f(a,b) = \sqrt{\frac{9\left(b^{\frac{2}{3}} - a^{\frac{2}{3}}\right)^2\left(b^{\frac{2}{3}} + a^{\frac{2}{3}}\right)^6}{b^{\frac{4}{3}}a^{\frac{4}{3}}\left(b^{\frac{4}{3}} + b^{\frac{2}{3}}a^{\frac{2}{3}} + a^{\frac{4}{3}}\right)^5}}. \quad (12)$$

Note that in this treatment a denotes the inner radius of the rf electrode and not the Mathieu a parameter, commonly used in the literature on Paul traps. The Mathieu a parameter, which corresponds to the inclusion of a dc potential in the equation of motion [Eq. (9)], is rendered superfluous in the point Paul trap as full three-dimensional confinement is achieved in this geometry by the rf field alone.

When the trap is operated such that $|q| \ll 1$, the equation of motion can be readily solved to yield

$$\tilde{z}(t) = \sigma_0\left[1 - \frac{q}{2}\cos(\Omega_{\rm rf}t)\right]\cos(\omega_z t). \quad (13)$$

This is the usual result, familiar also from the four-rod linear Paul trap, where the motion is composed of two distinct types of motion: a slow, so-called *secular*, motion with an amplitude σ_0 at a frequency

$$\omega_z = \frac{q}{2\sqrt{2}}\Omega_{\rm rf} = \frac{QV_{\rm rf}}{\sqrt{2}M\Omega_{\rm rf}}f(a,b) \quad (14)$$

and a superimposed, fast *micromotion*, with a lower amplitude of $\frac{1}{2}q\sigma_0$ and at sideband frequencies of the rf drive $\Omega_{\rm rf}$. Neglecting the micromotion—a reasonable approximation for $|q| \ll 1$—we can define an approximate harmonic potential that describes the ion motion near the quadrupole zero by the following

$$\Psi(z) = \frac{1}{2}M\omega_z^2(z-z_0)^2 = \frac{Q^2V_{\rm rf}^2}{4M\Omega_{\rm rf}^2}f^2(a,b)(z-z_0)^2, \quad (15)$$

thereby showing the charge-confining capabilities of the three-electrode point Paul trap, provided that $f^2 > 0$.

C. Trap optimization and results

While the harmonic potential of Eq. (15) provides an intuitive connection to the physical, time-averaged motion of the trapped ion in the vicinity of the rf node, it does not reveal any information about the dynamics where the inequality $|z - z_0| \ll z_0$ is not satisfied. For instance, in a real device there is necessarily a finite trapping volume and trap depth. These quantities originate from the shape of the potential significantly beyond the harmonic region. In the limit $q \ll 1$, the effective potential energy beyond the harmonic regime—commonly referred to as the *pseudopotential*—may be expressed directly through the gradient of the electric potential, here written in terms of κ, as [26,27]

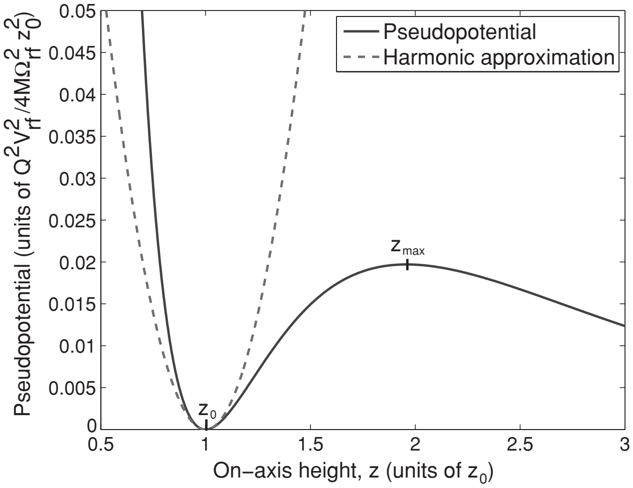

FIG. 3. The harmonic potential approximation [Eq. (15); dashed line] for the point Paul trap is shown on top of the pseudopotential [Eq. (16); solid line]. The latter identifies the trap turn-around point $z_{\rm max}$ in addition to the trap location z_0. Trap geometry (a,b) is chosen as in Table I.

$$\Psi(z,\rho) = \frac{Q^2V_{\rm rf}^2}{4M\Omega_{\rm rf}^2}|\nabla\kappa(z,\rho)|^2. \quad (16)$$

The solid line in Fig. 3 shows the pseudopotential for the planar point Paul trap. Superimposed is the harmonic approximation (dashed line). Inserting the expression for κ from Eq. (7) into the expression for the pseudopotential [Eq. (16)] yields two physically meaningful extrema,

$$z_0 = \sqrt{\frac{b^{4/3}a^{4/3}}{b^{2/3} + a^{2/3}}} \quad (17)$$

and

$$z_{\rm max} = \sqrt{\frac{b^{6/5} - a^{6/5}}{a^{-4/5} - b^{-4/5}}}. \quad (18)$$

Here, z_0 is the coordinate of the pseudopotential minimum, and $z_{\rm max}$ denotes the turning-point of the confining pseudopotential. The difference $z_{\rm max} - z_0$ can be taken as a linear measure of the effective trap volume. Furthermore, the corresponding trap depth can now be defined as $D = \Psi(z_{\rm max}) - \Psi(z_0)$. Using Eqs. (17) and (18), one finds that the trap depth is positive for all values of $b > a > 0$ and is equivalent to:

$$D = \frac{Q^2V_{\rm rf}^2}{4M\Omega_{\rm rf}^2}\left[a^2\left(a^2 + z_{\rm max}^2\right)^{-\frac{3}{2}} - b^2\left(b^2 + z_{\rm max}^2\right)^{-\frac{3}{2}}\right]^2. \quad (19)$$

TABLE I. Results of numerical optimization of the trap depth for a fixed trap height z_0. The choice of units allows for direct comparison with the three-dimensional linear Paul trap.

$a(z_0)$	$b(z_0)$	$z_{\max}(z_0)$	$q(q_{4\text{rod}})$	$D(D_{4\text{rod}})$
0.651679	3.57668	1.957965	0.471565	0.019703

The trap depth is a reasonable quantity to be optimized in the design of the point Paul trap. However, unconstrained optimization of Eq. (19) over (a,b) will influence not only the trap depth but also the trap height z_0 above the surface through Eq. (17). Often in experiments, the trap height is a parameter of importance and so a more reasonable strategy is to optimize the trap depth for a fixed value of z_0. This can in principle be done analytically; however, the results are more useful in their numerical form. Table I summarizes the results of this optimization. For the purpose of comparison with the four-rod linear Paul trap we have defined

$$q_{4\text{rod}} \equiv \frac{2QV_{\text{rf}}}{M\Omega_{\text{rf}}^2 z_0^2} \quad \text{and} \quad D_{4\text{rod}} \equiv \frac{Q^2V_{\text{rf}}^2}{4M\Omega_{\text{rf}}^2 z_0^2}, \tag{20}$$

which corresponds to the q parameter and the trap depth, respectively, for the three-dimensional four-rod Paul trap with an ion-electrode distance of z_0.

From the optimization results of Table I, it is seen that the q parameter of the point Paul trap is roughly a factor $\frac{1}{2}$ of the four-rod linear Paul trap while the trap depth is about a factor $\frac{1}{50}$. By comparison, the surface electrode linear Paul trap design that has recently attracted much attention in the context of quantum computing [28,29] has a q parameter and a trap depth that are approximately a factor $\frac{1}{2\sqrt{3}}$ and $\frac{1}{72}$, respectively, of the four-rod linear Paul trap [7].

D. 3D potential of the point Paul trap

To extract information about the three-dimensional shape of the pseudopotential, we insert the full expression of Eq. (7) into Eq. (16) and integrate numerically at discrete values of ρ and z. This yields a contour plot as shown in Fig. 4, where the trap dimensions are chosen according to Table I for a trap height of $z_0 = 1$ mm. It is seen that the confinement is tighter along the axial direction of the trap than along the radial direction. Also shown (see inset) is the isosurface corresponding to the edge of the trap.

A unique feature of this trap design is that confinement is achieved in three dimensions using only an rf field as opposed to the linear trap designs that also require static dc-potentials along the axis defined by the nodal line of the rf quadrupole field. One consequence of this is that, similar to the four-rod linear Paul trap but in contrast to the linear surface electrode Paul trap, the point Paul trap is naturally compensated and dc potentials are in principle not required for stable trapping.

Another implication of achieving three-dimensional confinement with a single rf field is that the ratio of the axial and radial secular frequencies is fixed by the geometry of the trap. From quadratic fits to the central harmonic region of Fig. 4, the ratio of the radial to the axial trap frequency is found to be $\frac{\omega_\rho}{\omega_z} \simeq 0.50$.

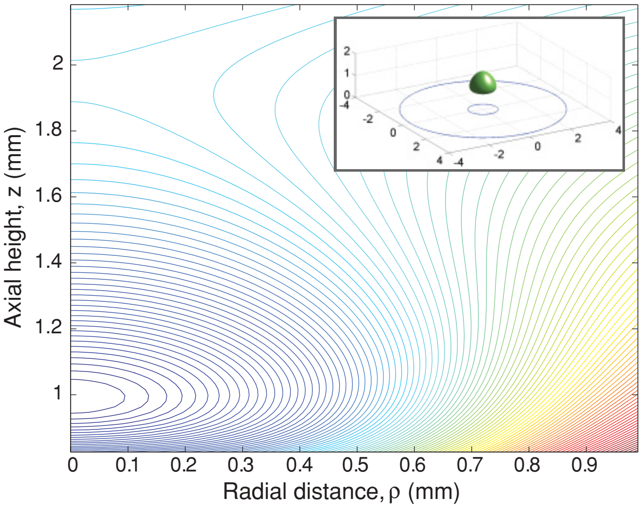

FIG. 4. (Color online) A contour plot for the pseudopotential [Eq. (16)] of a $z_0 = 1$ mm trap, using the optimal geometry of Table I. The inset shows the trap isosurface in relation to outlines of the rf ring electrode (units in z_0).

E. Scheme for variation of the nodal point of the rf field

We mentioned previously that the ion height above the trap surface is often a parameter of interest and designs are generally optimized with some focus on this parameter. Controlling the ion position *in situ* is a desirable capability for a variety of experimental applications. To mention a few examples, in experiments incorporating optical cavities, careful alignment of the cavity with respect to the ion is necessary to achieve the highest possible coupling between the ion and the cavity mode [30–33]; and in the study on anomalous heating in ion traps the ion height is a key parameter, with the scaling of the heating rate currently believed to follow a z_0^{-4} trend [20]. The ion position may be adjusted via the addition of dc potentials; however, unless the rf quadrupole potential is adjusted accordingly, the ion location will not coincide with the zero of the rf field and as a result its motion will be driven by the rapidly changing rf fields, resulting in broadening of the atomic transitions [34]. It is possible to align the trap relative to external objects such as mirrors by physically moving the trap [30,32,33]; however, recently a method for translating the node of the rf quadrupole field has been developed and used both in four-rod Paul traps [35] and in planar surface traps [36,37] to shift the ions without introducing excess micromotion.

The basic principle of this method is to apply different amplitudes of rf potential on individual electrodes, thus causing a shift of the rf field node relative to those electrodes. Implementation of this technique is particularly simple in our geometry where it is achieved by adding an rf field to the central, previously grounded, electrode. The resulting boundary conditions for the electric potential then becomes

$$\Phi(\rho,0) = \begin{cases} \epsilon V_{\text{rf}} \cos(\Omega_{\text{rf}} t + \theta) & \text{for } 0 < \rho < a, \\ V_{\text{rf}} \cos(\Omega_{\text{rf}} t) & \text{for } a \leqslant \rho \leqslant b, \\ 0 & \text{for } b < \rho < \infty, \end{cases} \tag{21}$$

where ϵ and θ accounts for the amplitude and phase difference between the inner and the outer rf electrodes.

Before proceeding to find a solution to the potential in this configuration, it is useful analyze the scenario in qualitative terms to gain some intuition about the influence of this second rf potential:

Along the z axis, the rf field from the outer ring electrode reverses its sign around the quadrupole zero point z_0, while the field from the inner rf electrode is always in the same direction on the z axis, pointing away from the trap surface. If the two electrodes are driven in-phase, their fields will be of opposite sign for $z < z_0$ and the same sign for $z > z_0$. In that case the effect of the second rf field is to decrease the magnitude of the field below the original trap location and increase it above, thus bringing the rf node closer to the electrodes. Similarly, if the two rf electrodes are driven out of phase the trapping point will move away from the electrode surface.

To develop a quantitative model, we again solve the potential for the boundary conditions of Eq. (21) but for the case of either in-phase ($\theta = 0$) or out-of-phase ($\theta = \pi$) drives. The scenario where the two electrodes are related by some other relative phase should be avoided, as it will result in excess micromotion, analogously to the case of the four-rod linear Paul trap [34]. Absorbing the phase into the sign of ϵ, the spatial part of the resulting potential reads

$$\kappa(z,\rho) = \int_0^\infty dk e^{-kz} J_0(k\rho)[bJ_1(kb) - (1-\epsilon)aJ_1(ka)]. \tag{22}$$

We again focus on the case of $\rho = 0$ to find an analytic expression for $\kappa(z,0)$:

$$\kappa(z,0) = \frac{1}{\sqrt{1+\left(\frac{a}{z}\right)^2}} - \frac{1}{\sqrt{1+\left(\frac{b}{z}\right)^2}} + \epsilon\left(1 - \frac{1}{\sqrt{1+\left(\frac{a}{z}\right)^2}}\right), \tag{23}$$

where $\epsilon > 0$ and $\epsilon < 0$ correspond to the in-phase and out-of-phase drives, respectively.

Inserting the expression for $\kappa(z)$ into Eq. (16) and using the geometry of Table I we may plot the pseudopotential for various values of ϵ. Figure 5 shows such example plots for various values of ϵ. It is seen that, in accordance with the qualitative model, the in-phase drive ($\epsilon > 0$) lowers the trap height z_0, while the out-of-phase drive ($\epsilon < 0$) increases the height.

The new trap location and turning point can be found analytically as in Sec. II C, yielding:

$$z_0'(\epsilon) = \sqrt{\frac{b^2a^{4/3}(1-\epsilon)^{2/3} - a^2b^{4/3}}{b^{4/3} - a^{4/3}(1-\epsilon)^{2/3}}} \tag{24}$$

and

$$z_{\max}'(\epsilon) = \sqrt{\frac{b^2a^{4/5}(1-\epsilon)^{2/5} - a^2b^{4/5}}{b^{4/5} - a^{4/5}(1-\epsilon)^{2/5}}}. \tag{25}$$

We also find an expression for the q parameter, which is derived analogously to Eq. (11) using (23):

$$q'(\epsilon) = \frac{2QV_{\rm rf}}{M\Omega_{\rm rf}^2}\left[\frac{3a^2z_0'(1-\epsilon)}{\left(a^2+z_0'^2\right)^{5/2}} - \frac{3b^2z_0'}{\left(b^2+z_0'^2\right)^{5/2}}\right]. \tag{26}$$

In addition to the ion height variation, the presence of a second rf modifies the overall shape of the pseudopotential and hence also the effective trap depth, as evidenced in Fig. 5. Namely, the out-of-phase regime is limited by a diminishing barrier on the side further away from the trap, and the in-phase drive causes a lowering of depth on the side toward the plane. For an optimal $z_0 = 1$ mm trap for ^{88}Sr$^+$, Fig. 6 summarizes the variation in ion height z_0', the Mathieu q' parameter, and overall trap depth D' as a function of ϵ under typical operating parameters. In particular, note the cusp in trap depth at $\epsilon \approx 0.7$, due to the rapidly diminishing trap barrier on the side toward the trap. Conservatively, a range of $0 < \epsilon < 0.7$ leads to a dynamic range of about $0.6z_0 = 600$ μm that is achievable without suffering any decrease in trap depth from the single-rf configuration. Of course, a reduction in the trap depth due to this technique may be compensated by varying the magnitude of the rf voltage and the rf frequency.

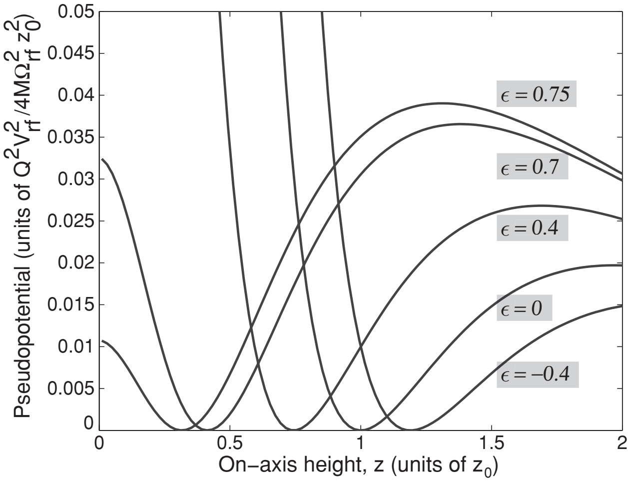

FIG. 5. Variation in the on-axis pseudopotential Ψ with the addition of secondary rf at various values of ϵ. The trap dimensions a and b are as in Table I.

Compared with previous work on shifting the rf nodal line of a four-rod linear Paul trap [35], this range is a significant

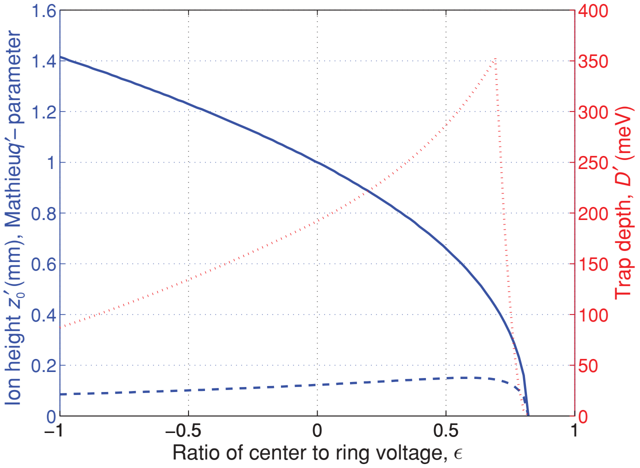

FIG. 6. (Color online) The variation in trap height (solid blue line), Mathieu q parameter (dashed blue line), and the effective trap depth (dotted red line) as a function of the amplitude of the secondary rf. These parameters are computed for an optimal $z_0 = 1$ mm (under single rf) ^{88}Sr$^+$ trap, with $V_{\rm rf} = 300$ V and $\Omega_{\rm rf} = 2\pi \times 8$ MHz.

increase. The underlying reason is that the geometry of the point Paul trap is more favorable for such a scheme in that a shift in the ion height does not change the symmetry of the trap axis with respect to the electrodes, in contrast to the implementation in the four-rod linear Paul trap [35] but similar to recent work on a related surface electrode ion trap [37].

The ability of the point Paul trap to vary the ion height without incurring micromotion would be of tremendous value in the search for the origin of anomalous heating in ion traps [20,21]. Previous work on this problem have either used a technically challenging setup in which the trap electrodes were moved *in situ* [20] or has relied on systematic testing of traps of identical geometry but different scales, making this method prone to random errors associated with the fabrication of the individual traps [21].

Anomalous heating is believed to originate from fluctuating patch potentials on the electrodes. The model describing this effect predicts a scaling of the heating rate of $1/z_0^4$; however, only one experiment has thus far been able to conduct a systematic study to confirm this in a single trap geometry [20]. As the suggested scheme for the point Paul trap in principle allows for *in situ* variation of the ion height by almost an order of magnitude (with modest adjustments in drive rf), it provides for an extremely sensitive test of the patch potential model without complications associated with physically moving the trap electrodes and without the errors and difficulty in obtaining good statistics associated with the use of individual traps for each value of z_0.

III. EXPERIMENTAL SETUP

To validate the model presented in the previous section we have tested a planar point Paul trap with an electrode geometry similar to that of Sec. II B and characterized its trapping of $^{88}\mathrm{Sr}^+$ ions. The trap itself is based on a printed circuit board (PCB) with copper electrodes on a low-rf-loss substrate (Rogers 4350B, fabricated by Hughes circuits) [38]. Figure 7 shows a picture of this trap mounted in a ceramic pin grid array (CPGA) chip carrier. The radius of the inner ground electrode is $a_1 = 550\ \mu$m, the inner radius of the rf ring electrode is $a_2 = 650\ \mu$m, and its outer radius is $b = 3.24$ mm. Due to the 100-μm gap between the electrodes, the ratio $\frac{a_{1,2}}{b}$ deviates by about 10% from the optimum geometry of Table I and produces in an ion height of $z_0 = 960\ \mu$m using a_2.

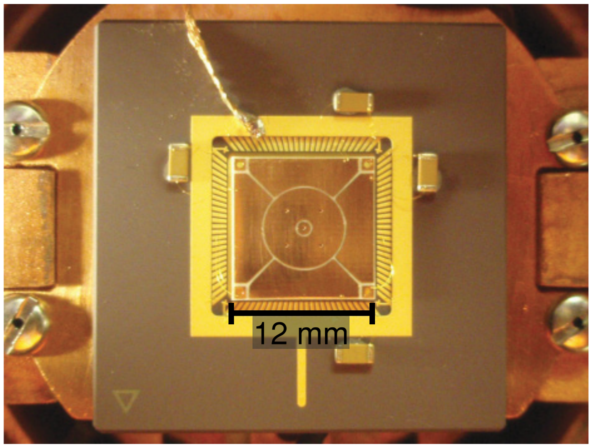

FIG. 7. (Color online) Image of the PCB trap mounted on the CPGA and installed on the 8K base plate of the closed-cycle cryostat. Capacitors are connected to the DC electrodes in order to minimize rf pickup.

In this particular realization of the model system of Fig. 2, the outer ground has been segmented into four electrodes and their independent potentials can each be adjusted to compensate for stray electric fields in the vicinity of the trap. Boundary element analysis of the exact electrode configuration predicts an ion height of 940 μm, in agreement with our analytical model. This analysis also finds the ratio of radial to axial secular frequencies to be $\frac{\omega_\rho}{\omega_z} \simeq 0.50$, again in good agreement with the analytic result.

The trap is mounted on the 8K baseplate of a close-cycle cryostat described in Ref. [39]. Ions are loaded via resonant photoionization of an atomic beam from an effusive oven that is heated resistively to a few hundred degrees Celcius during loading. Once ionized, the ions are Doppler-cooled using light at 422 and 1092 nm. The relevant level scheme is shown in the inset of Fig. 8 along with the lifetimes of the excited states. Typically, 20 μW of 422-nm light focused to a 50-μm waist at the location of the ion is used for the $5\,^2S_{1/2} \leftrightarrow 5\,^2P_{1/2}$ transition, while about 20 μW of 1092 nm focused to a 150-μm waist repumps the ion on the $4\,^2D_{3/2} \leftrightarrow 5\,^2P_{1/2}$ transition. Dark states of the $D_{3/2}$ manifold are destabilized by polarization modulation of the 1092-nm light at 10 MHz as described in Ref. [40]. Fluorescence from the ions is collected with a numerical aperture $\simeq$0.5 lens mounted inside the vacuum chamber and imaged onto a CCD camera (Andor Luca R) and a photomultiplier tube (PMT) (Hamamatsu, H7360-02), the latter achieving an overall detection efficiency (including losses on optics in the imaging system) of 0.6%. We ensure that the ions are located at the nodal point of the rf field by minimizing the micromotion amplitude using the correlation measurement technique as described in Ref. [34].

Radial and axial secular frequencies can be measured by applying a small sinusoidal voltage to a DC electrode, thus

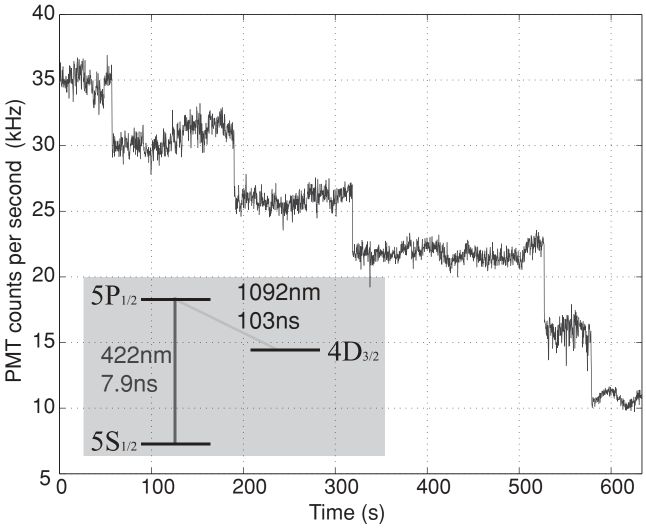

FIG. 8. Telegraph log shows the discrete loss of five ions from the PCB trap, as measured by scattered 422-nm light from the $5\,^2S_{1/2} \leftrightarrow 5\,^2P_{1/2}$ transition (see inset).

exciting motion along the corresponding direction [41]. At the resonant frequency of the trap, the strong increase in the amplitude of this driven motion is detected as a sudden change in the fluorescence from the ion and can also be corroborated by increased motion along an axis by the imaging system. Depending on the trap depth, amplitude of the perturbative signal, and the sweep rate, this allows a measurement of the secular frequencies with a typical accuracy of about ±5 kHz.

Finally, the shift in ion height with the addition of a second rf drive is determined by the translation of the Doppler cooling beam necessary in order to maximize ion fluorescence. The spatial position of the beam is calibrated by a digital translation stage with submicron resolution. However, the accuracy of this method is ultimately limited by the finite waist of the laser beams.

IV. RESULTS

The purpose of this section is to validate the model presented in Sec. II. Figure 8 shows a time log of the fluorescence signal detected with the PMT as five ions are loaded and then lost from the trap. This rapid ion loss was observed prior to compensation of the stray dc fields and optimization of Doppler cooling. The discrete steps in photon counts provides a calibration of the scale to distinguish a single ion from two or more. Once compensation is optimized, we find that the trapping is stable for several hours when Doppler cooling is applied, limited only by the long-term stability of our lasers.

In addition to the discrete PMT logs, we have been able to resolve individual ions in 2D crystals involving up to nine ions, which is summarized in Fig. 9. As noted in the introduction, such lattices could be used for quantum simulations of, for instance, frustrated spin systems [18,19]. The effect of micromotion in planar crystals on quantum simulations has been considered in Ref. [42].

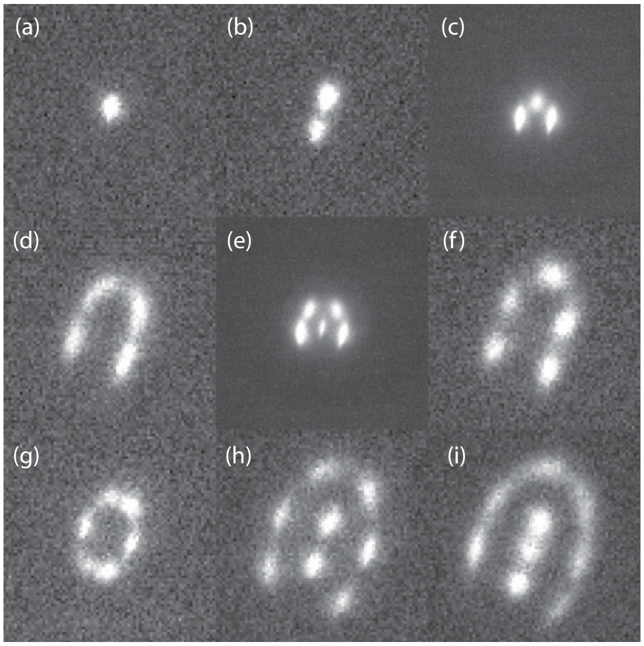

FIG. 9. Summary of the ion crystals that were observed with the PCB trap. The crystals in panels (c) and (e) were observed at an ion height of 940 μm ($V_{\mathrm{rf}} = 360$ V, 10-s exposure) where the panel's field of view is 70 × 70 μm. The remaining crystals were observed at a height of about 600 μm ($V_{\mathrm{rf}} = 275$ V, $\epsilon \simeq 0.52$, 500-ms exposure) where each panel corresponds to approximately 40 × 40 μm.

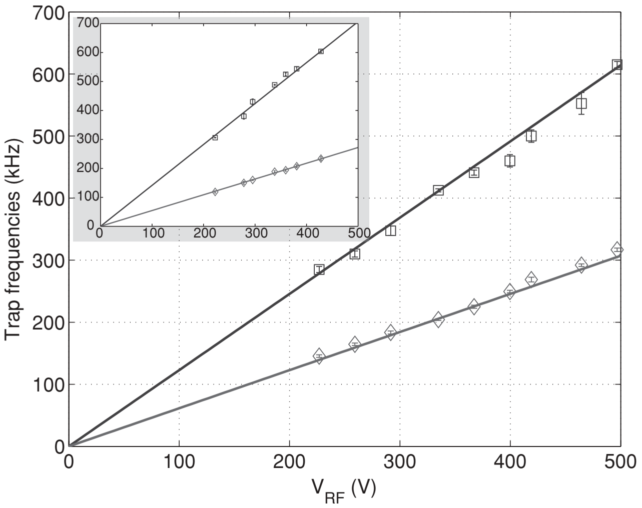

FIG. 10. Measurements of axial (square markers) and radial (diamond markers) secular frequencies of the point Paul trap. Data were taken at $z_0 = 940$ μm under the single-rf drive at $\Omega_{\mathrm{rf}} = 2\pi \times 8.07$ MHz. Also shown are theoretically expected secular frequencies (not fits) according to Eq. (14). (Inset) Measured axial (squares) and radial (diamonds) trap frequencies and their linear fits at an ion height of 600 μm (same units as main figure).

The pseudopotential model for the point Paul trap is evaluated by measuring the secular frequencies of the trap for various applied rf voltages V_{rf} at a constant rf drive frequency of $\Omega_{\mathrm{rf}} = 2\pi \times 8.07$ MHz. The results are shown in Fig. 10 for a single ion held at 940 μm (using the numerical result) under the single-rf scheme. Solid lines are the theoretically expected trap frequencies (not fits) according to the model of Sec. II, where the rf voltage has been calibrated independently by characterizing the driving helical resonator. Fits through the measured data yields a ratio of the radial to axial secular frequencies of $\frac{\omega_\rho}{\omega_z} = 0.51 \pm 0.01$, in excellent agreement with the numerically predicted $\frac{\omega_\rho}{\omega_z} = 0.50$.

To establish the validity of the ion height variation model, we have explored the in-phase ($\epsilon > 0$) parameter space. The implementation of a second in-phase drive was achieved by connecting a trim capacitor between the ring and center electrodes, which then formed a capacitive divider for the center electrode in combination with the intrinsic capacitance from the PCB. Figure 11 shows the results. Experimentally, we found that stable trapping was extremely straightforward to achieve, and single ions and crystals were trapped as close as 200 μm from the surface of the trap. Further approach was prevented by scattering the incident laser beams from the trap surface, which interfered with ion detection.

In addition, we were also able to measure secular frequencies when the ion was offset to a height of 600 μm, as shown in the inset of Fig. 10. The comparable linearity in secular frequencies between the single- and dual-rf cases—as well as the well-resolved ions of Fig. 9 at an offset height—suggests that the addition of a secondary rf has not

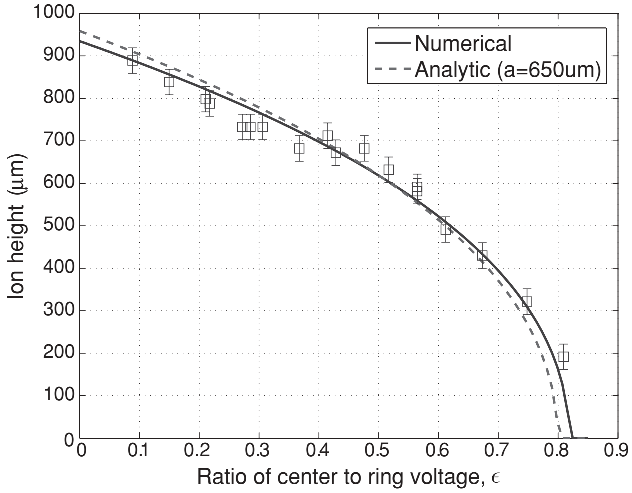

FIG. 11. Variation in ion height with the addition of the second rf on the innermost electrode. Solid curve shows the results of the numerical boundary element analysis, while the dashed curve shows the height as predicted by Eq. (25).

added significant micromotion. The measured ratio of radial to axial secular frequencies was $\frac{\omega_\rho}{\omega_z} = 0.38 \pm 0.01$, which deviates significantly from the expected 0.50 (according to the model, the ratio remains unaffected by the addition of the second rf). Possible sources for deviation from the ideal model include the dc potentials, which were added to ensure a well-compensated trap but which could have shifted secular frequencies. In particular, as the ion is brought closer to the trap surface, it is more susceptible to the effects of dc potentials. Such fields may also break the degeneracy of the radial modes. We have, in fact, observed such separate radial modes, although in the case of the data in Fig. 10, they were only separated by about 20 kHz, and thus average radial values are presented in that figure. We have numerically confirmed that the trap's dc potentials yield simultaneously a splitting of 20 kHz in the radial modes and a modified secular frequency ratio of 0.40.

V. CONCLUSIONS

We have presented an analytic model of a circularly symmetric rf surface trap and its experimental validation. This particular geometry offers several advantages for further investigations in quantum information processing. First, the shape of the resulting potential leads to confinement of 2D ion crystals, which may be used as a platform for quantum simulation of interacting spins. Second, because the confinement is achieved through the ring electrode alone, the trap permits a straightforward scheme for variation of ion height *in situ*. In this work, we have demonstrated almost an ion height variation over 200–1000 μm, which may then, for instance, be used for a stringent test of the supposed z_0^{-4} scaling in anomalous ion heating. Finally, the axial symmetry of the trap lends itself to natural integration with optical fibers. Such a device, in turn, could serve as nodes in a quantum network or provide an interface medium between ions and cold neutral atoms.

ACKNOWLEDGMENTS

This work was supported by NSF CUA, and the COMMIT project funded by the ARO. T.H.K. was supported by the Siebel Scholar Foundation. P.F.H. is grateful for the support from The Carlsberg Foundation and the Lundbeck Foundation.

---

[1] W. Paul and H. Steinwedel, Z. Naturforsch. A **8**, 448 (1953).
[2] T. Rosenband *et al.*, Science **319**, 1808 (2008).
[3] M. A. Nielsen and I. L. Chuang, *Quantum Computation and Quantum Information* (Cambridge University Press, Cambridge, UK, 2000).
[4] R. Blatt and D. Wineland, Nature **453**, 1008 (2008).
[5] P. F. Staanum, K. Hojbjerre, P. S. Skyt, A. K. Hansen, and M. Drewsen, Nat. Phys. **6**, 271 (2010).
[6] T. Schneider, B. Roth, H. Duncker, I. Ernsting, and S. Schiller, Nat. Phys. **6**, 275 (2010).
[7] J. Chiaverini, R. B. Blakestad, J. Britton, J. D. Jost, C. Langer, D. Leibfried, R. Ozeri, and D. J. Wineland, Quantum Inf. Comput. **5**, 419 (2005).
[8] J. Kim, S. Pau, Z. Ma, H. R. McLellan, J. V. Gates, A. Kornblit, R. E. Slusher, R. M. Jopson, I. Kang, and M. Dinu, Quantum Inf. Comput. **5**, 515 (2005).
[9] D. R. Leibrandt *et al.*, Quantum Inf. Comput. **9**, 901 (2009).
[10] C. E. Pearson, D. R. Leibrandt, W. S. Bakr, W. J. Mallard, K. R. Brown, and I. L. Chuang, Phys. Rev. A **73**, 032307 (2006).
[11] C. E. Pearson, master's thesis, Massachusetts Institute of Technology, 2006.
[12] S. Stahl, F. Galve, J. Alonso, S. Djekic, W. Quint, T. Valenzuela, J. Verdu, M. Vogel, and G. Werth, Eur. Phys. J. D **32**, 139 (2005).
[13] R. G. Brewer, R. G. DeVoe, and R. Kallenbach, Phys. Rev. A **46**, R6781 (1992).
[14] R. Schmied, J. H. Wesenberg, and D. Leibfried, Phys. Rev. Lett. **102**, 233002 (2009).
[15] S. Olmschenk, D. N. Matsukevich, P. Maunz, D. Hayes, L.-M. Duan, and C. Monroe, Science **323**, 486 (2009).
[16] L.-M. Duan and C. Monroe, Rev. Mod. Phys. **82**, 1209 (2010).
[17] D. Porras and J. I. Cirac, Phys. Rev. Lett. **92**, 207901 (2004).
[18] R. J. Clark, T. Lin, K. R. Brown, and I. L. Chuang, J. Appl. Phys. **105**, 013114 (2009).
[19] K. Kim, M.-S. Chang, S. Korenblit, R. Islam, E. E. Edwards, J. Freericks, G.-D. Lin, L. Duan, and C. Monroe, Nature **465**, 590 (2010).
[20] L. Deslauriers, S. Olmschenk, D. Stick, W. K. Hensinger, J. Sterk, and C. Monroe, Phys. Rev. Lett. **97**, 103007 (2006).
[21] J. Labaziewicz, Y. F. Ge, P. Antohi, D. Leibrandt, K. R. Brown, and I. L. Chuang, Phys. Rev. Lett. **100**, 013001 (2008).
[22] J. H. Wesenberg, Phys. Rev. A **78**, 063410 (2008).
[23] R. Schmied, New J. Phys. **12**, 023038 (2010).
[24] J. Jackson, *Classical Electrodynamics*, 3rd ed. (John Wiley & Sons, New York, 1999).
[25] M. Abramowitz and I. A. Stegun, *Handbook of Mathematical Functions with Formulas, Graphs, and Mathematical Tables* (National Bureau of Standards, Washington, DC, 1964).
[26] H. G. Dehmelt, *Radiofrequency Spectroscopy of Stored Ions I: Storage* (Academic Press, New York, 1967), pp. 53–72.

[27] P. K. Ghosh, *Ion Traps* (Oxford University Press, New York, 1995).
[28] S. Seidelin *et al.*, Phys. Rev. Lett. **96**, 253003 (2006).
[29] S. X. Wang, J. Labaziewicz, Y. Ge, R. Shewmon, and I. L. Chuang, Phys. Rev. A **81**, 062332 (2010).
[30] M. Keller, B. Lange, K. Hayasaka, W. Lange, and H. Walther, Nature **431**, 1075 (2004).
[31] P. F. Herskind, A. Dantan, J. P. Marler, M. Albert, and M. Drewsen, Nature Physics **5**, 494 (2009).
[32] D. R. Leibrandt, J. Labaziewicz, V. Vuletic, and I. L. Chuang, Phys. Rev. Lett. **103**, 103001 (2009).
[33] F. Dubin, C. Russo, H. G. Barros, A. Stute, C. Becher, P. O. Schmidt, and R. Blatt, Nat. Phys. **6**, 350 (2010).
[34] D. J. Berkeland, J. D. Miller, J. C. Bergquist, W. M. Itano, and D. J. Wineland, J. Appl. Phys. **83**, 5025 (1998).
[35] P. F. Herskind, A. Dantan, M. Albert, J. P. Marler, and M. Drewsen, J. Phys. B **42**, 154008 (2009).
[36] M. Cetina, A. Grier, J. Campbell, I. Chuang, and V. Vuletic, Phys. Rev. A **76**, 041401 (2007).
[37] A. P. VanDevender, Y. Colombe, J. Amini, D. Leibfried, and D. J. Wineland, Phys. Rev. Lett. **105**, 023001 (2010).
[38] K. R. Brown, R. J. Clark, J. Labaziewicz, P. Richerme, D. R. Leibrandt, and I. L. Chuang, Phys. Rev. A **75**, 015401 (2007).
[39] P. B. Antohi, D. Schuster, G. M. Akselrod, J. Labaziewicz, Y. Ge, Z. Lin, W. S. Bakr, and I. L. Chuang, Rev. Sci. Instrum. **80**, 013103 (2009).
[40] D. J. Berkeland and M. G. Boshier, Phys. Rev. A **65**, 033413 (2002).
[41] H. Naegerl, R. Blatt, J. Eschner, F. Schmidt-Kaler, and D. Leibfried, Opt. Express **3**, 89 (1998).
[42] R. J. Clark, Ph.D. thesis, Massachusetts Institute of Technology, 2009.

Appendix B

Surface-electrode ion trap with integrated light source

An atomic ion is trapped at the tip of a single-mode optical fiber in a cryogenic (8 K) surface-electrode ion trap. The fiber serves as an integrated source of laser light, which drives the quadrupole qubit transition of $^{88}\mathrm{Sr}^{+}$. Through *in situ* translation of the nodal point of the trapping field, the Gaussian beam profile of the fiber output is imaged, and the fiber-ion displacement, in units of mode waist at the ion, is optimized to within 0.13 ± 0.10 of the mode center despite an initial offset of 3.30 ± 0.10. Fiber-induced charging by 125 μW of 674 nm light is observed to be $\sim$ 10 V/m at an ion height of 670 μm, with charging and discharging time constants of 1.6 ± 0.3 s and 4.7 ± 0.6 s, respectively. This work is of importance to large-scale, ion-based quantum information processing, where optics integration in surface-electrode designs may be a crucial enabling technology.

APPLIED PHYSICS LETTERS **98**, 214103 (2011)

Surface-electrode ion trap with integrated light source

Tony Hyun Kim,[a] Peter F. Herskind, and Isaac L. Chuang
Department of Physics, Center for Ultracold Atoms, Massachusetts Institute of Technology, 77 Massachusetts Avenue, Cambridge, Massachusetts 02139, USA

(Received 25 March 2011; accepted 3 May 2011; published online 27 May 2011)

An atomic ion is trapped at the tip of a single-mode optical fiber in a cryogenic (8 K) surface-electrode ion trap. The fiber serves as an integrated source of laser light, which drives the quadrupole qubit transition of $^{88}\mathrm{Sr}^{+}$. Through *in situ* translation of the nodal point of the trapping field, the Gaussian beam profile of the fiber output is imaged, and the fiber-ion displacement, in units of the mode waist at the ion, is optimized to within 0.13 ± 0.10 of the mode center despite an initial offset of 3.30 ± 0.10. Fiber-induced charging by 125 μW of 674 nm light is observed to be ~ 10 V/m at an ion height of 670 μm, with charging and discharging time constants of 1.6 ± 0.3 s and 4.7 ± 0.6 s, respectively. This work is of importance to large-scale, ion-based quantum information processing, where optics integration in surface-electrode designs may be a crucial enabling technology. © *2011 American Institute of Physics*. [doi:10.1063/1.3593496]

An array of trapped ions in optical cavities, connected by a network of optical fibers, represents a possible distributed architecture for large-scale quantum information processing[1] (QIP). Due to the necessity of efficient light collection, laser cooling and qubit state manipulation, the realization of a quantum network or processor at the level of tens and hundreds of qubits strongly motivates the integration of optics in surface-electrode ion traps.[2] However, the potential benefits of integrated optics have long been overshadowed by the challenge of trapping ions in the proximity of dielectrics,[3] as well as the difficulty of guaranteeing good spatial overlap of the trapped ion with the field mode of the integrated element.

In the past, there have been demonstrations of integration of bulk mirrors,[4–6] multimode (MM) optical fibers,[7] and phase-Fresnel lenses[8] into radio frequency (rf) traps with three-dimensional electrodes. More recently, integration of MM fibers[9,10] and microscopic reflective optics[11] for collection of ion fluorescence has been demonstrated in microfabricated surface-electrode traps. Complementing such efforts on light collection, the present work demonstrates light delivery through an integrated single-mode (SM) fiber in a scalable, surface-electrode design, and an *in situ* micrometer-scale positioning of the ion relative to the integrated structure. Future developments in optics integration, such as microcavities for the realization of quantum light-matter interfaces,[1,12] or lensed fibers for faster gate times and optical trapping of ions,[13] will employ sub-10 μm waists,[11] underscoring the importance of *in situ* ion positioning.[14]

We report on the construction of a fiber-trap system, and demonstrate the ability of the integrated light source to drive the 674 nm quadrupole transition of $^{88}\mathrm{Sr}^{+}$. The 674 nm transition is of particular interest in QIP with trapped ions, where it serves as the optical qubit,[15] as well as in metrology, where it constitutes an optical frequency standard.[16] The ion-fiber spatial overlap is optimized *in situ* by micromotion-free translation of the ion using segmented rf electrodes. We use this technique to map out the Gaussian profile of the fiber mode along a single transverse axis. With the ion over the center of the mode, we quantify the magnitude and timescale of fiber-induced charging.

Fiber-trap integration is achieved by embedding the fiber within the trap substrate. Figure 1(a) shows a schematic of the ion trap design, which is a modified version of the surface-electrode point Paul trap described recently.[17] The center, grounded electrode has a diameter of 1.1 mm. The elliptical rf pad has major- and minor-axis diameters of 5.9 mm and 2.8 mm, respectively, and is shifted by 500 μm along the minor-axis relative to the center of the ground electrode. Electrode gaps are 100 μm. This design achieves an ion height of 670 μm and the electrode asymmetries uniquely define the principal axes of the trap, which are tilted by 30° in the yz-plane for achieving projection of the cooling

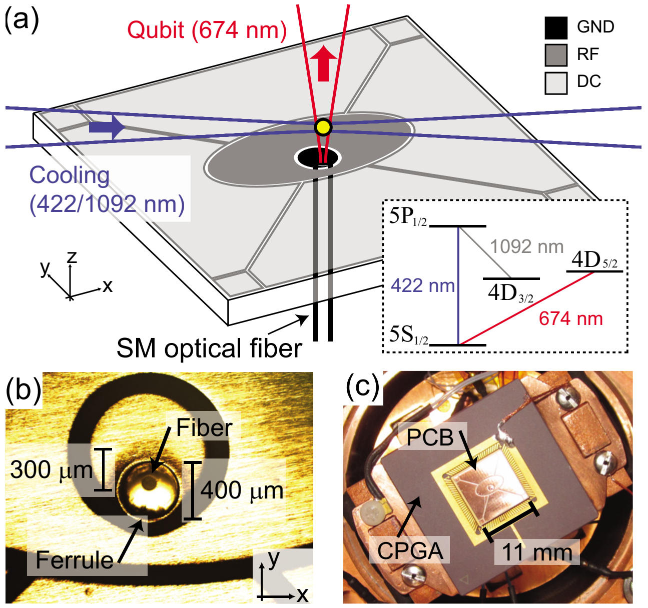

FIG. 1. (Color online) (a) Schematic of the surface-electrode ion trap with integrated optical fiber. The $^{88}\mathrm{Sr}^{+}$ qubit laser is delivered axially (along z) through the fiber, while Doppler cooling beams propagate horizontally along $\vec{e}_x - \vec{e}_y$. (b) Alignment of the optical ferrule with respect to the trap electrodes. The ferrule is rotated until the fiber is aligned with the minor-axis of the trap. (c) Fiber-trap system mounted on a CPGA and installed on the 8 K basplate of a closed-cycle cryostat.

---

[a] Electronic mail: kimt@mit.edu.

0003-6951/2011/98(21)/214103/3/$30.00

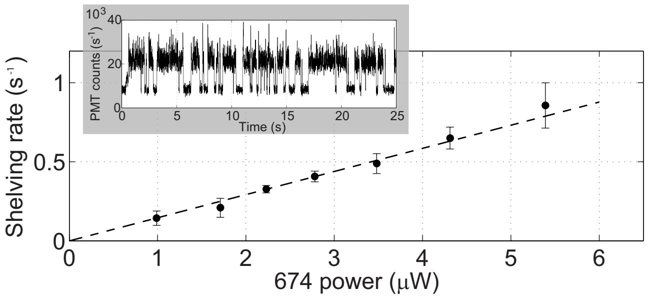

FIG. 2. Shelving rate as a function of 674 nm power coupled to the trap fiber. Inset: telegraph log of a single ion as it is shelved into the dark 4D$_{5/2}$ state by 5.4 μW of fiber light.

beam on all principal axes. The side electrodes are used for dc compensation of stray electric fields, as well as radial translation of the rf node by use of additional rf voltages, as discussed later, and shown in Fig. 3. The trap is defined on a printed circuit board (PCB) with copper electrodes on a low-rf-loss substrate (Rogers 4350B, fabricated by Hughes circuits). The PCB includes a 400 μm diameter plated via in the center ground electrode for the insertion of an optical ferrule. The via is offset by 300 μm with respect to the ground electrode to account for the displacement of the trapping point that accompanies the shift in the elliptical rf electrode.

The optical fiber (OZ Optics, PMF-633-4/125-3-L) is SM for 674 nm and is conventionally prepared (i.e., cured in fiber epoxy and flat-polished) in a stainless steel optical ferrule (Thorlabs, 10125A) whose tip has been machined to match the 400 μm diameter of the PCB via. Assembly of PCB and ferrule is performed under a microscope, as in Fig. 1(b), where machining imprecision of the ferrule is evident in the form of ~100 μm nonconcentricity between the fiber and the ferrule. The ferrule is rotated with respect to the PCB to place the fiber roughly along the minor-axis of the trap, and is cured using cyanoacrylate adhesive.

The fiber-trap system is installed on a ceramic pin grid array (CPGA) and mounted on the 8 K baseplate of a closed-cycle cryostat[18] as shown in Fig. 1(c). The fiber is routed through a hole in the CPGA and a hole in a flange of the vacuum chamber, where it is sealed in place with TorrSeal UHV epoxy. The trap is operated at a typical rf frequency of $2\pi\times 6$ MHz and 250 Vpp amplitude, achieving secular frequencies of $\omega_{z'}=2\pi\times 410$ kHz, $\omega_x=2\pi\times 240$ kHz, and $\omega_{y'}=2\pi\times 170$ kHz. We produce ^{88}Sr$^+$ ions by resonant photoionization,[19] which are Doppler cooled on the 5S$_{1/2}\leftrightarrow$5P$_{1/2}$ transition at 422 nm, while simultaneously driving the 4D$_{3/2}\leftrightarrow$5P$_{1/2}$ transition at 1092 nm [see Fig. 1(a)]. Ion fluorescence at 422 nm is collected by a 0.5 NA lens inside the chamber and imaged onto a charge coupled device (CCD) camera and a photomultiplier tube.

Interaction between the ion and the fiber mode is demonstrated using the electron shelving method.[20] The ion is driven on the 5S$_{1/2}\leftrightarrow$4D$_{5/2}$ transition by 674 nm light from the fiber while being simultaneously illuminated by the 422 and 1092 nm beams. Upon shelving to the 4D$_{5/2}$ state, no 422 nm photons are scattered and the ion remains dark until it decays spontaneously back to the 5S$_{1/2}$ state, as illustrated by the single ion telegraph in the inset of Fig. 2. An effective shelving rate can be quantified by counting the bright-to-dark transitions per total bright time. In Fig. 2, the linear relationship between shelving rate and 674 nm power coupled to the fiber is shown, as expected for a weak driving field.

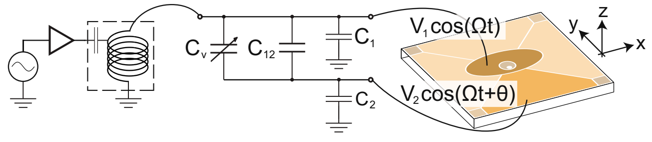

FIG. 3. (Color online) A circuit model for implementation of two in-phase rf drives through a capacitive network. Variable capacitor C_v is used to adjust the rf ratio $\delta=V_2/V_1$.

Because of the exponential fall-off in intensity along the transverse plane of a Gaussian mode, a method for *in situ* control of the ion position is highly desired. While dc fields may achieve ion translation, the resultant displacement of the ion from the rf node incurs excess micromotion that broadens atomic transitions,[21] which limits the range and usefulness of dc translation. In contrast, micromotion-free translation can be achieved by shifting the quadrupole field node itself, as has been demonstrated recently,[9,14,17] by using multiple rf voltages applied to different trap electrodes. Here, we utilize multiple rf sources to achieve translation of the ion in the horizontal plane of a surface-electrode ion trap. Figure 3 shows our implementation for achieving two in-phase rf voltages through a passive network. Capacitances $C_1, C_2 \approx 30$ pF are intrinsic to the trap electrodes and cryostat wiring, as is $C_{12}\approx 3$ pF, which accounts for the intrinsic capacitive coupling between the two electrodes. We introduce a mechanically tuned capacitor $C_v=0.5-30$ pF (Voltronics Corp.) in order to adjust the ratio $\delta=V_2/V_1$, effecting node translation along $\vec{e}_y+\vec{e}_z$. With an initial height of 670 μm, the intensity variation is dominated by the displacement along y.

Figure 4 shows the change in shelving rate as the ion is translated along the y-axis, across the mode of the fiber. The dashed line represents a Gaussian beam shape indicating good qualitative agreement with the shelving rate profile. The beam waist ($1/e^2$-intensity) at the ion height of 670 μm has been measured independently using an identical fiber to be 50 μm, which is used to calibrate the y-axis in Fig. 4 assuming a linear relationship between y-displacement and δ. In units of the measured mode waist, the ion is brought to within 0.13 ± 0.10 of the mode center, despite an initial displacement of 3.34 ± 0.10 arising from trap construction.

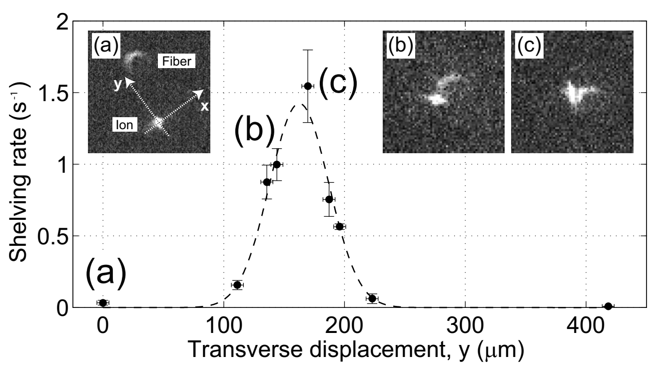

FIG. 4. Measurement of the mode profile of the integrated fiber using the ion as a probe. The dashed line is a fit to a Gaussian profile showing good qualitative agreement with the expected profile. Calibrating the transverse displacement by an independent measurement of the fiber mode, the initial fiber-ion offset is roughly 160 μm. Images show the relative position of a single ion and an unfocused image of the fiber.

CCD images show the ion displaced relative to the (unfocused) image of the fiber. In all measurements, the ion was positioned at the rf node by eliminating micromotion amplitude according to the correlation measurement technique.[21]

The ultimate precision of rf translation is limited by the stability and control of the relative amplitudes, and phase offsets between the multiple sources. The position uncertainty indicated in Fig. 4 is limited by the typical resolution of our imaging system to $\pm 5\ \mu\text{m}$ and is not fundamental to the rf node translation method. In our passive implementation, we expect a fractional variation in δ of $\sigma_\delta/\delta = 0.005\%/{}^\circ\text{C}$ given a typical temperature coefficient of $50\ \text{ppm}/{}^\circ\text{C}$ for C_v, while phase error θ arises from differential resistances of the two wire paths at 0.06° per differential ohm. With a 1 °C control in capacitor temperature and a sub-1° phase offset, our numerical simulations imply ~ 50 nm rms ion trajectory amplitude at the operational point (c) of Fig. 4. The sensitivity to rf control is trap design dependent, and may be reduced at the cost of total translational range.

With the ion centered in the mode, we have looked for effects of dielectric charging by the 674 nm fiber light.[3] In these tests, 125 μW of 674 nm light is coupled into the fiber while the amplitude of ion micromotion is recorded for several minutes to detect any dynamic shifts in the ion position due to a possible fiber-induced generation of charge. We observe induced fields of $\sim 10\ \text{V/m}$ by the fiber, with charging and discharging time constants of 1.6 ± 0.3 and 4.7 ± 0.6 s. Following initial generation, the micromotion amplitude remains constant for minutes, indicating saturation of fiber-induced charge.

In conclusion, we have demonstrated an ion trap with an integrated SM fiber for light delivery, and an *in situ* micromotion-free optimization of the ion-fiber spatial overlap. The fiber has been used to directly address the qubit transition of a single ion in the trap and, as such, the fiber-trap system represents a step toward optics-integration for large-scale QIP in surface-electrode designs. Moreover, our assembly is compatible with more advanced fiber systems, such as lensed fibers to achieve higher field intensities, or photonic crystal fibers that propagate all relevant lasers through a single integrated port. In a cryogenic environment, such an all-inclusive port may eliminate the requirement of free-space optical access, greatly reducing the heat load and enabling sub-Kelvin trap operation in a dilution refrigerator. An integrated trap that utilizes the fiber facet as one of the mirrors of an optical cavity could serve as a node in a distributed QIP architecture where the photon state can be extracted through the fiber.[1,12]

This work was supported by the IARPA SQIP program. T.H.K. was supported by the Siebel and Chorafas Foundations. P.F.H. is grateful for the support from the Carlsberg and Lundbeck Foundations.

[1] J. I. Cirac, P. Zoller, H. J. Kimble, and H. Mabuchi, Phys. Rev. Lett. **78**, 3221 (1997).

[2] J. Kim, S. Pau, Z. Ma, H. R. McLellan, J. V. Gates, A. Kornblit, R. E. Slusher, R. M. Jopson, I. Kang, and M. Dinu, Quantum Inf. Comput. **5**, 515 (2005).

[3] M. Harlander, M. Brownnutt, W. Hänsel, and R. Blatt, New J. Phys. **12**, 093035 (2010).

[4] G. R. Guthöhrlein, M. Keller, K. Hayasaka, W. Lange, and H. Walther, Nature (London) **414**, 49 (2001).

[5] P. F. Herskind, A. Dantan, J. P. Marler, M. Albert, and M. Drewsen, Nat. Phys. **5**, 494 (2009).

[6] G. Shu, N. Kurz, M. Dietrich, and B. B. Blinov, Phys. Rev. A **81**, 042321 (2010).

[7] A. Wilson, H. Takahashi, A. Riley-Watson, F. Orucevic, P. Blythe, A. Mortensen, D. R. Crick, N. Seymour-Smith, E. Brama, M. Keller, and W. Lange, arXiv:1101.5877 (unpublished).

[8] E. W. Streed, B. Norton, A. Jechow, T. J. Weinhold, and D. Kielpinski, Phys. Rev. Lett. **106**, 010502 (2011).

[9] A. P. VanDevender, Y. Colombe, J. Amini, D. Leibfried, and D. J. Wineland, Phys. Rev. Lett. **105**, 023001 (2010).

[10] G. R. Brady, A. R. Ellis, D. L. Moehring, D. Stick, C. Highstrete, K. M. Fortier, M. G. Blain, R. A. Haltli, A. A. Cruz-Cabrera, R. D. Briggs, J. R. Wendt, T. R. Carter, S. Samora, and S. A. Kemme, Appl. Phys. B: Lasers Opt. (2011).

[11] P. F. Herskind, S. X. Wang, M. Shi, Y. Ge, M. Cetina, and I. L. Chuang, arXiv:1011.5259v1 (unpublished).

[12] J. Kim and C. Kim, Quantum Inf. Comput. **9**, 0181 (2009).

[13] C. Schneider, M. Enderlein, T. Huber, and T. Schaetz, Nat. Photonics **4**, 772 (2010).

[14] P. F. Herskind, A. Dantan, M. Albert, J. P. Marler, and M. Drewsen, J. Phys. B **42**, 154008 (2009).

[15] R. Blatt and D. J. Wineland, Nature (London) **453**, 1008 (2008).

[16] H. Margolis, G. Barwood, G. Huang, H. A. Klein, S. Lea, K. Szymaniec, and P. Gill, Science **306**, 1355 (2004).

[17] T. H. Kim, P. F. Herskind, T. Kim, J. Kim, and I. L. Chuang, Phys. Rev. A **82**, 043412 (2010).

[18] P. B. Antohi, D. Schuster, G. M. Akselrod, J. Labaziewicz, Y. Ge, Z. Lin, W. S. Bakr, and I. L. Chuang, Rev. Sci. Instrum. **80**, 013103 (2009).

[19] M. Brownnutt, V. Letchumanan, G. Wilpers, R. C. Thompson, P. Gill, and A. G. Sinclair, Appl. Phys. B: Lasers Opt. **87**, 411 (2007).

[20] H. G. Dehmelt, Bull. Am. Phys. Soc. **20**, 60 (1975).

[21] D. J. Berkeland, J. D. Miller, J. C. Bergquist, W. M. Itano, and D. J. Wineland, J. Appl. Phys. **83**, 5025 (1998).